Combustion of pulverized biomass : impact of fuel preparation and flow conditions

Hassan Mohanna

THESE

Pour obtenir le diplôme de doctorat

Spécialité Physique Energétique
Préparée au sein de l'INSA Rouen Normandie

COMBUSTION OF PULVERIZED BIOMASS
IMPACT OF FUEL PREPARATION AND FLOW CONDITIONS

Présentée et soutenue par
Hassan MOHANNA

Thèse soutenue le 16 décembre 2020 devant le jury composé de		
M. Sylvain SALVADOR	Professeur, EMAC, Albi	Rapporteur
M. Nasser DARABIHA	Professeur, EM2C, Centrale Supélec	Rapporteur
M. Alexis COPPALLE	Professeur, CORIA, INSA Rouen Normandie	Examinateur
Mme. Céline MORIN	Professeur, Université Polytechnique Hauts-de-France	Examinatrice
M. Christophe PROUST	Directeur de recherche, INERIS	Examinateur
M. Benoit TAUPIN	Expert combustion, Veolia Recherche et Innovation	Examinateur
M. Jean-Michel COMMANDRE	Chercheur, Directeur de l'unité de recherche, CIRAD	Co-directeur de thèse
M. David HONORE	Professeur, CORIA, INSA Rouen Normandie	Directeur de thèse

Thèse dirigée par David Honoré Professeur CORIA - INSA Rouen Normandie et Jean-Michel Commandré Directeur de l'Unité de Recherche BioWooEB - CIRAD

INSA INSTITUT NATIONAL DES SCIENCES APPLIQUÉES ROUEN NORMANDIE

ED PSIME

CORIA UMR 6614

cirad

VEOLIA

ACKNOWLEDGEMENTS

At the end of this journey, almost four years past with their all ups and downs, I look back and see how valuable and exciting this experience was. One of the joys of the end is to look over the journey and remember all the people who supported me along this road and contributed to the completion of this project.

This work was carried out within the PTI pole of VERI in Limay, the BioWooEB team at CIRAD in Montpellier, and the Reactive flow team at CORIA in Rouen. I thank all the members of these three teams for welcoming me and for granting me endless assistance and happiness during my various stays.

First of all, I would like to express my sincere gratitude to my supervisor Prof. David Honoré for his guidance and fruitful discussions throughout the last years. Your presence and help during the last experiments showed your dedication and motivation for this work. Your availability and unfailing positivism have often made it possible to overcome the difficulties that marked the end of this thesis.

My deepest thanks to my supervisors at CIRAD, Dr. Jean-Michel Commandré, Dr. Bruno Piriou and Dr. Gilles Vaitilingom for their guidance, assistance, and friendship. I will always remember our rides to Albi and our long valuable discussions. This thesis is the result of your encouragement and confidence in my ideas.

My heartfelt gratitude goes to you Benoît who was not only my scientific supervisor at Veolia but also a real friend. Your great support, patience, humor and encouragements were the most needed in difficult times. I learned a lot from you and this project could not be finished without you. I also thank Gabriel Teixeira who helped me during the first year and positively influenced my scientific approach to the subject.

I thank VEOLIA for having funded my thesis work. A thought goes particularly to François Nicol and Franck Gelix who gave me the opportunity and trusted me during this work. Thank you for everything. Obrigado to Alexandre Lima for his great leadership spirit managing the project and providing us with all the necessary means to fulfill our objectives.

Many thanks to Sylvain Salvador and Nasser Darabiha for the honor they have done me by agreeing to be rapporteurs for this work. It gives great value to my work to be judged by professors of your quality.

My stay at CIRAD was one of the best periods during this thesis, personally and scientifically. I made a lot of friends and learned so much from their interests and cultures. Maria Jose, Luke, Gwendal, Adrian, Luis, Eleanora, Huynh and Sébastian. Shukran, Merci, Thanks, Gracias, Grazie, Cảm ơn bạn for every one of you. I will certainly remember all of the happy moments with you. All the meals, evenings, pause cafés, Rosetta board, football games... Many thanks also to Charlene and Jeremey for your advice and technical assistance during the experiments. It was a real pleasure to share these many moments spent by your side.

To the combustion team (launch team and board games team) at VERI: Alexandre, Benoit, Patrick, David, Nicolas, Thomas. I am grateful for the chance to be part of this family. Thank you for your support, friendship and the great working environment that you offered and

continue to offer after the thesis. And special thanks to Patrick for the technical assistance every day and the assistance on the pilot scale experiments. I must thank also the REI team at VERI: Fabien Roy, Romuald Malin, Cristophe Lemazier and Franck Louise-Adele for their suggestions and appreciated work on the pilot facility.

A big thank also to all the members of CORIA who worked with me on the pilot scale experiments. Many thanks to all the workshop technicians through Benjamin Quevreux for the quality work they have done fabricating the burner. Thanks also to Thierry Muller, Carole Gobin and Franck Lefebvre for their invaluable help installing the optical assembly on the reactor. Special thanks to all the Ph.D students in CORIA, especially Nelson and Petra, for their welcoming spirit that made my visits to CORIA a real pleasure.

And to whom I have shared my life with the last years, Hussein and Zakaria, I am deeply indebted to you for life, thank you for everything.

Thanks go to all my university friends Mahdi Mahdi, Mohammad Jradi, Daniel Sayegh, and the three Ali's (Bzeih, Khalil, and Atwi) and the three Hassan's (Atwi, Itewi, Ahmad) who have always been by my side. My friends in Montpellier: Hassan Bazzé, Ibrahim El Moussawi and the three Hussein's (Hussein, Saied and Fneish), and my dear friends in Paris Zeina, Nour, Ali, May and Ibrahim, you have been a source of joy and endless happiness. I am extremely grateful for having you all in my life.

I could never accomplish this success without the love and support of my family. Mama and Baba, thank you for your endless love and continuous prayers. To my siblings Hussein, Mohammad, Mohana, Riham, Zeina, thank you for being by my side every step in this road, encouraging, caring and comforting me despite the distance.

Finally, I end this acknowledgment by the one who made me a better man, my beautiful Laila. Although you weren't there from the beginning, you managed to be at the center of it all. Your touch can be found in every word in this thesis. Thank you for the love, joy and the mercy you bring to my heart.

If you have something like wood and oxygen. The oxygen comes and hits the carbon in the wood, but not hard enough. It just goes away.

*But if you can get it faster, by heating it up, somehow, some way, they come close enough to the carbon and **SNAP IN**, and that gives a lot of jiggly motion. Which might hit some other atoms making those go faster so they can climb up and bump against other carbon atoms and they jiggle, and make others jiggle, and you get a terrible catastrophe.*

THAT CATASTROPHE IS FIRE!

Richard Feynman

Table of Contents

Abbreviations

CFD	Continuum Fluid Dynamics
db	Dry Basis
DNS	Direct Numerical Simulation
DOM	Discrete Ordinate Model
DPM	Discrete Phase Model
DTF	Drop Tube Furnace
DRW	Discrete Random Walk
DW	Demolition Wood
FC	Fixed Carbon
HHV	Higher Heating Value
HTR	Horizontal Tubular Reactor
LES	Large Eddy Simulation
LHV	Lower Heating Value
PAFR	Primary Air Fuel Ratio
PCS	Particle Combustion Shadowgraphy
Pine	Raw Pine
Pin-T	Torrefied pine
Pin-P	Pyrolyzed pine
Pin-C	Carbonized pine
PSD	Particle Size Distribution
RANS	Random averaged Navier Stokes
RTE	Radiative Transfer Equation
Rxn	Reaction
SF	Shape Factor of a particle

TGA Thermogravimetric Analysis

VM Volatile Matter

Nomenclature

A surface area (m^2)

A_C Frequency factor for heterogeneous oxidation (kg $m^{-2}.s^{-1}.Pa^{-1}$)

A_V Frequency factor for devolatilization (s^{-1})

C Char content (kg of char / kg of particles)

C_D Drag coefficient

C_p Specific heat at constant pressure

C_{sw} Swelling coefficient

D_r Inner diameter of the reactor

D_{O_2} Mass diffusivity of oxygen ($m^2\ s^{-1}$)

D_w Mass diffusivity of water in the gas mixture ($m^2\ s^{-1}$)

d_P Particle diameter (m)

e_t Total specific energy (J kg^{-1})

E_C Activation energy for heterogeneous oxidation (kJ mol^{-1})

E_V Activation energy for devolatilization (kJ mol^{-1})

$f_{w,0}$ Initial mass fraction of water in a particle

$f_{v,0}$ Initial mass fraction of volatiles in a particle

f_{char} Initial mass fraction of fixed carbon in a particle (char)

F_j Volume force acting on the fluid in j-direction

g Gravitational acceleration (9.81 $m.s^{-2}$)

h Coefficient of heat transfer convection

H_C Heat of heterogeneous combustion (J kg^{-1})

H_w Enthalpy of vaporization of water (J kg^{-1})

I Radiant intensity (W m^{-2} sr^{-1})

I_b Black body intensity (W m^{-2} sr^{-1})

k_0 Frequency factor for volatiles reactions (s^{-1})

K_C Specific char oxidation rate ($kg.m^{-2}.s^{-1}$)

K_{diff} Specific oxygen diffusion rate coefficient (kgm^{-2} s^{-1} Pa^{-1})

K_v Devolatilization rate (s^{-1})

K_w Moisture releasing rate (s^{-1})

L_r Length of the reactor

m Mass (kg)

M Molecular mass ($g.mol^{-1}$)

n Apparent reaction order

N Number of measured points

Nu Nusselt number

p Pressure (Pa)

Pr Prandtl number

P_{O_2} Partial pressure of oxygen (Pa)

P_{sat} Vapor saturation pressure (Pa)

q_i Energy flux in energy equation (J m^{-2})

$\dot{Q}$ Heat source term in energy equation (J m^{-3})

$\vec{r}$ Position vector

R Universal gas constant (J mol^{-1} K^{-1})

Re Reynolds number

R_i Reaction rate of reaction i

$\vec{s}$	Direction vector
Sc	Schmidt number
Sh	Sherwood number
t	Time (s)
T	Temperature (K)
Ta	Activation temperature (K)
U	Unburnt fraction
u_p	Particle velocity (m s^{-1})
u_g	Gas phase velocity (m s^{-1})
m	Velocity component in i-direction (m s^{-1})
$\bar{u}_i$	Mean fluid phase velocity in i-direction (m s^{-1})
u'_i	Velocity fluctuations in i-direction (m s^{-1})
V_P	Particle volume
V	Volatiles content (kg of volatile matter / kg of particles)
V_k	Diffusion velocity of species k
W	Moisture content (kg of water / kg of particles)
x_i	Coordinate axis in i-direction (m)
X_w	Water fraction in the gas phase
Y_k	Mass fraction of species k
β	Radiative extinction coefficient (m^{-1})
λ	Thermal conductivity (W m^{-1} K^{-1})
δ	Deviation function between experimental and numerical values of oxygen
δ_{ij}	Kronecker delta
μ	Viscosity (kg m^{-1} s^{-1})
υ_c	Stoichiometric ratio of heterogeneous oxidation (kg O_2 / kg C)

υ_k Stoichiometric coefficient of oxidation reactions of species k (Kg species k / Kg O_2).

ρ Density (kg m^{-3})

ρ_p Particle density (kg m^{-3})

∅ Molar fraction of CO in the char oxidation reaction

Φ Scattering phase function (sr^{-1})

ε Particle emissivity

κ Radiative absorption coefficient (m^{-1})

σ Stefan–Boltzmann constant (5.67×10^{-8} W m^{-2} K^{-4})

σ_s Radiative scattering coefficient (m^{-1})

$\dot{\omega}_k$ Production rate of species k (kg m^{-3} s^{-1})

τ Particle relaxation time

τ_{ij} Viscous stress tensor

Subscripts

exp Experimental value

calc Calculated value

g Free gas stream

k gas species

O_2 Oxygen

p Particle

r Reactor

s Particle surface

v Volatiles

w Water

0	Initial values at injection (t = 0)

Background

Biomass is a renewable energy source, referring to materials of biological origin from agriculture, forestry, fishing and aquaculture, as well as biodegradable industrial and municipal wastes. All these sources are carbon neutral because they are derived from plants that absorbed CO_2 from the atmosphere when they were growing, therefore they do not contribute to the release of additional CO_2 to the environment. The abundance and sustainability of these sources present biomass as an important fuel for energy production in the view of the increasing demand of energy. This beside the threat of the environmental impact of fossil fuels and the increasing anxiety about their availability at economically acceptable cost, drive the global interest in biomass as a potential fuel for the energy transition. In 2016, biomass represented more than 49.4% of the primary production of renewable energy in the European Union, which places it at the forefront of the renewable energies used in the area, ahead of solar, hydraulic or wind [1].

Employing biomass in the energy sector can raise environmental concerns, as it leads to increasing use of land and resources [2]. Also, it can be linked to deforestation in some areas [3]. However, official European reports estimate that the primary potential of biomass in Europe represents 15-16% of the projected energy consumption of the EU in 2030 [4]. This significant amount of available biomass can support ambitious renewable energy targets under the current environmental constraints. At present, one of the main challenges is to develop efficient recovery sectors for dry biomass like recycled wood, which has gone beyond its primary use and is in plentiful supply, thus avoiding hundreds of thousands of tons of biomass from going to landfills.

Biomass can fuel the energy sector by directly burning it through direct combustion, or turning it into intermediate fuels through Gasification, Pyrolysis, Torrefaction, and Anaerobic Digestion. Direct combustion in a furnace is the most common method of producing heat from biomass that heats water to generate hot water or steam. Currently, most of the solid fuel power plants burn coal in pulverized mode to generate heat. The pulverized combustion mode is actually considered as the most efficient, the excess air can be kept very low. To reduce the CO_2 footprint of these power plants, the incorporation of a fraction of biomass with coal can be an effective solution. This reduces the dependence on fossil fuels and helps secure the supply of energy. Several coal power plants have been subject to cofiring projects. In Lodz in Poland, three cogeneration units have been installed on existing coal-fired power plants, making the co-combustion of coal and biomass from regional forestry operations possible [5]. In addition, some coal power plants even totally converted their consumption to biomass-derived fuels. Thunder Bay Unit 3 in Ontario [6] and Boardman power plant in Portland [7] entered service operating on 100 percent biomass instead of coal. Other power plants around the world are following the lead.

However, the co-firing process is largely dependent on the flame structure, which in turns is mainly driven by the biomass characteristics. This can significantly change the operation of the boiler. As a result, a better understanding of the combustion of pulverized biomass is important in the dual objectives of improving the energy efficiency and reducing the environmental impact.

Objectives

The pulverized combustion of solids has been widely studied but mainly in the case of coal and to a lesser extent for biomass, which is relatively recent. Therefore, the scientific knowledge is more limited on the characterization of reaction mechanisms involved in the pulverized biomass combustion, and more rarely is the nature of the flow involved in those studies.

The prediction of the behavior of new fuels – such as biomass – in industrial pulverized combustion systems requires an improvement of the understanding of the involved phenomena. For this purpose, this thesis aims to study the impact of biomass characteristics and its pretreatment on the kinetics of thermal conversion and burning at the particle scale. We also attempt to understand the heat and mass transfer phenomena, identify heterogeneous and homogeneous chemical reactions, and take into account the turbulent nature of the two-phase flow and every coupled phenomena encountered throughout the complex environment of the flame.

We investigate two areas of study in this thesis:

– Investigation at the particle scale

- Physicochemical nature of the biomass
- Experimental determination of intrinsic kinetics of combustion and the impact of the fuel nature
- Morphological evolution of the particle during the combustion,
- Obtaining experimental input data to model turbulent combustion in industrial flames

– Investigation of the turbulent flame of a cloud of particles

- Non-intrusive characterization of the flow structure and the reaction zone
- Analysis of the effect of volatile matter content on the flame structure
- Analysis of the effect of particle size on the flame structure
- Geometry of the combustion system.

This work is new in terms of experimental methods used for the combustion of biomass at particle and flame scale. The idea of studying both particle and flame scales is not usually found in one single project. Studies on pilot scale reactors usually rely on previous studies of characterization of biomass. Similarly, in the absence of data at particle scale, CFD numerical models adopt different assumptions and simplifications without evaluating the collective influence of the sub-models on the predicted results. In this study, we try to build up our knowledge of the combustion of biomass from a single particle scale to a flame scale. Numerical and experimental methods at particle scale are used to develop a model to simulate the flames of pulverized biomass and validate them experimentally. This methodology is important to draw a complete analysis of the combustion of pulverized biomass.

Scope of the thesis

The methodology of the thesis is based on two axes of research: particle scale and flame scale. *Figure S.1* summarizes the methodology of investigation used in the study.

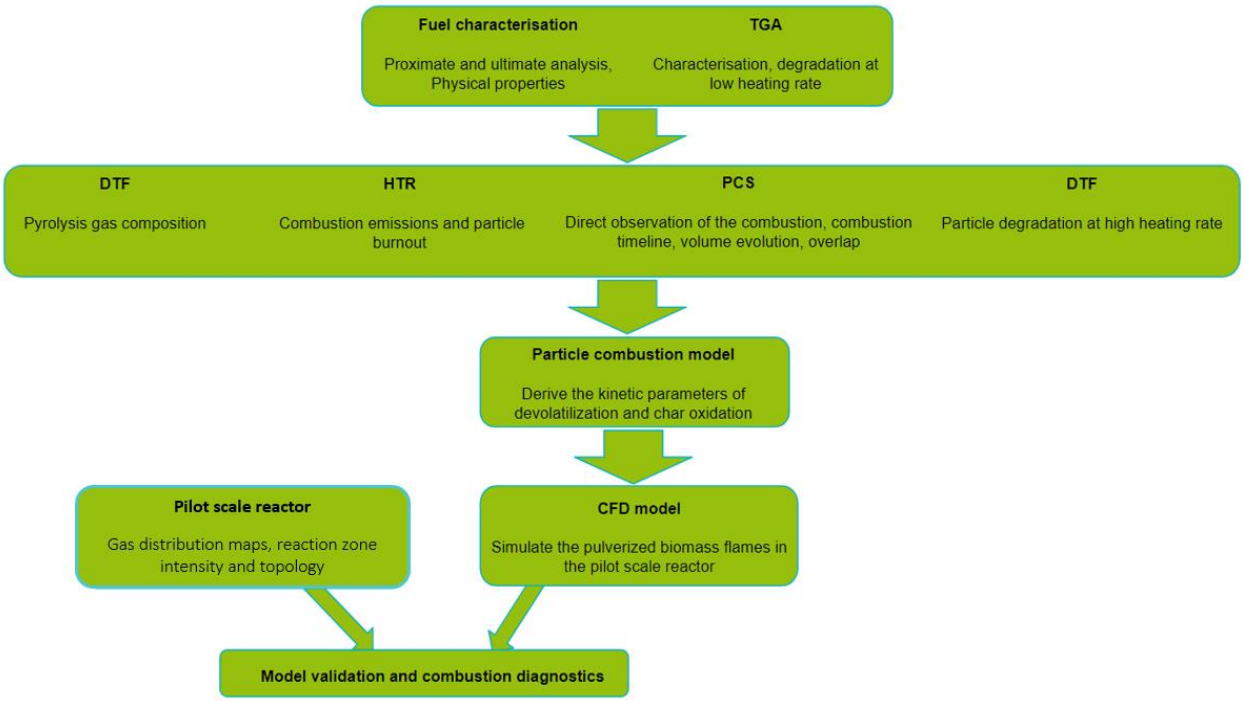

Figure S.1: A schematic figure of the methodology of investigation used in the study

The first part of the thesis is dedicated to investigate the combustion of a single particle of biomass and to compare the behavior of different fuel types and granulometry at high temperatures. This part is conducted in CIRAD BioWooEB in Montpellier, France. Five types of biomass are prepared containing different volatile matter content. Coal also is tested for comparison. The study is conducted using different experimental methods to uncouple the included phenomena:

1. The mass degradation at low heating rates is followed in the **macro-TGA** in order to characterize the fuels and compare their degradation curves.
2. The combustion emissions are measured along with the progress of the degradation process in a **horizontal tubular reactor (HTR)**.
3. Direct observation of the combustion of a single particle of biomass is performed in a specially designed apparatus using direct and shadowgraphy imaging techniques **(Particle combustion shadowgraphy (PCS))**.
4. Pyrolysis and combustion gas composition and the mass degradation at high heating rates are measured in a **drop tube furnace (DTF)**.

The experimental observations are used to develop and validate a numerical model simulating the combustion of a single isolated particle in the drop tube furnace. The model is coded on Matlab. It optimizes the numerical results to replicate the experimental data in order to determine the kinetic parameters of combustion and devolatilization of each tested fuel.

The second part of the thesis is conducted in Veolia Research and Innovation Center in Limay, France in collaboration with CORIA laboratory in Rouen, France. In this part, we develop a 20 kW pilot scale reactor capable of simulating the environment of industrial furnaces. The vertical reactor is equipped with a specially designed bluff-body burner fabricated by CORIA. Long jet flames of three types of biomass are studied using experimental and numerical methods:

1. The experimental methods include gas probing, temperature measurements and OH* chemiluminescence imaging.
2. The numerical study consists of implementing the single particle combustion model, developed in the first part of the thesis, in a CFD ANSYS Fluent model of the pilot scale facility.

The experimental data of the particle scale investigation are used to adjust the parameters of the CFD model simulating the flames of pulverized biomass. The CFD model calculate the particle history using the particle combustion model developed at particle scale. The results of the model are then validated by the experimental results of gas measurements collected in the reactor. The OH* chemiluminescence imaging can be compared to the reaction zone predicted by the model. Once validated, the experimental and numerical results are used to analyze the structure of the flame and the behavior of the particles within it. This shall be compared to the conclusions of the first part of the thesis to evaluate the approach followed in this study.

The thesis consists of eight chapters.

Chapter 1 introduces the properties of biomass and the fundamentals of its combustion. The combustion technologies are presented and compared to lay the ground for our choice of studying the combustion of biomass in pulverized mode. After that, the literature is reviewed for the experimental investigation of the combustion of biomass at particle and flame scale.

Chapter 2 presents the experimental methods used at particle scale: thermogravimetric analysis, horizontal tubular reactor, drop tube furnace and particle combustion shadowgraphy. The experimental procedures and the methodology of the treatment of experimental results are explained in this chapter.

Chapter 3 describes the experimental methods at flame scale. The methodology of design of the pilot scale reactor and the criteria of the design of the bluff-body burner are explained. We first review the characteristics of some pilot scale reactors used previously for the combustion of pulverized biomass flames. This chapter also explains the choice of materials of the pilot scale reactor and its fabrication process. In addition, the measurement techniques implemented in the pilot scale facility are all listed and described.

Chapter 4 concentrates on the modeling of the combustion of a single particle of biomass and the biomass flames using computational fluid dynamics. The different sections introduce the main equations and the adopted sub-models that describe the combustion of pulverized biomass in a reactive flow. The experimental data of the particle scale investigation are used to tune the numerical models.

The following chapters represent the results of the thesis.

Chapter 5 discusses the experimental results of the six tested fuels at particle scale. The degradation process is studied at low (TGA experiments) and high heating rates (Drop tube

furnace, Horizontal Tubular Reactor and Direct Visualization Chamber). Pyrolysis gas composition, combustion emissions and direct observation of each fuel type are presented, compared and discussed thoroughly.

This gives way for **Chapter 6**, which presents the numerical results of the combustion of a single particle of biomass in the drop tube furnace. The results in chapter V are used to tune the particle combustion model presented in chapter IV. The model predictions are compared to the experimental data in the drop tube furnace. The identified kinetic parameters are listed here and compared to the ones reported in literature. This chapter also contains a sensitivity study of the determined kinetic parameters to the adopted sub-models of the volume evolution scenario and drag coefficient model of the particle.

Chapter 7 includes the experimental results of the flames in the pilot scale reactor and the predictions of the CFD model. The results in chapter V and chapter VI are used to tune the CFD model presented in chapter IV. A detailed description of the aerodynamics generated by the burner and the particles history is presented in this chapter. Flame development, temperature fields and gas distribution contours are also addressed.

Finally, **Chapter 8** presents the main conclusions that were drawn at particle and flame scale, and discusses some observed links between both scales.

Chapter I. Literature review on pulverized biomass combustion

This Chapter introduces the properties of biomass and the fundamentals of its combustion. The combustion technologies are presented and compared to lay the ground for our choice of studying the combustion of biomass in pulverized mode. After that, the literature is reviewed for the experimental investigation of the combustion of biomass at particle and flame scale.

I.1 Introduction

Energy storage has always been one of the serious problems of the world. Many different renewable energy resources are continuously being developed and employed but with no way of storing the excess energy in the times of peak production. However as usual, nature offers a solution through its natural energy storehouse consisting of the plant life, which transforms solar and chemical energy to produce and store the so-called biomass energy using the process of photosynthesis. In our struggle towards a green energy dependent world, biomass represents a good alternative for the limited fossil fuels as it is considered a renewable clean energy that can contribute to reduce the greenhouse gases emissions.

The abundant and sustainable resources of biomass can be cultivated in several ways including biochemical (ex: fermentation) and thermochemical (pyrolysis, gasification, combustion) conversion techniques to either produce biofuels or directly generate useful heat. In many countries, biomass is a growing energy sector in the recent years for what it represents of local economic development and easy-to-reach fuel, despite the low public awareness of biomass as a form of renewable energy with respect to other forms like solar and wind that are more recognized [2], [3], [8].

The ability of being used in the existing infrastructure of energy production is a great advantage of biomass energy. While biogas and bio-oil can be burned in usual internal combustion engines, direct combustion or co-combustion in pulverized form is also possible with great potentials. The latter technique includes many complex phenomena of homogenous and heterogeneous reactions influenced by the fuel properties, which vary in the view of the huge diversity of feedstock. The flexibility to fuel composition is then demanded while keeping efficient combustion and low emissions of pollutants in order to increase its large-scale implementation. For this purpose, we attempt to study the thermochemical conversion of pulverized biomass through direct combustion and to understand the impact of fuel preparation and flow conditions.

I.2 Biomass fuel properties

I.2.1 Biomass basic constituents

Biomass is a general term defining a wide range of biodegradable materials originated from agricultural sources, animals, industrial and municipal wastes. As part of our study, we are particularly interested in the so-called lignocellulosic biomass (wood in particular) and industrial wastes. Lignocellulosic biomass can be produced by dedicated crops, called energy crops, agricultural and forest residues from forestry and from livestock farming (manure, slurry, etc.). Whereas industrial wastes include what is refused from factories like graphite waste and used products like demolition wood and car tires.

The name of lignocellulosic biomass is derived from its basic constituents namely: hemicellulose, cellulose and lignin. These biopolymers are linked by alkoxy bonds (380-420 kJ/mol) that break up upon heat. They are arranged in a very complex way inside the biomass structure. *Figure I.1* shows the structure of a lignocellulosic biomass. Cellulose is concentrated inside the fiber; the outer walls of the fiber are composed mainly of lignin and hemicelluloses and the inter-fiber joining lamellae are composed mostly of lignin [9].

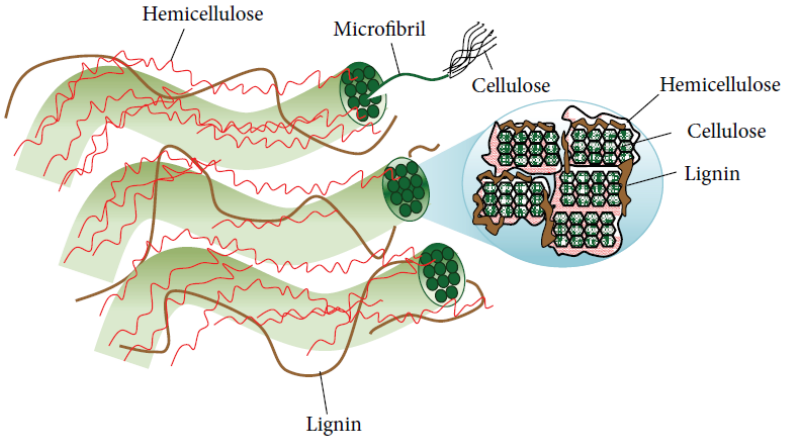

Figure I.1: Plant cell wall structure and micro-fibril cross-section (strands of cellulose molecules embedded in a matrix of hemicellulose and lignin) [10]

I.2.1.1 Cellulose

Cellulose (*Figure I.2*) is the most abundant renewable organic resource on Earth and is widespread in plants, bacteria, marine algae, and other biomass. It is a polysaccharide consisting of a linear chain of several hundred to many thousands of β(1→4) linked D-glucose units forming three-dimensional linear molecular composed of the crystalline regions and the amorphous regions [11]. It is an important structural component of the primary cell wall of green plants. Cellulose is usually assumed as $(C_6H_{10}O_5)_n$ in most biomasses. [12]

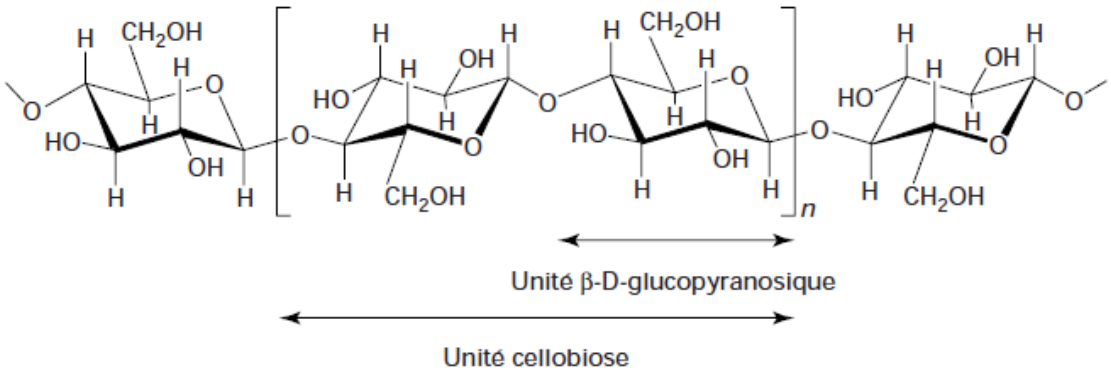

Figure I.2: Cellulose chemical structure [13]

I.2.1.2 Hemicellulose

Hemicellulose (*Figure I.3*) is a polysaccharide related to cellulose that comprises about 20% of the biomass of most plants. In contrast to cellulose, hemicellulose is derived from several sugars in addition to glucose, especially xylose but also including mannose, galactose, rhamnose, and arabinose [14]. Hemicellulose consists of shorter chains – between 500 and 3000 sugar units in a three-dimensional inhomogeneous molecular with a small crystalline region [11]. Furthermore, hemicellulose is branched, whereas cellulose is unbranched. An elemental formula is usually attributed to hemicellulose in all biomasses as $(C_5H_{10}O_5)_n$ and sometimes it is approximated as a xylose polymer $(C_5H_8O_4)_n$ [12]. However, the composition of polysugars that form the hemicellulose fractions is very different between different plants and wood types [15]. These compositions react differently when heated, so that reducing hemicellulose to xylose is not always a good approximation.

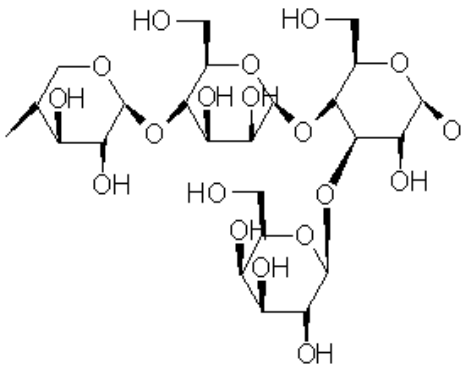

Figure I.3: Hemicellulose chemical structure [16]

I.2.1.3 Lignin

Lignin (*Figure I.4*) is an amorphous, inhomogeneous, nonlinear three-dimensional polymer [11]. It is a product of polymerization of three types of monolignols, i.e. pcoumaryl, coniferyl, and synapyl alcohols, incorporated into lignin in the form of p-hydroxyphenyl (H type lignin), guaiacyl (G type lignin), and syringyl (S type lignin), respectively [17]. The elemental formulas of H, G and S type lignin are $C_9H_{10}O_2$, $C_{10}H_{12}O_3$ and $C_{11}H_{14}O_4$, respectively [12]. Other characterization of lignin is also proposed by Ranzi et al. [12] to ensure the adoption of different reference components to the complex chemical structure of lignins: this means that the lignins are approximated by a mixture of reference components. They are identified by LIG-C, LIG-O, and LIG-H, which recall their characteristic of being richer in carbon, oxygen, and hydrogen, respectively. Lignin is not very sensitive to biological degradation and contributes to the natural protection of plants against certain parasitic attacks [11].

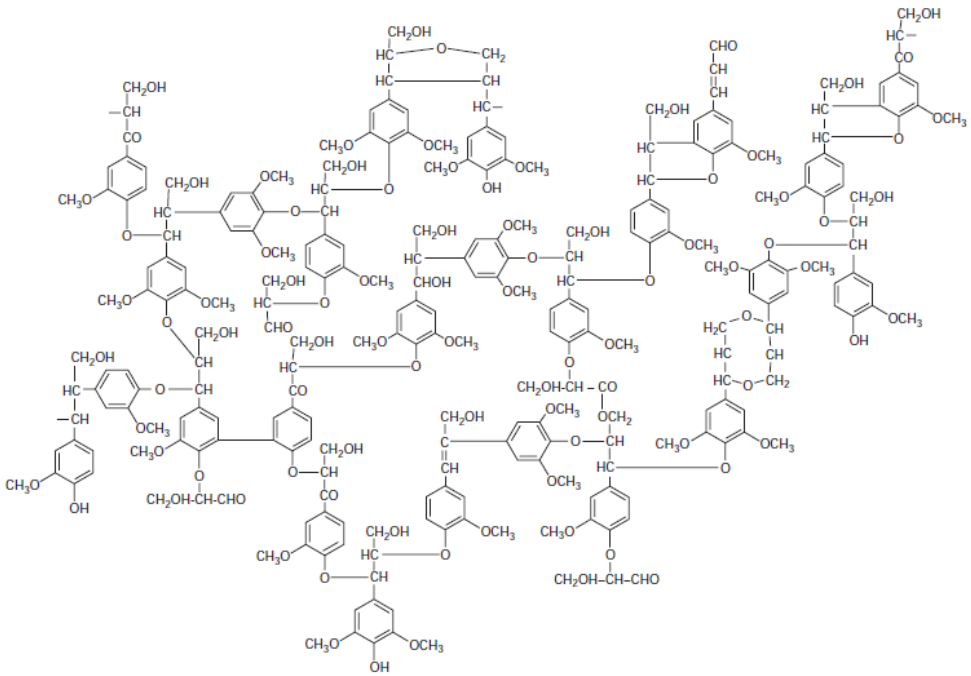

Figure I.4: Lignin chemical structure [13]

In addition to these elements, biomass can contain from 5 to 30% (by mass) of extractives (tannins, resins oils, etc.) that are soluble in either water or ethanol during exhaustive extraction

and they are released at temperatures below 200 °C [18]. Moreover, the ash contains inorganic constituents such as Aluminum, Silicium, Phosphor, as well as transition metals (Fe, Mn, Ni, etc.), alkali metals (K, Na) and alkaline earth metals (Ca, Mg) which can interfere in the thermochemical reactions as catalyzers or inhibitors. Fuentes et al. [19] made a survey of the influence of biomass mineral matter in the thermochemical conversion of short rotation willow coppice. The yields and distribution of pyrolysis products have been influenced by the presence of the catalysts. Most notably, both potassium and phosphorous strongly catalyzed the pyrolysis, modifying both the yield and distribution of reaction products. Results show that char combustion is catalyzed by all the metals, while phosphorus strongly inhibits the char combustion. Certain minerals like potassium and phosphorus have a large influence on tar composition. Ash quantity and composition can lead to slagging and fouling problems so it should be taken into consideration when designing the furnaces and the post treatment system.

Biomass composition strongly varies by species (*Table I.1*; *Table I.2*), but also by multiple parameters such as soil type, growing conditions, tree age, or slaughter period. Variations can be found even within different parts of the same plant (see pine branches and pine roots in *Table I.1*). This explains the disparity of characterization of biomass types found in literature.

biomass	Cellulose (%)	Hemicellulose (%)	Lignin (%)
Wheat straw	33,2	24	15,1
Rape straw	37,6	31,4	21,3
Pine branches	36,9	33,7	35,0
Pine roots	44,6	25,6	31,3
Rice husk	30,8	15	26,4
Poplar	48,3	22,5	21,5
Beech	46,3	19,4	25,2
Miscanthus	45,7	22,8	20,2
Ash wood	39	21,9	26,3
soft wood	40,1	26,7	33,2
hard wood	49,8	33,2	17

Table I.1: Lignocellulosic constituents of some biomass types [12] [20]–[23]

I.2.2 Proximate and ultimate analysis:

The used methods for biomass characterization are mostly adapted from those used for coal characterization. Proximate and ultimate analyses are determined experimentally to represent the quality of the biomass. Proximate analysis gives the volatile matter, moisture, fixed carbon and ash composition. Ultimate analysis gives results that are more comprehensive on the elemental composition of the fuel (i.e. C, H, N, and O). Biomass usually has high moisture content so it is better represented on dry basis. Volatile matter is the major constituent (up to 84 %m db) in biomass that is mainly released by the degradation of cellulose and hemicellulose. All hydrogen, nitrogen and oxygen are considered as volatiles while a part of carbon concentrates as fixed carbon in the char. Oxygen forms up to 45% of biomass, which reduces its heating value. Compared to coal, biomass has low sulfur content while nitrogen is generally lower except some cases like fermentation and grain residues.

	Ultimate Analysis				Proximate Analysis			
biomass	C	H	N	O	Moisture	Volatiles	fixed Carbon	Ash
Wheat straw	47,7	6	0,5	44,4	8	71,7	15,1	5,2
Rape straw	44,5	6,4	-	45,2	3,7	76,5	12,1	3,7
Pine	48,5	6,5	0,2	43,2	8,5	81,5	9,7	0,1
Miscanthus	38	6,21	0,6	50,6	11,3	83,3	12,3	4,4
Willow	49,1	5,8	0,5	44,6	6	84,4	15,1	0,5
Rice husk	31,6	5,2	0,7	37,8	8,4	65,3	10,04	24,6
Poplar	45,7	5,8	0,2	45	8,2	82,6	14,2	3,2
Olive stone	42,6	6,5	0,1	50,3	8,83	72,2	27,2	0,6
Nut shell	43,4	6,4	0,2	49,8	10,95	78,7	21,1	0,3
Eucalyptus	48,7	5,7	0,2	42,4	5,9	88,3	8,7	3
Saw dust	47,5	5,9	0,1	39,2	6,7	78,4	14,4	0,5
Fermentation residue	70	4,8	1,5	31,1	14,7	60,4	17,6	7,3
Grain residue	40,3	5,4	2,1	33,5	12,1	66,2	15,5	6,2
Sewage sludge	38,6	5,9	0,9	20,6	5,9	61,2	7,9	25
Oak Sawdust	44,1	5,5	0,2	39,8	10	78,8	14,7	0,4
Norway spruce	48,1	5,6	0	36,3	5,8	79	11,1	4,1
Bagasse	55,6	7,3	1,3	35,7	7,2	67,1	5,6	20,1

Table I.2: Proximate and ultimate analysis of biomass [21], [23]–[32]

I.2.3 Classification of biomass

Classification criterions are suggested to account for the huge variety of biomass. Van Krevelen diagram (*Figure I.5*) classifies the fuel according to their H/C and O/C atomic ratios [33]. Fuels lie in the same cluster on the diagram are said to have similar characteristics. It was originally set for coal but Chen et al. [34] verified that it could be successfully employed for biomass.

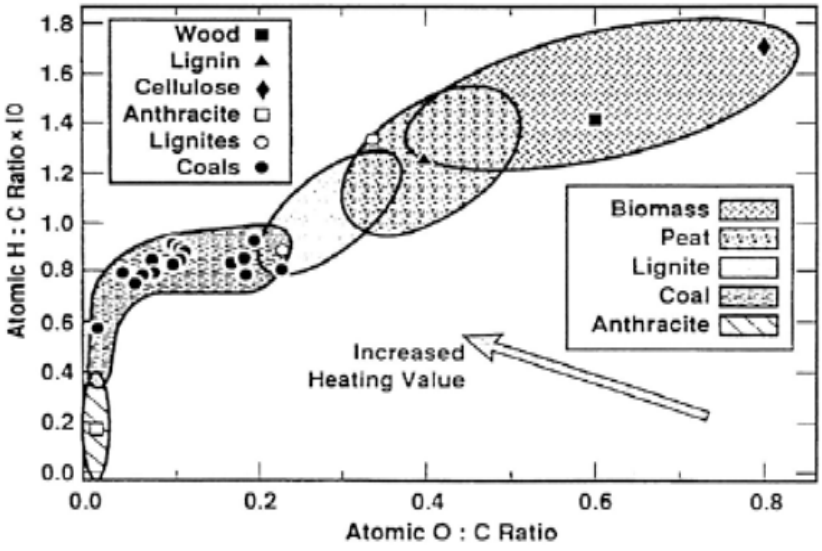

Figure I.5: Van Krevelen diagram

Some studies showed that this approach could well predict the calorific value and other properties. However, other fuel parameters such as volatile matter and fixed carbon correlate less with this approach. In general, biomass possesses O/C ratio close to one in contrast to the near zero ratio for coal. Comparable hydrogen content can be measured for biomass and coal (~6% wt) giving higher H/C ratio for biomass when considering the lower C content.

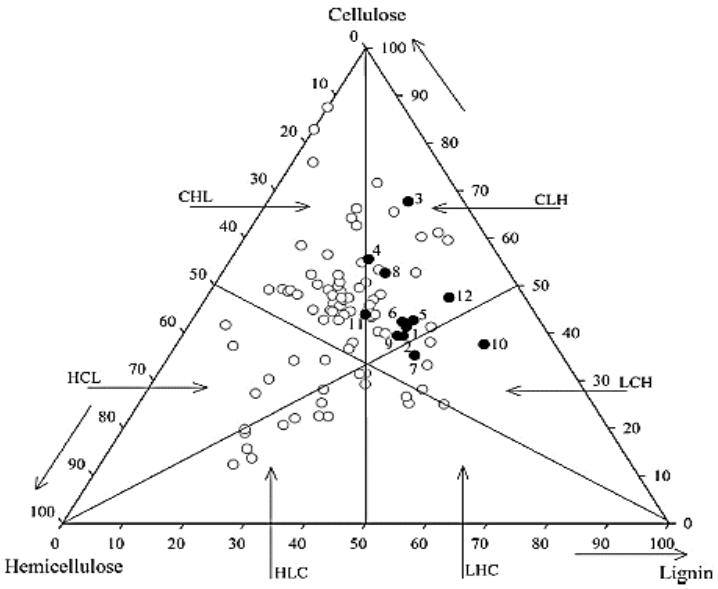

Figure I.6: LCH classification diagram

Other classifications are proposed according to the polymer constituents (*Figure I.6*). Studies showed that the addition of the behavior of the three constituents could predict quite well the behavior of the biomass [35]. However, the complex arrangements of the polymers inside the biomass give rise for complex interactions during the thermal degradation. It is reported that cellulose-hemicellulose and cellulose-lignin interactions do exist during the thermal conversion process [15] [16].

I.3 Fundamentals of biomass combustion:

Jenkins et al. [38] provided a global reaction for the combustion of a biomass fuel in air in the following form:

$$\begin{aligned} C_{x1}H_{x2}O_{x3}N_{x4}S_{x5}Cl_{x6}Si_{x7}K_{x8}Ca_{x9}Mg_{x10}Na_{x11}P_{x12}Fe_{x13}Al_{x14}Ti_{x15} + n_1H_2O \\ + n_2(1+e)(O_2 + 3.76N_2) = n_3CO_2 + n_4H_2O + n_5O_2 + n_6N_2 + n_7CO \\ + n_8CH_4 + n_9NO + n_{10}NO_2 + n_{11}SO_2 \\ + n_{12}HCl + n_{13}KCl + n_{14}K_2SO_4 + n_{15}C + \dots \end{aligned}$$

Where the first reactant compound is a biomass fuel and xi represents the mean elemental composition of each element in the biomass. Moisture is represented in the reactants by $n_1.H_2O$, which has a key role in the reaction activation. The major products of the combustion are carbon dioxide and water. Emissions like nitrogen oxides and carbon monoxide are also released and they depend mainly on the combustion environment and on the fuel. The products also include those of the reactions among inorganic species that lead to fouling and slagging, such as the alkali chlorides, sulphates, carbonates and silicates.

The history of biomass particle when injected in a high temperature medium is composed of four stages that overlap and may occur simultaneously (*Figure I.7*). The particle starts to heat up due to the convection and radiation heat transfer to set off the sequence of processes that convert biomass into heat.

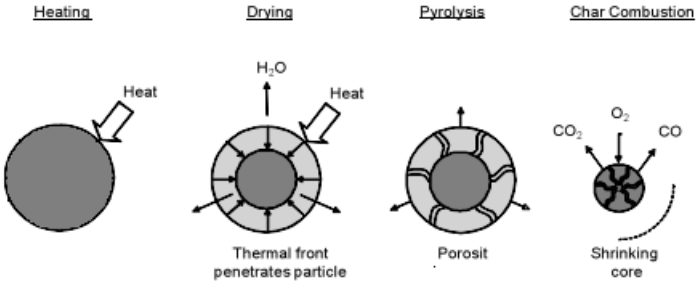

Figure I.7: Particle combustion sub-processes

I.3.1 Drying

Drying is the first step occurring meanwhile the particle reaches 100 °C, at which water is released off the particle. Water in biomass takes two forms—free water and bound water.

Free water exists as liquid and vapor in cell cavities while **bound water** is part of the cell wall materials. As the particle dries, it loses first the free water from the cell cavities, which would not shrink the cell and the particle keeps its shape. The deformation starts once the bound water starts to leave the cell wall as the particle dries further. At this point, micro-fibrils come closer together causing the particle to shrink [39].

The energy required to dry biomass fuel is a function of:

- The energy needed to heat the fuel to 100°C, which is a function of the specific heat of the fuel;
- Energy needed to heat the water to 100°C, which is related to the specific heat of water;
- The heat of vaporization of water at 100°C, which is 2.26 MJ/kg;
- The energy necessary for desorption of the bound water in the fuel, which typically is 35.8-14.3 kJ/kg.

At high heating rates, the required energy is offered almost constantly via the radiation from the flame and furnace wall and the convection with the hot surrounding gas. The release of water is mostly controlled by the mass transfer of water to the environment gas. First order Arrhenius type expressions and mass transfer equations are often used while modeling the drying process.

I.3.2 Devolatilization

When the temperature of the dry biomass reaches between 200°C and 350°C, the volatile gases are released. The volatile products include carbon monoxide (CO), carbon dioxide (CO_2), methane (CH_4) and high molecular weight compounds (tar) that condense to a liquid if cooled. The char, the solid residue after devolatilization, is a fuel that has lower H / C and O / C ratios than the original particle.

In literature it is postulated that devolatilization is a first-order reaction process, with the reaction rate being proportional to the amount of volatile matter in the biomass fuel or to the

mass of the sample [40]. In simpler models, the mass loss is modeled in Arrhenius form considering activation energy to represent the release of volatiles.

The devolatilization rate defined as: $\frac{dv}{dt} = k(V^* - V)$

Where:

- the rate constant k is assumed to have the form: $k = A.\exp(-E/RT)$
- V* is the initial volatile content
- V is the amount of the released volatile

A and E are assumed universal. This is following a criterion set initially for coal where the chemical bonds in various coals are fundamentally the same [41]. The result depends only on the final temperature and the heating conditions. The activation energy of the global reaction rate (k) presents widely variable values, roughly comprised between 56 and 174 kJ/mol. This can be the result of the different heating conditions established in the experimental devices, which include tube furnaces, entrained and fluid bed reactors, screen heaters, drop tubes and classical thermogravimetric, the different sample characteristics (size or mass and biomass variety) and the mathematical treatment of the experimental data.

Another model is used based on two first-order competitive reactions [40]. The model separates the volatiles evolved at low temperature from those produced at high temperature, typically above 1000°C. Each reaction is given a particular rate constant, with different values of A and E. In the first step, the primary pyrolysis, the solid phase thermally decomposes into gases, tar, and char. The conversion of tar into gas and char is summarized as second pyrolysis [42]. Some models [43] attribute kinetic parameters for the production of each pyrolysis product (gas, tar and char). In addition, models based on the functional group concept predict the different paths for the gas composition tar and char [26] [36]. *Table I.3* shows the variety of values coming from different models.

Fuel	Model	E (kJ/mol)			A (1/sec)		
Palm kernel shell (PKS) [45]	Kobayashi scheme	low T: 42,5	high T: 130		Low T: 602	High T: 8000	
Torrefied PKS 10% torr degree [45]		57	145		6,40E+03	1,98E+05	
Torrefied PKS 20% torr degree [45]		59,8	147		5,48E+03	2,15E+07	
Torrefied PKS 30% torr degree [45]		60,2	159		3,27E+03	2,10E+07	
Wheat straw [25]	(FG-DVC)	239			9,1 E+13		
Dry Wood [43]	-	Gas	Tar	Char	Gas	Tar	Char
		88,6	112,7	106,5	1,44 E+04	4,13 E+06	7,38 E+05
Switch grass [46]	Direct	77,448			22,5 E+06		
Big bluestem [46]		75,413			15,16 E+06		
Corn stalks [46]		62,747			1,268 E+06		
Cynara cardunculus [31]	DTF model	11			47,17		

Table I.3: Kinetic parameters using different models

Di Blasi [47] has summarized the kinetic constants for one-component mechanisms of wood/biomass pyrolysis. The data leads to the following classification, taking into account the temperature range investigated:

- High-temperature data (up to 1400 K) with E=69–91 kJ/mol
- Low-temperature data (below 700–800 K) with E=56–106 kJ/mol
- Low-temperature data (below 700–800 K) with E=125–174 kJ/mol

Thunman et al. investigated a degree of separation of drying and devolatilization within a fuel particle and defined the drying number (Dr). A drying number provides information on the temporal relation between drying and devolatilization, which is useful when choosing a model, where drying and devolatilization can be modeled separately if the Dr number is small (<0.1), if the drying number is very high (>100), the drying and devolatilization occurred simultaneously, therefore, the process description can be simplified by the rate of evaporation instead of the rate of the conversion of moisture and volatiles.

I.3.3 Homogenous combustion

Homogeneous combustion corresponds to the oxidation of volatile matter in the vicinity of the particle. This oxidation can cause a local depletion of oxygen, which will slow the heterogeneous oxidation of the solid.

The reactions that occur in homogeneous phase are complex, and generally poorly known. There are two types of approach:

- Simplified global chemistry: it consists of describing all (numerous) reactions from a few reactions that globally represent the evolution of all gases. This approach uses the kinetics of the entire combustible gas mixture. Momeni et al. [48] adopted such criteria as shown in *Table I.4*.

Sub-process	Reactions	Rate expressions	Kinetic data and heat of reaction			
			A [1/s]	b	E [kJ/mol]	ΔH [kJ/kg]
Light combustion gas	$CO+O_2 \rightarrow CO_2$	$r_8 = \frac{\partial[CO]}{\partial t} = k_8 [CO][O_2]^{0.25}[H_2O]^{0.5}$	1e+12.35	0	167	10110
	$H_2+O_2 \rightarrow H_2O$	$r_9 = \frac{\partial[H_2]}{\partial t} = k_9 [H_2][O_2]^{1.42}$	1e+12.71	0	171.3	120900
	$C_xH_yO_z+O_2 \rightarrow CO+H_2$	$r_{10} = \frac{\partial[HC]}{\partial t} = k_{10}[HC]^{0.5}[O_2]$	1e+4.32·T·P^0	0	80.2	41600

Table I.4: Light combustion reactions kinetics [48]

- Detailed chemistry: it is described from several hundred reactions that accurately represent the evolution of all gases. This approach is cumbersome in terms of calculation time. Detailed chemical schemes involve several dozens of species and several hundred reactions.

The energy generated by the light gases combustion is the result of liberating the heating value of the produced volatiles. This parameter depends on the composition of the gases, which in turn depend on their production conditions. D. Neves et al. [49] provided a compilation of some literature data on the lower heating value of the permanent gases (*Figure I.8*). The LHV increases from 2-5 MJ/kg to 15-18 MJ/kg with the temperature increase from 300 to 900 °C. Beyond this temperature, the composition of the gas becomes

closer to the chemical equilibrium composition given enough residence time. This gives a LHV in the range of 16-21 MJ/kg.

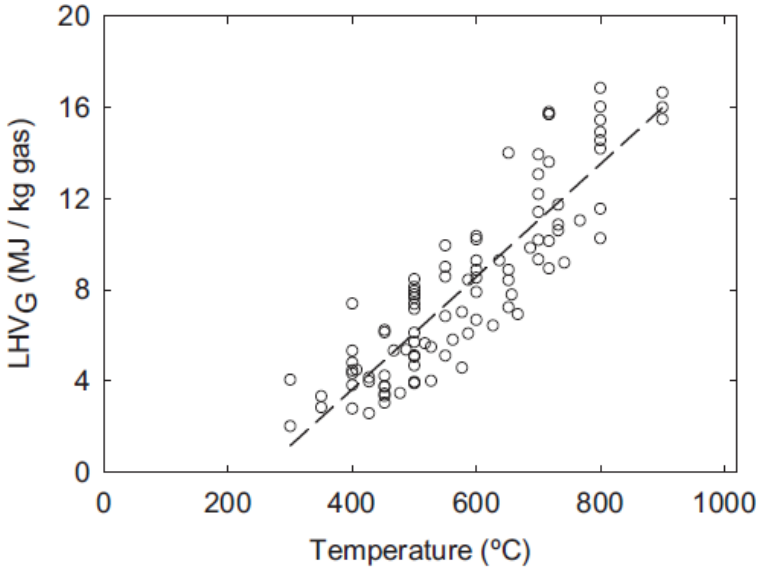

Figure I.8: Lower heating value of pyrolysis gas (LHVG) as a function of pyrolysis peak temperature [49]

I.3.4 Char combustion

Char is considered a product of the pyrolysis of the biomass. Many factors can alter the characteristics of the char before its oxidation starts. For instance, some authors suggest that the oxygen concentration can modify to some extent the characteristics of the char during devolatilization. In fact, in the devolatilization tests, some particles were reported to noticeably inflate, whereas they were not observed in combustion runs with analogous degrees of devolatilization [50].

The heterogeneous (gas-solid) reactions can be subdivided into the following constituent processes:

- Transport of the oxidizing species to the surface by convection and/or diffusion.
- Adsorption of the oxidizing species on the surface.
- Elementary reaction steps involving various combinations of adsorbed molecules, the surface itself, and gas-phase molecules.
- Desorption of product species from the surface.
- Transport of the product species away from the surface by convection and/or diffusion.

The process is then controlled by two important factors:

1- Mass transfer: including oxygen delivery to the surface, pore diffusion, and product diffusion away from the particle
2- Chemical kinetics: which depends mainly on temperature conditions and fuel characteristics.

Indeed, the whole process is controlled simultaneously by the latter factors. A three-zone-theory is widely accepted to explain how the boundary layer and pore diffusion and chemical reactions

alternate to control the rate of the heterogeneous combustion [51]. The theory postulates that one or more process in parallel control the reaction rate in three different temperature regimes (*Figure I.9*).

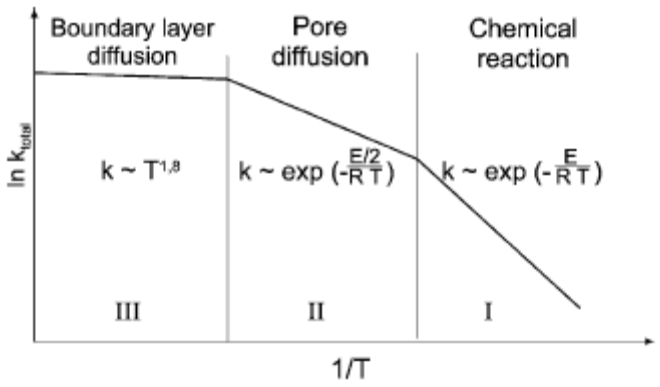

Figure I.9: The three-zone theory of char combustion

In zone 1, oxygen is easily delivered to the particle surface and thus the mass transfer is sufficiently rapid so that the reaction rate is determined by the intrinsic kinetics of the chemical reaction. At this stage, the temperature and the concentration are homogeneous within the particle. With the particle consumption, the density decreases while keeping the initial size of the particle.

As the temperature increases to zone 2, a temperature gradient forms within the particle. This limits the internal diffusion through the pores and creates a concentration gradient. In this zone, the reaction is controlled by both chemical reaction and pore diffusion.

Zone 3 occurs at very high temperatures where the products form a layer around the particle limiting the mass transfer. As a result, the heat and mass transfer in the boundary layer are insufficient to renew the reactants. In this case, carbon consumption occurs only at the particle surface. The particle core shrinks with a constant density [52].

Figure I.9 illustrates the three zones and the relation between the overall reaction rate and temperature [53].

I.3.5 Pollutants from biomass combustion

As shown in the global reaction of biomass combustion mentioned before, pollutants are formed alongside the main combustion products (CO_2 and H_2O) from the reactions of N, S, Cl, K as well as the unburnt fractions of the volatiles. Besides being produced as a product of incomplete combustion of hydrocarbons included in the volatiles due to factors like local depletion of oxygen, temperature and residence time, CO is released with volatiles as the major constituent and at high temperatures as the product of the heterogeneous oxidation of char. Both ways, CO then undergoes oxidation with the ambient oxygen, which is not homogenously distributed in the furnace. The same factors contribute to the release of PAH, fine char and soot with other tar species (like levoglucosan) because of incomplete combustion. Metal based gas species such as KCl and KOH either are released as aerosols or problematically deposit in combustion chambers.

I.3.5.1 Sulfur oxides

Similar to CO, Sulphur can be released during both volatiles and char combustion. The sulfur contained in the biomass mainly generates, during its combustion, gaseous emissions of sulfur

dioxide (SO_2) and smaller amounts of sulfur trioxide (SO_3), as well as the formation of alkaline or alkaline earth metal sulfates. Although Sulphur content is not so significant in biomass compared to coal, its presence in the flue gas can still be problematic. When cooled in the boiler, Sulfur oxides (SOx) form sulphates, so they either condense on the heat exchanger surface or form fine particles of ash, or react directly with the ash particles already deposited on the heat exchange surfaces.

Studies have shown that up to 60-90% of the sulfur in the biomass was found in the ashes during the combustion [54]. In the case of burning wheat straw, only 40 to 55% of the sulfur from biomass was in the ash. The effectiveness of sulfur fixation in ash depends on the concentration of alkali and alkaline earth metals, particularly Ca, in the fuel [55]. Residual sulfur remains in the flue gases as aerosols, SO_2 and in small amounts as SO_3.

I.3.5.2 Nitrogen oxides NO

NO formation mechanisms

Nitrogen oxides pass by producing and reducing paths during the combustion. The literature identifies three types of NO:

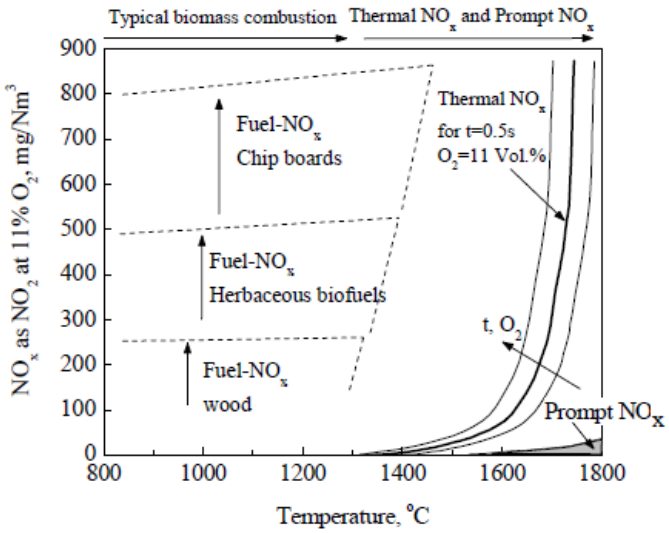

Figure I.10: Influence of temperature on NO emission in biomass combustion [56]

a. Thermal NO:

It is the direct oxidation of the nitrogen contained in air. At ambient conditions, oxygen and nitrogen do not react but at elevated temperatures (>1300°C) encountered in furnaces, they interact to form nitrogen oxides. The temperature dependent chemical reactions are known as Zeldovich mechanism:

$$N_2 + O \rightleftharpoons N + NO$$

$$N + O_2 \rightleftharpoons O + NO$$

$$N + OH \rightleftharpoons H + NO$$

It appears that thermal formation is independent of fuel type. Rather it is generated as a function of temperature and air to fuel ratio and is more pronounced when the mixture is on the fuel-lean

side of the stoichiometric ratio [57]. The reaction rate increases exponentially with temperature to the extent that the production rate doubles for every 90 K temperature increase beyond 2200 K [58]. The main method to impede the production of thermal NO is by reducing the peak temperature (*Figure I.10*). Techniques like exhaust gas recirculation and mild flameless combustion are usually used to achieve this by diluting the reactants with the combustion products.

b. Fuel NO

In biomass combustion, the majority of nitrogen oxides comes from nitrogen in the biomass [56]. They are called in this case fuel-NO. The NO formation of the fuel during the biomass combustion is carried out by oxidation of the released nitrogenous species among the volatile species, as well as by the oxidation of the nitrogen retained in the char. The majority of volatile nitrogen species are ammonia (NH_3) and hydrogen cyanide (HCN). Generally, NH_3 can decompose into NH_2 and NH radicals, which either are oxidized by oxygen (O_2) or react with available NO and OH radicals to form N_2 [59]. The reduction reaction of NO by the NH_i radicals is called the thermal De-NOx reaction.

HCN can decompose into NCO by action of an oxygen radical, which will then react with NO to form N_2O. Nitrogen bound to the char is then burned to form NO, N_2O and N_2 [56]. However, low concentrations of NO_2, HCN, NH_3 suggest that NO is practically the only product formed during the char combustion [60].

A general diagram of the conversion of nitrogen present in the biomass during its combustion is presented in *Figure I.11* [61].

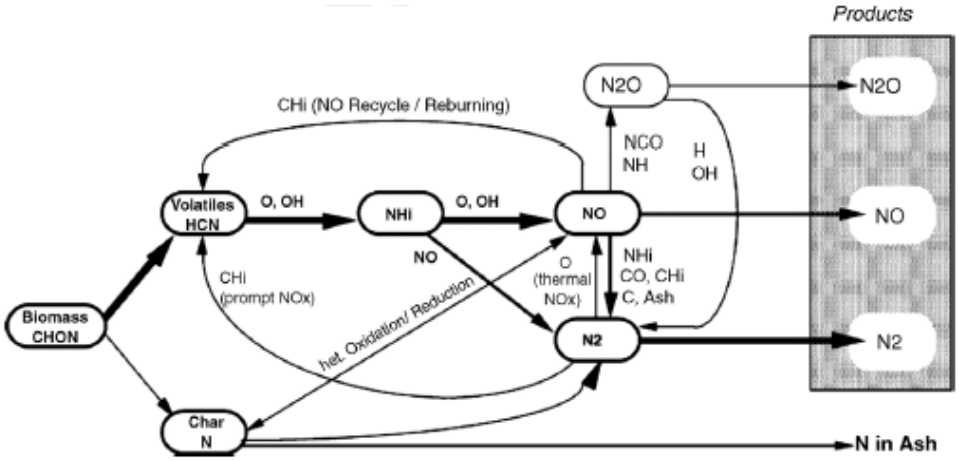

Figure I.11: Mechanisms of NO formation [61]

It has been found that as the nitrogen content in biomass increases, more NO is released. However, the conversion rate of nitrogen to NO decreases. Less than 20% of fuel-N is converted to NO biomasses containing more than 0.7% (db) of N. It can reach up to 70 % for lower N content [56][54].

c. Prompt NO

Prompt NO are marked in the general scheme above by the paths involving the reaction of hydrocarbon radicals with atmospheric nitrogen to produce NCN and hence HCN and NO via the same complex series reactions followed for the volatile NO [60]. Thus, the mechanisms that

are effective for the reduction of fuel NO are also effective for minimizing prompt NO. The mechanism is promoted with elevated temperatures but still has the least contribution in biomass combustion to the total emissions (about 5%) even at very high temperatures (*Figure I.10*).

NO reduction mechanisms

a. Gas phase reduction

In order to limit the N-NO conversion, it is necessary to dilute the oxygen concentration, which is one of the reactants. Therefore, lowering excess air as much as possible is preferable [62]. This leaves, however, more unburned species in the exhaust. Extra air should be added later by air staging techniques to ensure complete combustion. Indeed, the weak excess air in the first stage favors the reduction of NO to N_2 by the thermal de-NOx mechanism [63].

This mechanism, where the NH_i radicals react with NO to produce N_2, may be affected by other parameters than the excess oxygen. The composition of biomass can indeed play a role in this mechanism. More volatile matter ensures more nitrogen species in the gas phase including NH_3, HCN and HCNO. The proportions of these species are determined by several factor such as the volatile matter content and inorganic content (notably Ca and K) [64], thus making available a greater or lesser amount of NH_3 compared to other nitrogen precursors. The ash inorganic content such as calcium (as CaO or CaS), iron, or potassium also influence the reduction mechanisms through CO and C_xH_y [65]. Being abundant during devolatilization, CO reacts with NO to produce N_2 and CO_2. The reaction also occurs during the char combustion phase where CO is the major product at high temperatures.

b. Char phase reduction

The NO formed during the oxidation of nitrogen atoms contained in the biomass char can be re-adsorbed on the char surface and reduced to N_2. The overall reaction can be written as follows:

$$NO + C\ (char) \rightleftharpoons 0.5\ N_2 + CO$$

Commandré et al. [66] have determined the kinetic reaction rate on different carbon residue, and showed that pore size is important in this reaction. The presence of inorganic elements such as potassium, calcium, magnesium or iron could catalyze such reactions. The effect of calcium on the mechanisms of formation or reduction of NO is however discussed, as contradictory results exist in the literature [54].

c. Secondary reduction methods

NO reducing reactions are also triggered in the exhaust by the so-called selective catalytic reduction (SCR) and selective non-catalytic reduction (SNCR). A reducing agent, usually ammonia or urea, is injected to reduce NO present in the flue gas to N_2, in the presence or absence of a catalyst (platinum, titanium, vanadium). This technique is not effective for biomasses with high ash content, which can deactivate the catalyst.

I.4 Solid biomass combustion technologies

The combustion of solid-fuel is the oldest known method for generating heat for humankind and it continues until now with different fuels and technologies responding to different applications and increasing demands. The used technologies for biomass combustion are classified according to the preparation method of the fuel and the flow conditions inside the combustion chamber. The simplest form of biomass combustion is that used in domestic stoves. But at industrial scales, larger controlled installations are built limited by the availability of feedstock and the envisaged application. The most used combustion technologies in the case of biomass are: fixed bed reactors (FBR), Fluidized bed reactors (FBR) and pulverized fuel burners (PFB).

I.4.1 Fixed bed combustion

Fixed bed combustion is the oldest technology that is used in the domestic stoves up to grate boilers with a typical range of 1-80MW. It is suitable for small power applications and with the advantage of low fuel preparation cost regarding grinding and drying. That is why it tolerates broad range of material with high moisture and ash content, including municipal waste and wood chips, which is the most common fuel type used in grate boilers. Temperatures in fixed bed systems typically reach 900–1400 °C.

The principle of grate firing is shown in the *Figure I.12*. Biomass is transported into the boiler on a grate that may be fixed, mechanically driven (moving or rotating) or vibrating. Once loaded, the wet raw material undergoes a drying phase followed by pyrolysis and finally, as it moves forward in the furnace, volatile and char oxidation. Primary burning air is fed below the grate while secondary combustion air (+tertiary) is supplied from the top of the grate. The combustion gases are led to the heat recovery system while bottom ash is discharged from the bottom of the grate boiler.

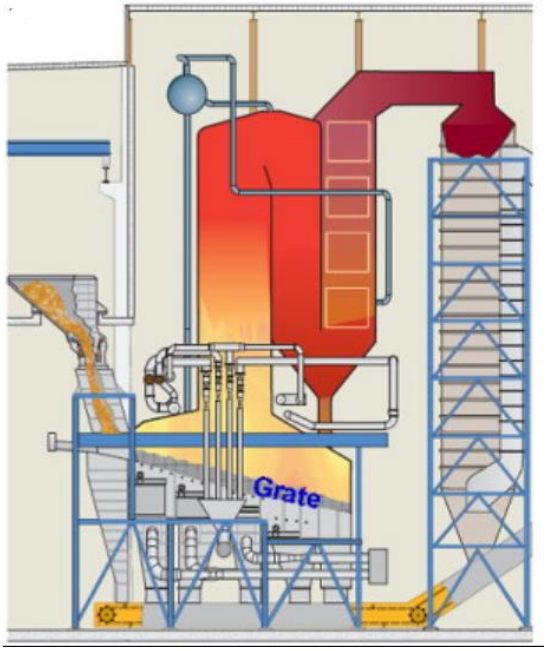

Figure I.12: Grate fire power plant scheme [67]

Fixed grates are usually inclined to allow fuel sliding by gravitational forces. Some flexible grates allow slope adjusting to adapt to the loaded material specifications but this is limited by the danger of fuel avalanches. The moving or mechanical grate consists of movable rows of grate bars that transport the fuel inside the furnace. It is more fuel flexible and is usually used for higher capacities and high ash content fuels. However, non-uniform distribution is a disadvantage for both grate types. Vibrating grates ensures the even distribution of fuel on the grate to avoid higher NO levels emitted from high local temperatures.

Limits of this technology are its low efficiency due to the excess oxygen in the system. The combustion is not as homogenous as in fluidized bed and pulverized burners.

I.4.2 Fluidized bed combustion

The fluidization is a technology in which solid particles act like a bubbling fluid when blown by air from the bottom at certain conditions. This technology is used in the fluidized bed boilers where biomass particles fed on a thick inert bed (about 1m) are fluidized by combustion air that is injected through a perforated bottom plate (*Figure I.13*). As a result, a larger heat transfer surface is created, which improves the heat and mass transfer conditions leading to complete combustion during a long residence time. Secondary and tertiary air is fed above the bed to achieve total combustion. In addition, excess air can be kept low (1-4 % by volume) and consequently higher efficiency is achieved. Fluidized beds typical capacity ranges from 10-150 MW with variable fuel features including high ash content materials (up to 50%), and it requires no drying of the feedstock. NO emissions are usually kept low as the reactor operates at relatively low temperature between 800-900°C. Other emissions can also be reduced by additives to the inert bed materials.

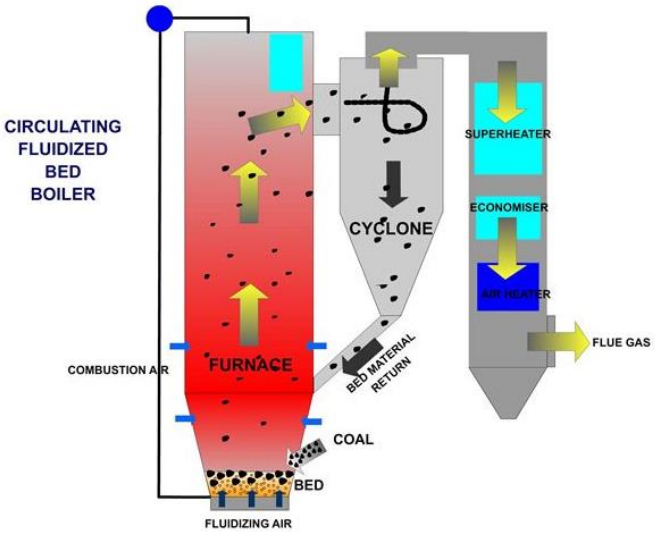

Figure I.13: fluidized bed combustion chamber [68]

Fluidized bed systems are of two types: bubbling fluidized bed (BFB) and circulating fluidized bed (CFB). In BFB, the air velocity is limited to the entrainment velocity of the particles, so that no particles are picked up by the gas flowing upward to the exhaust. Higher velocities are used in CFB mode allowing lighter particles to be carried by the gas stream to a cyclone, which separates them and returns the solid back to the reactor. Large particles shrinks while burning until they become light enough to join the circulating stream.

I.4.3 Pulverized fuel combustion

I.4.3.1 Technology

The combustion of fine particles is a thermochemical process widely used in large installations of coal power plants (
Figure I.14). It is indeed considered the most effective mode of solid combustion as the excess air can be kept very low (4-6%) with possible NO reduction by proper air staging [9].
These burners have higher specific capacity, which means that they produce more energy from the same reactor volume or space, and produce flame similar to oil and gas fired burners. Biomass is pneumatically transported by the primary air to be injected into the furnace, which is already heated up by an auxiliary start-up burner. High temperatures are attained in pulverized fuel boilers and the residence times are usually short (seconds), which is sufficient when dealing with the high burning velocity of biomass particles.
Compared to the two previous technologies, the pulverized combustion technology offers higher electric power generation efficiency, lower operating costs and better load control [69]. However, this mode suffers high preparation costs and low fuel flexibility. Abbas et al. [70] found that the grinding of biomass consumes energy almost two times more than the required energy for coal. Biomass have to be dried (moisture < 15%) and crushed to fine particles (<2 mm) and then carefully fed to the furnace due to the explosive risk of the fine biomass particles. High ash content can lead to slagging formation and serious corrosion problems.

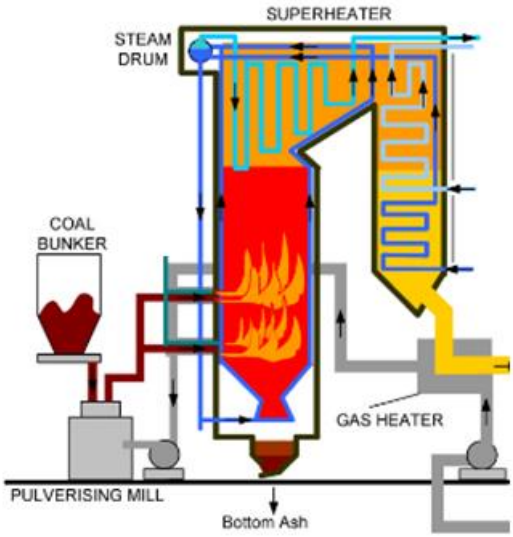

Figure I.14: Pulverized solid fuel power plant [71]

Reducing the preparation cost can boost this technology and favor it in front of the other technologies. Especially there is a great opportunity of biomass to replace coal (partially or completely) that is the second source of primary energy (roughly 30%) worldwide [72] and completely burned in pulverized combustion power plants. For example, we can take advantage of the biomass wastes that are being continuously produced in pulverized form such as sawdust and fine shavings so that grinding costs are eliminated.

I.4.3.2 Status of pulverized burners

Conventional pulverized or dust burners operate by rapidly mixing fuel and air to produce short hot flames inducing efficient burnout (*Figure I.16*). These flames are NO prolific zones due to high temperature and excess oxygen. NO reduction comes with air staging systems associated with fuel rich zone near the burner, which is created by the delayed mixing of fuel and air. NO

reduction mechanisms are then favored to attenuate N-NO conversion reactions. The tertiary air completes fuel oxidation downstream. Tertiary air can be injected by the burner (internal air staging) or it can be added externally just above the burner. In this case, it is called furnace air staging.

The geometry of the burner plays a key role on profiling the flame and enhancing its stability. The aerodynamics generated by the burner's geometry control the heat and mass transfer between the air and the fuel particles. Swirl burners are most often used for generating a turbulent environment and increase the residence time. The swirl induces the recirculation of hot gases downstream to the near burner zone. These internal zones help stabilize the flame depending on the degree of swirl which can be controlled by adjusting the swirl angle and injection velocities [73]. Alternative technique to stabilize the flame is established in bluff-body burner (*Figure I.15*). Flame is stabilized on a bluff-body where the lower pressure behind the body creates an internal recirculation zone to mix a part of the fuel and air [47] [48].

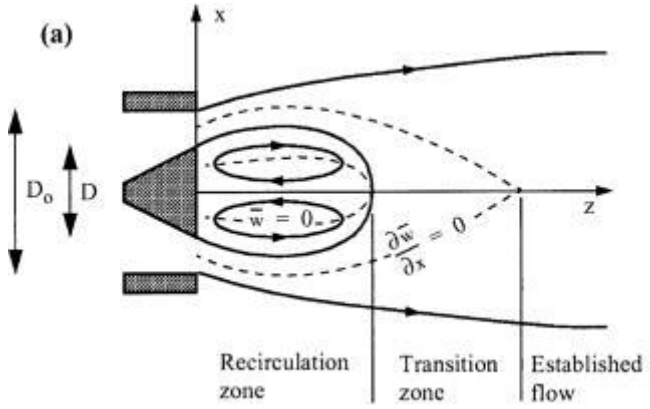

Figure I.15: Bluff body burner [76]

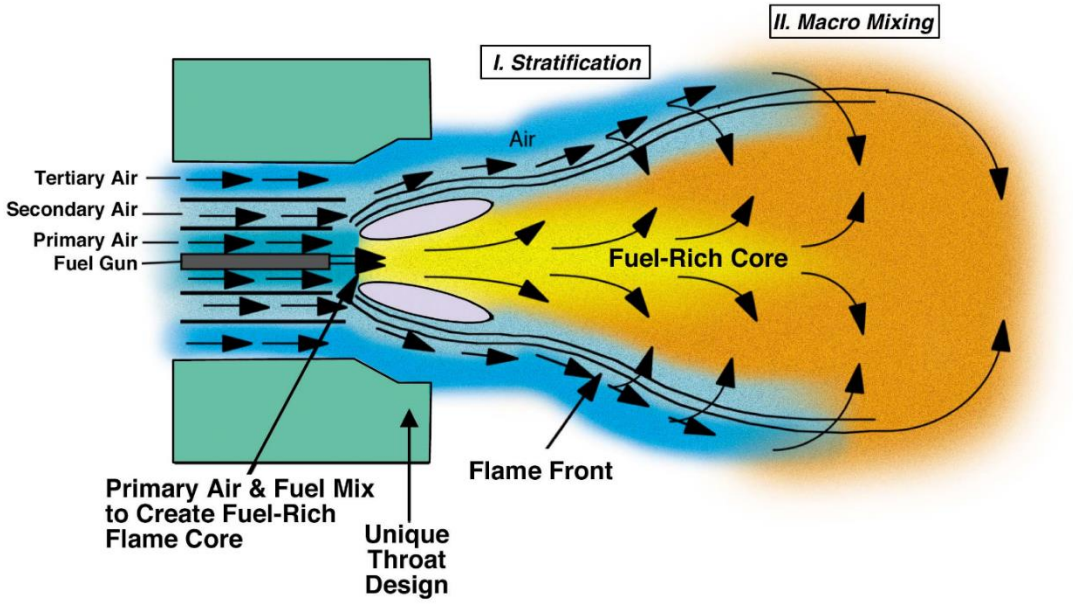

Figure I.16: GE power low NO burner [77]

Commercial models of pulverized biomass burners exist with different feeding systems and stabilizing techniques. Specially designed burners are adapted to existing combustion chambers to burn biomass powder. Here are some available models [78]:

- VTS and Petrokraft are low NO burners with internal air staging.

- LMB Multifuel Burner (LBE)
- COEN Dual Air Zone Scroll Burner
- BioSwirl for dust fuels and crushed pellets
- Petro Bio burner (Vyncke group)
- GE power low NO burner (*Figure I.16*)

These burners are used in biomass power plants and even in coal power plants separately from the coal burner. Existing coal burners can also be used for co-firing by mixing the prepared biomass fuel upstream with coal before firing. Incorporating 10-30% of biomass with coal shows a great advantage on reducing pollutant emissions and improving the heat release. Many plants in Europe are in a trial or demonstration stage. However, many coal plants like Longannet Coal fired power station in Scotland, UK, are now co-firing with biomass (sewage sludge). A survey issued by the European Biomass Industry association (*Figure I.17*) reported that co-firing power stations in the Netherlands, Denmark, Finland and Sweden and other countries are mostly operating on a commercial basis [79]. According to the Dutch government agency for enterprise, almost 60% of the available subsidies budget in Netherlands in 2016 has gone to biomass and two-thirds of this to co-firing biomass in the coal-fired power plants.

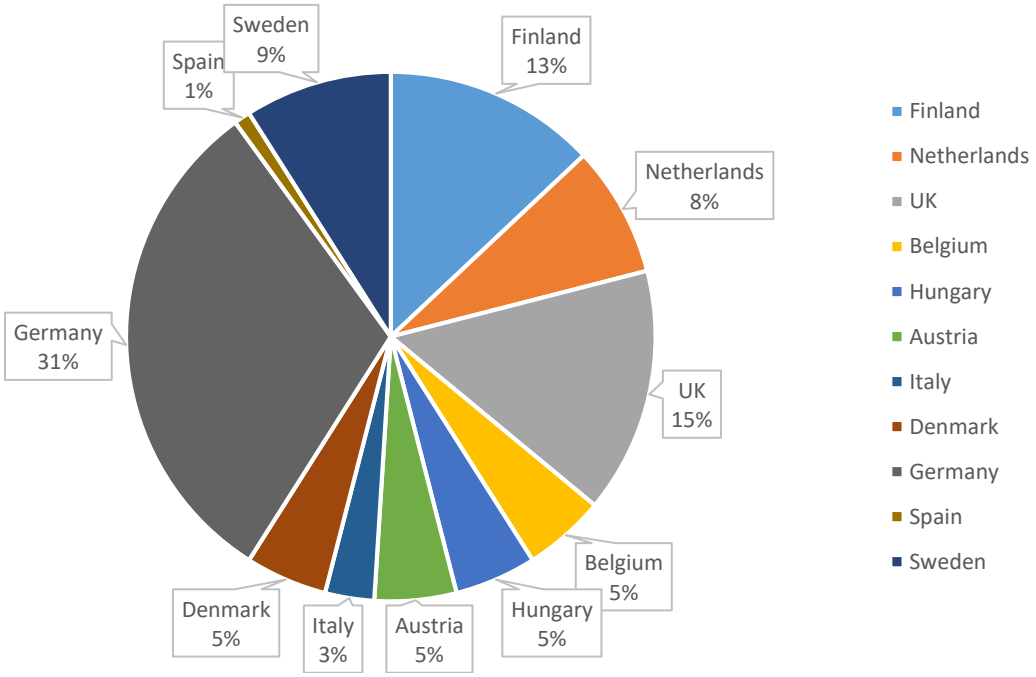

Figure I.17: Co-firing power plants in Europe [79]

I.5 Review of the experimental investigations of biomass combustion

Many studies have addressed the combustion of biomass experimentally and numerically. Two categories can be distinguished: lab-scale studies and pilot-scale studies.

The majority of the previous work was done at particle scale using laboratory equipment especially TGA and on drop tube furnaces. Such experiments are necessary to understand the evolution of biomass particle with temperature rise but they do not depict the complete picture of the behavior of the particles in industrial flames. The link between the obtained results at this level and the industrial flames is poorly understood, partially because the experimental conditions of the studies don't simulate those encountered in industrial furnaces and, on the

other hand, because of the relatively low number of studies that are done at industrial scale, which is costly, risky and impractical for the power plants. The transition between the two levels is done by a fundamental experimental study at pilot scale. Experimental pilot facilities are expensive to construct and operate compared to laboratory rigs. Moreover, since the pulverized combustion of biomass is considered as a fairly new technology, a few studies can be found in literature at the flame scale. It should be noticed that biomass was traditionally fired in grate-firing and fluidized bed furnaces and the study on pulverized fuel flames was focused on coal. Therefore, a lot of work should be done to shift our knowledge on coal flames to biomass.

Combustion of different types of solid fuels is found in literature: combustion of wheat straw, rape straw, pine, olive stone, rice husk, RDF, coal etc. Studies focused on the influence of the composition of the fuel especially from the point of view of its polymer constituents. Some investigations concentrated on the influence of fuel pretreatment like drying, grinding and torrefaction level on factors like degradation rate, volatile composition, ignition time in both pyrolysis and combustion environments.

Since the biomass combustion process is a coupling of different sub-processes as heat and mass transfers, and reaction such as drying, pyrolysis, homogenous volatile matters oxidation, heterogeneous solid residue oxidation, the investigation is usually performed to uncouple the events.

I.5.1 Influence of biomass composition

I.5.1.1 Moisture content

Water vapor is the first species to come out from the wet particle in the course of heating to the combustion temperature. A part of the energy used for vaporization comes from the energy produced by the combustion. This lowers the temperature of the furnace and slows down the combustion process. Fuels with high moisture content consume much energy to dry, making it difficult to maintain the combustion. Fuels with moisture content around 60% liberate insufficient energy to satisfy evaporation. In this case, most furnaces require a supplemental fuel, such as natural gas [78]. In addition, CO and other products of incomplete combustion may be emitted in greater quantities depending on the design of the combustor [17][52].

The high fuel moisture content reduces the calorific value of the fuel resulting in reduced adiabatic combustion temperature so that biomass fuel requires a longer residence time in the combustion chamber. That is why in pulverized combustion the moisture content should be limited. Bryden et al. [81] studied numerically the impact of moisture on the pyrolysis of biomass. Results show that the particle is maintained at a constant temperature during drying and consequently delay the temperature rise to the imposed temperature. Mahmudul Hasan et al. [82] reported a heating rate peak after the end of drying (at 200°C). Moisture content creates a temperature gradient in the inner layers of the biomass particle, which triggers the jump in the heating rate profile once moisture evaporation is over. The release of tar and light hydrocarbons is then delayed (*Figure I.18*). Pollard et al. [83] found that moisture content in biomass shortens the co-firing flame length. The author argued that some biomass particles could break through the volatile flame without being completely pyrolyzed in the flame zone as measured experimentally. Higher moisture content promoted the breakthrough effect and thus reduced the flame length. Similarly, in a packed bed, Yang et al. [84] found that a decreasing moisture content leads to an increasing influence of the devolatilization rate. So that burning a dry fuel could be up to four times faster than a very wet fuel [85].

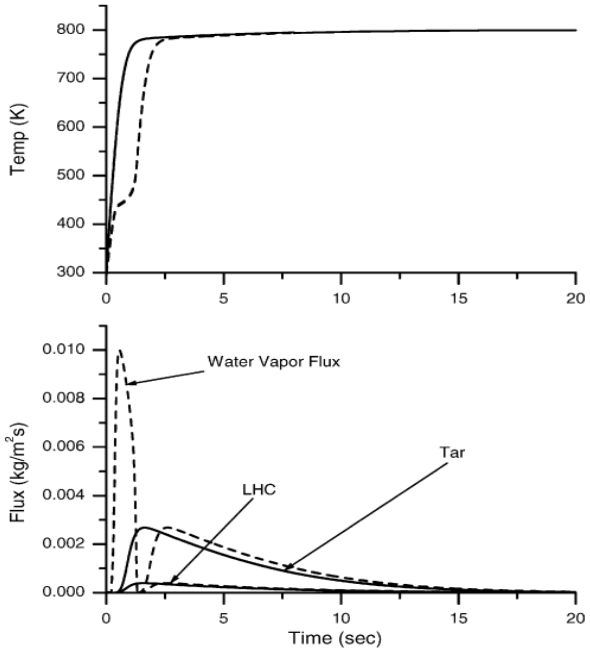

Figure I.18: Temperature and mass flux vs. time for poplar with a 50 mm half-thickness exposed to 800 K radiant temperature, — dry, - - - 30% moisture content [81]

Previous studies showed that biomass has delayed ignition compared to coal despite the lower ignition temperature of biomass [86]. This was attributed in the first place to the high inherent moisture content and large biomass particles which heat slower than coal to the ignition temperature. Lu et al. [87] studied the co-firing flames of coal and biomass. Flame imaging showed that the addition of biomass shifted the ignition points away from the burner nozzle than the coal flame. An interesting exception was the flame with a 10% high-protein biomass addition. The low moisture content in the high-protein biomass helps to speed up the heating process, resulting in shorter ignition times in comparison with other biomass fuels. Moreover, not only the onset of the devolatilization process is delayed, moisture also interferes in the cracking process in which it influences the product composition. It is shown that the yield of total oil increases with increasing the initial moisture content of samples pyrolyzed at intermediate pyrolysis temperature (400-500°C). This encourages char formation from heavy tar radicals. It also alters the physical and chemical properties of the tar, as they tend to be less viscous [86] and less toxic [88]. At higher temperatures (1000°C), Xiong et al. [88] demonstrated that the moisture content in sewage sludge increased the production of hydrogen rich fuel gas and intensify the ejection of volatiles, but also reduced the solid yield. This has implications on char structure and reactivity.

I.5.1.2 The lignocellulosic constituents

The pyrolysis characteristics of hemicellulose, cellulose and lignin show great differences of the pyrolysis behavior among the three main components (*Figure I.19*). Hemicellulose is easy to be degraded, and its pyrolysis is focused at 220–315 °C with 20% solid residue found even at 900°C. The pyrolysis of cellulose mainly occurs at 315– 400 °C with very low solid residue, while lignin is the most stable and decompose over a wide temperature range (150–900 °C) leaving the highest solid residue. The activity of the chemical bonds in lignin covers an

extremely wide range, which leads to the degradation occurring in a wide temperature range [12].

Ramiah et al. [89] reported that at low temperatures (<500 °C), the pyrolysis of hemicellulose and lignin involves exothermic reactions while those of cellulose are endothermic. However, inverse observations are made at high temperatures (>500 °C). The same result is reported by Yang et al. [90]. This shows that the charring process is highly exothermal whereas volatilization is endothermal [91]. With the much higher solid residues generated from hemicellulose and lignin pyrolysis, the exothermal peaks observed in hemicellulose and lignin pyrolysis could be attributed to the charring, while the full decomposition of cellulose might be attributed to the quick devolatilization reactions, leading to very few solid residues left. The same conclusion was drawn by J. Shen et al. [46] and by L. Burhenne et al. [26] when comparing three types of biomass with one constituent being dominant in each. The decomposition of spruce wood and bark, which represent the high lignin fuel, was highly exothermic.

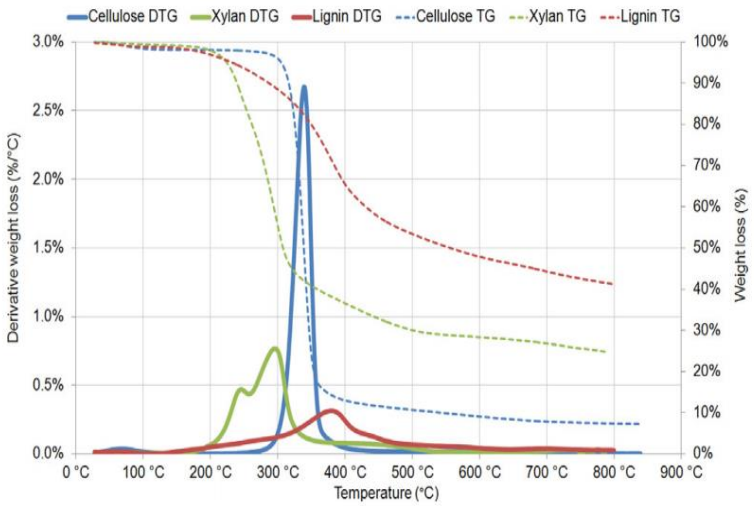

Figure I.19: TGA and DTG curves for the degradation of hemicellulose (or xylan), cellulose and lignin [92]

Whereas the decomposition was faster in the wheat straw containing high cellulose content and in rape straw which reveals a decomposition peak that is higher, narrower and at lower temperatures (307 °C) than the peak of the woody biomass samples (at 407 °C). This behavior was ascribed to hemicellulose decomposition, occurring typically in the temperature range between 225 and 325 °C, followed by a high cellulose devolatilization.

I.5.1.2.1 Composition-based modeling

Several mathematical models were proposed to reproduce the TGA curves based on the Arrhenius kinetic parameters. Some models assumed that the combustion is pure addition of cellulose, hemicellulose and lignin combustion. Gronli et al. [35] tested four hardwoods (alder, beech, birch, and oak) and five softwoods (Douglas fir, redwood, spruce, and two species of pinewood). A common set of activation energies (100, 236, and 46 kJ/mol for hemicellulose, cellulose and lignin respectively) was found to apply for all of the tested wood types. The differences in the characteristic reaction temperatures and the yields of char between hardwoods and softwoods are taken into account by pre-exponential factors and total volatile fractions.

These types of models can be successfully applied for a wide range of wood but some deviations occur when used for other types of biomass like rape straw [26] and for types with three-peak DTG curves instead of two-peak curve obtained in the case of almost all woody biomass (*Figure I.20*). A peak is ascribed for hemicellulose followed by a cellulose decomposition peak. A three-peak curve is less often observed but it is reported in the case of sugarcane bagasse for example [93].
Varhegyi et al. [94] suggested that in this case, the two lower temperature peaks are associated with hemicellulose decomposition and the highest with cellulose pyrolysis. These deviations can be explained by the different nature of the polymers contained in each biomass and probably by the interactions between cellulose and lignin, which is more likely to occur in herbaceous biomass than woody biomass due to a higher degree of covalent bonding between cellulose and lignin in the herbaceous biomass than woody biomass. The physical and chemical interactions within cellulose−hemicellulose−lignin in the real biomass could create different local reaction conditions than would be present in a simple physical mixture of the individual components [15] [16]. Another important problem facing the numerical models in general is that many parameters are derived from TGA curves and thus they are dependent on the heating rate that is low in this case. Changing the heating rate would change the activation energies and the combustion behavior influenced by many aspects like different morphological evolution [95].

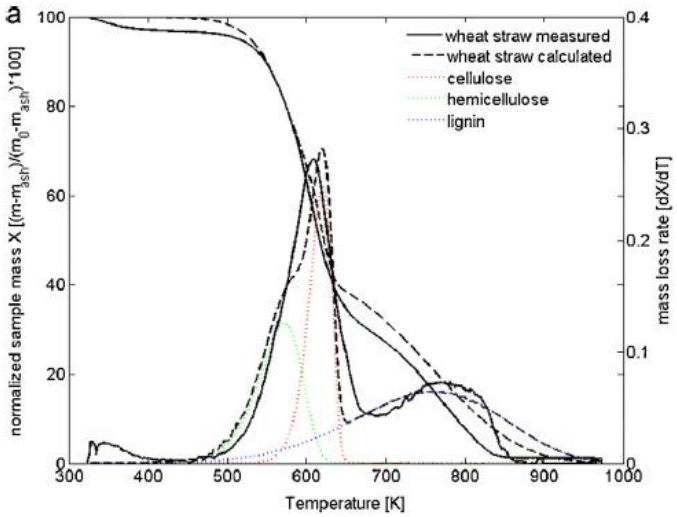

Figure I.20: Convolution of the contribution of the three basic constituents of biomass [26]

Ejecting volatiles at low and intermediate heating rate does not necessarily deform the shape of the solid as encountered in high heating rates. This would definitely change the predicted active surface area and thus the reactivity of the char oxidation. Moreover, devolatilization yield was measured to be 1.15 to 1.35 times the predicted ASTM volatile matter content due to higher heating rate [96]. Peaks tend to merge at higher heating rates and decomposition shifts to higher temperatures. This makes the determined parameters specified for certain conditions and generalizing them is still difficult.

I.5.1.2.2 Volatile Matter content

The composition and amount of volatile matter play a key role in determining the flame ignition distance and heat release, and on the stability of the turbulent flame depending on the ignitability, flammability and the calorific value of the volatiles. In pulverized biomass

combustion, the homogenous ignition is mostly encountered. This happens, once the volatiles mix with oxygen and their concentration passes the flammability limit at a given temperature, which in turn depends on the volatile composition [97]. A trend is reported by A.C. Sarroza et al. [98] where the distance to ignition increases with the volatile matter content in the biomass when injected in a drop tube furnace, in contrast to what was observed with the coal tests. The results suggest that the ignitability of biomass is correlated with the temperature at which the peak degradation occurs. Lower peak temperature, as viewed by TGA curves, means shorter distance to ignite regardless of the peak value. Large volume of volatile contents in biomass decomposes to yield a lot of soot and oily tars, in addition to the effect of particle size that will be discussed later. This is backed by the delayed ignitions of the co-firing flames mentioned previously [87]. However, different observation was made by Grotkjær et al. [99] who asserted that the coal trend extends also to biomass. The authors also discussed that, as biomass particles contain a large amount of volatiles, both homogeneous and heterogeneous ignitions can occur during particle combustion. Similar conclusion on ignition delay can be derived from the work of Li et al. [45] on pulverized torrefied biomass flames. The lift-off distance of the flame decreases with the liberation of more volatile matter.

The contradiction of the two inferences could be due to different moisture content as discussed and due to different fuel composition, especially different ash activity. In the case of pulverized combustion, the aerodynamic impact of the different burners' configurations could explain the different results. The burner geometry determines the parameters of the recirculation zone, which determines whether the particles have sufficient residence time to ignite near the burner exit or further downstream. This case is described by Damstedt et al. [100] in the penetrating and non-penetrating flames. The burner geometry and flow conditions define the internal recirculation zone and whether fuel particles devolatilize/ oxidize in the boundary between the recirculation zone and the main flow channel (non-penetrating flame), or they penetrate into the recirculation zone, where devolatilization and char oxidation occur (penetrating flame).

Moreover, besides being associated with larger flame volume, larger amount of released volatile matter is deemed responsible of increasing the active surface area (ASA) in the char. Exposing a particle to high temperature results in a pressure within the pore structure. More fragments are then expelled rapidly and cross-linking reactions are limited, thereby increasing fuel conversion. This leads to enhanced char porosity and reactivity [101]. In fact, The ASA is maximum at the end of devolatilization [96].

I.5.1.2.3 Volatiles composition

The main emitted species during the pyrolysis process of biomass are CO_2, CO, H_2, CH_4, H_2O and heavier hydrocarbons with proportions dependent on the operating conditions and fuel type. Two cracking phases are reported whenever a sufficient residence time is provided [90][102]. Yang et al. [90] measured the gas product from the pyrolysis of the three polymers in a packed bed coupled with micro-GC (*Figure I.21*). CO_2 and CH_4 mainly evolves out at 400–600 °C, H_2 at a high temperature (>400 °C), and the yield of H_2 increased with pyrolysis temperature increasing. It was suggested that different chemical structures of biomass components induce different gas product releasing properties. Hemicellulose, with higher carboxyl content, accounted for a higher CO_2 yield. Cellulose displayed a higher CO yield, mainly attributed to the thermal cracking of carbonyl and carboxyl. With a higher presence of aromatic ring and methoxyl, the cracking and deformation of lignin released out much more H_2 and CH_4.

The released heavy hydrocarbons are usually condensed and referred to as bio-oil. Their proportion decreases with high temperatures as they decompose to simpler chains producing eventually methane and hydrogen [103]. Heavy HC are rarely found in combustion conditions but they are considered as intermediates when modeling the devolatilization process. Cellulose derived bio-oil mainly consisted of saccharides, furans and ketones. Acids and ketones are the main ingredients of the bio-oil from hemicellulose pyrolysis, while the main compounds of bio-oil from lignin pyrolysis are phenols.

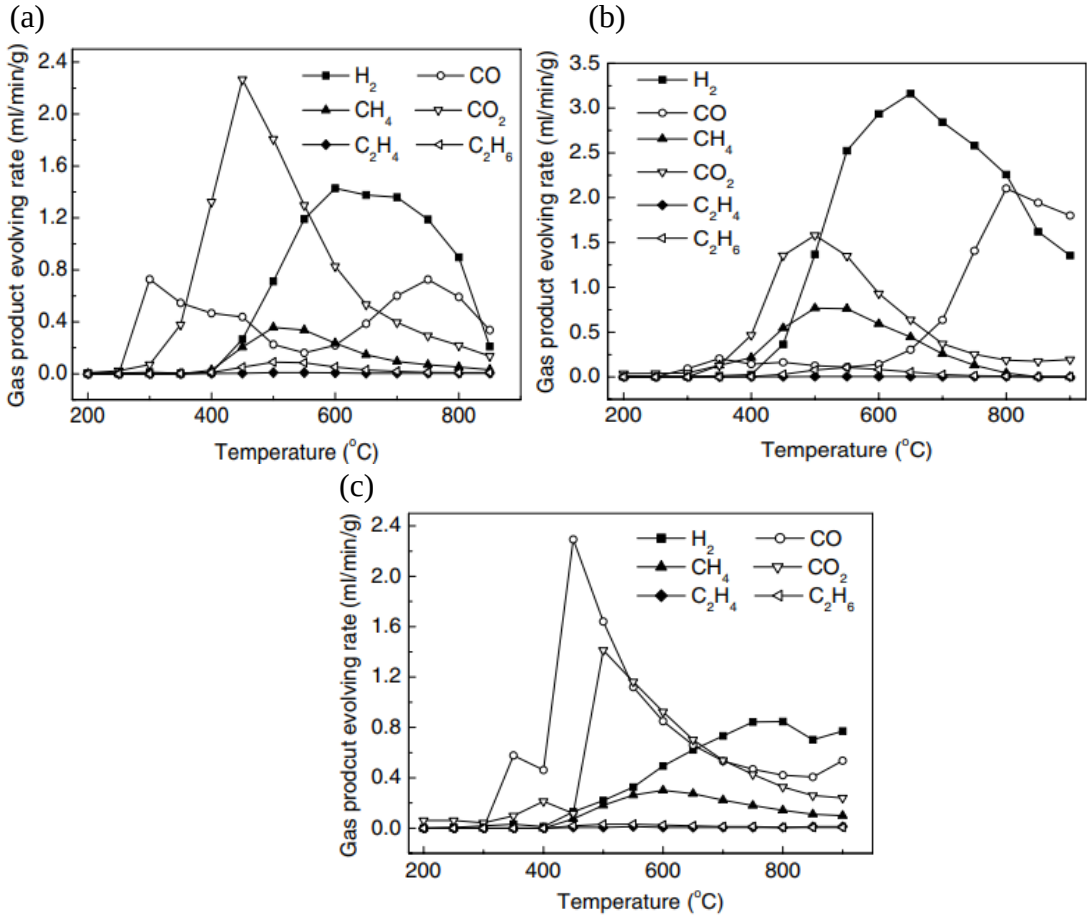

Figure I.21: Volatiles of a) hemicellulose, b) cellulose, and c) lignin respectively in packed bed [90]

The differences at the components level give rise to huge differences when dealing with variety of feedstock. However, general trends can be concluded. Di Blasi et al. [42] showed that H_2 yield increases significantly at high temperatures so that it is expected to find high quantities of H_2 in combustion furnaces. CO also makes the major share of the permanent gases (around 40 g/g biomass). At high temperature (>1000 °C), the composition is expected to be close to the chemical equilibrium composition where H_2 and CO_2 are the dominant contents. Commandré et al. [104] compared the H_2/CO ratio obtained experimentally with the supposed ratio at thermodynamic equilibrium. The difference tends to get narrower as they increase temperature from 650 to 950 °C but never reaches zero even at higher temperature (up to 1400°C) as reported by S. Septien et al. [105]. H_2O and CO_2 are theoretically very close to zero, which is never observed. Indeed, pyrolysis water decreases with temperature but still found to be stable for temperatures within 1000–1300 °C and residence time of 2 sec during the thermal treatment of a surrogate pyrolysis gas [106]. Dupont et al. [107] produced up to 15 % *(w% of dry biomass)*

of pyrolysis water from the pyrolysis of a mixture of two softwoods (sylvester pine and spruce) at 1000°C. However, CO_2 proportion increases and stops at a certain level for biomasses like wood (about 5-16 g/g of biomass) while for other biomasses (rice husk, straw, grape residue…), it then continues with even higher rate [42]. The plateau of the CO_2 is attributed to less favored CO_2 producing reactions in this temperature range, which are mainly primary decompositions of cellulose and hemicellulose. The successive increase (apart from wood) is attributed to secondary reactions. The differences between experimental results and thermodynamic equilibrium can be explained by kinetic limitations of the involved reactions.

I.5.2 Influence of fuel preparation

The major drawback of pulverized combustion technology is the high preparation costs including drying and grinding. However, grinding biomass is difficult compared to coal due to its fibrous nature and moisture. Some solutions like torrefaction help improve the quality of biomass fuel but the feasibility of such techniques could be questioned. The type of pre-treatment has an impact on the combustion performance of the pulverized fuel. Several studies discussed the influence of particle size and shape, torrefaction degree and moisture content.

I.5.2.1 Particle shape and size

For technical requirements, biomass should be milled to less than 2-3 mm in order to be pneumatically transported and injected by pulverized fuel burners. Conditions associated with a grinding technique (knives, hammers, balls) will influence the final particle size distribution. It is therefore important to carry out sieving steps to diagnose the grinding process that will produce the best morphological characteristics of the particles. Shape and aspect ratio differences affect the heat transfer and thereby show measurable differences in combustion performance and flame profile and its propagation velocity [24]. Due to lower surface to volume ratio, near spherical particles lose mass slower than aspherical particles with twice the conversion time (*Figure I.22*), while the flake like particles devolatilize slightly faster than cylinder like particles. In addition, spherical particles produce slightly lower volatile yields relative to other shapes [108].

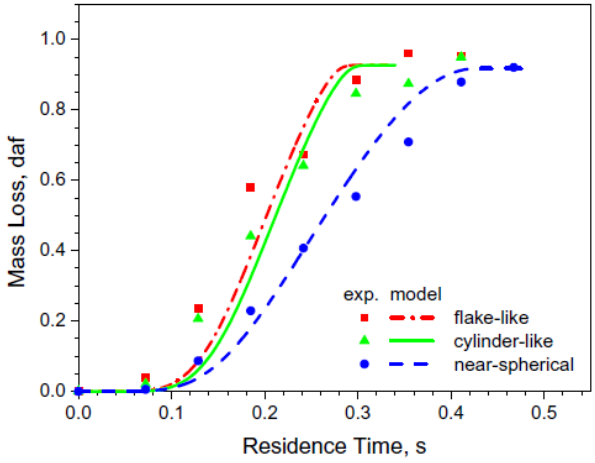

Figure I.22: Effect of particle shape on mass loss [108]

Similarly, fuel size affects the burnout of the biomass. It is reported the size is directly responsible for the yields of char, tar and gas. L. Chen et al. [109] obtained 10% higher gas yield and 3 % lower char yield with particles sieved at 0.8 mm compared to 6 mm particles

(*Figure I.23*). Beside yields, gas composition and char structure are determined by the initial size of the particle. Smaller particles devolatilize more intensely, which leads to lower heat release rates during the char oxidation process and, consequently, lower temperatures. A decrease in the burnout performance is usually observed as the particle size increases [110]. In fact, in a pulverized combustion furnace, if the particle size is large the oxidation reactions move closer to the furnace outlet, thereby causing incomplete oxidation [111] and delayed ignition as larger particles ignites at higher temperatures [112] and acquires higher inertia and penetration length [31]. The influence of the initial particle size on the subsequent char structure is even greater than the impact of the amount of volatiles released. Avila et al. [113] reports that for certain biomass types in intermediate-heating-rate experiments, small particles (100 µm) showed significantly more loss of initial biomass structures during charring than large particles (800 µm) did. This appears to be logical: the gas release occurs more slowly in larger particles due to heat transfer limitations and hence the gas can be released without destroying the initial solid structure. This is in line with G. Wang et al. [64] who found that coal shows a comparable initial burnout as biomass despite the lower volatile matter content when oxidized in a drop tube furnace at 1273 k, which was attributed to the smaller particles of coal.

Volatile composition also varies with the particle morphology. Wei et al. [114] studied the effect of particle size (from 0.10 mm to 1.2 mm) on the formation of products of rapid pyrolysis of pine sawdust and cores of apricot at 1073 K. Mass and heat transfers have little influence on training products of pyrolysis in case the particle diameter is less than 0.20 mm. On the other hand, for the particles of diameter greater than 0.20 mm, pyrolysis is mainly controlled by mass and heat transfers within the particle.

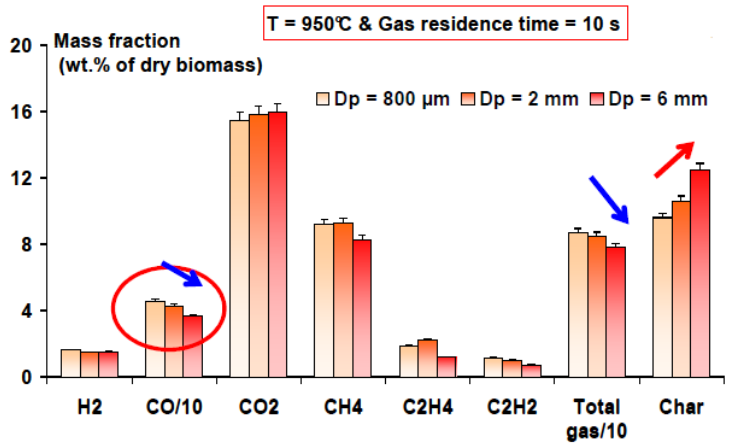

Figure I.23: Effect of particle size on pyrolysis products [109]

In the literature, there is much work concerning the influence of the size of particles on the formation of pyrolysis products. The results show that the smaller the particle size, the higher the gas yield [109], [115] with variations in species concentrations. For instance, hydrocarbon yield decreases because of the longer residence time obtained after being rapidly expelled from the small particles. The cracking reactions have sufficient time to take place [115].

I.5.2.2 Torrefaction

Torrefaction is a set of complex thermochemical reactions that occur between 200 and 300 ° C, at atmospheric pressure and in an inert environment or low oxygen presence (*Figure I.24*). This process is commonly used in the coffee and cocoa industry to create flavors. In the case of

lignocellulosic biomass, the chemical reactions govern the devolatilization of a part of the volatile matter. Research focused on the torrefaction process was already performed in France in the 1930s but no significant publications remain. Torrefaction retains typically 70% of the mass as a solid product, containing 90% of the initial energy content while 30% of the mass is converted into torrefaction gases, but contains only 10% of the energy content of the biomass due to the loss of water vapor and carbon dioxide, for which the lower heating value is zero. Hence, a considerable energy densification can be achieved, typically by a factor of 1.3 on mass basis [116]. Since mainly hemicellulose degrades during torrefaction, biomass suffers a decrease in polysaccharides content and an increase in aromaticity, a micro-porosity development and shrinkage in the cell walls, resulting in a multilayered structure. Biomass loses its capability of hydrogen bonding due to the destruction of OH groups during torrefaction. This improves the hydrophobicity and grindability of the biomass. Torrefied biomass is practically preserved from biological degradation, as often observed for untreated biomass [116].
Bourgois and Doat [117] experimented the influence of torrefaction on two tropical and two temperate wood samples. Results showed that torrefaction at 270-275 °C of eucalyptus and a mixture of chestnut and oak, increased the calorific value of the wood from 18.6 to 22.7 MJ/kg and 17.9 to 21.5 MJ/ kg, respectively. Torrefied biomass is more brittle of nature compared the raw biomass it was derived from. This is crucial for establishing the desired grindability, but has the drawback of decreased mechanical strength and increased dust formation [116]. The torrefaction of Beech wood at 280 °C reduces the required grinding energy by factor of eight [118].

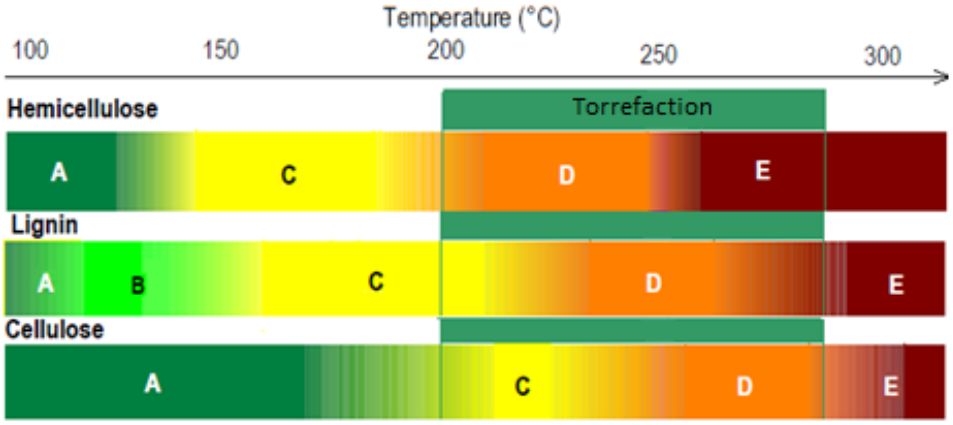

Figure I.24: Torrefaction process at the basic constituents level: (A) Drying, (B) Glass transition/softening, (C) Depolymerization and recondensation, (D) Limited devolatilization and carbonization, (E) Extensive devolatilization and carbonization [116]

Despite the similarity in mass loss, the chemical transformation of the different biomasses by torrefaction is different. E.R. Alonso [23] studied the solid chemical evolution in torrefaction of ash-wood, miscanthus and wheat straw at 300 °C. They suffer similar mass losses, but they exhibit different evolutions in terms of chemical composition and structure of the solid phase. The evolution of proportion of crystalline cellulose through carbons shows different trends among biomasses affected by lignin, which is likely to play a protecting role towards cellulose during thermal treatment. As a conclusion, the chemical evolution of the solid during torrefaction would depend on three parameters: Xylan content in hemicellulose, Lignin content in biomass and Cellulose crystallinity.

Less volatiles means less smoke produced during the combustion of torrefied biomass compared to untreated biomass [119]. However, the reactivity of biomass during pyrolysis and char combustion decreases when torrefied as published by Fisher et al. [95]. When raw biomass is rapidly pyrolyzed, the resulting rapid release of volatiles deforms biomass structures and typically leads to higher macropore surface areas and thus to higher reactivity [120]. It appears that torrefaction, which shifts volatiles release to the low-heating-rate torrefaction process, could reduce this effect, thus lowering the reactivity of high-heating-rate chars. The natural porosity produced during torrefaction allow the escape of volatiles in contrast to the raw material. This explains why raw particles suffer notable changes in surface area and morphology from the parent particles [27], which does not significantly happen for torrefied particles. The reactivity of high heating rate chars can be reduced by a factor of about two as obtained by E. Fisher et al. [95]. Another cause of lower reactivity is the risk of thermal annealing because of macropore coalescence [27], [121]. At high temperatures, the biomass particles may begin to melt resulting in a loss of the cell wall structure. The smaller particles associated with torrefied samples obtained from their improved grindability and particle fragmentation in some cases (ex: wheat straw) [122], would heat up faster and thus have longer residence times at peak temperature. Moreover, some studies found that torrefaction promotes particle fragmentation during combustion thus exposing more surface to volume ratio [122]. This however emits considerably higher yield of PM10, than that for raw biomass [111].

The combined impact of lower volatile content and smaller particle size can be considered a result of torrefaction. For instance, Li et al. [45] simulated numerically the effect of torrefaction on flame geometry. The simulations showed that torrefaction reduced the flame volume and increased the peak flame temperatures of the biomass under the studied conditions. A clear explanation of the results is the volatile content of raw and torrefied biomass. The higher volatile content improved the diffusion of the combustible gases, causing a larger flame volume and a large flame diameter for raw biomass. However, torrefaction improves the calorific value of the volatiles, which explains the higher temperature predictions for torrefied biomass.

I.5.3 Influence of flow conditions

The influence of flow conditions is generated by the flow velocity and the aerodynamic effects in the flame. These effects are studied in pilot and industrial scale furnaces using probing and imaging techniques to assess the flame parameters.

Experiments in pilot-scale facilities are practical to represent the operating conditions encountered in full-scale. Most of the studies at this scale of pulverized combustion are done with coal. Biomass pilot-scale studies are more oriented towards grate-firing beds and fluidized beds. The interest of studying biomass at this scale started with co-firing biomass with coal. The research on the pulverized combustion of biomass as a standalone fuel is rather new and no much technique have been applied especially advanced non-intrusive techniques like laser diagnostics. Such studies deepened our understanding of the phenomena associated with pulverized coal combustion and helped developing new combustion technologies like flameless combustion [125][126].

Schematically, a pulverized wood flame consists of different zones illustrated in *Figure I.25* [111]:

I- Preheat zone in which the gas and fuel particles are heated up;
II- Drying and devolatilization zone where the moisture and volatile release from the wood particles;
III- Oxidation zone where volatile and char are oxidized with air,
IV- Post-flame zone.

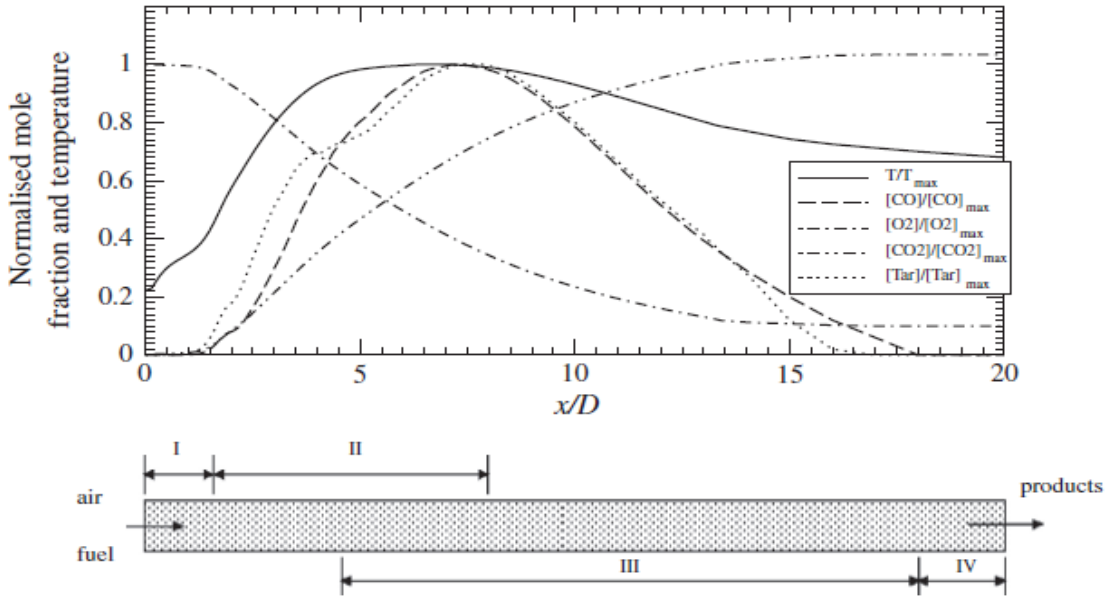

Figure I.25: Pulverized biomass flame structure [111]

Unlike the gaseous fuel flames, the reaction zones of the pulverized wood flames are very thick and they depend on the geometry of the combustor, the particle size and shape, the injection speed of the particles and the flow velocity. The structure of pulverized wood flames is sensitive to the physical and operational parameters such as the feeding rates, the heat capacity, and the shape of the particles. CFD studies characterized biomass flames to be significantly longer and wider with smaller recirculation zone compared to coal flames [45][127][128].

Elfasakhany et al. [111] carried out experimental and numerical investigations of pulverized wood flames in a laboratory vertical furnace. The results show that with higher velocity of the particles and higher flow speed the heating and devolatilization processes as well as the combustion process of the particles are delayed downstream. The ejection of the volatiles through the particles' pores, which are unevenly organized in different directions, creates the so-called rocket force that acts on the particles and influence their distribution in the combustion chamber. The emission of unburned volatile such as hydrocarbon species and CO is caused by the thickened oxidation zone. To reduce the emissions, one should make the preheat zone, the drying and devolatilization zone and the oxidation zone thinner and the post-flame zone thicker (using swirl in industrial scale burners or using smaller particles).

Comparison to coal flames was done by Weber et al. [29], [129] for biomass and RDF in jet flames using a 15 kW combustion facility with a co-axial no-swirl burner. In accord with

Elfasakhany [111], results show that the ignition of the coal flames occurs closer to the burner than ignition of biomass and RDF flames, despite the high volatile content of the RDF, its combustion extends far into the furnace and after 1.8 s residence time only a 94% burnout has been achieved. This effect has been attributed not only to the larger particle size of fluffy RDF particles but also to differences in RDF volatiles compared to coal volatiles. Substantial amounts of oily tars have been observed in the RDF flames even though the flame temperatures exceeded 1300°C. The presence of these tars has drastically enhanced the slagging propensity of RDF flames as rapidly growing deposits of high carbon content have been observed. The tar compounds from RDF were also measured by E. C. Efika et al. in a horizontal tubular reactor with higher heating rates accompanied with increasing tar quantities [130]. Ash deposition was three times higher for biomass fuels than coal, and the deposition rate was found to increase with the temperature. Up to 60% of the fuel-nitrogen was converted to NO in the case of woody biomass compared to 17% for coal.

The aerodynamic conditions in these studies were fairly laminar to simplify experimental conditions. Velocimetry is still not employed in biomass studies to allow experiments with high turbulent conditions. The poor knowledge of the aerodynamic effect on biomass flames set limitations for development of new burner geometries. Conditions that are more turbulent were investigated experimentally by Ballester et al. [31] in semi-industrial furnaces with swirl burner designed for coal firing which limited the information for biomass combustion, since the residence time was not enough for biomass particles to complete combustion. A two staged flame configuration was observed resulted by the complex aerodynamic motion generated by the burner geometry used in the study. The wide size distribution of biomass particles promotes the existence of two reaction zones along the axis of the furnace, where small particles burn in the first stage while secondary stage is where the larger particles complete devolatilization and burn. This configuration is also observed in co-combustion mode with high contribution of biomass [100]. Such an air-staged flame leads to relatively low NO emissions because of the formation of fuel-rich zones, which allow fuel nitrogen to evolve in a fuel-rich environment, producing N_2. In addition, the reburning of already formed NO in these eddies reduce NO concentrations [100]. Gas concentration maps obtained by probing revealed CO, HCN and NH_3 concentration peaks along the furnace axis and NO peak to be found on the flame boundaries, while very low NO concentration are measured along the axis.

Adapting new technologies to biomass require testing many other aspects under different conditions. Oxygen enrichment for example would increase the average surface temperature and consequently increase the radiant heat flux intensity to the furnace walls [131]. Currently, one of the most interesting technologies is the co-combustion of coal and biomass. This interest emerges from the high dependency on coal in many parts of the world. Co-firing may be a transition stage towards a full switch to pulverized biomass combustion that can benefit from the existing power plants.

The addition of biomass appears to stabilize the flame, improve the combustion efficiency due to the lower CO concentration, and higher char burnout level in co-firing. However, Alkali metals have been found to increase under co-firing. This maybe the source of furnace problems such as slagging and corrosion, as higher alkali metal content would result in a lower melting point of the ash [68]. The addition of biomass reduces SO_2 emissions while NO emissions depend on the type of biomass and volatile composition that may promote the NO production or reduction mechanisms. Moreover, the large quantity of released soot possesses high radiant intensity and therefore high temperature. This consequently produces brighter flames as verified

by Gang Lu et al. [87]. They also reported that the ignition delay observed in biomass flames due to large particles and high moisture content, also delays the ignition point in co-combustion mode, but the ignition point can still be shifted close to the burner under excess air.

I.6 Conclusion

As deemed by several studies, biomass is a source of interest for the green energy production. Its abundance and renewability are advantages over other fuel types. The combustion in a pulverized mode produces flames similar to oil and gas flames so it is widely used in industrial power plants. It is considered the most effective mode of solid combustion as it produces more energy from the same reactor volume.

The combustion of pulverized solids involves several phenomena: particle-heating, devolatilization, homogeneous oxidation of volatile matter, and heterogeneous oxidation of the carbon residue. Devolatilization is characterized by the release of volatile materials mainly composed of hydrocarbons, CO, CO_2, H_2, H_2O, and tars. Once released, these volatile materials oxidize in gaseous homogeneous phase. The oxygen then enters the particle where the oxidation of the carbonaceous solid takes place, a reaction that will form CO and CO_2.

The literature offers many case studies on a wide range of feedstock materials; each possesses a behavior influenced by its composition and the process conditions. A lot has been done on particle scale especially at low heating rates concerning the influence of preparation and reaction temperature on the devolatilization behavior, volatile composition and char oxidation as well.

However, the high heating rates in flames are found to alter the combustion behavior and reaction kinetics. Many aspects of the thermochemical phenomena are influenced by the aerodynamic conditions and the particle-particle interaction in flames. These effects are poorly understood and have been investigated in few studies at pilot scale using probing techniques. Until now, in the view of the variety of fuel types, no clear criterion is offered for the classification of biomass that can give a first impression of the fuel behavior on industrial scale. This is necessary for the design of combustion burners and boilers.

Chapter II. Experimental methods at particle scale

This Chapter presents the experimental methods used at particle scale: thermogravimetric analysis, horizontal tubular reactor, drop tube furnace and particle combustion shadowgraphy. The experimental procedures and the methodology of the treatment of experimental results are explained in this chapter as well.

II.1 Fuel choice and characterization

Despite the increasing international awareness of the polluting role of coal combustion in power plants, it is still the second source of primary energy (roughly 30%), mostly used for electricity generation (over 40% of worldwide electricity is produced from coal). Alternative energy resources like biomass should present a better ecological and economical way of energy production when compared to coal.
However, the valorization of biomass by combustion is problematic regarding its mineral content and the variability of its composition.

II.1.1 Fuel choice and preparation

The fuel choice is in the purpose of investigating the volatile matter content influence on the combustion process. The variability of the composition of biomass can be simulated by varying the volatile content of the biomass. Volatile matter is the major constituent of most biomasses and therefore, the combustion process depends mainly on its mass fraction. The latter can be varied using torrefaction at different temperature levels and specified residence times.

Specifying a reference biomass type is important in terms of comparison and evaluation of the performance of different types to be studied. Maritime pine, which is extensively studied by the research community, is chosen in the present study as a reference material due to its abundance and low ash content. It is naturally growing in the west of the Mediterranean basin, standing on over 10% of the total French forest, covering about 1 360 000 ha [132], and it can be considered as the main biomass sources for energy in countries like Spain. Its scientific name is Pinus pinaster and it belongs to Pinacea family. Demolition wood was also used as representative "problematic" fuel, beside coal for comparison. It is the waste wood of demolished furniture, so it contains high impurities. Studying coal serves to evaluate the feasibility of the biomass taking the lead as an alternative fuel. Venezuelan coal is chosen because of its relatively high volatile matter content. This could help us understand the influence of the physical properties of the fuel when comparing coal with a biomass with close volatile matter content and close elementary composition.

Another influencing parameter on the combustion and the preparation cost is the particle shape and size. Many studies have addressed this issue showing a very important role of the size distribution on the thermal conversion of biomass. Large particles have a long devolatilization time and internal heat and mass transfers limitations resulting in a delayed ignition, while small particles are easy to burn as more surface area is exposed to heat and oxygen [31] and few transfer limitations. However, unlike coal, biomass is difficult to grind requiring high preparation cost for small size particles.

Three types of thermally treated pine were prepared: torrefied pine, pyrolyzed pine and carbonized pine. Using TGA and lab scale experiments, we determined the operating conditions of the torrefaction process. Pine was torrefied at 280 °C for 25 min and pyrolyzed at 450 °C for 15 min. A longer residence time of 20 min at 450 °C released most of the volatiles and produced carbonized pine. The mass yield in the first production conditions (280 °C, 25 min) reaches 78% (on dry basis), while the pyrolyzed pine production yield (at 450 °C, 15 min) was 32% (on dry basis). The yield of the production of carbonized pine (at 450 °C, 20 min) is 23% (on dry basis).

The influence of particle size on combustion phenomenon is a parameter in our study. In our case, maritime pine, torrefied pine, pyrolyzed pine, carbonized pine and coal were milled to two particle sizes: <500µm and < 1mm. In order to ensure minimum preparation cost for the problematic fuel, demolition wood was not milled but sieved using 2 mm sieve. Only 15% (by mass) are refused during the operation.

In the following, pine, torrefied pine, pyrolyzed pine, carbonized pine, demolition wood and Venezuelan coal will be referred to as Pine, Pin-T, Pin-P, Pin-C, DW and coal respectively.

II.1.2 Fuel composition analysis

Analysis of fuel composition is performed on the fuel obtained after preparation. The proximate analysis of a solid determines the percentages of ash content, volatile matter and fixed carbon present in this solid. It is made according to the following standards:

- In order to compare composition of Pine, Pin-T, Pin-P and Pin-C the same standard used usually for coal characterization is used. The ash content is determined by quantifying the mass of solid remaining after oxidation of 1 g of solid for 2 h at 710°C in air. The amount of ash recovered after oxidation corresponds to the amount of mineral material initially present in the solid (EN 15148).
- The percentage of volatile matter (VM) is determined by quantifying the mass loss of the solid (1 g) after 7 min of pyrolysis at 900°C (EN 15148).
- Fixed carbon is the complement to 100 of the sum of the contents of moisture, ash and volatile matter:

$$FC = 100 - ash - VM - Moisture$$

	Maritime Pine (Pine)	*Torrefied Pine (Pin-T)*	*Pyrolyzed Pine (Pin-P)*	*Carbonized Pine (Pin-C)*	*Demolition Wood (DW)*	*Venezuelan Coal (Coal)*
Ash	*0.87*	*1.33*	*2.54*	*3.24*	*2.13*	*2.03*
VM	*81.22*	*73.62*	*44.83*	*19.59*	*78.29*	*37.08*
FC	*18.58*	*25.05*	*52.62*	*77.17*	*19.57*	*60.89*
C	*51.68*	*55.10*	*67.77*	*79.87*	*48.51*	*82.14*
H	*5.93*	*5.68*	*4.50*	*3.44*	*5.63*	*5.57*
N	*0.22*	*0.29*	*0.32*	*0.39*	*4.39*	*1.54*
O (by difference)	*41.27*	*37.52*	*25.15*	*16.28*	*40.58*	*8.71*
LHV (MJ/kg)	*18.45*	*19.74*	*25.30*	*28.33*	*17.70*	*32.34*

Table II.1: Fuels proximate and ultimate analysis on dry basis

The ultimate analysis of a solid determines the percentages of carbon (C), hydrogen (H), nitrogen (N) and sulfur (S) present in this solid. The percentage of oxygen (O) can be measured, but it is usually calculated as being the 100's complement of the sum of the percentages of carbon, hydrogen, nitrogen, sulfur and ash. The proximate and ultimate analyses of the fuels

are listed in *Table II.1* in addition to the heating value, which was measured in a bomb calorimeter (Isopéribole PAAR).

II.2 Fuel characterization using macro-thermogravimetric analysis

The use of thermogravimetric analysis (TGA) technique has become a common place for characterizing the fuel behavior with rising temperature.

II.2.1 General description of TGA

The macro-TGA (Biowooeb, CIRAD) consists of an electrically heated insulated furnace where a crucible containing the sample is placed. The crucible is held by an alumina wire connected to a balance of 0.1 mg precision. The mass of the sample is continuously monitored throughout the experiment indicating the mass loss by devolatilization and combustion (*Figure II.1*).
The apparatus available in CIRAD allows a maximum capacity of 500 mg (depending on the fuel type), which is much higher than usual laboratory TGA (8-10 mg). The crucible used here has a volume of 800 µl whereas commercial analyzers generally have crucibles of 50 - 150 µl.

For each experiment, a sample of 100 mg (±1mg) sieved to 500µm is introduced into a crucible of 4 mm depth and 16 mm diameter, forming a layer of about 2 mm. This mass has been chosen as a compromise between two constraints:

- Given the accuracy of the analytical balance, a sufficient mass of sample was required to obtain accurate mass loss profiles;
- The height of the bed should be low enough so that the heat transfer time in the bed is negligible compared to the reaction time.

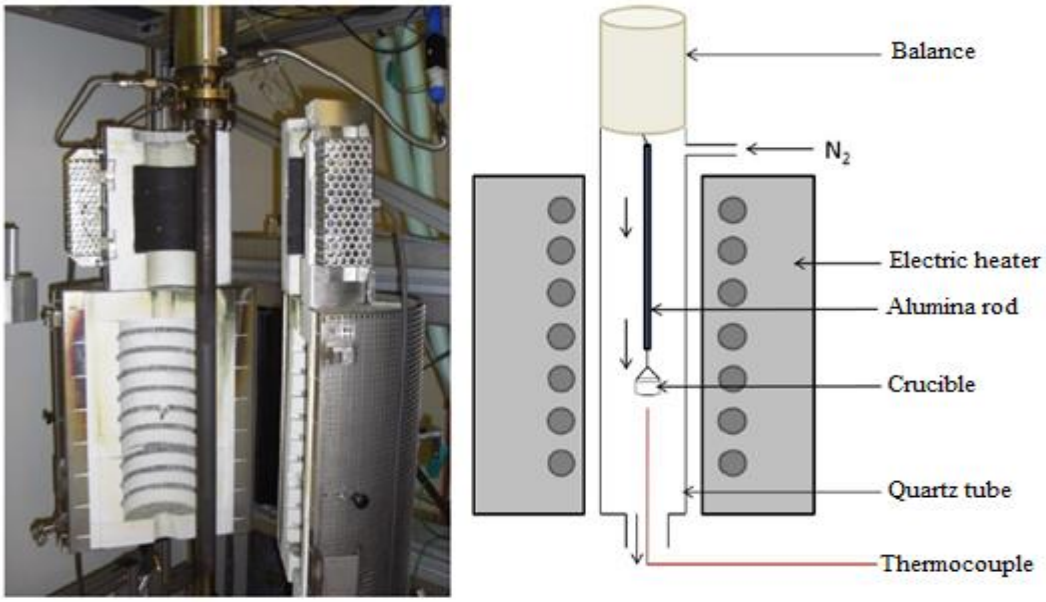

Figure II.1: Photo and scheme of the macro-TGA in Cirad

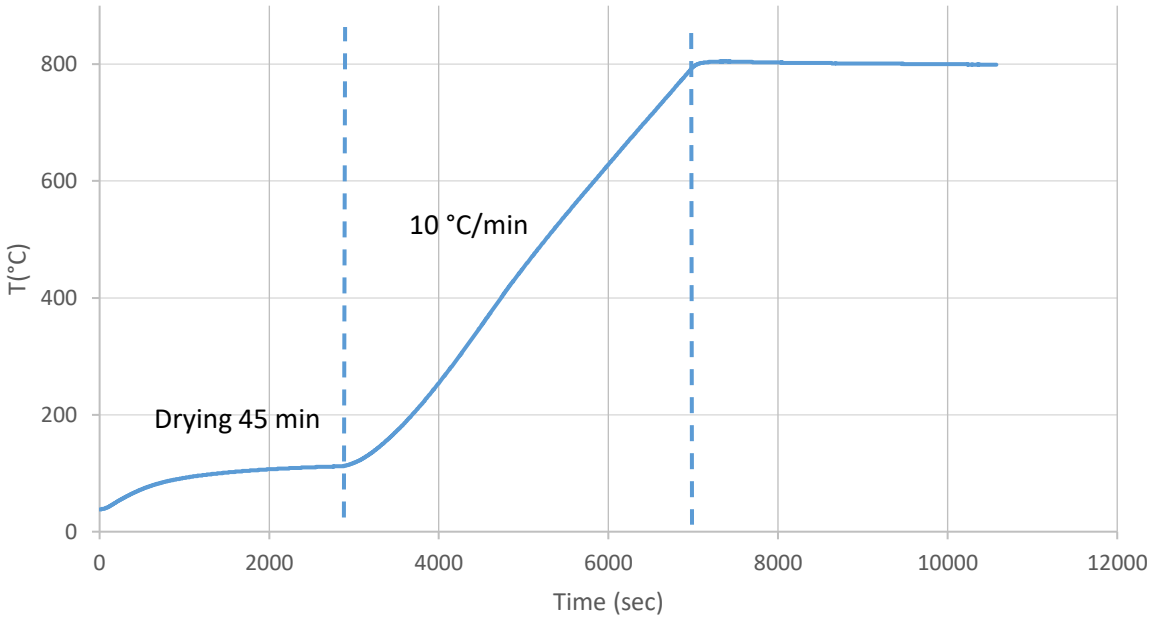

Figure II.2: Sample temperature history during the TGA experiments

The reactor is continuously swept by air at 165 ml/min. The airflow is chosen to avoid oxygen deficiency during the combustion experiment. Each experiment was repeated at least three times in order to be certain that the result is workable, and to quantify the repeatability of the measurements.

Once introduced into the reactor, the sample is first heated to 120°C with a heating rate of 20°C/min, and then kept at this temperature for 45 min to be dried until its mass is stable. A second heating phase then consisted in raising the sample temperature to 800°C, with a heating rate of 10°C/min. The temperature is left constant at 800°C for 60 min to ensure the complete degradation of the sample. *Figure II.2* shows the temperature history imposed on the tested sample.

II.2.2 Data treatment

Dedicated software recorded the mass and temperature of the sample every 5 seconds during the experiment. The sample conversion X is expressed by the normalized sample mass:

$$X = \frac{m_t - m_{ash}}{m_0 - m_{ash}} \qquad \text{(Eq.}II.1\text{)}$$

Where m_t is the actual sample mass, m_0 the initial sample mass after drying and m_{ash} the final ash mass. The rate of conversion is calculated as the first derivative of X with time

$$\left(\frac{dX}{dt}\right)_t = \frac{X_{t+\Delta t} - X_{t-\Delta t}}{2.\Delta t} \qquad \text{(Eq.}II.2\text{)}$$

Δt is the time step size of the derivation.

Considering the uncertainty of weighing and the slight mass variation within 5 seconds, the value of the calculated rate had to be smoothed. A centered moving average was then applied

to the calculated first derivatives. A range of 9 points was chosen to highlight the results without much altering the information.

$$\left(\frac{dX}{dt}\right)_{average,t} = \frac{1}{9}\sum_{j=-4}^{+4}\left(\frac{dX}{dt}\right)_{t+j.\Delta t} \quad \text{(Eq.}II.3\text{)}$$

The conversion and the rate of degradation are plotted as a function of temperature. In order to compare the degradation profiles of different fuels, some characteristic points are considered (*Figure II.3*):

- T_{onset}: temperature associated with the beginning of the sample conversion. It is defined by extrapolating the slope of the devolatilization rate in correspondence with the first local minimum in the second derivative of the conversion curves [35].
- $T_{peak.dev}$: temperature corresponding to the maximum devolatilization rate;
- $\left(\frac{dX}{dt}\right)_{max,dev}$: maximum devolatilization rate
- $T_{peak.char}$: temperature corresponding to the maximum char consumption rate
- $\left(\frac{dX}{dt}\right)_{max,char}$: maximum char consumption rate
- $T_{burnout}$: the temperature where the rate of mass loss decreases consistently to less than 1%/min

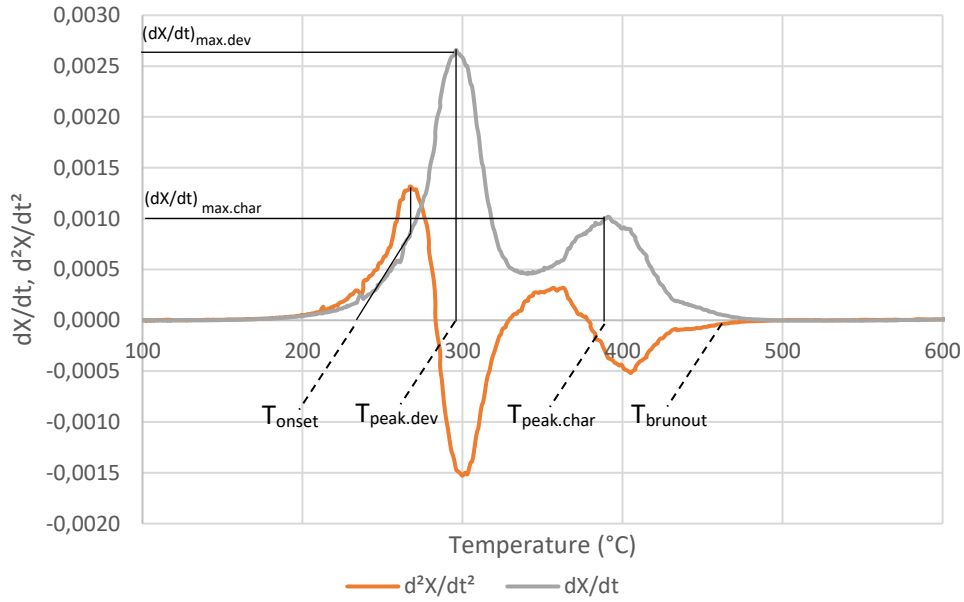

Figure II.3: Illustration of the characteristic reaction temperatures on the first and second time derivatives of the conversion as a function of temperature.

These values are determined for each sample. The characteristic points are the average of all the experiments of each fuel.

II.2.3 Kinetic parameters

The decomposition of biomass is generally expressed by the following equation [134]

$$\frac{dX}{dt} = A\ exp\left(-\frac{E}{RT}\right)(1-X)^n \qquad \text{(Eq.}II\text{.4)}$$

X is the normalized conversion calculated from the mass loss curves and n is the reaction order. A (1/sec) and E (kJ/mol) are the Arrhenius parameters known as the frequency factor and activation energy respectively. A, E and n are obtained using several methods where the simplest is the direct method.

The direct method consists of taking the logarithm of both sides of equation *II.4*. Considering n=1 implies the following equation

$$\ln\left[\frac{1}{(1-X)} \times \frac{dX}{dt}\right] = \ln(A) - \frac{E}{RT} \qquad \text{(Eq.}II\text{.5)}$$

Equation *II.5* can be written in the form of straight line (y=ax+b) by setting x abscissa and y ordinate as:

$$y = \ln\left[\frac{1}{(1-X)} \times \frac{dX}{dt}\right] \quad and \quad x = \frac{1}{T} \qquad \text{(Eq.}II\text{.6)}$$

The slope of the line is proportional to the activation energy and the pre-exponential factor is calculated from the y-intercept.

II.3 Horizontal tubular reactor

Combustion tests were performed in laboratory in an electrically heated horizontal tubular furnace to determine composition of gases obtained from the combustion of different biomasses.

II.3.1 General description

Combustion tests were performed in Biowooeb, CIRAD, in an electrically heated horizontal tubular furnace (*Figure II.4*). In contrast to boiler combustion, where air and biomass are continuously supplied in proportions that maintain a constant excess of oxygen (λ), the combustion tests were conducted in batch mode. A sample of biomass was then introduced at a time t_0 in the furnace preheated to the set temperature, swept by a constant and controlled flow rate of feed gas (air).

Figure II.5 presents the experimental rig used to carry out the combustion tests of biomass to measure the resulting variations in gas concentrations (CO, CO_2, NO, O_2). The used furnace (4) (PYROX VK65 / 550) consists of a stainless steel tube (Ø = 5 cm, L = 60 cm) insulated and electrically heated to a maximum temperature of 800°C. Another electric heater (6) is placed at the exit of the furnace, which limits the heat loss at the exit. *Figure II.6* shows the temperature profile of the heated zone with a set point of 800°C and 650°C for the furnace and heater (6) respectively. A 15cm isothermal zone (785°C - 798.3°C) is obtained at 30 cm from the tube entrance.

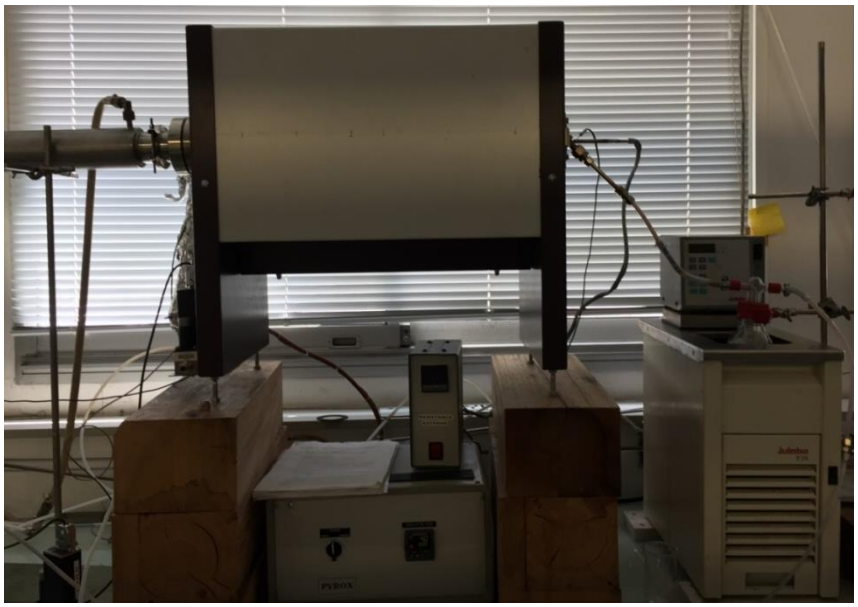

Figure II.4: Horizontal tubular reactor

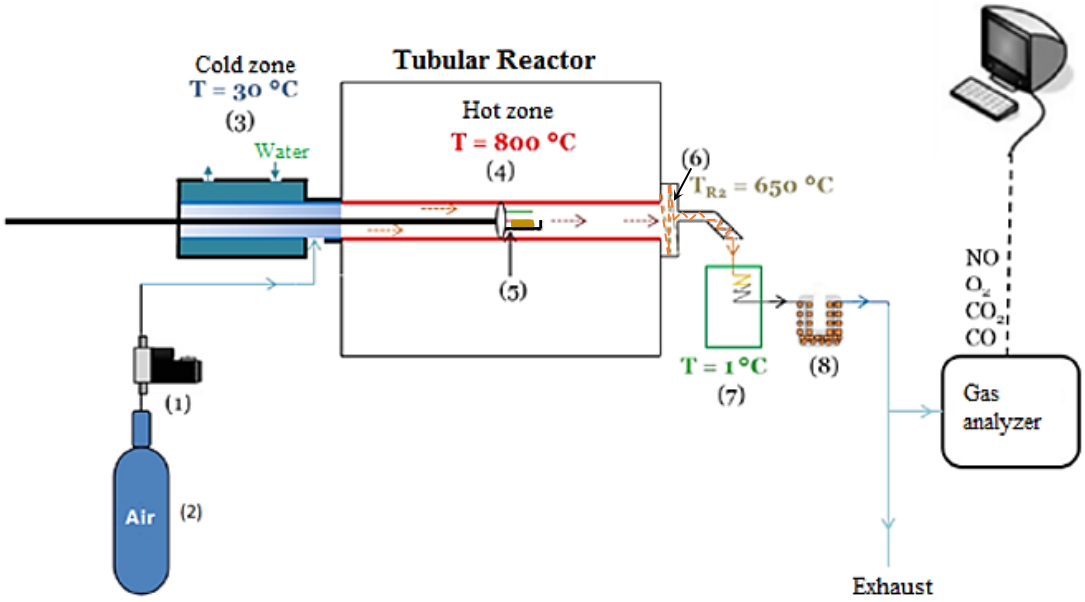

1. *Mass flow meter*
2. *Air bottle*
3. *Cold zone*
4. *Heated zone*
5. *Rectangular crucible fixed on the sliding rod*
6. *Electric heater*
7. *Cooling bath*
8. *Filter*

Figure II.5: Horizontal tubular reactor scheme

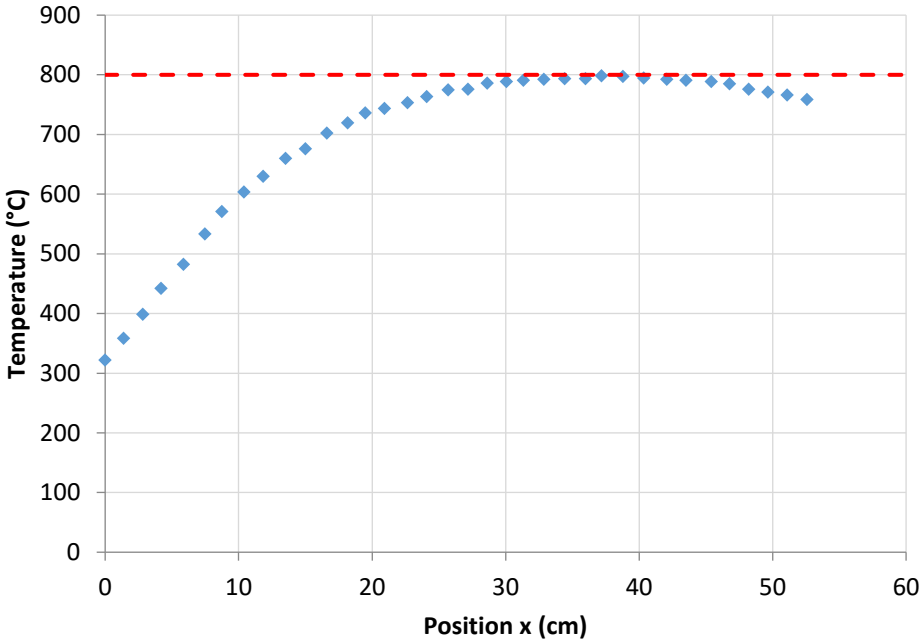

Figure II.6: Temperature profile inside the furnace

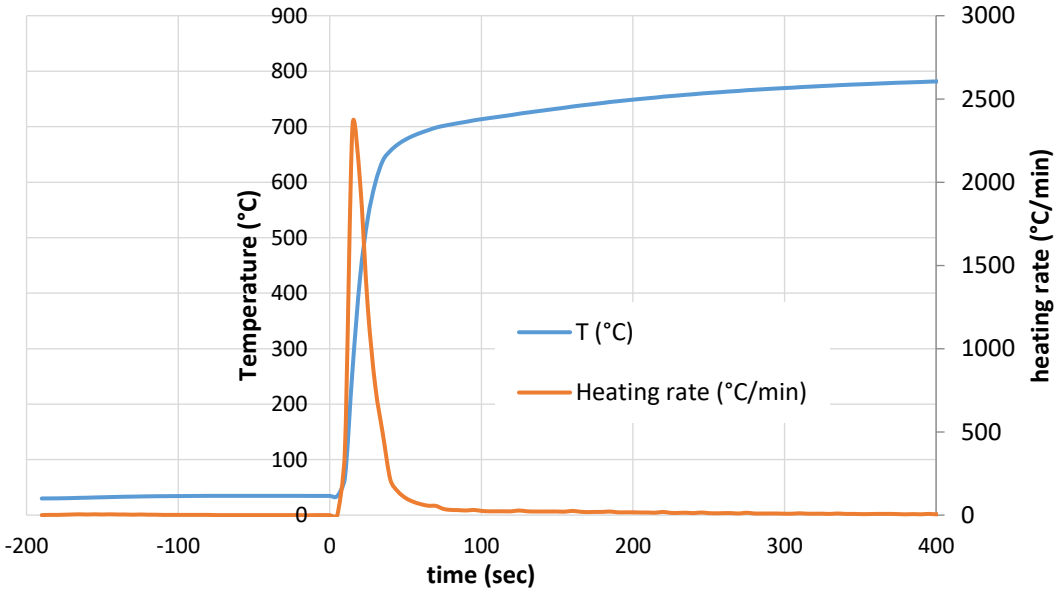

Figure II.7: Typical sample temperature evolution (insertion at t=0)

The ambient gas (air) is supplied and regulated by means of thermal mass flowmeters controller Brooks 5850S, (1). The delivered flow rate is checked using a volume meter before each experiment. The value of the gas flow determines the residence time of the produced gases inside the furnace. A cold zone (3) is located at the inlet of the furnace, consisting of a water-cooled double-jacket exchanger. This zone maintains the sample at room temperature (30°C) before it is introduced into the heated zone once the operating conditions are stable and the composition of the gaseous atmosphere are established. The sample is placed in a rectangular crucible (L = 12 cm, l = 4 cm, h = 1 cm) made from a sieve mesh (200 µm), which can be attached to a sliding rod (5). For each experiment, a sample of 250 mg (±1 mg) is introduced to the same position in the isothermal zone. A ø1mm thermocouple is positioned above the sample

to measure the temperature at the position of the sample during combustion. A typical sample temperature evolution is introduced in *Figure II.7*. A high heating rate is reached (2034 °C/min) shifting the reaction to higher temperatures. A peak should be observed indicating the flame temperature during the homogeneous combustion phase as previously observed with large biomass particles [54]. It was never caught by the thermocouple probably because the sample was distributed with less than 3 mm thickness over the crucible, and the thermocouple was never exposed to the flame.

When the exhaust gas concentration reaches again the air composition (21% O_2, 0% CO_2, NO, CO), the crucible is pulled out to the cooling zone and the experiment is over. The combustion gases exiting the furnace are directed to a bottle containing silica gel placed in a cold bath set at 1°C (7). At this temperature, the water vapor produced by the combustion reaction is condensed and absorbed by the silica gel contained in the bottle. The cotton filter (8) then collects the particulates entrained with the exhaust dry gas. This post treatment procedure helps to protect the gas analyzer downstream.

II.3.2 Gas treatment and analysis

A fraction of the purified combustion products is sent to a gas analyzer (testo 350) using a pump (1 L/min) to measure the concentrations of O_2, CO, NO, NO_2, and SO_2 (using electrochemical sensors) during the combustion with 2 Hz measuring frequency. CO_2 is not measured, but calculated by the analyzer. The total produced gas was then sampled in five sampling bags; the mean concentration of produced gases are then analyzed by the micro-GC (µGC Varian CP 4900). So the total quantity of each species measured by integrating the testo 350 curves during time was then verified by the µGC. The accuracy of the testo 350 gas analyzer is presented in *Table II.2*.

	Measurement range	**Accuracy**	**Resolution**
O_2	0…25 vol.%	± 0.2Vol.%	0.01 vol.%
CO	0…10000 ppm	± 10ppm (0…199ppm) ± 5% of reading (200…2000ppm) ± 10% of reading (rest of range)	1 ppm
NO	0...4000 ppm	± 5ppm (0…99ppm) ± 5% of reading (100…1999ppm) ± 10% of reading (rest of range)	1 ppm
NO_2	0...500 ppm	± 5ppm (0…99.9ppm) ± 5% of reading (rest of range)	0.1 ppm
SO_2	0...5000ppm	±5ppm (0…99ppm) ±5% of reading (100…1999ppm) ±10% of reading (rest of range)	1ppm

Table II.2: testo 350 gas analyzer specifications

The repeatability of gas concentration measurements during combustion of a sample was evaluated by repeating at least three combustion tests per sample. The circuit and the gas

analyzer are purged with air before and after each experiment. The furnace exit is regularly purged with acetone to remove the tar accumulated in the tubes before the cooling bath.

II.4 Particle combustion shadowgraphy (PCS)

Studies performed in TGA or in lab-scale reactor give information on kinetics or on the produced gas, but very few results about the behavior of each biomass particles during pyrolysis, volatile matter and solid residue oxidation. In this aim, a specific device has been developed to observe the behavior of biomass particles during the different stages of combustion.

II.4.1 Single particle reactor

An experimental apparatus was put in place to visualize the shadow of a solid particle during its thermal conversion. This apparatus, initially developed to study the evaporation of liquid fuels droplets [135], has been modified to make possible the observation of a single particle. The advantage of this technique is that it can surpass the flame barrier during the combustion of volatiles and get access to the particle shape and projection area evolution with time. Usual visible imaging techniques are usually interrupted by the flame brightness, which prevents receiving any information about the particle degradation in this stage. The installation (*Figure II.8*) consists of a 12 x 13 x 14 cm^3 heated combustion chamber fixed on a horizontal plateau alongside with two cameras and a LED lamp. The chamber is electrically heated to a set point of 800°C maximum. A 3 cm thick wall supported with a 2.5 cm insulation layer maintains the chamber at the set temperature.

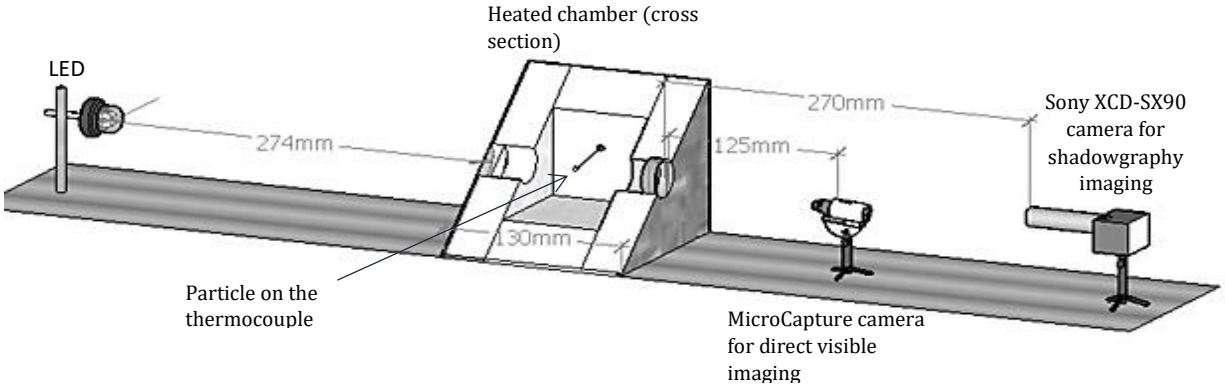

Figure II.8: Particle combustion shadowgraphy experimental rig

	Working distance range (mm)	Magnification	N.A. Object Side	Resolution Limits (microns)	Depth of field (mm)	Resolution (pixels)
Sony XCD-SX90	300 – 370 (nominal 356)	0.9x	0.018	9.4	1.59	850x850
MicroCapture	0-150	10x~300x	-	-	-	352x288

Table II.3: The specifications of the used cameras

Two ø3cm optical quartz windows (thickness: 1cm) are situated on opposite sides of the chamber. A monochrome camera and a MicroCapture camera are situated on the same side.

The monochrome camera (Sony XCD-SX90) is situated at 27 cm from the chamber and equipped with:

- "Navitar precise eye" lens,
- 0.25x lens attachment to increase the working distance,
- 2.0x adapter producing suitable magnification

The specifications of the lens are listed in *Table II.3*. The camera is adjusted to capture the particle position at the center of the chamber at 37 frames/sec with 0.2 ms exposure time. Another MicroCapture camera is fixed at 11 cm from the chamber allows recording the combustion in RGB at 30 frames/sec. Both cameras are held at a fixed distance from the particle position to achieve a consistent optical magnification.

II.4.2 Experimental procedure

Prior to an experiment, a particle is glued to the tip of a 250µm K-type thermocouple measuring the temperature variation of the particle at a temporal resolution of 12 Hz. The frequency is deemed sufficient to trace the temperature history at the heating rate imposed by the chamber.

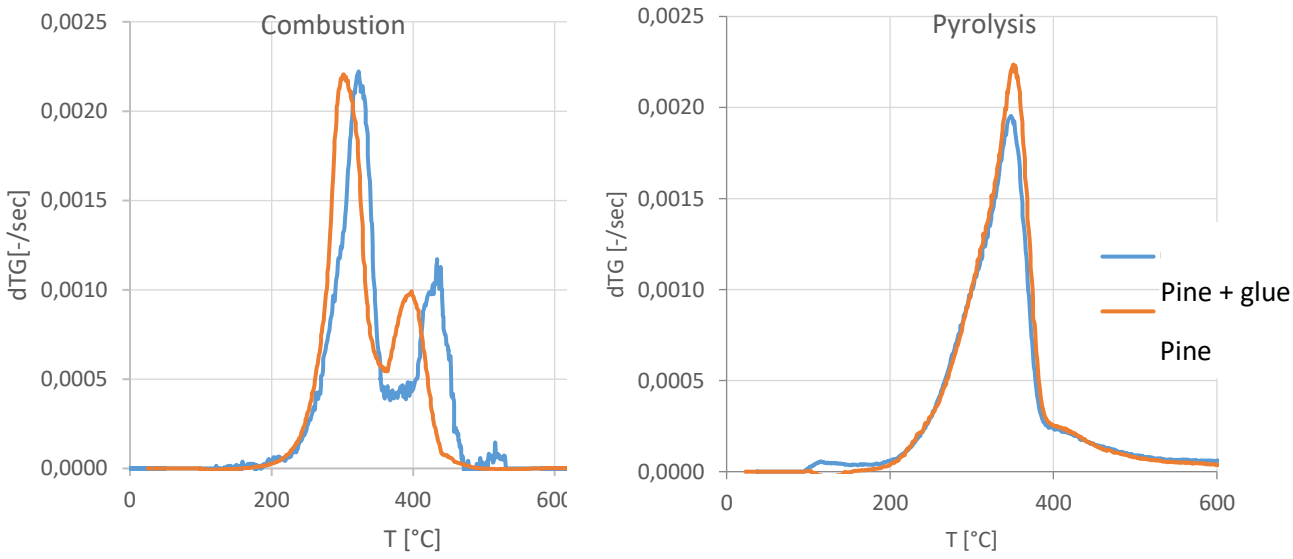

Figure II.9: TGA of Pine and Pine + glue to determine the influence of glue on the combustion (left) and pyrolysis (right) of Pine

The glue is a high-temperature nonorganic glue used at the tip of the thermocouple to ensure little interference with the occurring thermochemical phenomena. Several types of glue were tested for this reason in order to choose the one creating less influence. The influence was evaluated using the TGA results of a sample of particles covered from one side with the glue and held in a wide crucible. *Figure II.9* displays the comparison of the derivative of normalized mass loss of Pine and Pine with glue in pyrolysis and combustion. Under inert atmosphere, the chosen glue seems to have little effect on the pyrolysis behavior. However, the combustion tests revealed that the glue shifts slightly the degradation peaks to a higher temperature and separates

more the char and volatile oxidation processes. However, little to negligible difference on the values attained by the peaks, processes durations, and ignition temperature is observed when comparing both curves. So, the effect of the glue is limited and it allows the comparison of results obtained with different fuels using same methodology.

Once the chamber attains and stabilizes at the experiment temperature, the particle is inserted quickly to the chamber by the help of a guiding rod fixed to the external wall of the chamber. The particle position is adjusted to lie always in the field of view of both cameras during the whole process.

II.4.3 Samples' properties

Table *II.4* shows the physical properties (shape and size) of the tested particles of each tested fuel. They are samples of the prepared fuels described in §II.4.3. So their size is in the range 0.5 to 1.5 mm possessing different aspect ratios (defined as the ratio of the maximum length to the maximum width of the particle) and their mass is up to maximum 2 mg. Pine particles are mostly flake-like while torrefied pine, Pine char and coal are between cylindrical and spherical particles. Demolition wood particles are mostly thick flakes made of small compressed fragments of wood and other impurities like paint, giving it a brittle nature. In addition, Venezuelan coal was tested aiming to show the different behavior of combustion of biomass and coal even when containing a high volatile content.

	Pine	***Pin-T***	***Pin-P***	***Pin-C***	***DW***	***Coal***
Particle shape	*Needle-like*	*cylindrical*	*cylindrical*	*Near-spherical*	*Flake-like*	*Near-spherical*
Aspect ratio	*2.50 ± 0.70*	*1.67 ± 0.40*	*1.65 ± 0.41*	*1.41 ± 0.29*	*2.08 ± 0.48*	*1.28 ± 0.26*
Particle size (mm) (min-max)	*0.68 - 1.57*	*0.42 - 1.15*	*0.49 - 1.25*	*0.49 - 1.02*	*0.50 - 1.74*	*0.48 - 0.93*
Mass (mg) (min-max)	*0.1 - 1.8*	*0.1 - 1.3*	*0.1 - 1.1*	*0.1 - 1.1*	*0.5 - 2.1*	*0.6 - 1.6*
Number of tested particles	*32*	*29*	*30*	*16*	*31*	*25*

Table II.4: Physical appearance of the tested particles

The samples are dried for 24 hours before every experiment considering the high variation in moisture content (Pin-P: 13%, Pin-T: 1.9%), which can hugely influence the particles behavior and ignition delay. The particle-to-particle variations are expected especially for the thermally treated samples for which the conditions of preparation are not very homogeneous. This is evident from the color difference among the particles of torrefied and char Pine. For this reason, a high number of particles were tested to reduce the deviations and to allow a better determination of the trends and average values.

II.4.4 Video analysis

The monochrome videos of PCS experiments are saved in avi formats. They are then converted into binary videos using ImageJ in order to facilitate the detection of the particle contours. The videos passed through thresholding procedures after subtracting their background based on the "rolling ball" algorithm described in [136]. The algorithm creates a smooth continuous bright background, while darkens the objects of interest. During the progress of the combustion, the particle brightness changes after the flame extinguishes. Oxygen attacks the surfaces and char oxidation is triggered radiating near infrared wavelengths. Therefore, it was necessary to apply a first threshold procedure for the frames during the flame, followed by a second different threshold procedure when the brightness of the particle increases significantly in the char combustion frames.

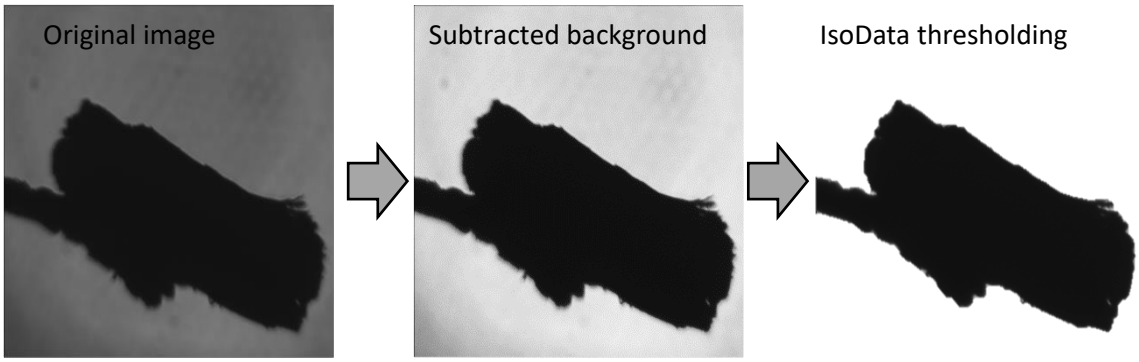

Figure II.10: Image processing for the flame part

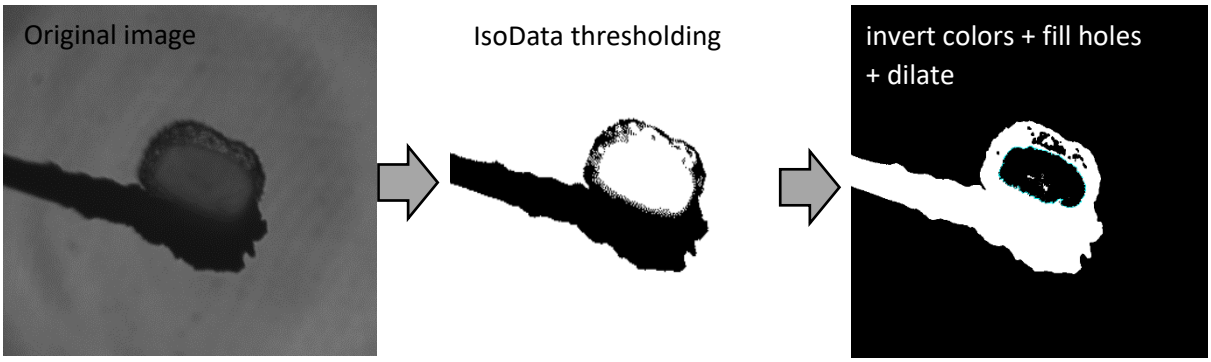

Figure II.11: Image processing for the heterogeneous reaction zone detection

During the flame part, an iterative procedure based on the IsoData algorithm is used [137]. The procedure (*Figure II.10*) divides the image into object and background by taking an initial threshold, and then the averages of the pixels grey levels at or below the threshold and pixels above are computed. The averages of those two values are computed, the threshold is incremented and the process is repeated until the threshold is larger than the composite average. That is,

$$threshold = (average\ background + average\ objects)/2$$

For the char combustion part, the external contour in the particle image was more difficult to detect as the threshold depends strongly on the particle brightness, which varies with time and particle conditions. The particle brightness in the heterogeneous reaction zone was similar to

that of the background, so the bright zone of the particle and the background are both above the specified threshold limit, and they are then highlighted similarly in white by the algorithm as shown in *Figure II.11*. As a result, the particle and the background are blended together in white, and the external contour of the particle cannot be identified from such image. Therefore, other algorithms should be adopted to extract the external area in this period. ImageJ software could produce a montage with thresholding results from seventeen methods to explore which method segments the data best. The methods are described in [138]. With a stack of images, it takes a lot of time to process each slice individually. Therefore, only the slice with the highest brightness and probability of error was manually chosen here. *Figure II.12* displays the montage with the raw image of a torrefied pine particle displayed at the end. The method that fits best the data in this case (i.e. with sufficient background subtraction and smooth continuous contour) is the Mean method (framed in green in *Figure II.12*) in this case is chosen to run over the whole stack.

Hence, the extraction of the external contours of the particle involves two thresholding methods: the IsoData method for the flame phase and the Mean method for the char combustion phase.

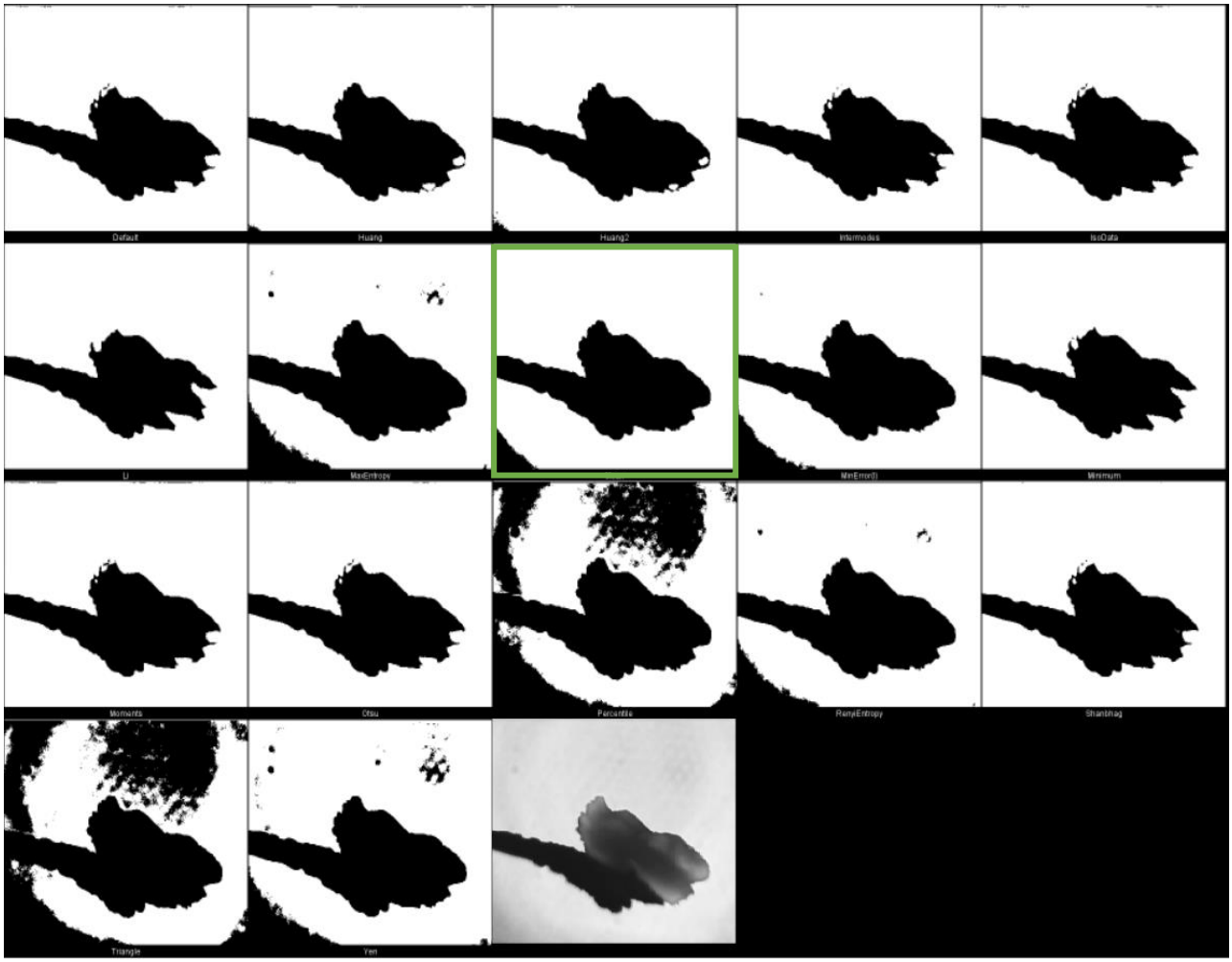

Figure II.12: thresholding methods on ImageJ (raw image at the end)

Moreover, the IsoData threshold during the char combustion highlights another region of interest in *Figure II.11*, which is the region where the char is being oxidized. Indeed, the bright zone inside the particle (in the original image) is the region of the particle where the

heterogeneous reaction takes place, while the surrounding black region is the burnt part of the particle. It is noticeable how the reaction zone during the char combustion separates from the external area of the particle. The particle undergoes internal combustion, which will be discussed later in details. Hence, the IsoData method was repeated in this stage with additional treatment and the purpose was now to follow the evolution of the reaction bright zone, which is directly related to the progress of the combustion. Binary images were inverted to keep the detection zone black for the inner contour detection later. Further treatment including automatic dilating and filling holes was performed to distinguish and follow as much as possible the zone of interest.

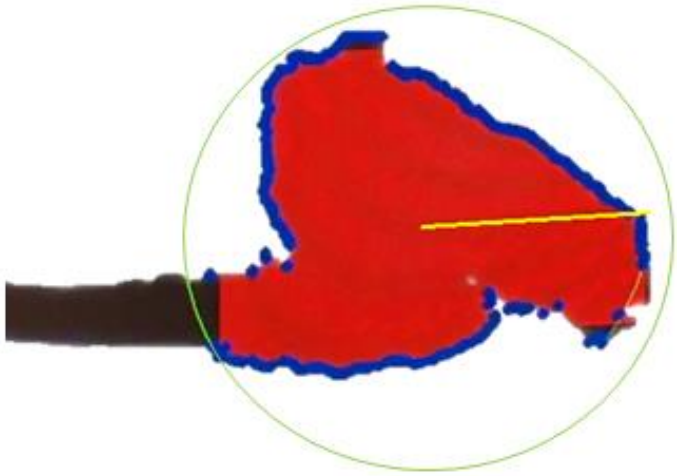

Figure II.13: Contour detection of the particle

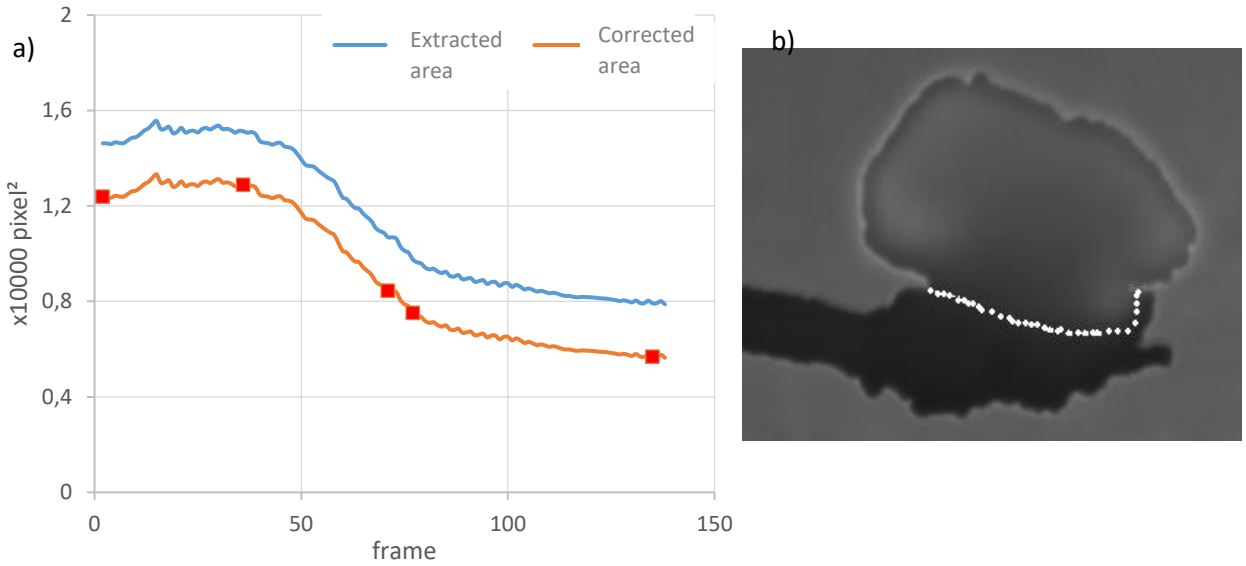

Figure II.14: Correction of the particle projection area: a) subtraction of the glue area from the detected particle surface; b) distinguishing the particle from the glue during char combustion based on brightness.

The treated videos are then processed by a contour detection code capable of generating the evolution curve of the projection area of the black zone as a function of time. The algorithm passes by the following steps:

- Estimate the black particle center then determine a measurement circular zone (in green *Figure II.13*).
- Search for edges (in blue) on radial lines (in yellow) defined in the search zone. An edge point is determined by the change in contrast along the radius. The threshold contrast, signifying the transition from the particle region to the background, can be manually regulated to optimize the detection.
- The list of blue points defines the edge of the particle, whose corresponding pixels are represented in red.

The accuracy of detection can be regulated by reducing the angle between the searching radii, consequently the distance between the detection points. The code can detect also the thermocouple and subtract it from the calculation by predefining its radius and slope. Indeed, the area of the glue between the particle and the thermocouple is included in the red area, and has to be removed. The distinction between the particle and the glue is obvious during the char combustion (white points *Figure II.14*.b).

In order to subtract the glue area and eliminate the sensitivity to the thresholding grey values, the curves were then rectified by validating several points on each curve (*Figure II.14.a*). This was done using manual integration of some specified frames in each untreated video. The frames checked in the external area curves and the heterogeneous reaction curves correspond to the flame ignition area, heterogeneous ignition area, flame extinguish area and internal combustion area. On the external area curves, two additional points were checked corresponding to the area at t=0 and final area. While on the reaction zone curves, two points were measured between the internal combustion moment and the complete burnout. The error on the external area zone was higher due to the glue area.

II.4.5 Data correlation

The two videos and the thermocouple data are temporally zeroed at the insertion moment. Superposition of the data helps to identify the events associated to each phenomenon. A typical result is shown in *Figure II.15* gathering:

- ✓ Particle area extracted from the binary videos in addition to the char combustion events,
- ✓ Temperature as measured by the thermocouple, and
- ✓ Flame events from colored videos,

Moreover, superposing both imaging techniques provides the moment of the onset of heterogeneous combustion even during the flame phase. In fact, the combustion sub-processes occur simultaneously at high heating rates, but the overlap of homogenous and heterogeneous combustion is difficult to evaluate experimentally from conversion curves like TGA and drop tube furnace (DTF) curves. Then, it is usually neglected in analyzing similar horizontal tubular reactor (HTR) results by accounting only for the major contribution of both phases. However, using shadowgraphy we can monitor the particle throughout the whole combustion experiment. During devolatilization, volatile materials are released from the particle and burn in a diffusion flame at a distance from the fuel particle [139]. The volatile release is usually non-uniform and this enables overlapping of char combustion during devolatilization. The brightness of the heterogeneous combustion zone becomes much more visible after the flame is completely extinguished.

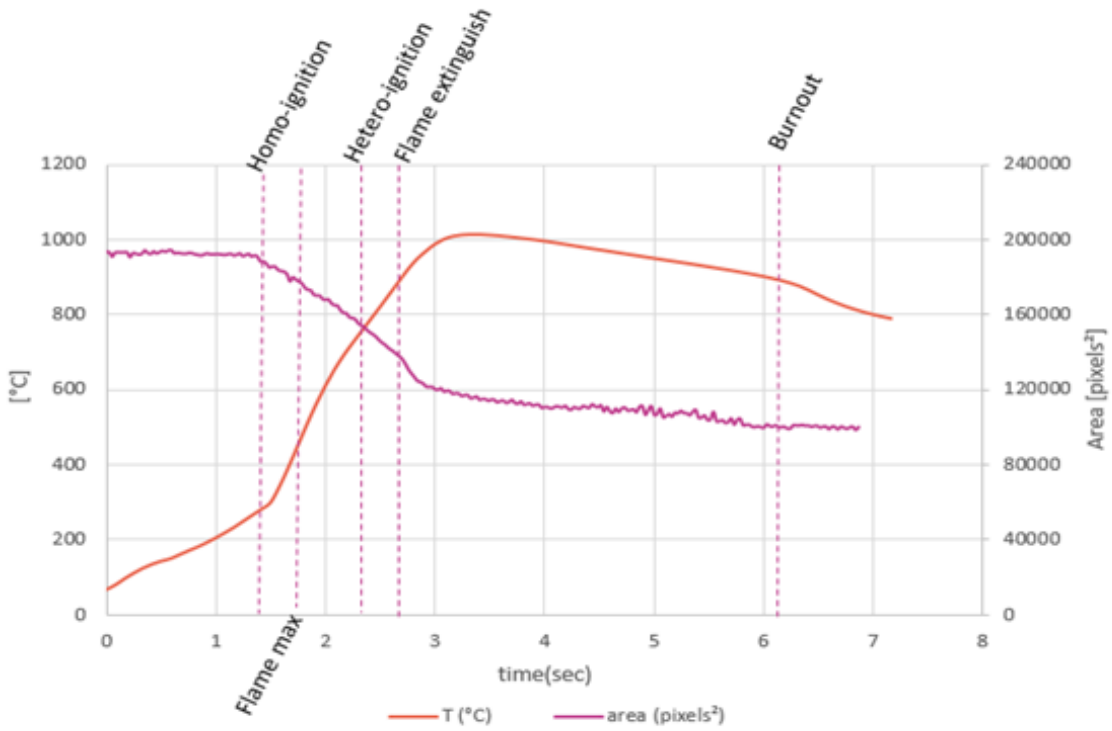

Figure II.15: Typical Superposition of the projection area evolution, particle temperature and the main combustion events measured by the PCS at 800°C

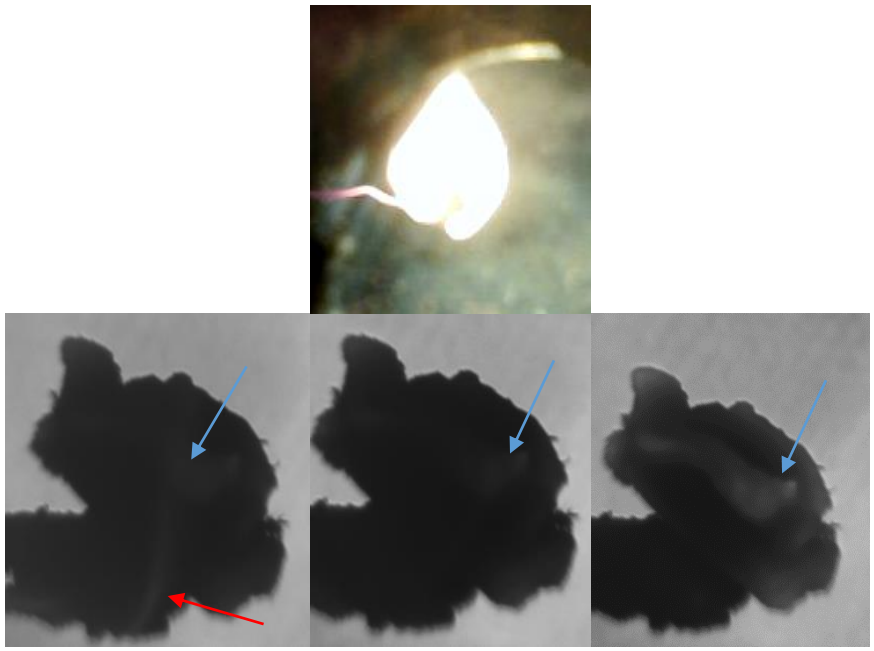

Frame-(time): 5-(135 ms) 6-(162 ms) 11-(297 ms)

Figure II.16: Identifying the moment of heterogeneous ignition on the shadowgraphy frames of a Pine particle combustion. The direct emission image above is the moment of heterogeneous ignition corresponding to shadowgraphy frame 6. The blue arrows point to the zone of heterogeneous ignition while the red arrow points to a region reflecting the flame fluctuations. The numbers below are the corresponding frame number and time (insertion frame: 1-(0 ms)).

Nevertheless, it can be also traced back to its onset during the flame period, and since the moment that oxygen attacks, the char surface is associated with a slightly increased brightness. *Figure II.16* and *Figure II.17* explain the technique. The clear brightness in frame 11 can be traced back to a slight brightness observed at the blue arrow position in frame 6, while the flame still appears to radiate on the RGB frames at the same time. By following the grey value (which indicates the brightness of a pixel) at the position of the blue arrow, the heterogeneous ignition moment (yellow marker *Figure II.17*) is characterized by an increase in grey value.

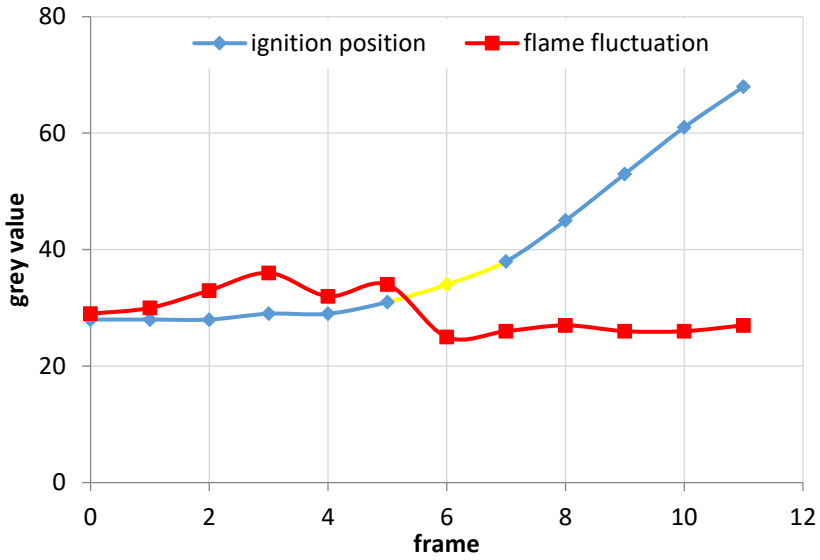

Figure II.17: variation of grey value due to char combustion and flame fluctuation at the arrow positions in Figure II.16

The grey value must continue to increase afterwards to ensure that the brightness is not produced by the flame, which is the case in frame 5 (red arrow). This occurs sometimes but not for so long as the flame fluctuates and disappears afterwards causing the decrease in the grey value as traced by the red curve in *Figure II.17*.

Once identified, the time difference until the flame extinguishes is defined as the homo-hetero overlap. Its duration varies as a function of the particle size and composition. It is also dependent on the operating conditions as the oxygen diffusion to the surface is a function of the particle and gas temperatures, but this aspect is not examined herein.

II.5 Drop tube furnace

II.5.1 General description

The drop tube furnace located at Ecole des Mines d'Albi-Carmaux is a heated reactor designed to reproduce the thermal conditions encountered in an industrial furnace with high heating rate. Particles are assumed isolated in a heated flow of gas. The scheme of the experimental installation is illustrated in *Figure II.18*. The 2m long reactor is an ø80mm alumina tube inside a three zones electric furnace covered with insulation fibers, which helps to maintain an isothermal flow. The reactor works at atmospheric pressure and can reach temperatures up to 1600°C. More information can be found in several PhD thesis [9], [140]–[145].

The mixture of the carrying gas is produced using thermal mass flow meters. This mixture is, at first, preheated to the set temperature of the furnace before entering the tube creating an

isothermal laminar flow (Re <2000) medium. The thermal cycle of a particle begins at the moment it leaves the injection probe and immerses in the hot gas flow.

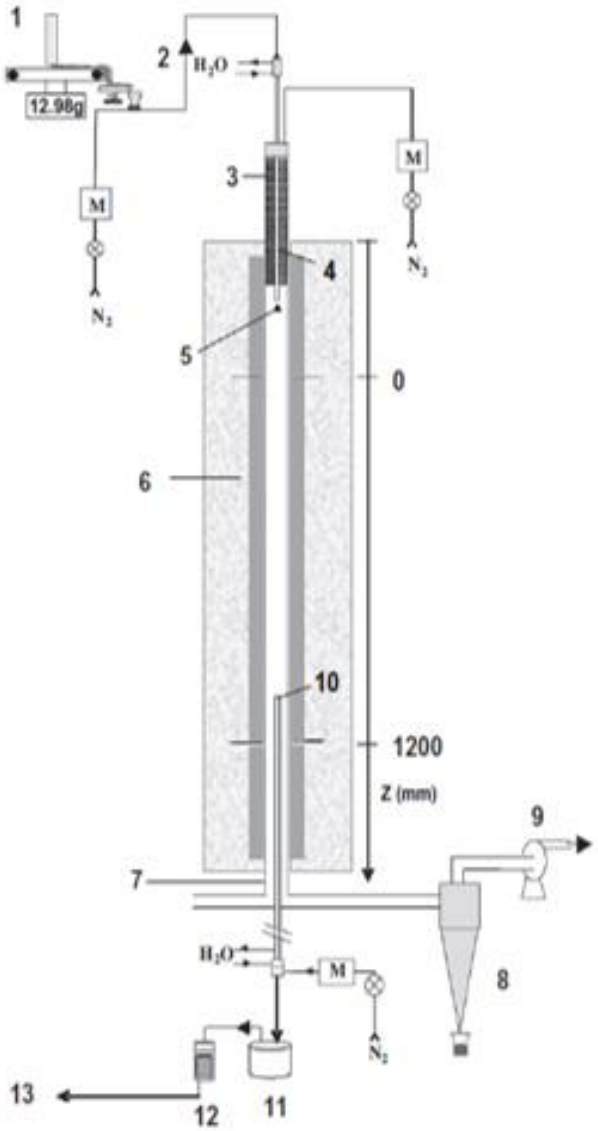

1. Controlled weighting system
2. Pneumatic transport
3. Electrical preheater
4. Water cooled feeding probe
5. Dispersion dome
6. Three zones electrical furnace
7. 75mm i.d. alumina tube reactor
8. Cyclone collector
9. Exhaust fan
10. Oil cooled sampling probe
11. Char pot
12. Filter
13. Gas analyzer

M: Mass flow controller

Figure II.18: Scheme of the drop tube furnace

II.5.2 Fuel feeding

The feeding device allows controlling the fuel flow on a conveyor belt with a length of 1m, which moves at a constant speed of 9 cm/min. The fuel is at first prepared on a V-shaped rail by spreading the pre-weighed desired fuel quantity over 90cm by means of a calibrated wedge. The biomass is then deposited on the conveyor, which delivers the particles to a vibratory conveyor at its extremity. The role of the latter is to de-agglomerate the fuel packets formed by the cohesive effect of the solid fuel. The particles are then entrained by the transport gas by Venturi effect. The transport gas flow is reduced as much as possible to prevent introducing

cold air into the reactor while allowing fuel entrainment. High transport gas flow would actually decrease the heating rate of the particles.

The fuel is transported in a water-cooled feed probe. At the end thereof, a 12mm diameter stainless steel dispersion dome (5 on *Figure II.18*) is held integral with the injector by three rods of 0.5mm diameter at a distance from the orifice of 1.2mm. It disperses the fuel in an ideally homogeneous manner over the reactor cross-section (Figure *II.19*). The particles as seen from the bottom of the reactor are isolated from the moment of their insertion. Besides, the flow is highly diluted so that the particle-to-particle interactions are negligible.

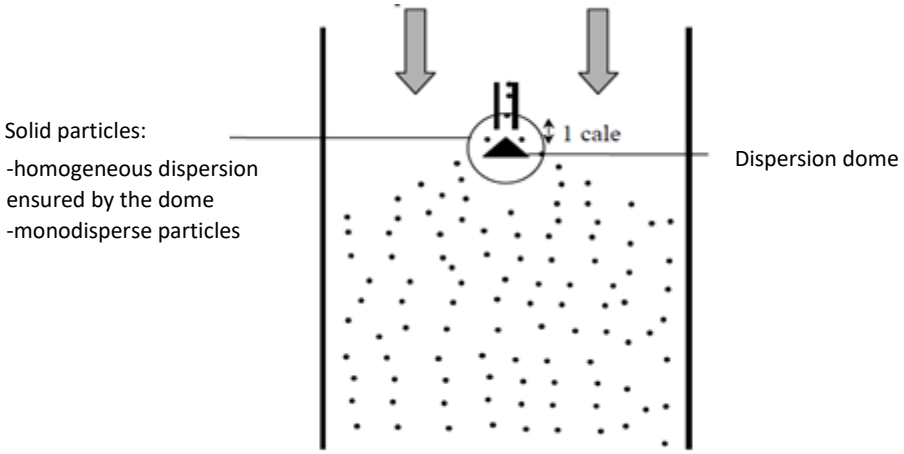

Figure II.19: dispersion of the particles inside the drop tube furnace

II.5.3 Sampling Probe

A sampling probe inserted through the outlet section permits sampling the gaseous effluents and solid particles along the centerline axis at any height starting at 60 cm from the injection point. Indeed, previous temperature measurements indicated that the isothermal zone starts at 30 cm from the injector [104]. The distance travelled by the particle from the injection point to the probe determines its residence time in the combustion or pyrolysis atmosphere. The probe has a 12 mm internal diameter and 38 mm external diameter. In between oil circulates at 150°C to cool the probe in order to quench the ongoing chemical reactions by a sudden decrease in the medium temperature and prevent the tars from condensing at the same time. In addition, the probe is insulated by ceramic fibers to limit heat exchange with the furnace wall.

Two-third of the total flow is sucked by the probe to ensure collecting a representative sample. It is important to note that the presence of the probe inside the flow is intrusive downstream the sampling point, while upstream, the flow is not considerably affected. Subsequently, the solid particles are collected in a bin at the bottom of the sampling probe. Later, fine particles are trapped on a filter. Water is then separated in a condenser before conveying the dry gases via a set of heated lines either directly to the testo gas analyzer (combustion products) or to sampling bags that are analyzed later by a micro gas chromatograph (µ-GC).

Chapter III. Design, fabrication and completion of the pulverized fuel combustion test facility

This Chapter describes the experimental methods at flame scale. The methodology of design of the pilot scale reactor and the criteria of the design of the bluff-body burner are explained. We first review the characteristics of some pilot scale reactors used previously for the combustion of pulverized biomass flames. This chapter also explains the choice of materials of the pilot scale reactor and its fabrication process. In addition, the measurement techniques implemented in the pilot scale facility are all listed and described.

III.1 Literature Review

Throughout the past century, it has been a common practice to characterize solid fuels in terms of their chemical and mechanical properties; i.e. proximate and ultimate analysis, ash fusibility, Abrasiveness Index and Hardgrove Grindability Index, that are often determined using experimental scale instruments like drop tube furnaces, flat flame burners, single particle reactors and thermogravimetric analysis. Each method has its limitations, which don't allow to directly project its results on an industrial environment. The fuel combustion behavior in a particular boiler would be obtained from a full scale test burn in the plant itself, but this is impractical, costly, and risky to the plant. For these reasons, pilot scale facilities are usually designed as a scale down version of the full-scale plant, while simulating the operating conditions of particle residence time, inlet conditions, excess air, temperature and other parameters that are encountered in full-scale plants. This offers a practical means of characterizing differently prepared fuels under various controlled operating conditions to determine their impact on combustion and emissions.

Various designs have been proposed in the literature to maintain a similitude with the full scale plants. However, a criteria proposed by Juniper et al. [146] to achieve a correct simulation of fuel burnout and slagging, suggested designing the wall temperature for above 1000°C due to the high heat loss in these small furnaces. This would set the ambient gas temperature in the chamber close enough to the flame temperature to obtain similar fuel burnout.

III.2 Design specifications

The scientific purposes mentioned above determine the design specification of the installation. The schematic diagram of the instalation is presented in *Figure III.1*.

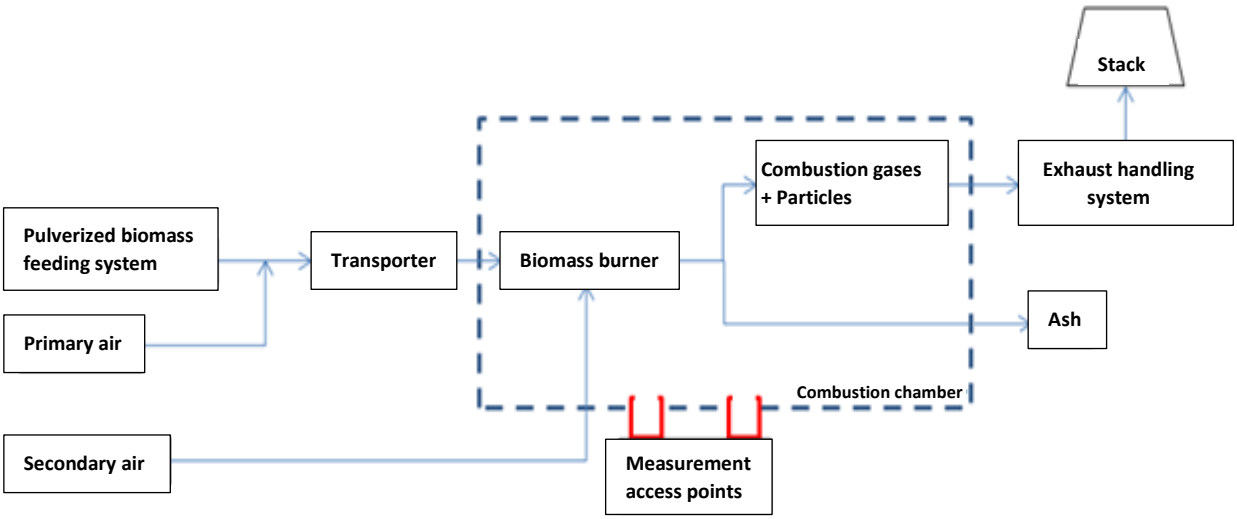

Figure III.1: schematic diagram of the combustion facility

It is meant for studying the combustion of pulverized biomass using in situ optical diagnostics and probe measurements. Therefore, the facility shall include:

1. Furnace and burner
2. Fuel preparation and feeding system
3. Air handling system (preheaters, flowmeters…)

4. Exhaust handling system (extraction, cooling system…)
5. Measuring equipment and access points in the combustion chamber
6. Laboratory safety systems
7. Data acquisition system with safety features for emergency situations
8. Platforms and supports

III.3 Orientation

Horizontal furnaces are normally preferred for easier accessibility. However, the orientation of the furnace depends on Froude number (Fr) which represents the ratio of the initial jet momentum flow to the buoyant force experienced by the flame. The global flame Froude number can be expressed as [147]

$$Fr = \frac{u_e f_s^{3/2}}{\left(\frac{\rho_e}{\rho_\infty}\right)^{1/4} \left[\frac{T_f - T_\infty}{T_\infty} g d_j\right]^{1/2}}$$

In which u_e is the jet exit velocity, f_s the stoichiometric mixture fraction, $\rho_e$is the density of nozzle fluid, and ρ_∞ is the ambient fluid density. T_f represents the flame temperature, which is approximately equal to the adiabatic flame temperature, while T_∞ is the ambient fluid temperature. Moreover, g is the acceleration of gravity, d_j is the nozzle exit diameter

i. Fr >> 1 Momentum-controlled: the flow is pulled by gravity downstream
ii. Fr ≈ 1 Transition (mixed)
iii. Fr << 1 Buoyancy-controlled: the flow can move upstream

In our operating conditions, the flow is always found to be buoyancy controlled (Fr ≈ 0.7 < 1). In this case, a vertical furnace is preferred to avoid the formation of asymmetric bended flames that would appear in horizontal mode due the buoyancy effect. Horizontal reactors also suffer from the ash deposition problem which demands frequent cleaning of the furnace.

III.4 Dimensions

The design should also provide an access for each combustion sub-process to be recorded and investigated. According to Elfaskhany et al.[111], the biomass flame can be divided into four zones:

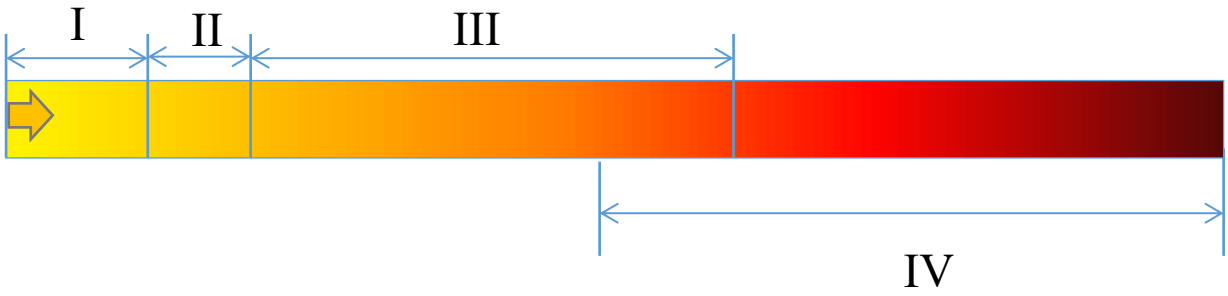

Figure III.2: Flame structure

I. Particle pre-heating zone
II. Drying zone
III. Pyrolysis zone
IV. Char combustion zone

A numerical study by Li et al. [45] to characterize the biomass combustion at high temperatures concluded that a 1 mm palm kernel shell particle at 700°C requires a residence time for each combustion step as follows in *Table III.1*.

Combustion step	**Heating to 700°C**	**Drying**	**Pyrolysis**	**Char oxidation**
Required time (s)	0.773	0.817	4.405	5.07

Table III.1: The required residence time for each combustion step of palm kernel shell particle at 700°C [45]

Simultaneous occurrence of devolatilization and char conversion may be established depending on fuel type and various operating conditions as reported by [148], [149]. This overlapping duration is subject to natural variability, but typically it can be taken about 20 % of the total duration of the two zones [111]. Therefore, the total residence time to study each process is 9-10 seconds which is consistent with different results in literature shown in *Table III.2*.

Study	**Granulometry (µm)**	**Specific conditions**	**Residence time (s)**
Jun Li [45]	1000	900°C	10
Elfasakhany [111]	25-1400		5-10
L. Ma [150]	90-1500	Industrial plant	5-10
Ballester [31]	555		4,94
Weber [129]	500	No swirl	10

Table III.2: Typical particle residence time in industrial furnaces and pilot scale reactors

Study	**Fuel**	**Flue gas velocity (m/s)**
Weber et al. [29], [129]	RDF, wood, Grain residue, etc.	0.34
J. Li et al. [45]	Palm kernel shell	1.33
Elfasakhany et al. [111]	Fine ground (Valbo & Harnosand)	0.79
Gonzalez-Cencerrado et al. [28]	Coal, poplar, Cynara	1.02
Ballester et al. [31]	Oak sawdust	0.55
Ogden et al. [151]	Coal	0.24
Muanza et al. [152]	Coal-biomass co-firing	1.5

Table III.3: Typical values of the flue gas velocity

Flue gas velocity inside the furnace should be a compromise between risking fouling at low values and the necessity to elongate the furnace length at high values to achieve the required residence time. Furnaces with low furnace gas velocity are more vulnerable to blockage of gas ducts due to excessive accumulation of fly ash [153]. *Table **III.3*** shows orders of magnitude of the flue gas velocity found in typical reactors. A flue gas velocity of 0.4 m/s is in the range of similar pilot scale reactors. Assuming a gas homogenous gas temperature in the furnace (at 1000°C), we estimate about 3.7 m furnace for the required residence time (9-10 sec) and the following spaces for each zone:

- Preheating and drying zone: 0.6 m,
- Pyrolysis: 1.76 m,
- Char oxidation: 2 m.

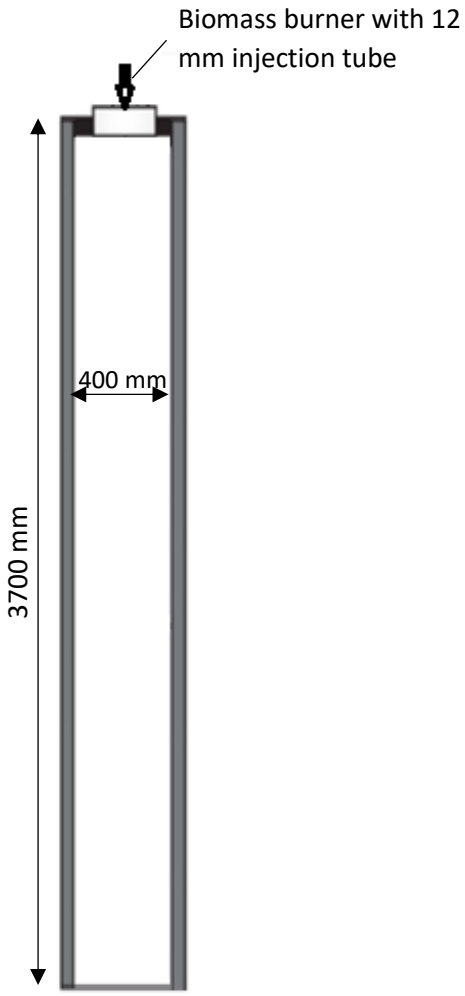

Figure III.3: Schematic representation of the reactor

A reactor this tall minimizes the exhaust effects on the flow characteristics within the hot reactive section. Moreover, the furnace diameter must be large enough to avoid impingement of the wall and the interaction of the flame with the wall. For this reason, *Ogden et al.* [154] suggested a furnace to inner jet diameter ratio of 30 while J. Zhang et al. [155] used 39. The injection tube carrying the particle laden flow is constrained by the risk of being blocked by the biomass particles. Given the maximum particle size as 1.5 mm, the injection diameter should be 6 - 10 times the maximum particle size to prevent obstruction by particles. According to P.A.

Shamlou [156], in solid-liquid suspension processes, pipes that are out of this range suffer sooner or later from blockage. An analogy can be used here for processing solid-gas suspension to give the minimum injection diameter as 9 mm. This criterion was further verified in the case of bridging and agglomeration of the particles, by calculating the area covered by the maximum allowed number of coalesced particles in our flow conditions, which is always less than the calculated minimum injection area. The pneumatic transport line is a 14 mm tube, so an injection tube of 12 mm is used in order to avoid an abrupt reduction of tube size, which would lead to injection problems during the calibration phase. Taking a furnace-to-inner jet diameter ratio of 30 (reference value in [154]), the minimum chamber diameter is about 40 cm for an injection tube of 12 mm. This furnace diameter is typical for laboratory reactors dedicated for the research in the near-flame region. Such facility can mimic the environment surrounding an individual burner without strong effect of confinement.

Operating conditions can be concluded from the specified parameters:

- ✓ Flue gas flow rate of 24.4 Nm^3/h can be estimated from its velocity and the furnace section area.
- ✓ A fuel flow rate of 4.14 kg/h produces this amount of flue gas
- ✓ Combustion power ~ 21 kW

III.5 Biomass Burner Design

The aerodynamics and the mixing of pulverized fuel with air are determined by the burner geometry. The exit dimensions of the burner are related to its power supply all while ensuring a stable flame in the reactor. The upstream geometry of the burner influences the aerodynamics as well. A simple axisymmetric configuration is preferred to simplify the mechanisms involved in the flame. This would allow isolating the physical parameters put under study and facilitate the experimental characterization. Most pulverized burners are coaxial with fuel injected in the central jet with transport primary air. The surrounding annular jets are designed for air staging, adding secondary and even tertiary air stages. A shear layer is created at the interaction location of the coaxial jets. This depends on several parameters such as the dimensions of the jets, their orientations, the flow velocities, the properties of the fluids, as well as their dependence on other parameters such as temperature. For the sake of simplification, a two coaxial jet burner is adopted here.

Swirl burners are mostly used in full-scale and even in pilot-scale facilities. However, despite the fact that a swirl would enhance the flame stability in the combustion chamber, the strong influence of the specific 3D aerodynamics of swirling flows on flame features would make it difficult to link the flame characterization in the pilot furnace to the study of the combustion at particle scale. Another type of burners that is widely used is the bluff-body burner (*Figure III.4*). A bluff-body burner consists mainly of co-flow streams centered on a circular body where the central fuel stream makes way through an orifice at its center. An internal recirculation zone (IRZ) forms on the wake behind bluff-body, due to the pressure gradient experienced by the jet in that region.

It is a good candidate as it generates a long stable flame suitable for the study of turbulence-chemistry interactions and it also bears a great similarity to practical combustors used in many industrial applications [157]. It is therefore a suitable compromise as a model configuration

because it has some of the complications associated with practical combustors while preserving relatively simple and well-defined boundary conditions.

The boundaries and structure of the recirculation zone can be controlled by varying the primary to secondary air velocities ratio (*Figure III.5*). At low velocity ratios, the high velocity annular flow dominates producing toric centripetal recirculation zone. In this configuration, the central flow recirculates back towards the bluff body surface. Increasing the velocity ratio produces a situation where neither the primary nor the annular jet dominates. Further increase in the velocity ratio causes the primary jet to penetrate the IRZ. In this configuration, small recirculation eddies exist between the central and annular jets. These configurations describe the dynamics of the gases and not the particles. It is up to the particle dimensions to determine whether they follow the flow or detach from it by their inertia. In solid fuel burners, especially biomass burners, it is more likely for the particles to acquire high inertia and penetrate the recirculation zones due to their inertia.

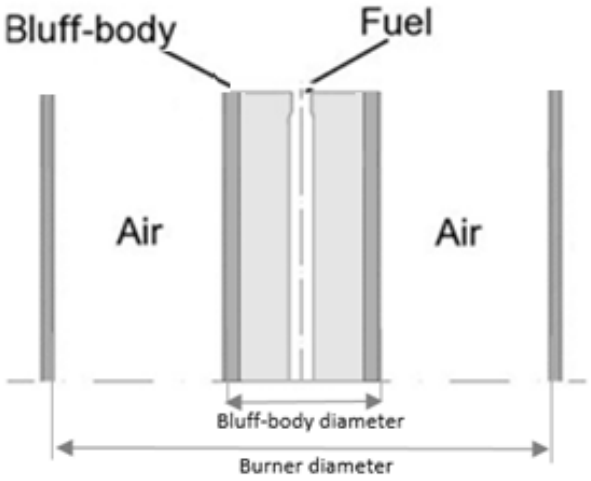

Figure III.4: bluff-body burner concept

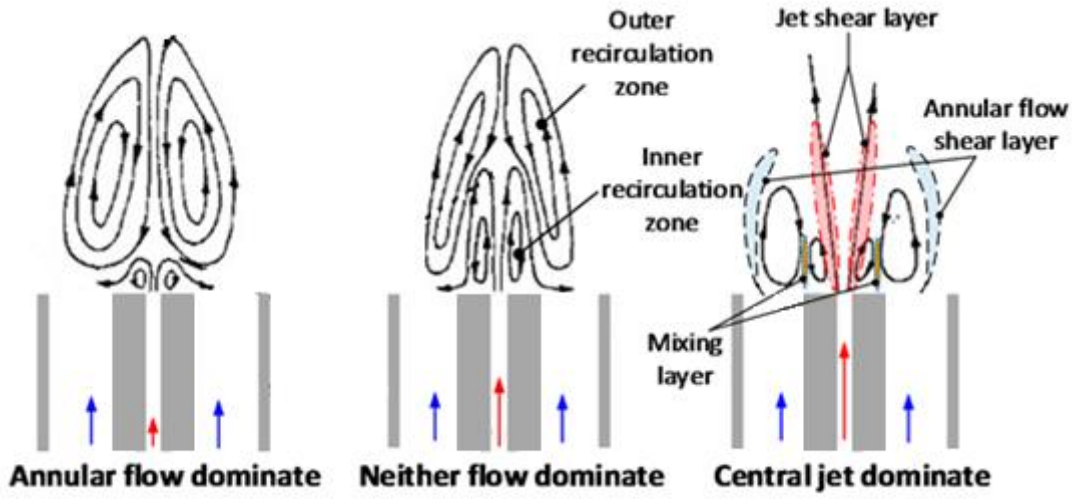

Figure III.5: Bluff-body burner aerodynamic configurations

The IRZ can also be controlled by the burner geometry using the blockage ratio defined as the square of the ratio of the bluff-body diameter to the burner diameter. In isothermal flow, Schefer et al.[75] and Taylor and Whitelaw [158] confirmed that the growth of the blocking ratio leads to an elongation of the recirculation zone with respect to the unconfined case. Quantitatively, for blocking ratios greater than 0.85, the confinement effect significantly lengthens the recirculation zone, which is approximately 2.7 times longer than in the unconfined case, while the length of this zone remains practically invariable when this ratio is less than 0.3 [75]. This value is suitable for a stable flame supported by small recirculation zone. In gas burners, a criterion is used to keep a burner whose aerodynamics is little disturbed by the edge effects associated with its confinement: the ratio of combustion chamber diameter / burner diameter must be at least 8. This criterion can be adopted to obtain a maximum burner diameter of 50 mm. A bluff-body diameter of 22 mm gives a blockage ratio equals 0.3 for an outer diameter of the annular section set to 40 mm (<50 mm).

Primary air to fuel ratio (PAFR) is constrained to the flammability of the biomass and its volatile content. A low PAFR would lead to a catastrophic backfiring to the mixing and even to storage zones. Very high PAFR on the other hand, necessitates higher primary air velocity that may cause flame blow-off. Typically, this ratio is in the range of 2 - 3 for biomass and 1 - 2 for coal. The latter is increased when co-firing biomass with coal [28]. This may seem odd since biomass is generally more flammable than coal. However, injecting more air with biomass is supposed to increase the injection velocity.

Study	**Fuel**	**Primary air to fuel ratio (PAFR)**
Weber et al. [29]	Biomass	3
J. Li et al. [45]		2.16 - 2.7
Jerrod et al. [159]		2.5 - 3
Burge et al. [160]	Coal	1.5
Molcan et al. [161]		1.7
Richards et al. [162]		2
Ballester et al. [31]	Coal	1.75
	Biomass sawdust	1.4 ($T_{primary\_air}$ = 53°C)

Table III.4: Typical values of the primary air to fuel ratio

With the primary air to fuel ratio (PAFR) set to 1 – 3, the primary air injection velocity is then 9-23 m/s given that the biomass load is 4,14 kg/h as calculated above. Flame stability is so sensitive to the injection velocity, as it should be managed to be notably higher than the flame propagation velocity in order to prevent the flame from flashing back [163]. The laminar flame velocity of biomass is not well investigated in literature. Most studies about the subject are more concerned with the explosion hazards of dust clouds, performing experiments in ISO 1 m^3 explosion vessels and Hartman tube [164]. The pressure rise in these tests doesn't simulate the process in the combustion chamber. However, these results can serve to set the safety precautions for fuel storage and handling.

*Table **III.5*** lists typical values of the primary and secondary air velocities used in similar burners. The range of the calculated primary air velocity (9-23 m/s) is typical. The secondary air velocity is consequently in the range of 8-12 m/s, which is also acceptable. It can be

increased also by preheating the secondary air stream before injection. This adds more stability to the flame.

Study	Burner	Fuel	Primary air and solid fuel velocity (m/s)	Secondary air velocity (m/s)	
Weber et al. [29], [129]	Co-axial no swirl	Biomass	35 - 47	4.5 – 8.3	
		coal	32.7	3.4 - 6	
J. Li et al. [45]	Co-axial no swirl	Biomass	9 – 20 - 30	-	
Burge et al. [160]	Coaxial swirl low NOx	Coal	21 (Optimal 18 - 24)	32.04 (1.5*$V_{primary}$)	
Ballester et al. [31]	Coaxial swirl	Oak sawdust	32.9	153.9	
		coal	40	163	
Muanza et al. [152]	Low NOx burner	Co-firing	25	60	
Mihaescu et al. [165]	Coaxial swirl	sawdust	25 - 35	30 - 35	20 - 30

Table III.5: Typical values of the primary and secondary air velocities

After setting the outlet dimensions of the burner (*Figure III.6*), care must be taken to obtain uniform velocities at the burner outlet. This is achieved by volumes of tranquilization, slight pressure losses and flow contraction ratios. Moreover, in the chosen burner configuration, the main aerodynamic constraint is the wake effects at the bluff-body.

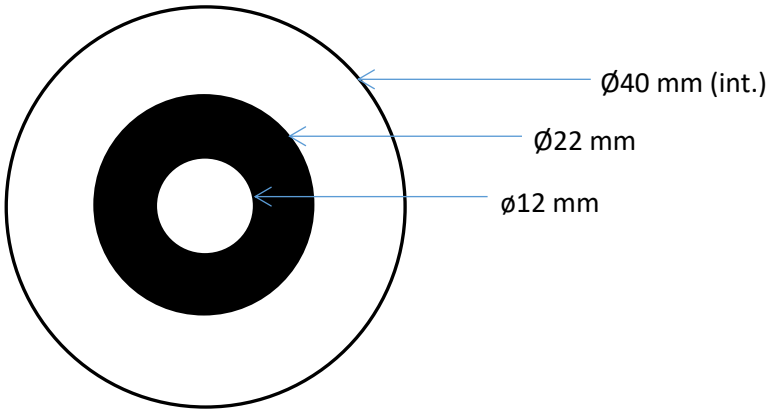

Figure III.6: bluff-body dimensions

To limit boundary layer detachment and thus avoid the appearance of vortex structures in the chamber, the length of the tubes should be well chosen, in particular the central tube to ensure homogeneity of the central flow and the establishment of the velocity profile before entering the combustion chamber. When a fluid enters a tube, it requires a development length L_e to form a stable velocity profile and to establish a convergence regime of the boundary layer developing inside a circular tube (*Figure III.7*). The boundary layer appears downstream the entrance where the velocity profile changes with the axial and radial position. After it is fully

developed, the velocity depends only on the distance from the pipe axis and no change is observed afterwards.

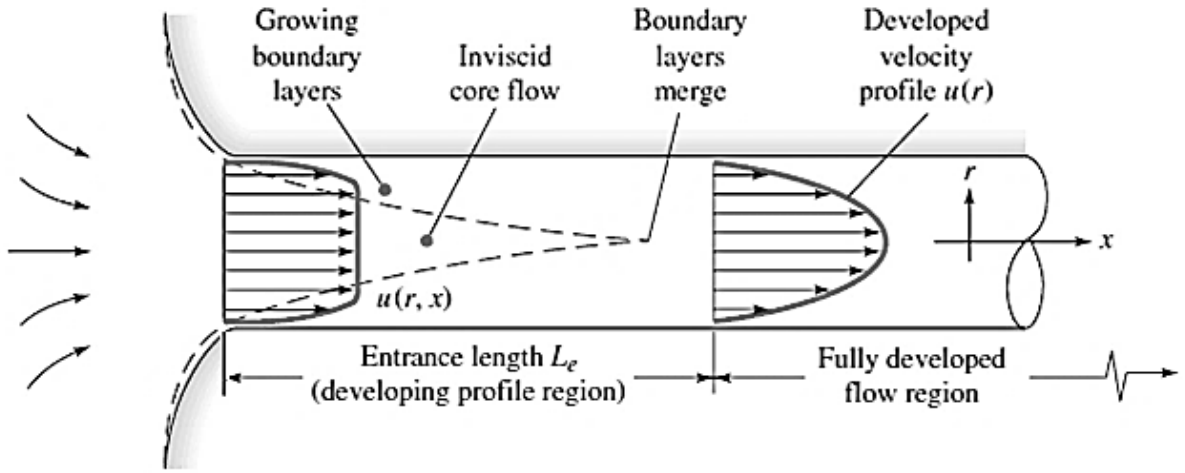

Figure III.7: Development of the velocity profile of a fluid in a circular tube [166]

The necessary length L_e depends on the nature and regime of the flow and it can be calculated as a function of the Reynolds number:

$$Le/D = \begin{cases} 0.06 \times Re, & laminar\ flow \\ 4.4 \times Re^{1/6}, & turbulent\ flow \end{cases}$$

The length Le of the injection tube with diameter D is determined with respect to the most unfavorable operating conditions at the maximum thermal power. Consequently, a tube of 240 mm is sufficient to obtain a controlled velocity profile at the outlet of the injector.

On the other hand, due to the high air flow rate in the annular section, the secondary injection was designed as a nozzle to reduce the mean-flow non-uniformities at the entrance of the chamber. The contraction of the secondary flow is dimensioned to avoid boundary layer detachments, following the contours of the convergent profiles in order to produce a controlled velocity profile at the burner outlet. One method for defining the profile of the burner remains the one established by Morel [167], which proposes an expression of the radius of a convergent defined by the combination of two cubic profiles defined as:

$$R(x) = \begin{cases} A + B\left(1 - \frac{1}{{X_m}^2}\left(\frac{x}{L}\right)^3\right), & x < x_m \\ A + B\left(\frac{1}{(1 - X_m)^2}\left(1 - \frac{x}{L}\right)^3\right), & x \geq x_m \end{cases}$$

Where $A = \frac{D_2}{2}$ and $B = \frac{D_1 - D_2}{2}$

D_1 and D_2 are the inlet and outlet diameter respectively. L is the nozzle length and x_m is the intersection point of both profiles. *Figure III.8* illustrates the profile parameters expressed by the equation of R(x).

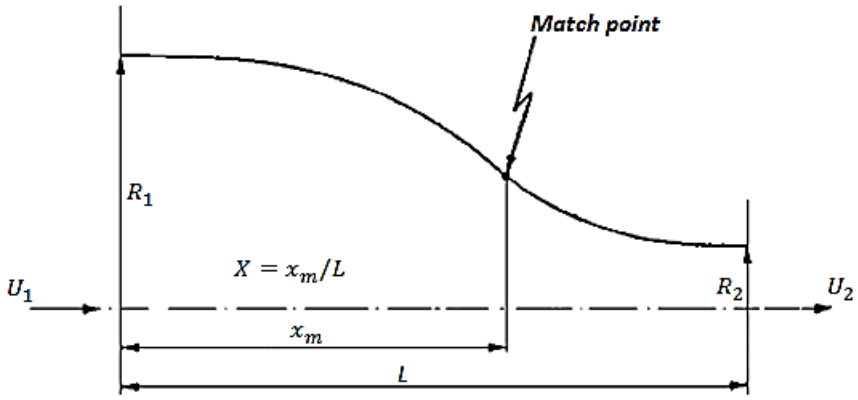

Figure III.8: wall contour constructed of two matched cubic arcs

Following the criterion of Morel, the design problem is reduced to the a priori determination of the contraction ratio ($CR=D_1/D_2$) and the values of the two wall-pressure coefficients C_{pe} and C_{pi}, at the points of maximum and minimum wall velocity respectively. Once chosen, the design parameters, namely nozzle length, wall shape and Reynolds number are determined for a proper space/cost compromise, beside the exit boundary layer thickness and the exit flow uniformity. The imposed contraction ratio gradually reduces the surface of the jet and induces an acceleration of the flow in the longitudinal direction towards the point of intersection x_m of the two cubic profiles. This has the consequence of reducing the viscous effects without increasing the boundary layer up to $x \leq x_m$. Downstream, in the section ($x > x_m$) of the convergent profile, the flow progressively reaches its maximum speed at the outlet of the orifice. There are two criteria which have to be satisfied at the narrow end of a nozzle: the avoidance of separation and the maximum acceptable flow non-uniformity. In most practical cases, the non-uniformity, will be required to be no more than 2%. For cubic nozzles, this translates into C_{pe}, < 0.06 (i.e., quite small), which means that there is no danger of separation for a turbulent boundary layer [167]. On the other hand, the only criterion for choosing C_{pi} is the avoidance of separation near the inlet. The value given in [167] as a good upper bound is 0.39, below which a turbulent boundary layer will not separate.

The design parameters were set to:

$$CR = 25 \; ; \; C_{pi} = 0.2 \; ; \; C_{pe} = 0.04;$$

The calculations and the charts in [167] lead to:

$$D_1 = 200 \text{ mm} \; ; \; D_2 = 40 \text{ mm} \; ; \; x_m = 130 \text{ mm} \; ; \; L = 190 \text{ mm} \; ;$$

This constructs the following wall contour:

$$R(x) = \begin{cases} 100 - 2.4857 \times 10^{-5}.x^3, & x < 130 \\ 20 + 806.248 \times \left(1 - \dfrac{x}{190}\right)^3, & x \geq 130 \end{cases}$$

The nozzle length L is calculated at 190 mm. However, the flow is neither parallel nor uniform for some distance within the straight section ahead of and after the contraction. Therefore, Morel suggests adding straight sections upstream and downstream the contraction to reduce the turbulence ahead, without causing non-uniform pressure drop and flow distortion, and to ensure

that the effect of the nozzle curvature decays to negligible levels after the nozzle. Hence, 30 and 20 mm are added before and after the contraction so that the total nozzle length equals that of the central injection tube (240 mm). In addition, the secondary air is distributed through eight orifices and then through a honey comb for better flow uniformity.

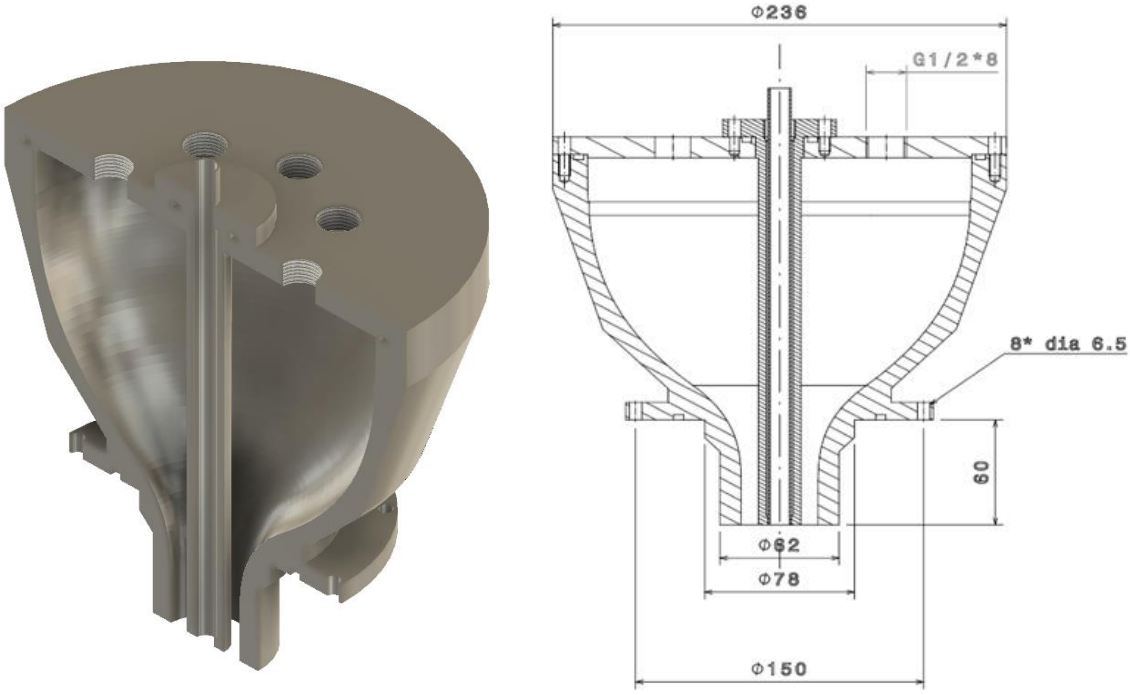

Figure III.9: Cross-section of the final burner

The design and manufacture of the laboratory burner are also subject to several constraints to avoid the impact of hot gas flows that can cause thermal degradation of the material (*Figure III.9*). The burner is made of alloy 310, a nickel / chromium alloy with good resistance to oxidation to allow better performance in high temperature conditions.

III.6 Materials and Construction of the reactor

The furnace consists of five segments along length in order to facilitate the fabrication, assembly and maintenance. The materials of construction are of major concern for the good functionality of the reactor. The wall materials should offer:

- High heat stability,
- Insulating capabilities,
- Structural durability,
- Machinability,
- Low thermal expansion.

Refractory castables are usually used for combustion applications. The use of castables has developed significantly with the variety of very demanding and severe applications as they offer good performance at a reasonable cost. They are a premixed combination of:

1. Refractory aggregates which constitute the basic skeleton of the castable with different particle size distribution and formulation. They determine the density and strength of the placed castable when in service.
2. Bonding agents (calcium aluminates, clay, silica, etc.)
3. Refractory fillers/modifiers are added to the castable composition in order to modify the mineralogy and enhance the bonding. They also play the role of filling out the particle sizing and improve expansion control.
4. Admixtures or additives that control the rheology characteristics of the castable. They are usually used in a very small amount (1%)

The proportions of the components of refractory castable make the desired mineralogy, physical and chemical properties of the end product: slag resistance, density, thermal insulating value, flow characteristics, etc. In combustion applications, the refractory castables are mainly based on Alumina or alumino-silicate which enhances their thermal shock resistance and allows their use to temperatures up to 1850°C.
Instead of attributing all the requirements to a single material, a multi-layer wall is constructed with each layer committed to a certain property. The wall thickness is constrained to limiting the field of view of a camera situated at the external wall. The camera acquires a wider field of view with a thinner wall and consequently fewer access points are required to capture the length of the flame. This would improve the furnace structure rigidity and resistance to crack propagation and also reduce the measurement time. Therefore, the camera settings and the demand of proper insulation at the same time set the wall thickness to 20 cm.

The composition of the combustion chamber is presented in *Figure III.10*. Four layers are put together in the following arrangement (from inside to outside):

Layer 1- This layer is the most exposed to radiation and the reactive environment. Dense refractory concrete (PLASTIL SF9806, 50 mm thickness) is used with the Alumina as its basic constituent**.** This improves its temperature, thermal shock and abrasion resistance. However, this dense concrete possesses a relatively high thermal conductivity, so the insulating role is left for the surrounding layers.

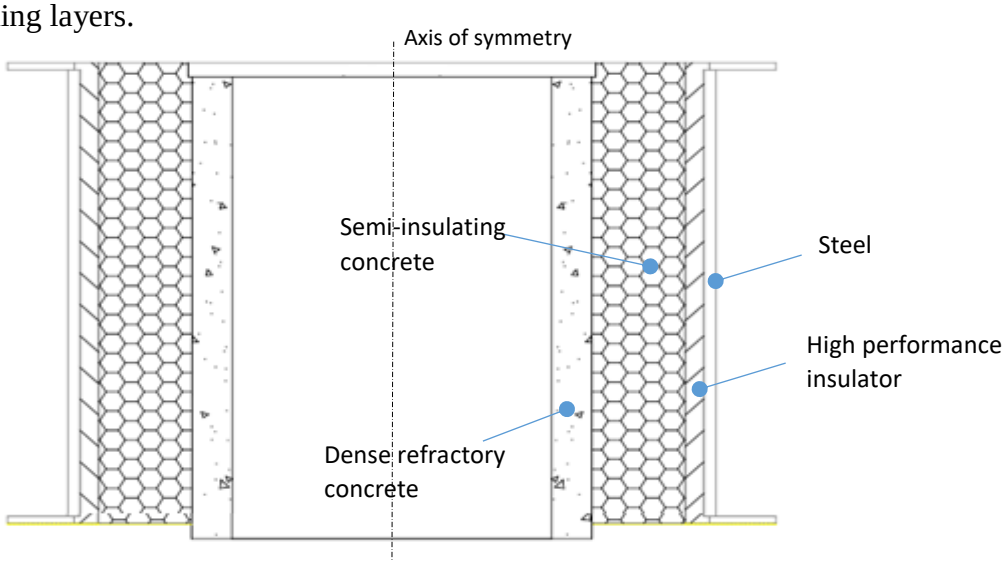

Figure III.10: Vertical cross-section of a segment with the construction materials of the wall layers

Layer 2- The second layer should offer some insulation and rigidity at the same time. Semi-insulating concrete (type: PLASTIL 34056, 117 mm thickness) is a suitable solution for this application. Beside the high thermal resistance of Alumina, the concrete is 50% Silica, which improves its insulation properties.

The properties of the castable used in these two layers are listed in **Annex A.**

Layer 3- After ensuring a good rigidity with the first two layers, the third layer is set for Insulation using WDS Ultra (SiO_2 approx. 80%; SiC approx. 15%; others approx. 5%). It is a microporous insulation material consisting mainly of inorganic silicates, which has an extremely low thermal conductivity coefficient imparting very good insulating properties. The main constituent is fumed silica; the other components are opacifiers to minimize infrared radiation absorption.

The furnace segments are of identical materials except for the bottom segment, which is made only of refractory concrete. With this composition, the material fulfills several functions:

- Insensitivity to high and low temperature thermal shocks (classification temperature 1000°C).
- Controls energy emissions, precisely
- Increase in effective volume
- Increase in heat retention (Thermal conductivity (W/m·K, ASTM C177): @200°C: 0.022; @400°C: 0.027; @600°C: 0.034; @800°C: 0.044)
- Reduces both weight and insulation volume (Nominal density kg/m^3 ≈ 200 – 250)

Layer 4- Stainless steel (Ferrule) is used as a casing for the inner layers and to hold together the reactor body.

Wall composition	Dense refractory concrete	Semi-insulating concrete	WDS Ultra	Stainless steel
Thickness (mm)	50	117	30	3
conductivity (W/m.K)	2.3	1.24	0.022	21.4

Table III.6: Reactor wall layers composition and thickness

The thickness of each layer is determined to achieve an acceptable temperature on the outermost layer (*Table III.**6***). The external temperature of the furnace is then calculated assuming interior gas temperature at 1000 °C and external air temperature at 27 °C (*Annex A*). *Figure III.**11*** shows the temperature profile inside the furnace wall layers. The concrete layers reduce the temperature to about 900°C while most of the insulation work is done by the WDS Ultra layer. The outermost temperature is 52°C which is acceptable for the user activity around the furnace.

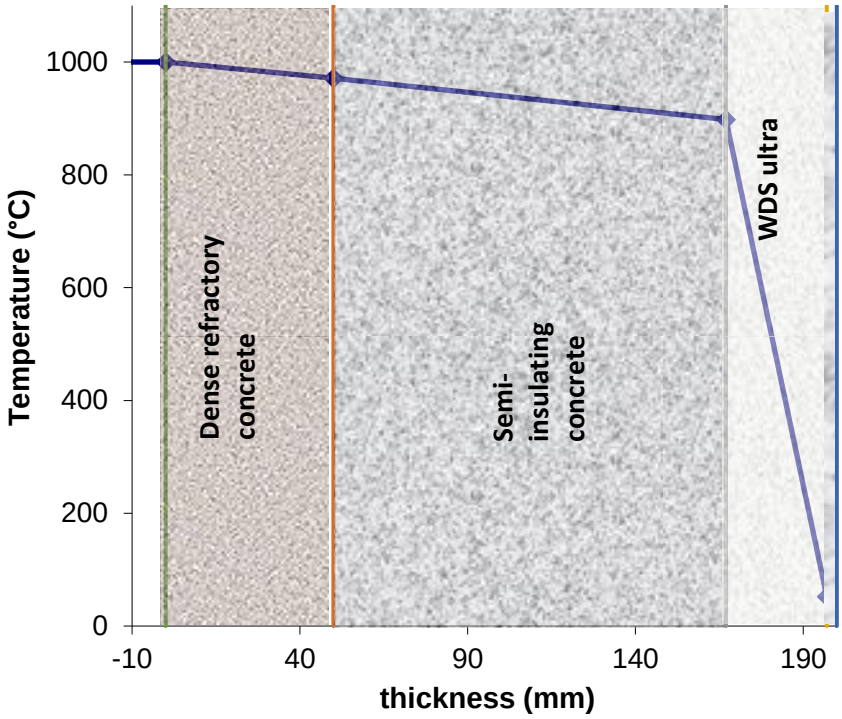

Figure III.11: Temperature profile inside the furnace wall layers

The burner is fixed on the top cover of the furnace. The cover is made of 42 mm thick dense refractory concrete and a 10 mm insulating layer (WDS Ultra) to thermally protect the burner. Both layers are held by a stainless-steel cover whose temperature is measured by a thermocouple to detect any overheating of the burner.

III.7 Sampling ports

Experimental investigation of a flame includes the use of intrusive and non-intrusive techniques that require a full-length access to the reaction zone. The design should therefore allow optical and probe access to the furnace to perform the following tasks.

- Optical diagnostics such as chemiluminescence imaging and Particle Image Velocimetry (PIV) that may be conducted using a water-cooled endoscope.
- Gas and particle sampling which can be done using special quenching probes.
- Measurements of furnace wall temperature using wall-embedded thermocouples and in-flame temperature using suction pyrometer.

All the measuring equipment need to be inserted via ports distributed along the reaction zone. Biomass flames in furnaces with comparable power extend about 1.2-1.4 meters through the furnace [45], [83], and may extend to more than 1.7 m in the case of some biomass types [29], [111].

For the purpose, seventeen ø80mm ports are fitted along the furnace with close meshing near the burner and more distant locations downwards:

- Five openings are set in each of the upper two sections with 15 cm spacing,
- Four openings in the third section with 23 cm spacing,

- Two openings in the fourth section 40 cm spacing,
- One opening in the bottom section

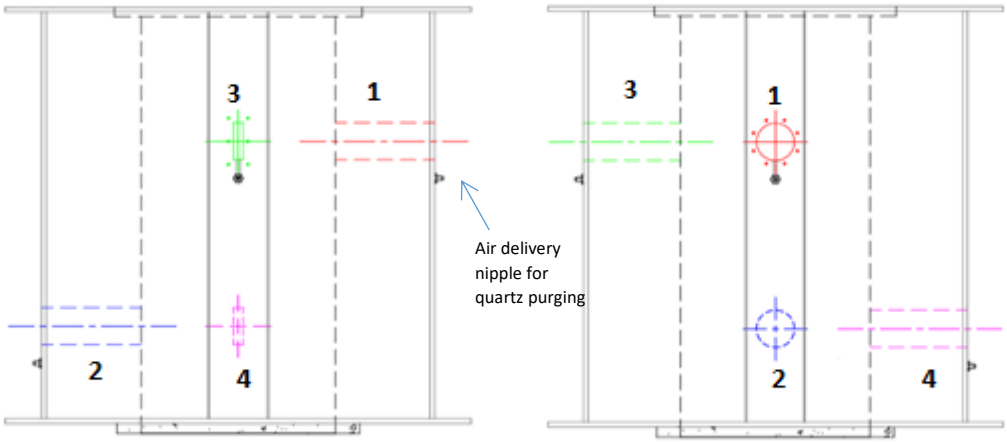

Figure III.12: Measurement ports arrangement (left: rectangular ports side view; right: circular ports side view)

With this arrangement, the furnace risks to be fragile especially the upper sections, so the ports were distributed successively on opposite sides. Besides, PIV technique requires a thin laser sheet in the measuring plane situated perpendicular to the camera axis. Consequently, other rectangular windows are added at 90° of each circular port. The final configuration is presented in *Figure III.12*.

When not used for measurements, the ports are closed with plugs made of insulating concrete in order to limit the heat loss through the ports. The plugs can serve also as K-type thermocouples stands to measure the wall temperature distribution.

III.8 Pilot burner

With the chamber diameter set to 40 cm, the calculated thermal power of 21 kW is not sufficient to maintain a high wall temperature and sustain the combustion. The furnace thus needs to be very well insulated to limit the heat loss and to keep low outer surface temperature for security reasons. The furnace should also include external heat source to warm up the facility and to support the 21 kW burner. Several solutions were considered:

1. Gas fired tubes configuration
2. Electrical heating
3. Auxiliary gas burner

The first solution consists of a gas-fired annulus producing high temperature gas to circulate in multiple tubes embedded in the furnace walls. The solution is not practical considering the design difficulties and the additional mass of the castable materials. Moreover, it imposes some constraints on the refractory materials like being thermally conductive but non-porous to ensure the separation of the reaction zone and the gas heaters.
Electrical heating is a practical solution and provides flexibility in controlling the wall temperature and the experimental conditions. It has been used in many studies in combustion research and for studying pulverized fuel flames. The resistors need to be embedded in the

walls, and thus they present a long-term risk due to the different thermal expansion properties than those of the wall materials. However, the major drawback is related to the high capital and operational cost of high temperature resistors and these cost requirements were not warranted.

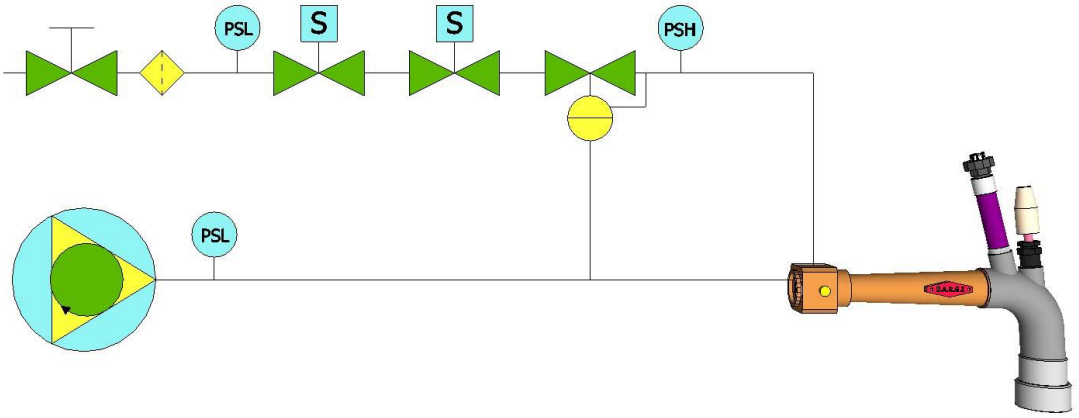

Figure III.13: Gas and air feeding circuits of the pilot gas burner

The third solution is the simplest, as it adds no major modifications to the furnace structure. A gas burner is installed on the top of the furnace near the biomass burner and it can be designed with sufficient energy to heat up the furnace to the set temperature prior to the experiment. The burner is tilted by 30° toward the axis of the reactor to help igniting the biomass flame and then shut off once the pulverized flame stabilizes. The thick insulation does the work later to keep the walls near the set temperature during the measurements. The gas burner can operate autonomously with thermal power of 50 kW. The power is controlled by the gas flow, and the supply of air is automatically regulated by commanding the velocity of the supplying fan. The burner is connected to a high-pressure gas supply. The gas circuit up to the burner is equipped with pressure sensors and security valves to turn-off the gas delivery in case of any danger or flame extinction. The latter is detected by a sensor implemented in the burner (*Figure III.13*).

III.9 Biomass Burner Feeding

A steady biomass feeding of the burner is essential for good experimental measurements and low variables fluctuations. Flame stability cannot be established with unsteady feeding including large error when performing stability studies. An unsteady fuel/air feeding also increases the unburnt fraction of the fuel and leads to a bad mass balance of the exhaust species.

III.9.1 Air supply

The primary air flow is adjusted by a mass flow controller. The high pressure (5 bars) in the primary air supply creates a Venturi effect in the ejector later on to suck the biomass. Similarly, the secondary air pressure is regulated to 1 bar and then the flow is controlled and delivered to a Sylvania SureHeat Max preheater. This 10 kW electrical resistor heats the secondary air up to the desired value (~400 °C). A thermocouple is installed ahead the preheater to control the temperature and to ensure the equipment operating limits are not exceeded. For this purpose, the preheater never operates without a continuous air flow (*Figure III.14*).

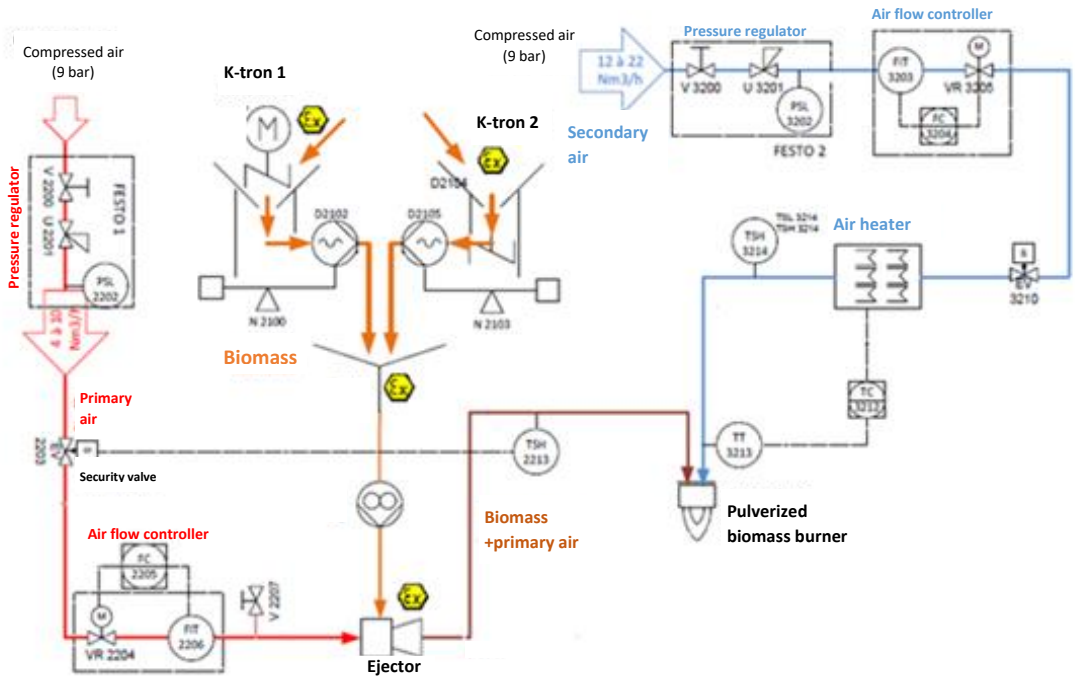

Figure III.14: Scheme of burner feeding circuits (primary and secondary air + fuel feeding)

III.9.2 Pulverized fuel feeding

Pulverized fuel feeding has always been a challenge regarding the accompanying problems of solid powder flowability and bridging. The necessary amount of fuel is provided by two loss-in-weight screw feeders. Both feeders have the same functioning mode. They include a hopper on top with an agitating rotor inside to reduce bridging. A horizontal agitator gently moves the bulk material to the large throat and then into the screws. The screw velocity is adjustable to provide a uniform flow rate of powder. The screw type and pitch also control the flow so they should be pre-calibrated and adapted to the materials being fed. The first feeder is a twin-screw feeder (K-TRON K-ML-D5-KT20) with the capacity of 0.5 to 12 kg/h, while the second one has a single screw with half the capacity (0.2 to 6 kg/h) (*Figure III.15*). The two feeders are used in parallel to acquire more flexibility concerning the optimal feeding rate and stability. Each feeder operates at a different motor speed, which helps to attenuate the oscillation of the supplied flow related to the pitch and velocity of the screws. In addition, the two feeders can be employed in future work on co-firing.

Figure III.15: Image of the feeding system: in the first sight the twin-screw feeder (K-TRON K-ML-D5-KT20), in the back, the single screw feeder and below the ejector

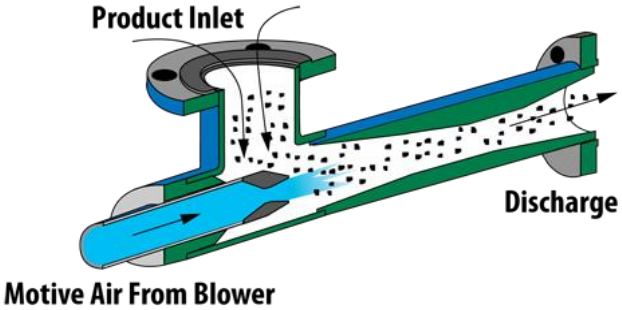

Figure III.16: Schematic view of the ejector feeder

The fuel is introduced to the air stream using an ejector feeder (*Figure III.16*). The ejector creates a pressure drop at the Venturi throat in order to suck the fuel into the air stream with a high velocity (Typical throat velocities are 2 to 3 times the velocity in the main duct). The pressure drop can be regulated by moving forward/backward the throat and controlling the product inlet area. The advantage of the Venturi system is that it comprises no moving part so it does not need frequent maintenance. However, operating problems were encountered when the ejector was directly connected to the hopper. Fuel bridging is frequent especially when dealing with wood powder and consequently causing stream blockage. To solve this problem, a vibrator is installed on the hopper, which assures a good flowability of the powder.

The pressure of the fuel-laden air decreases upstream the throat and continues directly to the central injector of the burner. Pneumatic conveying systems are practical and economical to install and operate on transporting bulk materials. They are preferred for their flexibility in terms of rerouting and expansion. Several pneumatic conveying methods have been developed including dilute-phase conveying, dense phase conveying, and air activated gravity conveying. In this facility, we used the first method where the air-suspended fuel is transported by maintaining a sufficient airstream velocity. The dilute-phase conveying is characterized by high velocity and a high air to solid loading ratio (>2.0). The airstream velocity is in the range of 16 - 40 m/s depending on the material and application.

III.10 Exhaust and cooling systems

The combustion products are evacuated from the combustion chamber by an induced draft fan. The created negative pressure in the chamber is monitored by a pressure transmitter inserted in the bottom section of the furnace. A control system commands the extraction fan speed for the desired chamber negative pressure. The ashes are collected on the ashtray at the bottom of the furnace. It is designed with two symmetrical exits to maintain the symmetry of the flow inside the furnace. Combustion gases therefore exit symmetrically through two opposite ducts that rejoin later and convey the gases to a water-cooled jacket and then to the stack.

The cooling system is designed to obtain a net stack temperature in the range of 160 - 260°C that is typical in such applications. These limits are set to prevent condensation and possible corrosion of the stack. The cooling water is pumped to an aero-convector placed outside the pilot scale facility building to be cooled by the external air. A flow detector in the water circuit ensures the well-functioning of the pump. The circuit is equipped with pressure and temperature sensors to control the heat extraction from the exhaust stream and to signal high-energy load on the system. In case of high load causing water evaporation and eventually high circuit pressure, a security pressure valve reliefs the system pressure. The water loss is then compensated by an external reservoir to maintain sufficient water level in the circuit. In case of condensation of the water in the flue inside the cooler, a draining line is capable of evacuating it from the bottom of the cooler (*Figure III.17*).

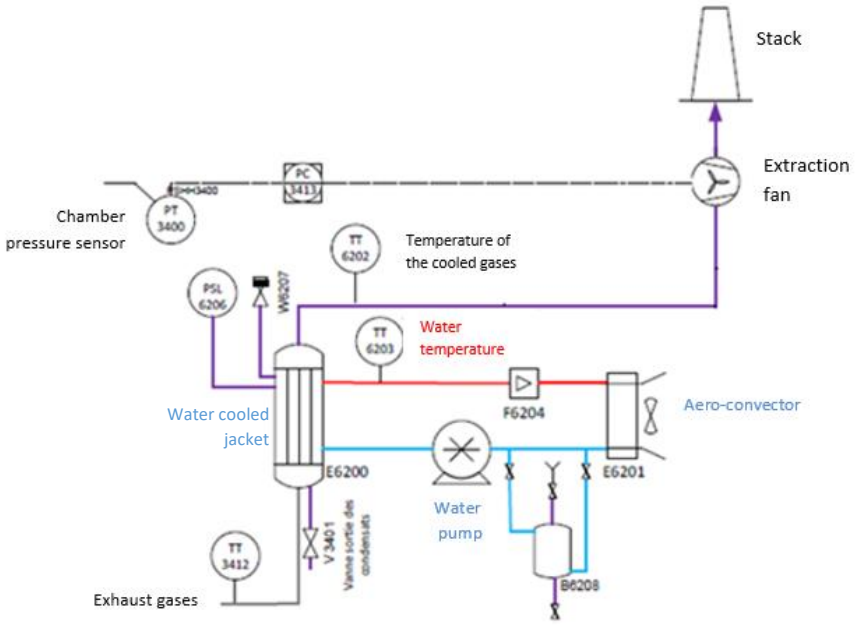

Figure III.17: Scheme of the exhaust and cooling systems

III.11 Data acquisition system

The data is collected and displayed at the furnace control panel by means of a computer data acquisition (DAQ) system. The data includes:

- The wall temperature (17 K-type thermocouples) and the roof cover temperature (K-type thermocouple)
- Exhaust temperatures before and after cooling (K-type thermocouples)
- Chamber pressure (pressure transmitter)
- Cooling water temperature and pressure (Pt100 and pressure sensor)
- Gas composition (ECOM J2KNpro) and oxygen exhaust composition (lambda probe)
- Biomass flame detection (UV detector)

The DAQ system includes sample averaging and data-logging features for monitoring and evaluation of experimental data. The DAQ also controls and monitors the transport airflow, secondary airflow and temperature, biomass mass flow, the power of the pilot burner and the speed of the extraction fan.

III.12 Security system and safety features

III.12.1 Flame supervision system

The flame safety is monitored through several sensors in order to detect any flame blow-off or flame flashback. The security system must regard the flame safety with high concern in order to limit any serious consequences. The extinction of the flame is hazardous with continuous accumulation of flammable and toxic gases in the chamber, which may trigger an unexpected explosion especially when the wall temperature is already very high.

During the heating process, an ionization sensor integrated in the gas burner ensures the presence and stability of the flame. Once the flame is lost, the burner automatically enters in the reset mode:

- Gas supply is cut off
- The feeding fan purges the burner
- The extraction fan purges the chamber
- Wait for user intervention to reboot

After the transition to biomass mode, another detector collects the ultraviolet radiation emitted by the flame. On loss of the UV signal, the safety procedures are launched:

- A security valve cuts off the primary air
- Fuel feeders stops the supply of biomass to the ejector
- Air preheater is shut off
- Secondary air flow continues sweeping the preheater and the combustion chamber
- Wait for user intervention to launch the rebooting protocol

On the other hand, a flashback scenario should be anticipated. The phenomenon occurs when the flame velocity is higher than the injection velocity, which causes the flame front to travel upstream inside the injection tube. The flashback damages the admission circuit, and if not carefully controlled, the fire may reach the fuel skid and lead to an explosion. For this reason, the primary air duct up to the burner is equipped with a fine thermocouple to detect the flame flashback with sufficient sensitivity and short response time. Once encountered the "flashback protocol" is followed:

- fuel and primary air feeding are set on standby
- Rotary valve locks and serves as an explosion non-return valve to arrest the fire from arriving to the skid.
- Air preheater is automatically shut off
- Secondary air continues flowing through it for some time afterwards to cool it down and purge the combustion chamber
- Wait the chamber to cool down below a predefined limit (usually 50°C) and launch manually the booting protocol

III.12.2 Exhaust safety system

The operating systems mentioned before around the chamber are vital for the stability of the flame. Any incidental error can lead to blow-off the flame or damage the materials and to a probable human risk. Therefore, every surrounding system is monitored with several sensors to feedback its status. Errors occurring in the feeding system will eventually lead to one of the scenarios mentioned in the flame safety section (flame blow-off or flashback). The procedures make sure to stop the systems and protect the equipment from possible deterioration. Other problems may happen in the chamber and in the exhaust system that will eventually translate into two main problems: Pressure loss in the chamber or cooling failure.

The pressure loss in the chamber can be caused by any leak to the chamber or to the exhaust system, or by malfunctioning of the extraction fan. An extraction failure can lead to lose the flame stability and to a pressure rise inside the furnace, which pushes toxic gases out of the chamber or may possibly provoke an explosion in case of accumulation of unburnt volatile gases. This requires an immediate stop of the flame following the protocol of 'gas flame blow-

off' during the heating period or that of 'biomass flame blow-off' during experimentation, while keeping the cooling and extraction (if possible). The rebooting is not possible unless the furnace cools down and a detailed inspection is carried on.
Moreover, a cooling failure will damage the cooling system itself and the equipment downstream, in which the induced draft fan is one of them (consequently lose the extraction). The high load on the cooling system is detected by measuring the temperature of the cooled gases and by the water temperature and pressure. The extra load can be held by continuously relieving the water pressure and add fresh water from the external reservoir. In case the system encounters any operating problems, or received a very high load, the DAQ system stops simultaneously the cooling, fuel feeding and the preheater. The whole circuit is left to cool down by the secondary air stream.

Besides, the pilot facility hall is equipped with several CO and fire detectors to alarm and stop the experiment whenever a risk is identified.

III.13 Instrumentation and diagnostic methods

III.13.1 Objective of structural measurements and flame stability

In-flame measurements in a pilot furnace representative of an industrial configuration give information on combustion features for the tested operating conditions. These measurements highlight the origins and causes of the possible limitations of combustion regimes, including flame extinction, causing the presence of unburned gases and thus a decrease of the thermal efficiency and a strong emission of pollutants. It provide also experimental data that can be used to validate (or not) the results of combustion modeling or any other tool informing us about the length, position and shape of the reaction zone in the reactor. For this purpose, optical diagnostics and probe measurements have been implemented in the pulverized biomass pilot reactor.

III.13.2 In-flame concentrations measurements by gas sampling

The radial sampling probe is a 1.6 m tube of 3 mm diameter, protected by another 16 mm diameter tube. It is connected to a combustion gas conditioner where the gas is sucked by a pump at 4 Nl/min then filtered and dried of combustion water and other condensable (tars). A fraction (2 Nl/min) of the sampled gas is thereafter sent to the ECOM J2KNpro gas analyzer to measure the composition of O_2, CO, CO_2, NOx and SOx (see *Table III.7*). Each measuring point is the average of a 5-minute sampling duration. The sampling is not carried out isokinetically because this method of sampling, avoiding the distortion of the current lines, is not applicable in the combustion chamber. In fact, the presence of the reactive jets and of the recirculation zones means that the speed standard and its orientation vary over a very wide range. Moreover, isokinetic sampling is critical when sampling solid particles, which is not our concern in this experiment.

The probe was water cooled during the preliminary tests. However, the condensation of tar and water continuously caused a total blockage of the probe and damaged the pump. The sampling duration had to be reduced and the probe had to be cleaned between two consecutive measurements. This elongated the time devoted to the experiment campaign and raised questions to if the short duration sample is representative of the flow.

	Measurement range	Accuracy	Resolution
O_2 electrochemical	0…21vol.%	±0.3vol.%	0.1vol.%
CO_2 NDIR sensor	0…20vol.%	± 0,5 vol.%	0.1vol.%
CO electrochemical	0…63000 ppm	±5% of reading (0…10000ppm) ±10% of reading (10000…63000 ppm)	1ppm
NO NDIR sensor	0...5000ppm	±5% of reading	1ppm
NO_2 NDIR sensor	0...1000ppm	±5% of reading	0.1ppm
SO_2 NDIR sensor	0...5000ppm	±5% of reading	1ppm

Table III.7: ECOM J2KNpro gas analyzer specifications

Cooling with heated oil was not available, so the sampling was then tested with no cooling of the probe. Considering the relatively small diameter of the chamber and the thick insulation layer, the temperature of the extracted gases dropped below 200°C inside the wall of the chamber. This was measured by tracing the temperature of the sample using a 0.5 mm type K thermocouple inserted inside the probe. With the available suction velocity of the pump (4 Nl/min), the residence time of the gases until the on-going reactions are stopped inside the wall is estimated around 7 ms. The quenching rate is estimated to be around 10^5 K/s. However, this is two orders of magnitude lower than the rate found by Lallemant et al. [168] in order to have a correct measurement of intermediate species like CO. This gives rise to measurement errors, particularly in the reaction zone where the kinetic times are relatively fast. In order to evaluate the error margin caused by the quenching rate, we carried out several measurements in the reaction zone with and without cooling. When the probe is cooled, the sampling duration was about 2 min.

Species	O_2	CO_2	CO	NO
With cooling	14,2%	6,42%	10875 ppm	138 ppm
Without cooling	14,5%	6,8%	9339 ppm	125 ppm
Measurement variation (% of the reading)	< 2%	< 5%	< 14%	< 10%

Table III.8: Measurement variation of different species with and without cooling the probe

Table III.8 presents the variation of the measurement of different species with and without introducing water to the probe. It is important to note that this variation is not uniquely caused by the quenching rate, rather, there are several factors inducing this variation, including the accuracy of the gas analyzer, the fluctuation of the flame, the accuracy of the position of the probe, the error produced by condensation of water and tar in the water cooled probe etc. O_2 and CO_2 are measured with acceptable variation. However as expected, CO is highly influenced

by the sampling process in the reaction zone. NO is less reactive than CO and the variation here could be mostly dependent on the ECOM accuracy.

As a result, O_2, CO_2 and NO measurements without cooling the probe can be fairly considered as representative of the gas composition at the sampling point. CO reading can still be qualitatively useful in the diagnostics of the biomass flames. The rise of CO is an indicator of devolatilization or marks the reaction zone of char. Moreover, the degree of uncertainty of CO measurement is lower outside the intense reaction zone, especially where the chemical reaction rate is reduced by combustion gas recirculation behind the burner, or by lower temperature and lower oxygen concentration in the lower sections of the chamber.

III.13.3 Chemiluminescence imaging

III.13.3.1 Physical principle of light emission from a flame

The flame is a rich medium of excited species and hot particles that radiate in all wavelengths depending on their nature and temperature. Nowadays, the optical emission from a flame is widely used as a relatively simple diagnostic to characterize the heat release and structure of the flame. Several phenomena cause the spontaneous radiation of the flame:

- Solid bodies (e.g., soot, ash or char particles) produce the continuous emission spectrum resulting from blackbody radiation and particles emissivity, which exhibits a peak at wavelengths decreasing with the temperature.
- Gas molecules at high temperatures display spontaneous emission.
- Some chemical reactions generate species in excited states, a part of which reaches their thermodynamic equilibrium ground state through the emission of light (chemiluminescence).

The spectrum of each phenomenon varies from one flame to another depending on the fuel type, temperature, turbulence and other operating parameters. In this study, we are interested by chemiluminescence radiation as a marker of the reaction zone as it is spontaneously radiated by the decay of excited species undergoing chemical reactions. During the combustion process, some radicals are generated in excited state by the chemical energy liberated with the reactions. These species subsequently emit photons due to the energy transition from an excited state to a lower level state, providing information on the conditions and location of the reactive zone. Therefore, the intensity of the emission depends on certain parameters in the reactive zone of the flame such as the heat release rate and excess air. The de-excitation takes place over a very short characteristic time making it possible to locate the reactive zone fairly precisely [169]. The reaction zone during the oxidation of hydrocarbons and hydrogen molecules, contained in the volatiles of biomass, is in general characterized by the chemiluminescence of certain chemical species such as CH*, OH*, C_2*, CO_2* [170]. They represent the electronically excited state for a given radical or molecule and are responsible for chemiluminescence radiation emitted in the visible and ultraviolet. Whereas, at typical flame temperatures, thermal radiation by solid bodies and gases is found in VIS-IR and IR, respectively. The presence of the spectra of these different species is strongly dependent on the chemical composition but weakly on the temperature [170]. Each species is characterized by its own spectrum consisting of numerous emission lines that makes it possible to identify in the flame emission spectrum.

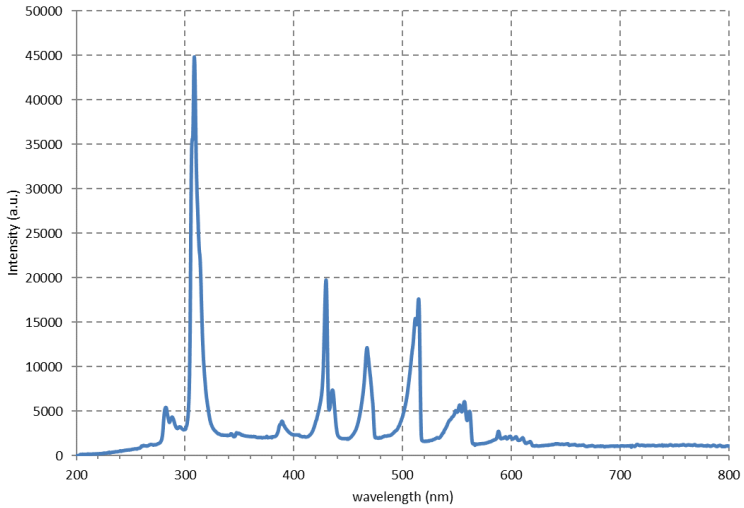

Figure III.18: Typical chemiluminescence spectrum observed in partially premixed flames [171]

Radical	Principal reactions of the formation of excited radicals		Wavelength (nm)
OH*	R1:	$CH + O_2 \rightarrow CO + OH^*$	285, 308.9
CH*	R2:	$C_2H + O \rightarrow CO + CH^*$	387, 431
C_2^*	R3:	$CH_2 + C \rightarrow C_2^* + H_2$	516
	R4:	$C_3 + O \rightarrow C_2^* + CO$	
CO_2^*	R5:	$CO + O + M \rightarrow CO_2^* + M$	Continuous spectrum 300-600

Table III.9: Formation routes of excited radicals and characteristic wavelengths [171]

A significant progress has been made in literature on the understanding of the formation mechanisms of these chemiluminescent species, even if there still exists uncertainty about the complete formation pathways. The most favorable formation routes of excited radicals and their characteristic wavelengths are presented in *Table III.9.*

Figure III.18 shows a typical chemiluminescence spectrum of a diffusion flame of hydrocarbons showing the appearance of various excited species at different wavelengths. The emission of CO_2* appears as a continuum which extends from 300 nm to 600 nm seen as blue color. In addition, the bands of C_2* between 436 nm and 564 nm called Swan bands are found in the visible region of flame spectra. The Swan bands of C_2* are visible mainly in the fuel rich conditions [170], [172]. OH* radical gives a strong UV spectrum with peak intensity at about 308 nm. The CH* signal is more intense in hydrocarbon-rich combustion zones at about 387 nm and at 431 nm, because it marks the decomposition of the fuel. It should be noticed in wood combustion due to tar decomposition so that it provides a good indicator for the onset of pulverized particle ignition and the volatile reaction region for heat release [173].

The main drawback of chemiluminescence imaging technique lies in its spatial resolution. The measured signal intensity at a certain pixel of the detector represents the entire emission signal of the excited species along the optical path of this position (i.e. along the flame thickness). It

is therefore not possible to determine from which part of the flame is the signal recorded by imaging. Moreover, quenching and local parameters such as excess air, turbulence and pressure can also influence the species' intensity of emissions and make chemiluminescence a complex diagnostics, which can only be interpreted qualitatively.

By collecting the OH* radicals chemiluminescence in the UV range, we are able to get rid of all radiative emissions from solid emitters (wall, soot, wood,…) even at high temperature, as such thermal radiation is very low in this spectral range. However, in pulverized fuel flames, the CH* signal is strong compared with the OH* signal because the continuous spectrum accompanied by the solid-body radiation from soot/coal/char is overlapped on CH band emission [174]. Indeed, these hot particles emit in a large visible spectrum. It is thus not possible to distinguish CH* emission from the emission of these particles [125]. But still, the signal from CH* signal can be used as an indicator in terms of strong sooty volatile flames including small portion of char reactions [175].

The interpretation of OH* chemiluminescence images allows us to obtain the average location of the reaction zones, presenting a signature of the flame at a given operating point. Depending on the intensity and the shape of the zones of heat release of the flame, chemiluminescence helps to define the topologies and the characteristic data of the different flames.

III.13.3.2 Experimental setup

The use of a sensor in ultraviolet, visible or infrared range is relevant for analyzing the quality of combustion. The chemiluminescence being locally created in an exothermic combustion zone, its recording with a two-dimensional sensor produces instantaneous images of the reaction zones. This diagnostic is relatively simple to implement, but it requires specific sensitive equipment because of the low signal level. For flames with a strong soot radiation (yellow flame oil, wood or coal) or in a hot radiating environment as a furnace, the use of a UV detector is preferred to better filter the reaction zone emission from other radiations.

Characterization of flame structures by chemiluminescence imaging in such 4 m length vertical combustion pilot is a challenging task as it requires several optical ports in a hot environment and the possibility to manage the imaging system over the whole of the reactor height.

Optical applications in such high temperature hostile environment demand a specific type of optical materials for the access ports. The HOQ310 quartz is an attractive option regarding its economical price and low bubble content. The good chemical resistance is suitable for the corrosive environment created by the combustion of biomass. In our pilot reactor, the 10 mm thick windows are continuously swept with pressurized dry air to avoid the accumulation of ash and the condensation of tar on its surface. A nipple is installed next to each window where a purging tube can be inserted to deliver dry air to blow off the ash fouling and help cooling the quartz. Moreover, HOQ310 quartz provides an excellent optical transmission from the UV into the IR spectral region (*Figure III.19*), including all spectral ranges of chemiluminescence species (OH*, CH*, etc.).

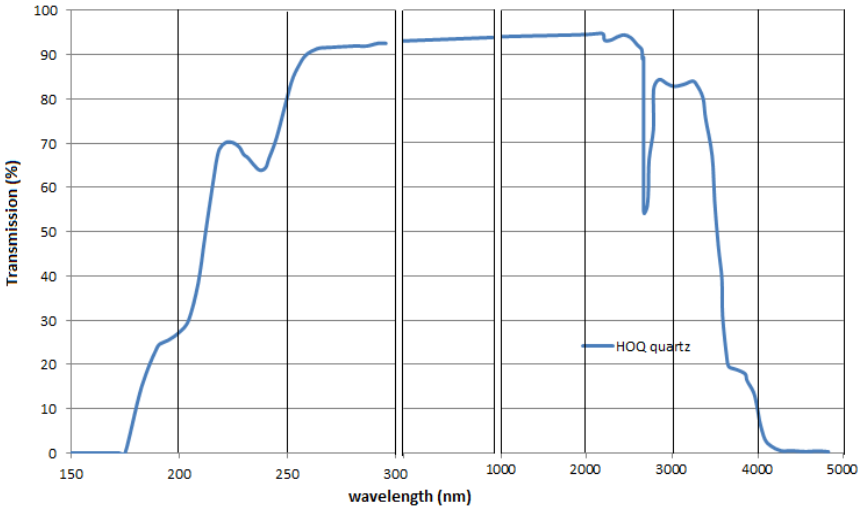

Figure III.19: HOQ310 quartz transmission spectrum

The acquisition system consists of a Princeton PI-MAX2:1003 camera (camera 1) with a 5MHz / 16-bit digitization and 1024x1024 pixel intensified CCD (ICCD) sensor, enabling a resolution of 0.25 mm / pixel. The camera is equipped with a CERCO 28mm-f/3.5 lens for UV emission. With this setup placed in front of the optical access, the camera captures a 14 x 14 cm² picture at the axis of the furnace. This field of view is not sufficient to overlap images taken at two consecutive ports. For this reason, a new collection system recently developed at CORIA laboratory consisting of a water-cooled UV-VIS endoscope has been implemented on the biomass reactor (*Figure III.20*).

The flamoscope consists of an optical system divided into five groups of lenses made of materials adapted to the visible and ultraviolet spectral range. The first group constructs a real image with a very small magnification, which is then transported by the four other groups of lenses to the photocathode of the intensified camera emICCD Princeton Instruments PIMAX4 (camera 2: 1024 x 1024 pixels - 16 bits) whose large and high dynamic range sensor provides high sensitivity and optimized spatial resolution for chemiluminescence imaging of large flames.

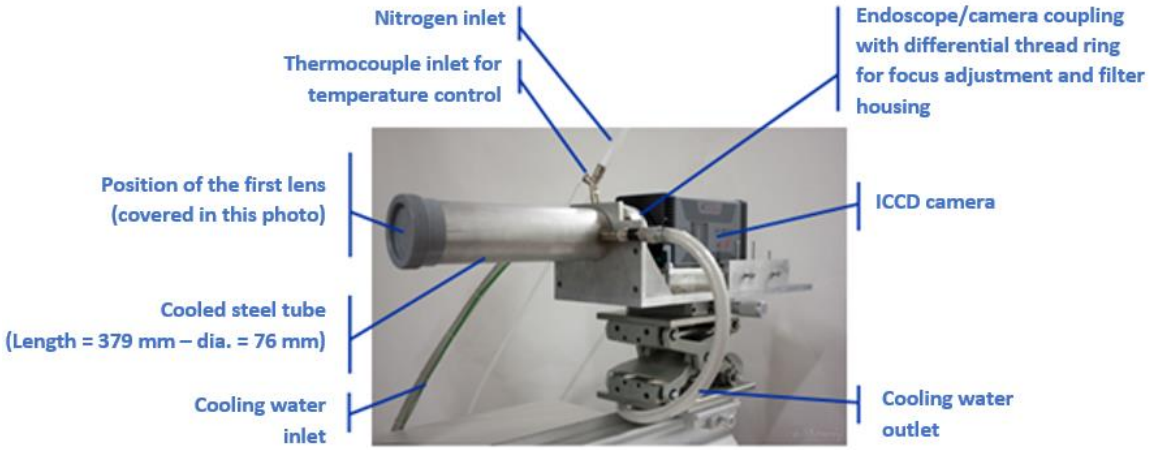

Figure III.20: The flamoscope developed in CORIA

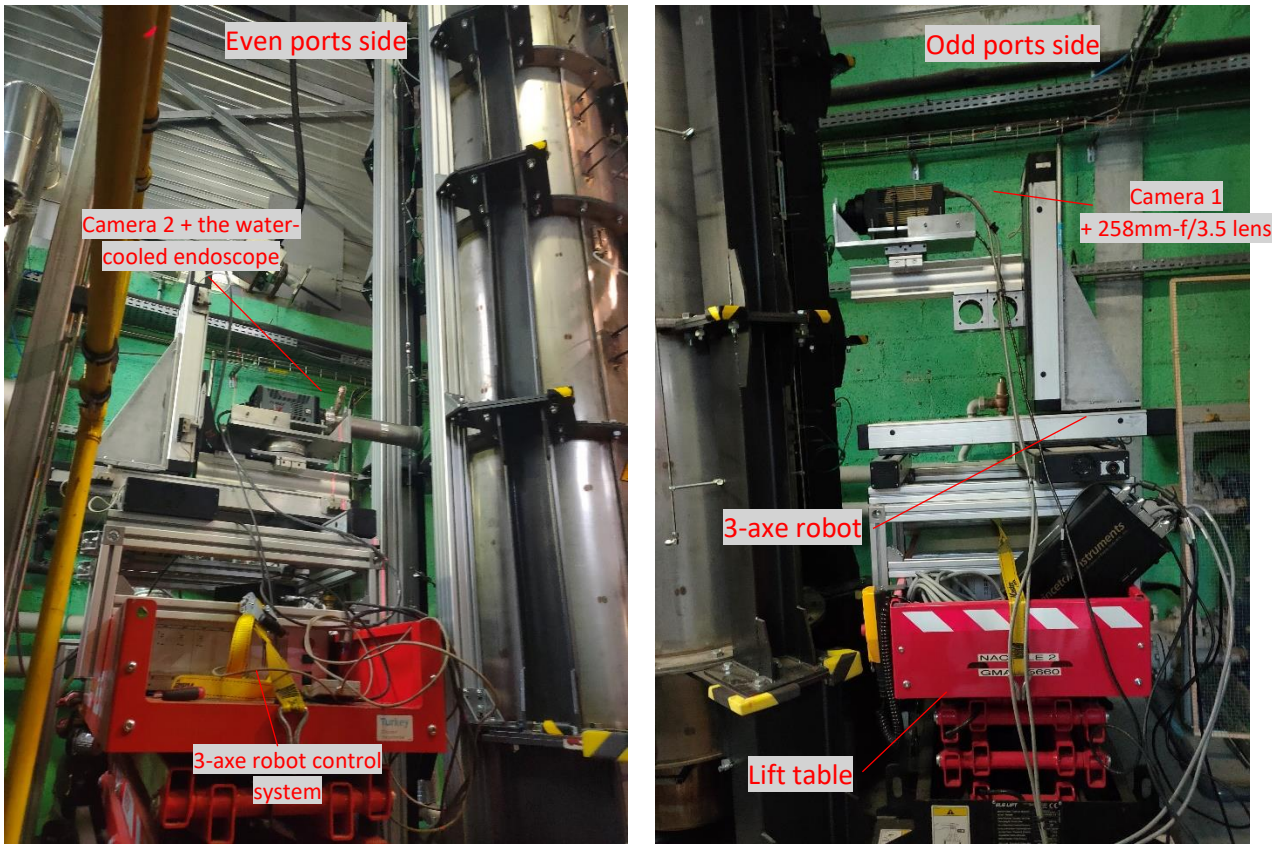

Figure III.21: The optical systems held by the 3-axe robot on the lift table from both sides of the chamber

This optical assembly with a total length of 370 mm is equivalent to a reflex photographic lens of the 'fisheye' type with a focal length of 12.8 mm for an aperture of f / 3.9, with an extended focus (0.2 m - ∞), a large field depth, low geometric distortion and a wide field of vision.
The set of lenses is placed in a stainless steel sheath cooled by water circulation. A flow of dry air passes through the optical tube and exits from a small pupil to thermally and mechanically protect the first lens. The coupling between the endoscope and the emICCD camera is carried out with a differential thread ring for fine adjustment of the focus. This same ring accommodates the spectral filters chosen for the spectral selection of the chemiluminescence of the OH* radical.

The flamoscope control system allows the adjustment of the nitrogen flow rate through the optical assembly and the adjustment of the flow rate of filtered water for cooling the endoscope; it also continuously controls the temperature of the endoscope at its front face. The chemiluminescence image sequences are digitized by an acquisition system with the Princeton Instruments LightField software, which allows the parameters of the emICCD camera to be adjusted (mainly: region of interest of the sensor, exposure time and intensification gain).
The flamoscope (camera 2) is used on the even ports (4, 6,…, 14) to extend the field of view to those seen by camera 1 from the odd ports through optical windows. When inserted 14 cm inside the furnace wall, the flamoscope enables to acquire twice the field of view obtained outside the chamber by camera 1 (27 x 27 cm). Both cameras are calibrated with a reference grid of UV LEDs outside and inside the chamber.

Both cameras are mounted on a 3-axe moving precise robot with a rotation movement around z-axis (parallel to the axis of the reactor). The robot is fixed on a 4 m lifting table as seen in the *Figure III.21*. A specific setup of spectral filters is placed in front of camera 1 lens or in the flamoscope in front of camera 2 to select a spectral transmission range centered on the emission of the OH* radicals. The selected filter is Schott UG11 filter. However, this filter has a small transmission peak at 720 nm (2.5%) which may induce the collection of thermal radiation emitted by the hot biomass particles and the high temperature furnace walls (*Figure III.22*). This bias is attenuated by adding three UG11 filters in series in order to ensure that the collected signal correspond solely to the OH* radicals. *Figure III.23* shows the collected images at the first port using the same gain and exposure time with 1, 2 and 3 filters. The acquired images were taken at a wall temperature of 800 °C with no chemiluminescence emission at this location. The wall radiation is totally blocked by 3 filters, and the transmission ratio in UV remains high enough to collect OH* chemiluminescence image with ICCD cameras.

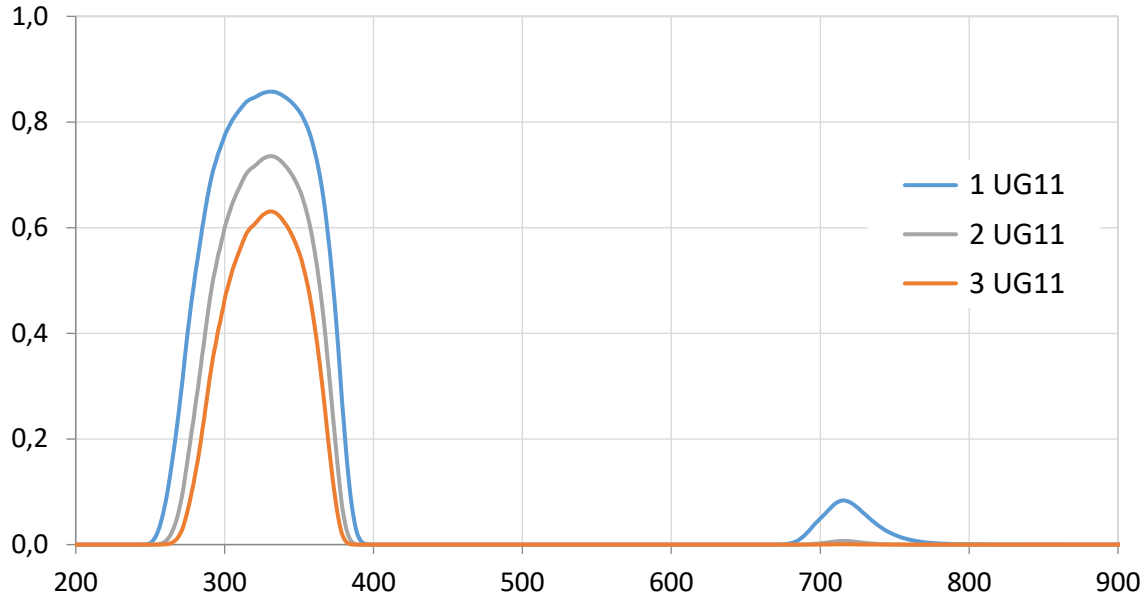

*Figure III.22: Comparison of the transmission range of 1, 2, and 3 UG11 filters relative to OH**

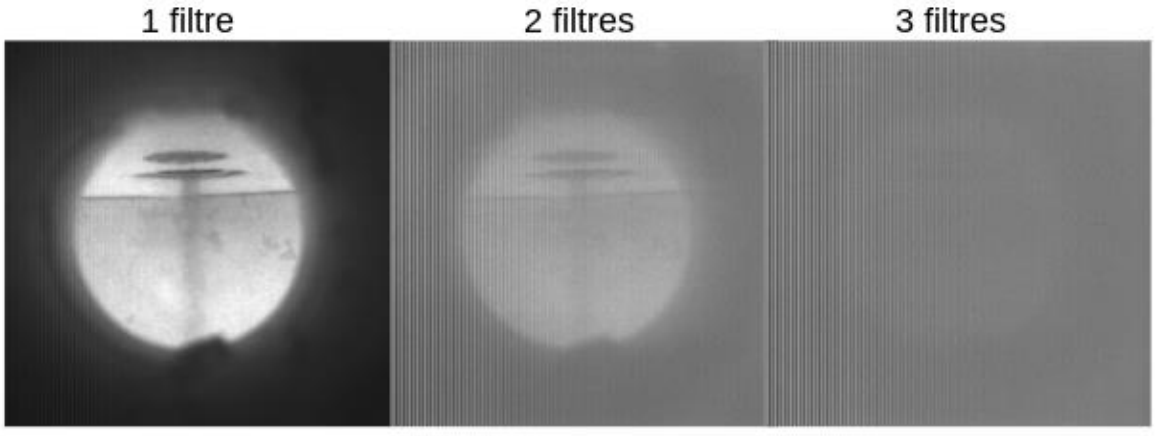

Figure III.23: Signal transmission to the ICCD using 1, 2 and 3 UG11 filters

The measurement was repeated at port 13 were the vast majority of the hot particles are undergoing char oxidation. With three UG11 filters, the Planck radiation of hot chars are no longer transmitted to the sensor, but some OH* chemiluminescence is still detected.

III.13.3.3 Image analysis and statistical methods

The recorded chemiluminescence images are digitized with a 16 bits dynamic range of 65,535 gray levels. The exposure times are around 400 to 750 µs on both cameras in order to take full advantage of the sensor capacity under different signal intensities, resulting from the different positions in the flame and different operating conditions. The intensifier gain is set close to the maximum value (250 on camera 1 and 9000 on camera 2). Each access point is the subject of a series of acquisitions with at least 2000 images at an acquisition frequency of 8 Hz for the camera 1 and 5 Hz for camera 2. These images will be used to calculate an average flame image, from which statistical data such as the standard deviation and the fluctuation rate will be deduced.

For both configurations, the magnification ratio is determined from the images of the UV LEDs reference grid. The origin of the axis is set at the exit of the burner on the centerline. Each series of images is centered at the longitudinal location of the corresponding optical access. The large field of view of the flamoscope and the chosen distance between two successive optical accesses on one side allow us to have a quasi-continuity of the image of the reaction zone in the combustion chamber.

During image post-treatment, an anomaly was observed in all the mean images obtained with the endoscope that was not detected during the acquisitions. A dark spot appeared on the left side of every image especially in the reaction region as seen in *Figure III.23*. This gave the impression that the flame is shifted to the right.

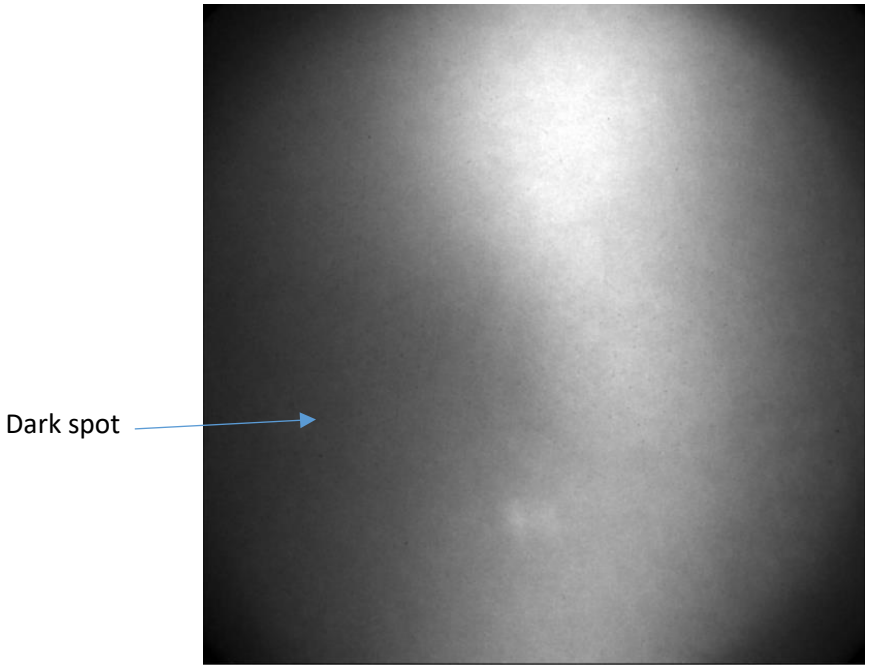

Figure III.24: OH chemiluminescenceof Pin-T flame at port 8, a dark spot is seen on the left side of the image*

However, after thorough examination of the setup, we discovered that the transmission of the optical system is not homogeneous on every pixel. This has not been observed on experiments performed previously with the flamoscope setup on other pilot combustion chamber. The reason is most likely attributed to a displacement of a lens in the flamoscope during the assembly of the setup on the biomass pilot reactor. Unfortunately, the experiments could not be repeated within the framework of this thesis because of the specific situation at the time at the end of the project. So the collected images were then corrected numerically using a base image of the transmission of the optical system. The latter is constructed by taking measurements of a UV LED on different pixels of the camera. The signal of the LED is continuous and constant, so the differences in the measured intensities from one pixel to another is related to the transmission of the optical system.

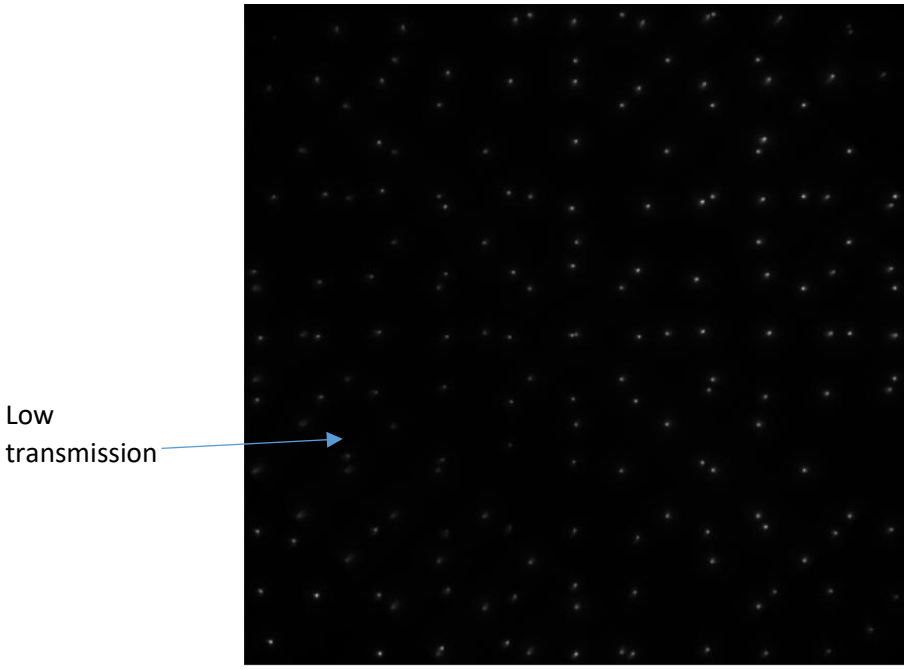

Figure III.25: Transmission signal of the UV LED on different pixels

Figure III.25 shows the measured intensities on different pixels using the same UV LED. Each point is the average of 200 images. The results clearly indicate a decrease in the transmission of the signal on the left side of the image. The LED signal is distributed over several pixels, so in order to calculate the signal at the targeted pixel, an average is calculated over a 5x5 matrix around the targeted pixel. The transmission in between the 80 targeted points was estimated by interpolating the measured data. The resulting image was then divided by the maximum measured signal, which is the theoretical intensity that should be captured by each pixel. This gives the ratio by which each pixel has to be multiplied by in order to correct its measured intensity.

Figure III.26 presents the correction ratio on each pixel. The figure indicated that 50% to 80% of the signal was lost on the left side pixels. This effect cannot be corrected, since the correction here would amplify also the noise signal and overcorrect the OH* signal. Fortunately, the right half had a good transmission ratio with acceptable losses. One can notice higher transmission in the top of the image compared to the center and the bottom. Therefore, only the right half of

each image was retained and corrected by this procedure, which is representative of the whole flames thanks to their averaged symmetry.

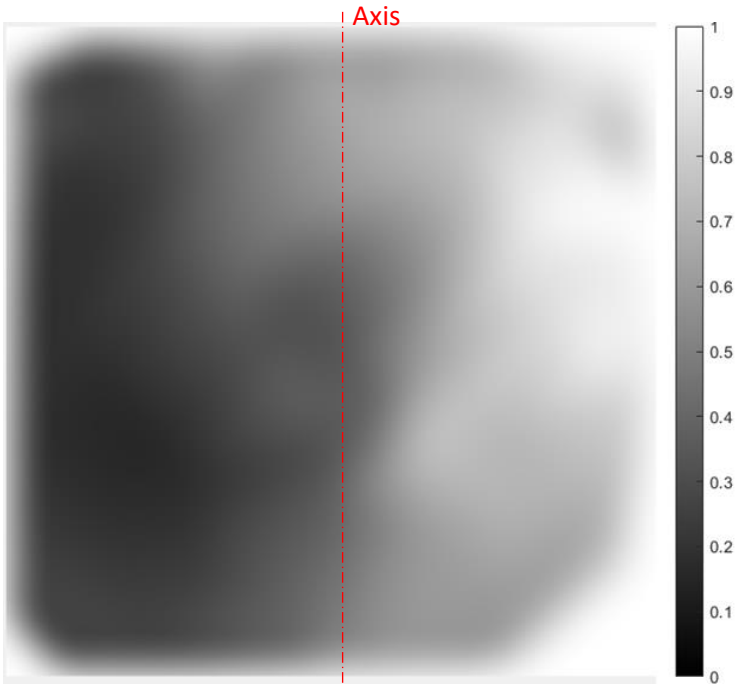

Figure III.26: Correction ratio of the images taken by the flamoscope

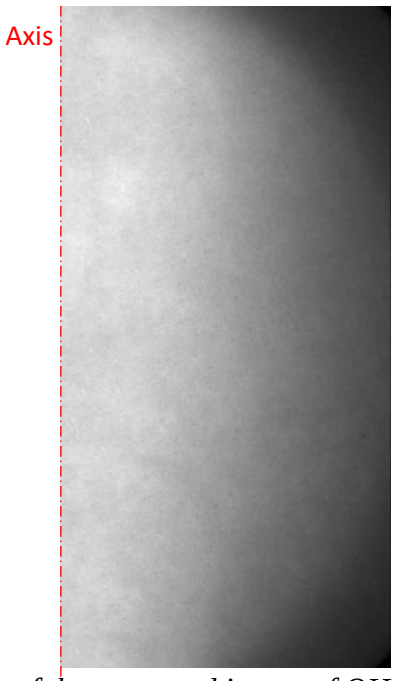

Figure III.27: The right side of the corrected image of OH chemiluminescence of Pin-T at port 8*

Figure III.27 shows the right side of the corrected image of the OH* chemiluminescence of Pin-T at port 8. It is important to note that the correction procedure on the right side slightly changed the main topology of the reaction zone along the pilot reactor. However, it still enables the comparison between the position and intensity of the chemiluminescence signal in the tested flames. Results show that, despite of this issue, the use of the flamoscope enables to have a quasi-continuity of the flame field of view in the pilot reactor.

Chapter IV. Modeling of the combustion of biomass particles in the drop tube furnace and biomass flames in the pilot scale reactor

This Chapter concentrates on the modeling of the combustion of a single particle of biomass and the biomass flames using computational fluid dynamics. The different sections introduce the main equations and the adopted sub-models that describe the combustion of pulverized biomass in a reactive flow. The experimental data of the particle scale investigation are used to tune the numerical models.

The mathematical modeling of biomass combustion is a combination of the degradation models of a single particle and the governing equations and reactions of the surrounding gases. When modeling the process under simple conditions similar to the drop tube furnace ones, particles are considered isolated and no particle-particle interactions are included. In such reactors, the flow is always laminar so that the main purpose of the experiments and calculations is focused on the kinetic parameters of the different undergoing reactions especially devolatilization and char combustion. However, in large-scale modeling of biomass flames, CFD calculations should take into consideration the turbulent interactions of the fluid and the particles. Considering these factors significantly changes the particle tracks and consequently changes the gas distribution maps and temperature profiles inside the continuum volume.
In the present study, we tried to reproduce the experimental data of the drop tube furnace using a 1D isolated particle model coded on MATLAB in order to determine the kinetic parameters of the devolatilization and char oxidation. In a second part of this chapter, the obtained kinetic parameters are used in CFD simulations on ANSYS Fluent commercial code to simulate the pulverized biomass flames in the pilot-scale reactor.

IV.1 Numerical modeling of single biomass particle combustion

Numerical models have been developed in a few studies to help analyze the data of the drop tube furnace and extract the kinetic parameters of devolatilization and char oxidation (Table IV.*1*), and subsequently predict other combustion parameters, as in Commandre et al. [176] for petcokes. Two approaches are proposed in this purpose: the model fitting approach and the 1D Lagrangian model. The first assumes that the combustion process in the DTF is performed by sections in which each section has its own set of kinetic parameters. Devolatilization occurs in the upper sections while char oxidation takes place in the lower sections. Costa et al. [177] applied this approach to determine the kinetic parameters of the devolatilization and char oxidation of raw and torrefied pine shells (Ev = 21.58 – Ec = 129.86 and Ev = 21.28 – Ec = 89.75 kJ/mol respectively). In the same study, similar trends, but with much higher activation energies, were estimated for raw and torrefied olive stones. Using this approach, Farrow et al. [178] also obtained apparent activation energies between 24.2 kJ/mol and 34.7 kJ/mol for the pyrolysis of pinewood sawdust. On the other hand, Ballester and Jimenez [179] developed a detailed 1D Lagrangian model to perform numerical calculations on the particle thermal history based on the experimental data. The model was applied originally to coal and then adapted to biomass giving Ev = 11kJ/mol and Ec = 63 kJ/mol [50]. Wang et al. [64] also used this approach to evaluate the combustion behavior of biomass waste derived fuels, pine and coal in drop tube furnace. Pereira et al. [180] applied both models to the combustion of poplar short rotation coppice. In comparison, the apparent activation energies in the devolatilization zone vary from 34.1 kJ/mol for the model-fitting approach to 12.8 kJ/mol for the detailed model proposed by Jiménez et al. [50], whereas in the char oxidation zone both models originate close apparent activation energies (73.2 kJ/mol and 69.0 kJ/mol). The distinct values are attributed to the simplifications considered in the model-fitting approach including the assumption of similar particle and gas temperature, which explains the higher activation energy of devolatilization, and the constant oxygen pressure at the particle surface along the furnace, which explains the higher activation energy of char oxidation. Simplifications and different assumptions taken using the same approach also influences the determination of the kinetic parameters. The

volume evolution model and the drag coefficient model are the main sub-models that change from one study to another.

Study	***Temperature (°C) – atmosphere – particle size***	***Fuel***	***Model approach***	***Ev (kJ/mol)***	***Ec (kJ/mol)***
Costa et al. [177]	*900, 950, 1000, 1050, 1100°C Air 30-1000µm*	*Raw pine*	*Model-fitting*	*21.58*	*129.86*
		Torrefied pine		*21.28*	*89.75*
Farrow et al. [178]	*900, 1100, 1300, 1450 °C CO_2 and N_2 125-250µm*	*Pinewood*		*24.2-34.7*	-
Pereira et al. [180]	*900, 950, 1000, 1050, 1100°C Air 20-1500µm*	*poplar short rotation coppice*		*34.1*	*73.2*
			1D Lagrangian	*12.8*	*69.0*
Ballester and Jimenez [179]	*1040, 1175, and 1300 °C Air 100-1000µm*	*Cynara cardunculus*		*11*	*63*
Wang et al. [64]	*1100°C Air 30-1128µm*	*Pine braches*		*55*	*93*

Table IV.1: Survey of the kinetic parameters of devolatilization and oxidation of biomass using different model approaches

In this study, we attempt to derive the kinetic parameters of the tested fuels using a 1D Lagrangian model. Different volume evolution scenarios and drag coefficient models are tested to study their influence on the obtained values of the kinetic parameters. The model was used to perform numerical calculations on the particle thermal history based on the experimental data collected from the combustion experiments in the drop tube furnace. The code determines the kinetic parameters of the physicochemical reactions that better reproduce the oxygen partial pressure obtained experimentally in the DTF. Note that the model is similar to what has been proposed in [50], [179] and [64].
The CFD model uses the parameters obtained with the corresponding volume evolution scenario and drag model in order to simulate the biomass flames in the pilot scale reactor.

IV.1.1 Main hypothesis

Considering the dilute flow of the experiments, the particle-to-particle interactions were neglected and the gas flow rate was considered constant at every point. Uniform temperature and homogeneous concentrations of chemical species are assumed in a horizontal section of the DTF.
The physical properties are described through the conservation equations of mass, momentum and energy. The devolatilization reaction and heterogeneous oxidation of char are described at the particle level.
The particle has a simplified composition, comprising only C, H, and O species. It has a spherical shape with the initial diameter equals to the average diameter of the sample. The model is described in the following.

IV.1.2 Drying model

The drying process of the particle is modeled using the diffusion approach. The moisture contained in the particle evaporates rapidly with the high heating rate. The vapor release to the gas is controlled by the mass transfer between the surrounding gas and the particle.

$$\frac{dW}{dt} = 18 \cdot 10^{-3} \cdot K_w \left(\frac{P_{sat}}{RT_p} - \frac{X_w}{RT_g} \right) \quad \text{(Eq.}IV.7\text{)}$$

$$P_{sat} = 1.1 \cdot 10^{-5} \cdot exp\left[11 \cdot \left(T_p - 273.15 \right)^{0.16} \right] \quad \text{(Eq.}IV.8\text{)}$$

$$K_w = \left(2 + 0.6 \cdot Re_p^{1/2} Sc^{1/3} \right) \cdot \frac{D_w}{d_p} \quad \text{(Eq.}IV.9\text{)}$$

gases in large excess of air		Diffusion coefficient, D_{12}, [cm^2/s] at atmospheric pressure and given temperatures					
		0 °C	**20 °C**	**100 °C**	**200 °C**	**300 °C**	**400 °C**
Water vapor	H_2O	0.219	0.242	0.399	0.638	0.873	1.135

Table IV.2: Diffusion coefficient of water vapor in the air [181]

Psat is the vapor saturation pressure (in Pa). Xw is the water fraction in the environment coming initially from the air humidity and then from the biomass moisture and the water produced by combustion. The Schmidt number (Sc) of the gas is set to 0.73. Dw is the diffusion coefficient of water in the gas mixture approximated by air. It is interpolated from the values listed in *Table IV.2* [181].

IV.1.3 Devolatilization and volatile combustion model

The release rate of volatiles follows a one-step Arrhenius mechanism. The model assumes that the process is a first step global reaction depending on the quantity of volatiles remaining in the particle.

$$\frac{dV}{dt} = A_v \cdot \exp\left(-\frac{E_v}{RT_p} \right) . (V_0 - V) \quad \text{(Eq.}IV.10\text{)}$$

V_0 is the initial volatile content and V is the amount of released volatiles. Av and Ev are the kinetic parameters, determined by iterations for the best match with experimental data.

The composition of the volatiles is determined by the pyrolysis experiments and it is assumed constant at all positions. The gas phase reactions are simplified in the oxidation reactions of the following combustible species (CO, H_2, and CH_4). The reactions are considered to be complete.

$$CO + \frac{1}{2} O_2 \rightarrow CO_2 \quad \text{Rxn. (}IV.1\text{)}$$

$$H_2 + \frac{1}{2} O_2 \rightarrow H_2O \quad \text{Rxn. (}IV.2\text{)}$$

$$CH_4 + 2O_2 \rightarrow CO_2 + 2H_2O$$ Rxn. (*IV*.3)

The reactions rate R_i is formulated under the Arrhenius form:

$$R_i = k_{0,i} exp\left(\frac{T_{a,i}}{T}\right).T^{b0}\rho_{a1}^{b1}\rho_{a2}^{b2}\rho_{a3}^{b3}$$ (Eq.*IV*.11)

$T_{a,i}$ is the activation temperature of reaction i. $\rho_{a,j}$ (kmol/m^3) is the molar density of the species aj. The parameters are given in *Table IV.3*.

Reaction i	$K_{0,i}$	$T_{a,i}$	b0	a1	b1	a2	b2	a3	b3
1	1.10^{15}	16000	-1.5	CO	1	O_2	0.25	H_2O	0.5
2	$5.16.10^{13}$	3430	-1.5	H_2	1.5	O_2	1	-	-
3	$3.55.10^{13}$	15700	-1	CH_4	1	O_2	1	-	-

Table IV.3: Values to be used for computations of gas-gas reaction rates [182]

IV.1.4 Char oxidation model

The last step for the particle combustion is the heterogeneous char oxidation. It starts once oxygen reaches the particle surface and reacts with carbon atoms. The reaction produces CO and CO_2 with a temperature dependent ratio [141]. At low temperatures, the ratio of [CO]/[CO_2] is low and it increases with CO being dominant at high temperatures. ($0 < \emptyset < 1$)

$$C + \left(1 - \frac{\emptyset}{2}\right)O_2 \rightarrow \emptyset CO + (1 - \emptyset)CO_2$$ Rxn. (*IV*.4)

$$R_c = \frac{[CO]}{[CO_2]} = 2500 \cdot \exp\left(-\frac{51843}{RT_p}\right)$$ (Eq.*IV*.12)

The stoichiometric coefficient of carbon oxidation (Kg C/ Kg O_2) is defined as

$$\upsilon_C = \frac{12}{32} \cdot \frac{1 + \frac{M_{CO_2}}{M_{CO}} R_c}{1 + \frac{1}{2}\frac{M_{CO_2}}{M_{CO}} R_c}$$ (Eq.*IV*.13)

Therefore, the rate of the oxidation depends on the diffusion rate of oxygen and the chemical reaction rate. Different scenarios were previously explained in the three-zone theory (Chapter I).

$$\frac{dC}{dt} = -A_p K_c P_{O_2,s}^n$$ (Eq.*IV*.14)

Kc is the chemical reaction rate coefficient. $P_{O_2,s}$ is the oxygen partial pressure at the particle surface supplied by molecular diffusion, which obeys Fick's law:

$$\dot{m}_{O_2} = \pi d_p Sh D_{O_2} \frac{M_{O_2}}{RT_g}(P_{O_2,g} - P_{O_2,s})$$ (Eq.*IV*.15)

Sherwood number (Sh) was set to 2. Note that the effect of the outward flow of the species is negligible and the supplied oxygen by diffusion is consumed by the heterogeneous reaction.

$$\dot{m}_{O_2} = -\frac{1}{v_c} \cdot \frac{dC}{dt} \quad \text{(Eq.IV.16)}$$

After arranging the above equations, the carbon consumption can be rewritten as follows:

$$\frac{dC}{dt} = -A_p \frac{1}{\frac{1}{K_{diff}} + \frac{1}{K_c}} P_{O_2,g}^n \quad \text{(Eq.IV.17)}$$

The diffusion and chemical kinetic coefficients are calculated:

$$K_{diff} = Sh.v_c \frac{D_{O_2}}{d_p} \frac{M_{O_2}}{RT_g} \quad \text{(Eq.IV.18)} \qquad K_c = A_c \cdot \exp\left(-\frac{E_c}{RT_p}\right) \quad \text{(Eq.IV.19)}$$

The remaining volatiles and char form the unburnt fraction U of the particle. The data obtained in the Particle Combustion Shadowgraphy (§II.4) were employed in the model through the evolution of the particle volume and density:

$$d_p = d_{p_0} f(U) \quad \text{(Eq.IV.20)}$$

$$U = \frac{C + (V_0 - V)}{C_0 + V_0} \quad \text{(Eq.IV.21)}$$

Where f(U) is a characteristic function of each fuel type in terms of the unburnt fraction.

IV.1.5 Heat balance

The particle temperature is different from gas temperature and wall temperature. The small size of the particle limits the temperature gradient within the particle, so they are considered thermally thin. This assumption is believed acceptable in our operating conditions [183]. Once introduced to the furnace the particle is exposed to heat by:

- Convection with the surrounding gas
- Radiation with the internal wall of the reactor

The heat balance can be converted into the following equation:

$$C_{pp} m_p \frac{dT_p}{dt} = h_p A_p (T_g - T_p) + A_p \varepsilon \sigma (T_w^4 - T_p^4) - \frac{dW}{dt} H_w - \frac{dC}{dt} f_h H_C - \sum \dot{m}_i C_{pi} T_p \quad \text{(Eq.IV.22)}$$

The parameters of the gas in the equation are calculated for an average film temperature $\left(\frac{T_p + T_g}{2}\right)$. The particle is treated as a gray body with constant emissivity. h_p is the coefficient of heat transfer by convection between the particle and the gas. It is evaluated using the correlation of Ranz and Marshall [184]:

$$Nu_p = \frac{h_p d_p}{\lambda_g} = 2 + 0.6 Re_p^{1/2} Pr^{1/3} \quad \text{(Eq.IV.23)}$$

C_{pp} is the specific heat of the particle at constant pressure. For biomass, an average value of C_p as a function of temperature found by Dupont et al. is used [185].

$$C_{pp} = 5.34 T_p - 299 \quad \text{(Eq.IV.24)}$$

The last three terms refer to the energy produced or absorbed by the thermal conversion of the particle:

- Energy absorption for particle drying
- Heat release by the combustion of char with f_h being the coefficient of heat release due to incomplete combustion.

$$f_h = 1 - 1.44 \cdot \left(1 - \frac{12}{32} \cdot \frac{1}{v_c}\right) \quad \text{(Eq.IV.25)}$$

- The last term represents the heat fluxes supplied to the environment by the gases leaving the particle. The heat fluxes provided by the gases entering the particle are neglected.

During their ejection, the volatiles exchange heat with the particle, as well as with the gas phase. The energy balance in the gas phase is given by:

$$C_{pg} \dot{m}_g \frac{dT_g}{dt} = h_p A_p (T_p - T_g) + h_r A_r (T_w - T_g) + \sum R_i \cdot H_i + \sum \dot{m}_i C_{pi} T_p \quad \text{(Eq.IV.26)}$$

A rise in the gas temperature is caused by the liberation of volatile energy through oxidation. Hi is the heating value of each volatile species i. In the balance, h_r is the coefficient of heat transfer by convection between the gas phase and the reactor inner wall. It can be calculated using Nusselt number. The Nusselt number is determined by Mill's model for convection in a vertical cylinder [186].

$$Nu_r = \frac{h_r D_r}{\lambda_g} = 3.66 + \frac{0.065 \cdot Re_g Pr_g \cdot \frac{D_r}{L_r}}{1 + 0.04 \left(Re_g Pr_g \cdot \frac{D_r}{L_r}\right)^{2/3}} \quad \text{(Eq.IV.27)}$$

D_r and L_r are the inner diameter and length of the tube, respectively.

IV.1.6 Particle trajectory

The motion of the particle is determined by Newton's second law as the sum of the forces acting on it. In a gas/solid flow, the drag and body forces are known to be the dominant forces. The velocity can be calculated by integrating the following equation:

$$m_p \frac{du_p}{dt} = \frac{\pi d_p^2}{4} \cdot \frac{\rho_g}{2} \cdot C_D (u_g - u_p)^2 + m_p g - \rho_g V_p g \quad \text{(Eq.IV.28)}$$

The Drag force, particle weight and Archimedes up-thrust are represented by the three terms on the right-hand side. This approach neglects the so-called rocket force or propulsion force, produced by the anisotropic release of volatiles from the fiber structure of the particle, causing the particles to accelerate suddenly. The drag coefficient C_D quantifies the resistance of the particle in air. It can be expressed in terms of the Reynolds number:

$$C_D = \frac{24}{Re_p} = \frac{24}{|u_g - u_p|\rho_g d_p/\mu} \quad \text{(Eq.}IV.29\text{)}$$

Equation (*IV.28*) can be rearranged in the following form:

$$\frac{du_p}{dt} + \frac{1}{\tau}(u_g - u_p) = \left(\frac{\rho_g}{\rho_p} - 1\right) g \quad \text{(Eq.}IV.30\text{)}$$

The right-hand side is related to the buoyancy of the particle in the airflow. τ is the particle relaxation time given by the product of the particle mass and its mechanical mobility. This term characterizes the time required for the particle to adjust its velocity to a new condition of forces.

$$\tau = \frac{\rho_p V_p d_p}{12\mu_g A_p} \quad \text{(Eq.}IV.31\text{)}$$

IV.1.7 Derivation of kinetic parameters

Oxygen is involved in the main chemical reactions occurring in the furnace. Therefore, $P_{O_2,g}$ is not constant and its evolution should be followed to provide the input parameters for the particle consumption. A relationship, established between the partial pressure of oxygen and the consumed volatiles and char, determines its value at a given position x.

$$P_{O_2,x} - P_{O_2,0} = \frac{\rho_g R T_g}{M_{O_2}} \cdot \frac{Q_f}{Q_g} \cdot \left(\sum_i \frac{1}{\upsilon_k} \cdot S_k + \frac{1}{\upsilon_c} \cdot (C_0 - C)\right) \quad \text{(Eq.}IV.32\text{)}$$

S_k represents each species of the volatiles (CO, H_2, CH_4) and υ_k is the corresponding stoichiometric coefficient of the oxidation reaction (Kg species k/ Kg O_2). The later oxidation of CO produced in the heterogeneous oxidation of char, is taken into account in the CO fraction.

The prediction is compared with the measured oxygen content (%vol.) along the furnace axis. The deviation between both values is calculated:

$$\delta = \sum \frac{1}{N} \cdot \left([O_2]_{exp} - [O_2]_{calc}\right)^2 \quad \text{(Eq.}IV.33\text{)}$$

N is the number of measured points, the indices exp and calc signify experimental and calculated entities respectively. The code runs in iterations in two rounds to spot the optimal pairs of kinetic parameters ((Av, Ev) and (Ac, Ec)) providing the best prediction by minimizing the deviation function.

Table IV.*4* presents the scanned ranges and the increment values of each parameter. The code runs a first round in these ranges to spot (Av1, Ev1) and (Ac1, Ec1). A second run is done in a more refined range around the values spotted in the first round with a smaller increment.

	Av (1/s)	Ev (kJ/mol)	Ac (g/m².s.Pa)	Ec (kJ/mol)
First run				
Range	1-500	1-100	0.01-5	1-100
Increment	1	0.5	0.01	0.5
Second run				
Range	Av1 ± 10	Ev1 ± 0.5	Ac1 ± 0.1	Ec1 ± 0.5
Increment	1	0.1	0.01	0.1

Table IV.4: The scanned ranges of the kinetic parameters

IV.2 CFD modeling of pulverized biomass flames in the pilot scale reactor

The particle model was integrated in a CFD Fluent model to predict the flame characteristics and flow behavior of pulverized biomass injections in the pilot scale reactor. The computational results will be validated by experimental data collected under similar boundary conditions. Once validated, the results will give insights to the behavior of each particle within the flame, and reveal how tuning the same underlying equations to the particle nature changes the flame structure. The tuned parameters are measured at particle scale: fuel analysis, the four kinetic parameters, volume evolution parameters, and volatile composition.

Due to the axisymmetric geometry of the reactor with no swirl, the problem is reduced to a 2D axisymmetric geometry. This can significantly reduce the computational time with finer mesh than with the actual 3D domain. Three simulation cases were studied for pine, torrefied pine and pyrolyzed pine at the same heat input and air injection configuration.

IV.2.1 Particle combustion model

Fluent offers a Lagrangian way to treat the particles injected in the computational domain called the discrete phase model (DPM). In the DPM of ANSYS Fluent, the particles effect on the flow field is included in the continuous phase equations via source terms (two-way coupling). Therefore, the particles can exchange heat, mass and momentum with the gas stream. The strategy for the simulation is to alternate the Eulerian flow field and Lagrangian particle trajectory calculations until a converged coupled solution is obtained.

The DPM models present six laws that are alternately activated and deactivated along with the temperature and mass evolution of the particle:

- Law 1: inert heating of the particle ($Tp < T_{evaporation}$ or $Tp < T_{Devolatilization}$)
- Law 2: water evaporation ($T_{evaporation} < Tp < T_{boiling}$ and $m_p > (1 - f_{w,0})m_{p,0}$)
- Law 3: water boiling ($Tp > T_{boiling}$ and $m_p > (1 - f_{w,0})m_{p,0}$)
- Law 4: Devolatilization ($Tp > T_{Devolatilization}$ and $m_p > (1 - f_{v,0})(1 - f_{w,0})m_{p,0}$)
- Law 5 : char surface oxidation ($m_p \leq (1 - f_{v,0})(1 - f_{w,0})m_{p,0}$ and $m_p > (1 - f_{v,0} - f_{char})(1 - f_{w,0})m_{p,0}$)
- Law 6: particle cooling ($m_p \leq (1 - f_{v,0} - f_{char})(1 - f_{w,0})m_{p,0}$)

Where $f_{w,0}$, $f_{v,0}$ and f_{char} are the initial mass fractions of water, volatiles and fixed carbon (char) respectively.

Law 1, the inert heating/cooling is applied after the introduction of the particle to the domain as long as the particle temperature is below the water evaporation temperature ($T_{evapration}$).

Once reached, the particle transfers to **law 2** where the water content in the fuel is evaporated until it is completely dried, or until the particle temperature has reached the boiling point temperature ($T_{boiling}$).

If the particle reaches the boiling point temperature before all the water has been evaporated, the rest of the water is being consumed via water boiling law (**Law 3**). **Law 1** may be applied again after the complete drying and boiling stage to heat the particle to the user-defined devolatilization temperature ($T_{Devolatilization}$).

Afterwards, the devolatilization law (**law 4**) begins. Finally, the char combustion stage initiates **law 5** as soon as the volatile fraction is consumed, and continues until there is only ash left in the particle.

Law 6, on the other hand, is applied after the complete burnout of the particle. Thereafter, the ash content of the particle is heated or cooled via **Law 6**.

	Raw pine	**Torrefied pine**	**Pyrolyzed pine**
Devolatilization parameters	A=248 s^{-1} E= 2.74 $.10^{+07}$ J/kmol	A=250 s^{-1} E= 3.2 $.10^{+07}$ J/kmol	A=2.81e+08 s^{-1} E= 1.28 $.10^{+07}$ J/kmol
Char oxidation parameter	C= 5.00 $.10^{-13}$ [-] A= 9.2 $.10^{-04}$ s^{-1} E= 6.35 $.10^{+07}$ J/kmol	C= 5.00 $.10^{-13}$ [-] A= 2.11.10^{-03} s^{-1} E= 7.20 $.10^{+07}$ J/kmol	C= 5.00 $.10^{-13}$ [-] A= 113 s^{-1} E= 5.89 10^{+07} J/kmol
Volatiles molar mass	21.67	22.12	22.12
Swelling coefficient	0.754	0.795	0.774
Reaction heat absorbed by the solid (%)	100	100	100
Specific heat	$5.34T_p - 299$	$5.34T_p - 299$	$5.34T_p - 299$

Table IV.5: The reactivity parameters and particle properties for both fuels in the pilot-scale reactor

With each law a series of equations are triggered to model the mass and heat transfer between the particle and the continuous phase. The equations are already covered by the particle model in the previous section. The only difference is the volume evolution model of the particle. During devolatilization, the particle diameter changes according to a user-defined swelling coefficient C_{sw}.

$$\frac{d_p}{d_{p,0}} = 1 + (C_{sw} - 1)\frac{(1 - f_{w,0})m_{p,0} - m_p}{f_{v,0}(1 - f_{w,0})m_{p,0}} \quad \text{(Eq.}IV.34\text{)}$$

The equivalent coefficient was calculated from the particle combustion shadowgraphy data so that the particle volume ends with the same value after devolatilization as in the shadowgraphy empirical model. However, during the char oxidation, the kinetic/diffusion limited model uses a constant volume scenario. This scenario of volume evolution is proved to give similar results to those produced using the shadowgraphy scenario.

The particle properties and the reactivity parameters are listed in *Table IV.5*. The kinetic parameters of Pine ant Pin-T are those determined by the DTF model. Due to the lack of experimental data for Pin-P in the DTF, the kinetic parameters of Pin-P are obtained by the kinetic modeling of the TGA degradation curves using the direct method.

IV.2.2 Continuous gas phase

IV.2.2.1 Conservation equations of the fluid flow

Navier-Stokes equations describe the motion of every fluid and form the basis of reactive flow calculations within defined boundaries. The equations treat the fluid as a continuum rather than a collection of single molecules. The Navier-Stokes equations can be expressed by the classical conservation equations in the following form [187]:

Conservation of mass:

$$\frac{\partial \rho}{\partial t} + \frac{\partial(\rho u_i)}{\partial x_i} = 0 \quad \text{(Eq.}IV.35\text{)}$$

Where, ρ is the density of the fluid, u_i are the velocity components, t stands for the time, x_i are the coordinate axes. This equation signifies physically that the total mass is conserved with time and displacement. Mass is neither created nor destroyed. However, species can react and change their mass fractions in the mixture. The chemical species are then governed by a second conservation equation [188]:

Conservation of chemical species:

$$\frac{\partial \rho Y_k}{\partial t} + \frac{\partial}{\partial x_i}[\rho Y_k(u_i + V_{k,i})] = \dot{\omega}_k \quad \text{(Eq.}IV.36\text{)}$$

Where the variation of the mass fraction Y_k of species k with time and position depends on its diffusion flux ($V_{k,i}$ is the i-component of the diffusion velocity of species k) and on the production rate $\dot{\omega}_k$ (mass per unit volume). The diffusion of flux is generally modeled by Fick's law, assuming that one of the constituents is dominant [187].

Conservation of momentum:

$$\frac{\partial(\rho u_i)}{\partial t} + \frac{\partial(\rho u_i u_j)}{\partial x_i} = -\frac{\partial p}{\partial x_j} + \frac{\partial \tau_{ij}}{\partial x_i} + F_j \quad \text{(Eq.}IV.37\text{)}$$

This equation is the conservation equation of momentum of a fluid mixture containing the species k=1, …, N. The momentum is related to the pressure p, and to the viscous stress represented by the tensor τ_{ij}. F_j is the volume force acting on the fluid in j-direction. In reactive flow, the mixture state (species fractions, density, etc.) is strongly dependent on the thermodynamic state of the fluid such as temperature and pressure. This requires additional equations to relate the mixture state variables with the thermodynamic state variables like the ideal gas equation. In practice, the fluid is considered Newtonian and the viscous stress tensor is given by Newton's law [187]:

$$\tau_{ij} = \frac{2}{3}\mu \frac{\partial u_k}{\partial x_k}\delta_{ij} + \mu\left(\frac{\partial u_i}{\partial x_j} + \frac{\partial u_j}{\partial x_i}\right) \quad \text{(Eq.}IV.38\text{)}$$

Where the dynamic viscosity μ is an intrinsic property of the considered fluid and δ_{ij} is the Kronecker delta.

Conservation of energy:

The general form of energy balance can be written from the definition of total energy e_t [188].

$$\frac{\partial \rho e_t}{\partial t} + \frac{\partial \rho u_i e_t}{\partial x_i} = \dot{Q} - \frac{\partial q_i}{\partial x_i} + \frac{\partial}{\partial x_i}[(\tau_{ij} - p\delta_{ij})u_i] + (u_i + V_{k,i})F_i \quad \text{(Eq.}IV.39\text{)}$$

Where $\dot{Q}$ is the heat source term including the radiative flux, not to be confused with the heat released by combustion, which is included in the species enthalpy. q_i stands for the energy flux in the mixture through heat conduction and through the diffusion of species with different enthalpies. The last two terms correspond respectively to the energy produced by the viscous forces and the volume forces.

IV.2.2.2 Turbulence

Modeling turbulence is essential to the closure of the transport equations and accurately include the mixing effect on the chemical reactions. A realistic description of turbulence can only be achieved using sophisticated closure strategies such as DNS or LES but the computational demands are very high. Instead, we turn to alternative averaging methods (RANS). The standard k- ε is most commonly used in many biomass combustion studies [189]–[193]. The Navier-Stokes equations are solved by introducing two new variables, the turbulent kinetic energy k and the turbulent kinetic energy dissipation rate ε. Both variables can be determined using equations derived from the Navier-Stokes equations. The model is capable of obtaining all Reynold Stresses (9 in total, 6 independent) by solving only two equations. However, it is generally considered inaccurate due to many assumptions made in deriving the equations. Hence, we used an improved approach: the realizable k-ε model, as it is the most appropriate model when turbulence transfer between phases plays an important role in gasification in the combustion chambers [194]. The realizable k-ε model differs from the standard k-ε model by using a new formulation for the turbulent viscosity and a new transport equation for the dissipation rate, ε, which is derived from an exact equation for the transport of the mean-square

vorticity fluctuation. As a result, it gives improved predictions for the spreading rate of jets, a superior ability to capture the mean flow of complex structures and for flows involving rotation, boundary layers, separation and recirculation. These fluid structures are present in our case and need to be well predicted.

IV.2.2.3 Gas phase reactions

The gas phase is treated as a mixture of gases constituting air, biomass volatiles and combustion products. The gas phase reactions of volatiles (CO, CH_4, H_2, CO_2) are reduced into two-step mechanism, which involves oxidation of volatiles to CO in the first reaction (Rxn. (*IV*.5)) and oxidation of CO to CO_2 in the second reaction (Rxn. (*IV*.7)):

$$volatiles + \vartheta_{O2} O_2 \rightarrow \vartheta_{CO} CO + \vartheta_{CO2} CO_2 + \vartheta_{H2O} H_2O + \vartheta_{N2} N_2 \qquad \text{Rxn. (}IV\text{.5)}$$

$$char\ (s) + S_b O_2 \rightarrow CO \qquad \text{Rxn. (}IV\text{.6)}$$

$$CO + \frac{1}{2} O_2 \rightarrow CO_2 \qquad \text{Rxn. (}IV\text{.7)}$$

Rxn. (*IV*.7) accounts for the CO produced by the char surface oxidation in Rxn. (*IV*.6). The volatiles are represented by a chemical formula CxHyOzNw, based on the molar fraction of carbon, hydrogen, oxygen and nitrogen in the volatile composition. The fractions are determined from the ultimate and proximate analysis and the user-defined molecular weight of the volatile gas. The latter as well as the heating value of the volatiles were calculated from the composition of the volatiles as measured in the drop tube reactor. The transport properties and the specific heats of the gaseous species were calculated using temperature dependent polynomial fits available in Fluent database and the kinetic theory. Since the reactor operates at a constant atmospheric pressure, the density of the gas mixture was obtained from the incompressible-ideal-gas equation. The specific heat capacity was calculated using the mixing-law approach.

The turbulence-chemistry interaction is included in the simulations by the Finite-Rate/Eddy-Dissipation model, which performs well with simple reaction mechanisms. The reaction rate is calculated directly using the turbulence variables (k and ε) and the species concentrations. The model calculates both the Eddy-Dissipation reaction rate, and the reaction rate from the Arrhenius equation that is written for the mean flow variables, and takes the net reaction rate as the minimum of these two.

IV.2.3 Radiation model

The heat transfer due to radiation can be described by the radiative transfer equation (RTE). The RTE for an absorbing, emitting and scattering medium can be expressed in the following form.

$$\frac{dI(\vec{r},\vec{s})}{ds} = \kappa I_b(\vec{r}) - \beta I(\vec{r},\vec{s}) + \frac{\sigma_s}{4\pi}\int I - (\vec{s_i})\Phi(\vec{s_i},\vec{s})d\Omega_i \qquad \text{(Eq.}IV\text{.40)}$$

Where, $I(\vec{r},\vec{s})$ is the radiant intensity at position $\vec{r}$ in the direction $\vec{s}$. κ, β, σ_s are the absorption, extinction and scattering coefficients respectively.

The Discrete Ordinates Model (DOM) solves the radiative transfer equation by discretizing both the Cartesian domain and the angular variables that specify the direction of radiation. Thus, the equation is solved for a finite number of discrete solid angles, and the integrals over these directions are replaced by numerical quadrature. The DOM considers the radiative transfer equation in a direction as a field equation, thus the RTE is transformed into a transport equation for radiation intensity in the spatial coordinates.

DOM allows activating the particle radiation interaction in the DPM to include the effect of radiation heat transfer to the particles. Additional properties for the particle materials (emissivity and scattering factor) are defined. Simulations without including this interaction delayed the temperature rise of the particle but arrived to very high temperature values during char combustion, which caused a rapid degradation at the given kinetic parameters. Therefore, it is necessary to activate the particle radiation interaction for the DOM model to predict the temperature rise of the particle and its reactivity.

IV.2.4 Particle trajectory

The particle trajectory is described by the same forces presented by equation (*IV*.28): particle weight, Archimedes up-thrust and drag force. The latter is modeled here for a non-spherical drag law proposed by Haider and Levenspiel [195]:

$$C_D = \frac{24}{Re_p}\left(1 + b_1 Re_p^{b_2}\right) + \frac{b_3 Re_p}{b_4 + Re_p} \qquad \text{(Eq.}IV\text{.41)}$$

The coefficients b_1, b_2, b_3, and b_4 are functions of the shape factor (SF) of the particle. The latter is defined as the ratio of the surface area of a sphere-equivalent particle (with the same volume), to the actual surface area of the particle. This expression is found to perform among the best of the correction methods when applied to a multitude of shapes [127]. It can be implemented into Fluent to correct for the irregularity of the particle shape. This is necessary to capture the dispersion of the particles in the flow [196].

In addition to these forces, the turbulent fluctuations in turbulent flow regimes have a significant effect on the particle trajectories. The trajectories of particles are predicted using the mean fluid phase velocity, $\bar{u}_i$, in the trajectory equations. $\bar{u}_i$ is obtained from the continuous phase calculations. Optionally, Fluent offers a stochastic method, termed as discrete random walk model (DRW), to take the random effects of turbulence into account. In DRW, the particle trajectory calculation includes the turbulent fluctuations $u_i(t)$ of the gas velocity by introducing the instantaneous fluctuation value $u'_i(t)$ to the average value using the Reynolds decomposed form:

$$u_i(t) = \bar{u}_i + u'_i(t) \qquad \text{(Eq.}IV\text{.42)}$$

The velocity fluctuations $u'_i(t)$ are modeled using a Gaussian probability distribution and the variables obtained from the turbulence model. The inclusion of turbulent velocity fluctuations is controlled by the number of tries of the DRW. The trajectory calculations can be repeated for a sufficient number of particles, so that the turbulent dispersion is extensively accounted for.

IV.2.5 Geometry and mesh construction

The geometry and computational mesh were created with ANSYS DesignModeler and Mesh respectively. Due to the axisymmetric geometry of the reactor, the problem is reduced to a 2D axisymmetric geometry (*Figure IV.1*). The burner geometry is simplified to two 20 cm coaxial tubes. The furnace is slightly elongated to increase the domain length after the region of interest. This way the outlet is set far from the region where some backflow might generate under some inlet boundary conditions. The reverse flow may destabilize the convergence of the solution, so it is preferred to be avoided by modifying the geometry rather than setting constraints to the boundary conditions.

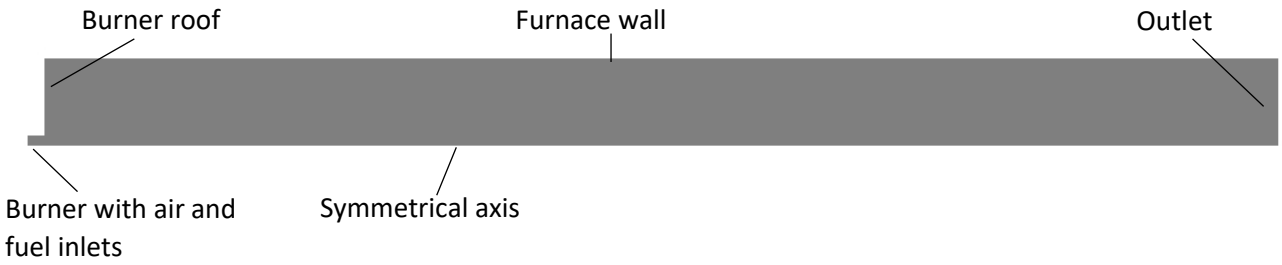

Figure IV.1: The simplified geometry of the 2D axisymmetric computational domain of the pilot-scale reactor

The surface is meshed by sizing the sides and using a mapped surface mesh to produce a uniform organized mesh, more refined at the axis and gradually coarsened towards the wall. The biomass jet and the near bluff-body zone are especially refined to establish a well-detailed calculation about the internal recirculation zone and the near-burner zone phenomena. The mesh constitutes of 288191 nodes and 286400 quadrilateral cells. It retains high quality with minimum orthogonality of 0.99994 and maximum skewness of 6.7 $.10^{-03}$.

IV.2.6 Boundary conditions

Both burner inlets are defined as velocity-inlets. The primary air is injected at room temperature carrying the biomass, while the combustion air is preheated to 380°C.

The biomass jet is introduced to the domain through a surface injection normal to the burner central inlet. The size distribution is represented in *Figure IV.2* by a Rosin-Rammler distribution that fits the fuel granulometry as measured using sieve analysis. The particles are approximated as spheres with their diameters equal to the sieving size. The average diameter is 475 µm, 230 µm and 260 µm for Pine, Pin-T and Pin-P respectively. The spread coefficient is 1.4, 0.89 and 0.84 for Pine, Pin-T and Pin-P respectively. The complete range of particle sizes between 10 µm and 1000 µm is divided into 20 sets of discrete size ranges, each possessing a mass fraction calculated by the Rosin-Rammler distribution. A total number of 1400 particles were tracked in each case.

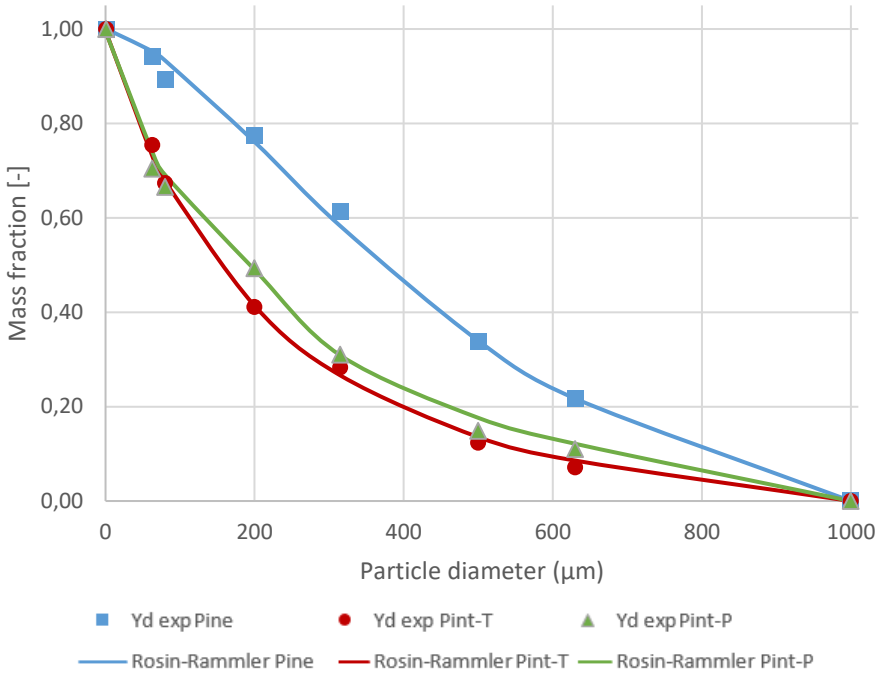

Figure IV.2: Particle diameter distribution of the simulated fuels and their corresponding Rosin-Rammler fit

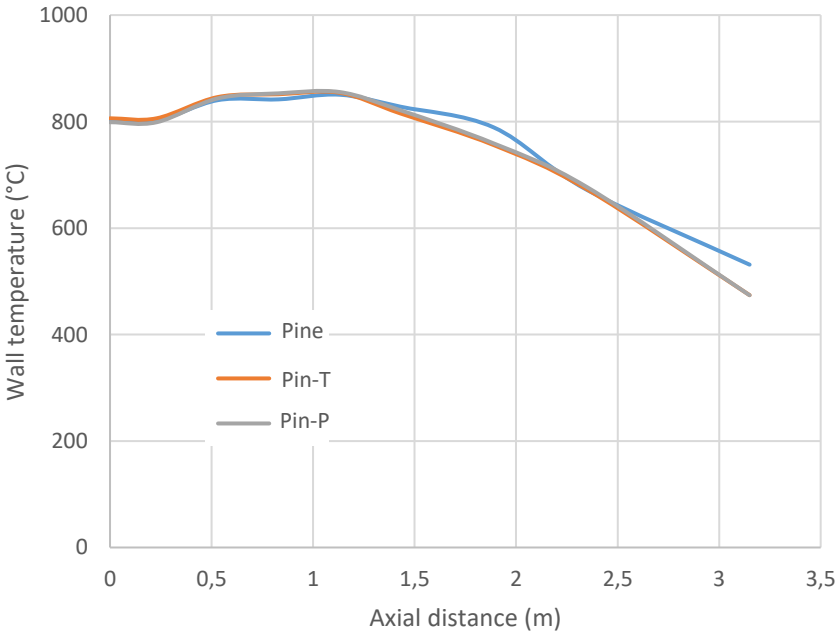

Figure IV.3: The wall temperature profile as measured during the combustion experiments

Case	#1	#2	#3
Fuel	Pine	Pin-T	Pin-P
Fuel feed rate	4.1 kg/h (~20.4kW)	3.7 kg/h (~20.5kW)	3.1 kg/h 3.2 (~20.5 kW)
Transport air velocity	14.74 m/s	14.74 m/s	14.74 m/s
Combustion air velocity	15.08 m/s	15.08 m/s	15.08 m/s
Combustion air temperature	380°C	380°C	380°C
Excess air	1.3	1.3	1.3

Table IV.6: Boundary conditions of the simulated cases

All walls were set to the steady-state temperatures measured experimentally by the thermocouples implemented in the walls. The chamber wall temperature is assigned via a user-defined function with the profiles shown in *Figure IV.3*. The roof temperature and the bluff body temperature are set to 400 °C. The burner walls temperature is approximated by the temperature of the air passing by.

Three cases were studied: Pine, torrefied pine and pyrolyzed Pine. The cases were made at iso-power, isokinetic and same excess-air conditions (*Table IV.6*). Although the different fuel load changes the particle-to-particle interaction, we consider under these conditions that the differences result only from the fuel properties.

Chapter V. Experimental analysis of the combustion of a biomass particle

This chapter discusses the experimental results of the six tested fuels at particle scale. The degradation process is studied at low (TGA experiments) and high heating rates (Drop tube furnace, Horizontal Tubular Reactor and Direct Visualization Chamber). Pyrolysis gas composition, combustion emissions and direct observation of each fuel type are presented, compared and discussed thoroughly.

V.1 General approach

The combustion of raw and torrefied pine, demolition wood and coal is studied using lab scale experimental methods allowing detailed investigation of the combustion events at the particle level. Thermogravimetric analysis gives the degradation profiles of the fuels at low heating rates. The pyrolysis gas composition is measured in the drop tube furnace (§V.2), while combustion gas composition are followed along the process using the horizontal tubular reactor (§V.4). Simultaneous shadowgraphy and direct emission imaging techniques give insight to the phenomena occurring at the particle surface and around it during the whole process, including the onset of heterogeneous ignition and the volume and shape evolution (§V.5).

The work is performed at 800°C on all experimental techniques in order to be able to discuss different results even if collected from different experimental methods and also to refer easily to similar literature works.

V.2 Pyrolysis gas composition

Experiments under pyrolysis conditions were performed in the DTF in the purpose of quantifying the gas composition produced during the devolatilization stage of the particle. The effect of fuel volatile matter content on the pyrolysis gas composition is studied using pine treated thermally at different degrees. Moreover, the effect of particle size on gas composition was studied by experimenting on two batches sieved thoroughly to obtain particles with a size of 400 µm in the first batch and 700 µm in the second one.

The reactor wall temperature was set to 800°C. 20 Nl/min of nitrogen is preheated to the wall temperature before introducing it to the furnace as sweeping gas. The solid fuel feed rate was 1 g/min transported by 2 Nl/min of primary nitrogen stream. Under these conditions, the gas residence time inside the furnace was estimated to be 2.8 sec. The gas was sampled at the exit of the reactor using well-sealed sampling bags after being filtered and dried, and then analyzed by a micro-GC to measure the pyrolysis gas composition.

The pyrolysis of biomass decomposes the lignocellulosic components into light gases, tar, pyrolytic water and char. Tar eventually breaks down into light hydrocarbons. The produced gas is mainly composed of CO, CO_2, H_2, CH_4 and a small proportion of light hydrocarbons such as C_2H_4, C_2H_6 etc.

V.2.1 Influence of fuel composition

The yields of the major constituents of the pyrolysis gas of Pine, Pin-T and DW at 800°C are presented in *Figure V.1*. Coal was also tested but showed small conversion. The higher moisture content in Pine (11.46%) and DW (6.32%) did not reduce the gas yield in front of the low moisture Pin-T. Indeed, an investigation on the fast pyrolysis of Pine with different moisture content in [104] concluded that the natural moisture has no influence on the amount and nature of the final pyrolysis gas.

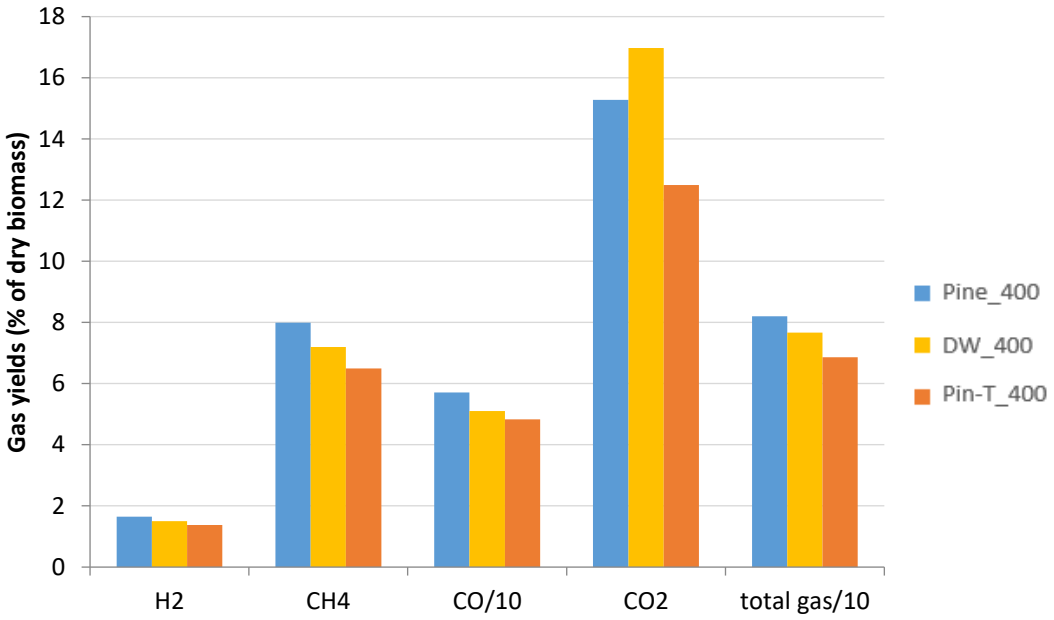

Figure V.1: Experimental pyrolysis yields: results on major gases (400 means 400 µm)

The fast pyrolysis at 800 °C produces mainly gas with char and pyrolytic water. Higher volatile content fuel ejects more volatiles during the experiment (Pine > DW > Pin-T) with higher CO, H_2 and CH_4 yields. CO_2 decreases with torrefaction whereas its reformation to CO was not favored in the case of DW probably due to high oxygen to carbon ratio. CO is quantified as the major part of the ejected gases followed by CO_2, CH_4 and H_2 respectively. µ-GC detected peaks corresponding for C_2H_2, C_2H_4 and C_2H_6 but they were too low to be quantified. Heavier hydrocarbons were not detected in the analysis possibly because of high heating rates, thus decreasing the stability of these intermediate species in the conversion pathway of volatiles. The polymerization and reformation of hydrocarbons lead to the formation of methane, hydrogen and soot. The reactions occurring at higher temperatures in the gas phase among the volatiles determine the final yields. This creates the temperature dependency of the gas compositions as verified in previous studies [103]. Therefore, the composition would be a bit different in an industrial furnace. CO_2 yield was reported to decrease with temperature to an invariable value at temperatures higher than 700 °C [197]. It has been highlighted by previous investigation [106] that CO_2 is active in the oxidation mechanism of hydrocarbons producing hydroxyl radicals. CO and H_2 increase with temperature as important products of the gas-phase reformation reactions. Methane decomposes through a complex mechanism, to reach ultimately the thermodynamic equilibrium composition at very high temperatures (> 1000°C) typically encountered in flames. An approximation of the equilibrium composition can be calculated, given the elemental composition of the fuel [105].

V.2.2 Influence of particle size

Residence time of biomass is high enough to allow a complete conversion of particles of 400 µm and 700 µm. The total gas yield decreases with larger particle size, which means that they yield more tar and char. The tendency is comprehensible, as larger particles need more time to undergo complete pyrolysis. The effect is especially noticed for demolition wood where gas yield decreases by 24%. This difference in demolition wood results is probably due to the

chemical heterogeneity of materials found in the feedstock. Larger particles composition may be different from smaller ones.

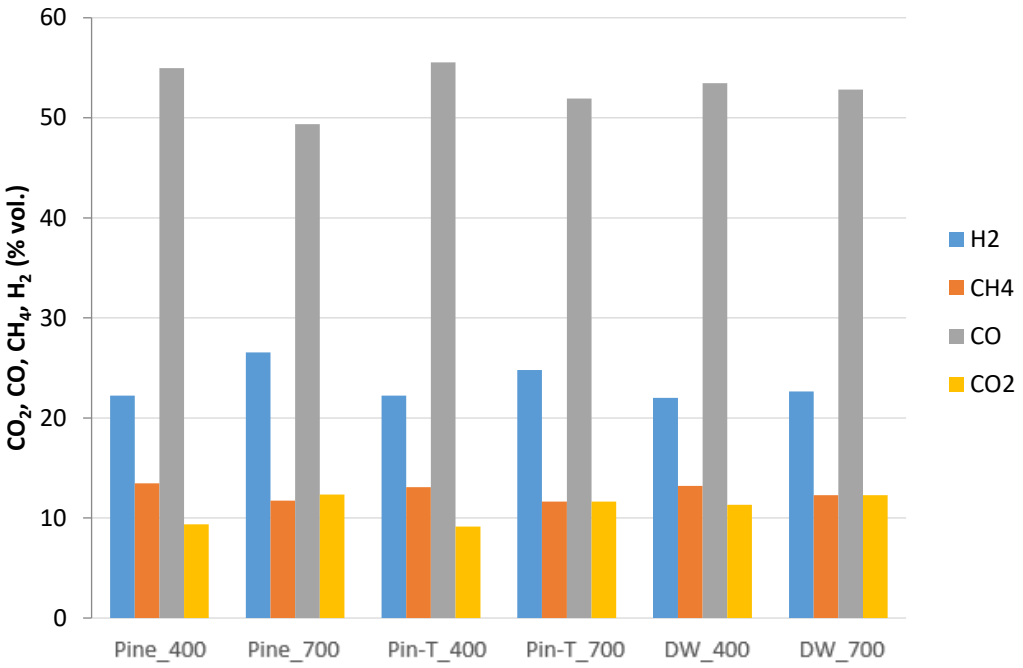

Figure V.2: Volatile composition of biomass pyrolysis products (400 and 700 means 400 µm and 700 µm)

	Pine_400	Pine700	Pin-T_400	Pin-T_700	DW_400	DW_700
LHV (MJ/kg)	14.35	13.75	14.28	13.63	13.79	13.38
Stoichiometric air-fuel ratio (kg Air/kg gas)	4.06	3.88	4.03	3.83	3.91	3.77
Density (STP) (kg/m³)	0.99	0.97	0.99	0.98	1.01	1.01
Gas constant (J/K.kg)	375.27	382.70	375.07	376.68	368.56	366.89

Table V.1: Physical properties of the gases produced during pyrolysis in the DTF of particles at 400 and 700 µm

The bar-diagram in *Figure V.2* shows the comparison of the composition of the pyrolysis gas of two particle sizes. *Table V.1* details the physical properties of the pyrolysis gases produced in the DTF. The volatiles from different fuels are produced in different quantities but the compositions of the gases are rather similar which explains the close physical properties. One can imagine that the primary cracking produced different gas compositions but the long residence time permits the secondary decomposition to bring the products to similar compositions. A similar lower heating value of the volatiles (13-14 MJ/kg) is found for all fuels, which falls in the typical range of the LHV of the pyrolysis gases at this temperature [49]. Slight decrease is noticed with larger particle size due to the higher CO_2/CO ratio. This lowers the required air to fuel ratio. Previous results in [105], [104] and [109] did not observe high influence of the particle size on the gas composition at temperatures higher than 900 °C. In our conditions, the difference is not very much pronounced. Nevertheless, we can identify a tendency to lower CO and CH_4 share accompanied with higher H_2 and CO_2 in the permanent gases of the coarser particles.

V.3 Combustion of biomass at low heating rate

V.3.1 TGA degradation curves and characteristic points

Figure V.3 and *Figure V.4* display the average profiles of conversion and the time derivative of the mass fraction of combustion of Pine, Pin-T, Pin-P, Pin-C, DW and coal in the macro-TGA (see Chapter II.2).

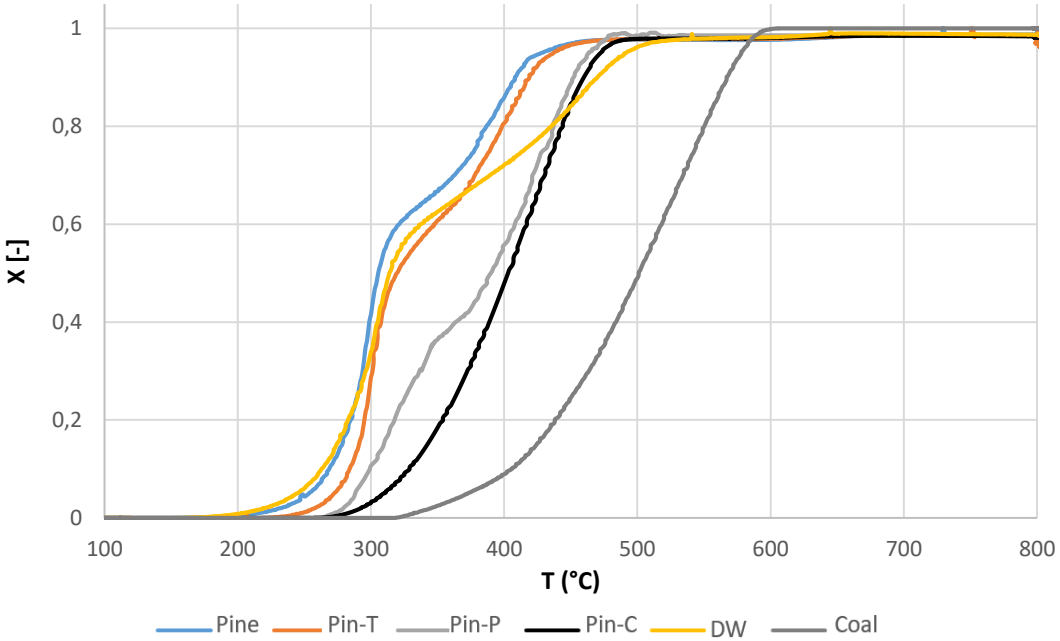

Figure V.3: Comparison of the conversion curves of the combustion of different fuels (10°C/min to 800°C with air)

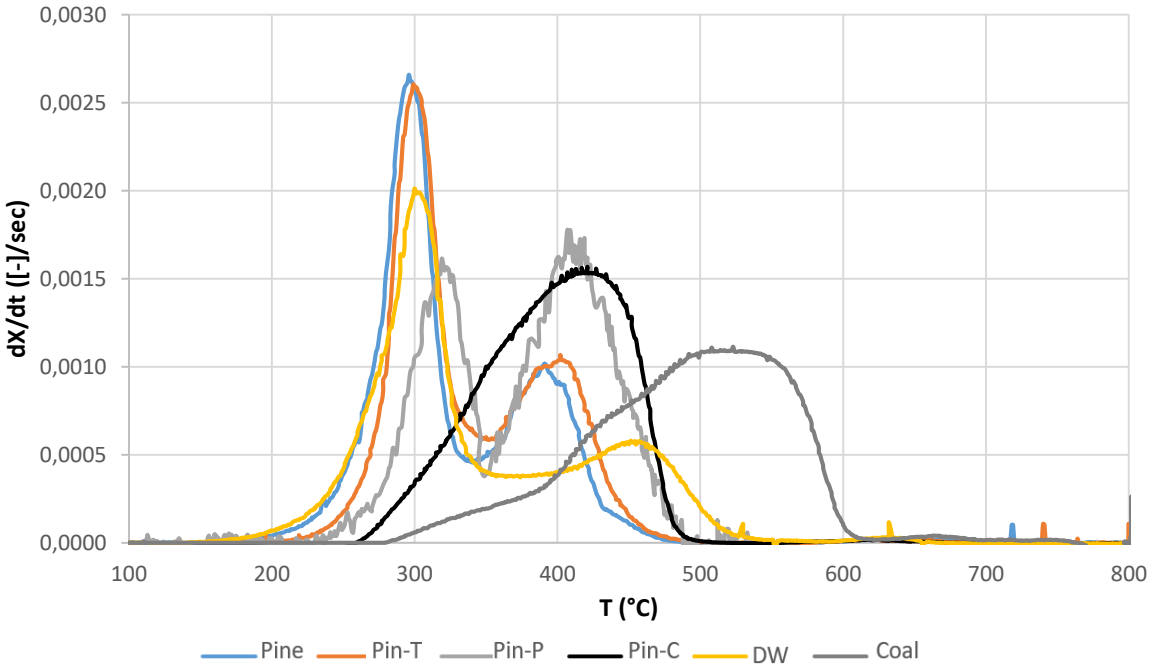

Figure V.4: Comparison of the time derivative of the mass fraction of the combustion of different fuels (10°C/min to 800°C with air)

Two peaks of first derivative are always observed for the different fuels (*Figure V.4*). The last peak is attributed to the char combustion usually at high temperatures. The devolatilization is

composed of a shoulder and a pronounced peak in the case of Pine and DW due to the degradation of hemicellulose and cellulose respectively. The shoulder disappears for Pin-T and Pin-P since hemicellulose is already released during the preparation step. With more severe preparation of Pin-C, the pronounced peak of devolatilization disappears and a shoulder appears instead, producing a coal-like profile at lower temperatures. In fact, cellulose also undergoes degradation during the thermal preparation to a certain degree depending on the process severity. With more cellulose released during the pretreatment, a lower degradation peak is obtained during devolatilization. This is obvious for Pin-P and Pin-C, while the lower pre-treatment temperature for Pin-T did not affect much the cellulose content so the difference with Pine is insignificant.

The degradation of coal occurs at higher temperature than that of biomass with only one pronounced peak. The difference emerges from chemical and structural differences with biomass. The rearrangement of carbon in a more stable form as well as the lower porosity in the material provide higher thermal stability for coal.

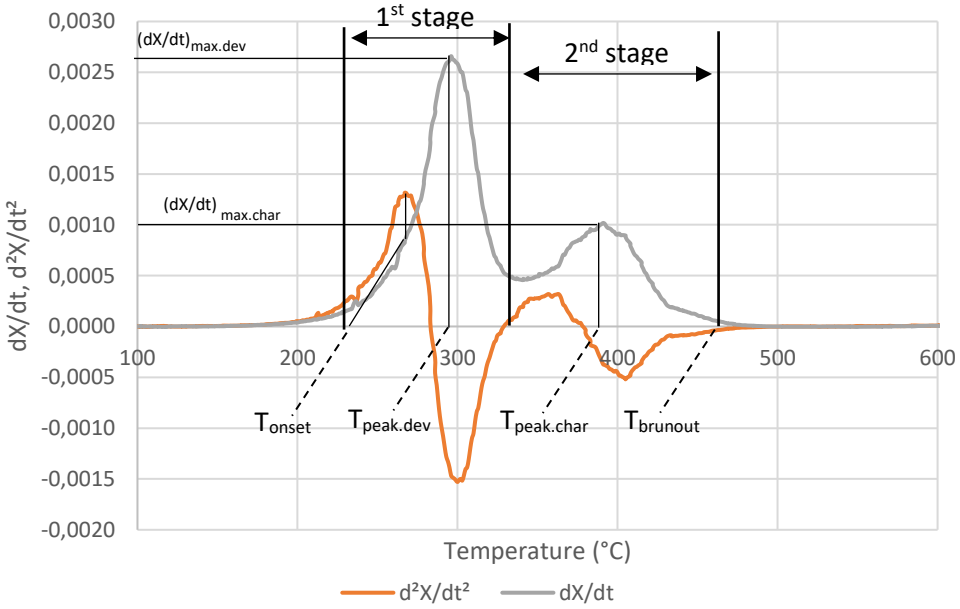

Figure V.5: First and second time derivatives of the mass fraction as functions of temperature for Pine and definitions of the characteristic reaction temperatures

	T_{onset}	$T_{peak.dev}$	$T_{peak.char}$	$T_{burnout}$	$\left(\frac{dX}{dt}\right)_{max,dev}$	$\left(\frac{dX}{dt}\right)_{max,char}$
Pine	230	296	391	453	0.00265	0.00101
Pin-T	241	299	403	459	0.0026	0.00106
Pin-P	259	315	416	483	0.00153	0.00151
Pin-C	275	-	421	496	-	0.00156
DW	209	300	453	522	0.00201	0.00056
Coal	349	-	523	597	-	0.00111

Table V.2: Characteristic reaction temperatures and degradation peaks of the tested samples

Figure V.4 shows the definition of the characteristic reaction temperatures defined in Chapter II. *Table V.2* lists the characteristic reaction temperatures and degradation peaks of the tested samples. The onset temperature of degradation of raw wood is 230°C. It gets closer to coal with higher torrefaction degree producing lower devolatilization peak and higher char consumption peak. In addition, the peaks shift to higher temperatures in both stages for the pretreated fuel with respect to the raw counterpart. This means that the presence of volatile matter promotes the reactivity of the biomass. Demolition wood can be distinguished from Pine by a smooth combustion in both combustion phases with low conversion peaks. The devolatilization and char oxidation peaks are more separated compared to the other fuels. This may be ascribed to the catalytic effect of ash present in demolition wood [94]. The delayed char combustion peak also can be due to high lignin content, which can be concluded from the relatively low peak intensity corresponding to the conversion of cellulose and hemicellulose content. Lignin is the most stable constituent of the biomass and its degradation takes place along a wide temperature range. For this reason, demolition wood burns over the widest temperature range among the other fuels.

V.3.2 Kinetic parameters at low heating rate

Table V.3 shows the kinetic parameters of the fuels obtained by direct method with the corresponding correlation coefficients R^2 of the best-fit regression. In order to extract the kinetic parameters of devolatilization and char oxidation from the TGA combustion curves, the model is applied for the temperature range where the main weight loss occurred was due to oxidation and removal of the volatile matters of the samples, and then to the second range where remaining char oxidation takes place. This method has been applied in several works [46], [198]–[202]. The temperature ranges are illustrated in *Figure V.5*. The first stage starts at the onset temperature and ends at the local minimum of the first derivative, which is assumed as a transition between the devolatilization and char oxidation ($d^2X/dt^2=0$). Except for Pin-C, the transition is assumed at the shoulder temperature where the second derivative approaches zero. The second stage starts at this temperature and continues to the burnout.

	First stage				Second stage			
fuel	**Temperature range (°C)**	**A (1/sec)**	**E (kJ/mol)**	**R^2**	**Temperature range (°C)**	**A (1/sec)**	**E (kJ/mol)**	**R^2**
Pine	230-344	$4.64 .10^{+07}$	112.79	0.988	344-453	$1.25 .10^{+02}$	42.63	0.962
Pin-T	241-348	$4.23 .10^{+07}$	113.89	0.983	348-459	$2.21 .10^{+02}$	47.60	0.993
Pin-P	259-351	$2.81 .10^{+08}$	128.00	0.935	351-483	$1.13 .10^{+02}$	58.95	0.972
Pin-C	275-364	$5.73 .10^{+04}$	91.93	0.945	343-496	$7.32 .10^{+03}$	81.95	0.975
DW	209-343	$1.39 .10^{+04}$	75.32	0.985	364-522	$1.04 .10^{+01}$	33.63	0.980

Table V.3: kinetic parameters of the fuels obtained by direct method for devolatilization (first stage) and char oxidation (second stage)

The literature offers a wide range of activation energies of devolatilization and char oxidation for the same fuel types. For Pine, it has been found as low as 22 kJ/mol [203] and high in the order of 200 kJ/mol [198], [204], [205]. The variation results from the kinetic model and the temperature range used for the regression, besides other influencing factors including the pyrolysis and combustion techniques. The torrefaction of biomass increases the activation energy obtained for the first and second stage. Higher activation energy means slower apparent reactivity and higher thermal stability. Only Pin-C stands odd to the activation energy trends.

However, this is compensated by strongly inversing the frequency factor trends, so that a slow conversion is calculated as a result. DW is the most reactive in the first zone given its early degradation compared to other fuels. However, despite the low activation energy for DW in the second temperature range, its low frequency factor translates to slow combustion process.

V.4 Composition of the combustion gas

The composition analysis of the evolution of the combustion products was performed in the HTR (see Chapter II.3). Several tests were performed at different flow rates until satisfactory combustion conditions are attained. The main criteria were

- Avoid oxygen deficiency (concentration close to 0% vol.) during combustion,
- A peak concentration of CO less than 0.1% vol. in order to avoid the saturation and damaging the CO cellule,
- Limiting the flow rate to the pick-up velocity of the solid matter, this was verified at room temperature.

These conditions were reached for a flow rate of 3.65 Nl/min of air, chosen so that oxygen is in large excess. Considering that the combustion gases are at 800°C, their residence time, from the point of insertion of the crucible to the outlet of the reactor, is then about 3,8 s which is sufficient for secondary cracking to take place. The value calculated for the Reynolds number in the 5 cm diameter tubular reactor at 800°C is 30, which indicates a laminar flow regime of the combustion gases.

V.4.1 Typical gas temporal emissions during combustion

Figure V.6 shows the temporal profiles of O_2, CO_2, CO and NO emissions during the combustion of maritime pine. This combustion behavior is reported for Pine only as a typical profile [59], [206]–[208].

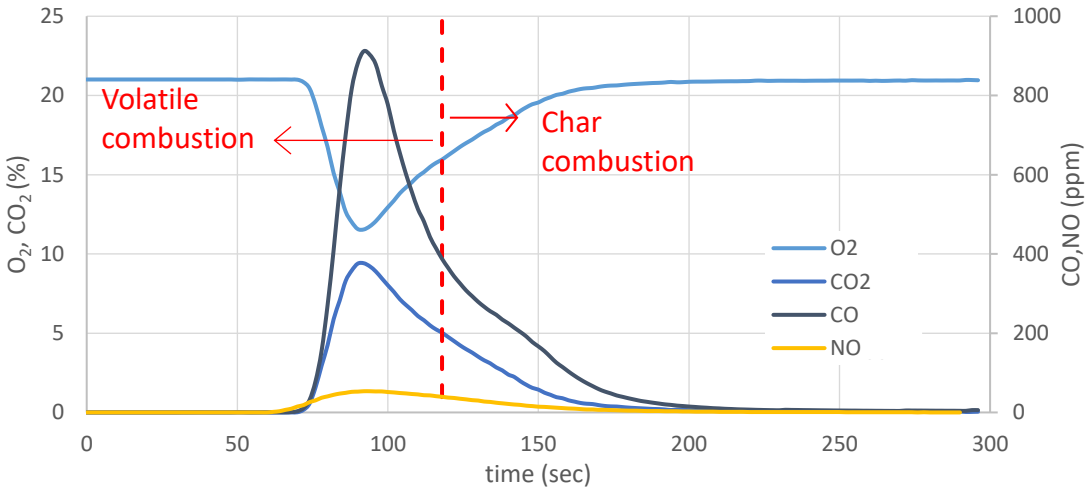

Figure V.6: Pine combustion temporal emission curves in HTR at 800°C

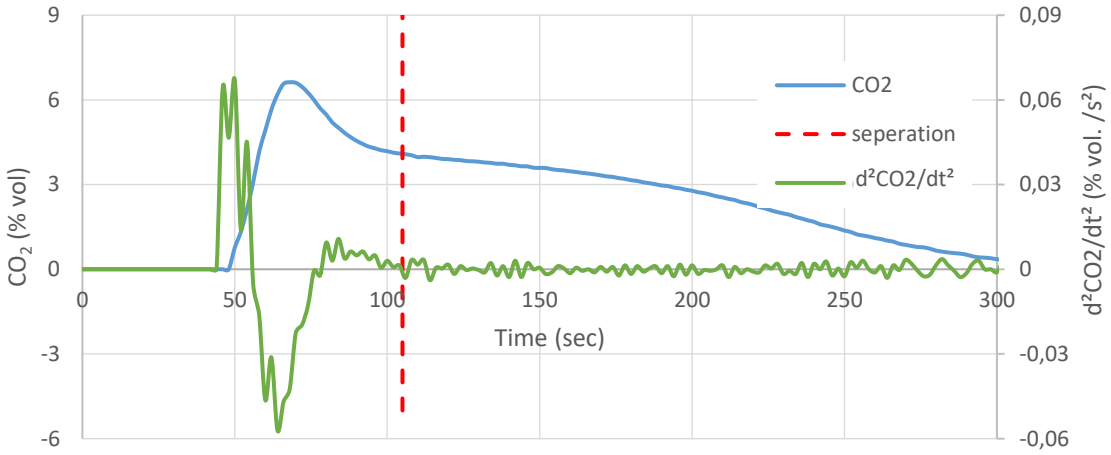

Figure V.7: Criterion of separation of combustion phases

The temperature rise of the fuel sample results in the release of the volatiles that are directly oxidized leading to the peak of oxygen consumption and consequently to CO_2, CO and NO peaks. Char combustion starts at higher temperature as seen in the TGA curves. Generally, the homogeneous combustion of volatile matter and the heterogeneous combustion of char may occur simultaneously with an overlap between the two stages [206]. No clear distinction can be done for the two stages. The only criterion found in literature is based on the transition of CO_2 release curve [54]. CO_2 increases to reach a peak during the volatile combustion phase, where emitted hydrocarbons and CO are oxidized, and then decreases until a point where it decreases linearly during the char combustion. The separation between the two phases is attributed to the moment when the second derivative of CO_2 becomes zero (<0.0001 %vol. /sec²) (*Figure V.7*). Note that this separation distinguishes the major contributions from one phase or the other and neglects the overlap.

V.4.2 Oxygen consumption

Figure V.8 presents the oxygen concentration profiles in HTR at 800°C during time of six fuel types with their relative separation moments between both combustion stages. The onset of the observed phenomena will not be discussed. Rather, the analysis compare the general behavior of the emissions of the fuel types. For better comparison, the curves are put together so that their peaks coincide at the same moment. Oxygen concentration peaks, as well as CO_2 curves, are approximately similar for Pine, Pin-T and DW with slightly higher oxygen consumption for torrefied pine accompanied with higher CO_2 release. On the other hand, the emission curves are approximately similar for Pin-P, Pin-C and coal with low consumption peak during devolatilization and long heterogeneous combustion duration. The combustion behavior of coal is different from that of raw and moderately treated biomass, which reflects the huge difference in fuel characteristics. Moreover, it seems that torrefaction shifts the combustion behavior towards that of coal with longer combustion time and more oxygen consumption during the second stage. Accordingly, it might be useful to think of biochars, including Pin-P and Pin-C, as coal-like fuels rather than biomass fuels.

Moreover, one can notice that the devolatilization duration does not change dramatically with different volatile content. Close durations are observed for Pine, Pin-T and DW while slightly shorter durations are recorded for biochars (Pin-P and Pin-C). However, the difference is insignificant considering the huge difference in the released volatile content. Pyrolysis

experiments conducted previously in the HTR (under nitrogen atmosphere) resulted in the release of 0.82 gram of volatiles (tar + gas) for a gram of Pine while for Pin-T, Pin-P and DW the measured value is 0.76, 0.45, 0.78 g/g of biomass, respectively.

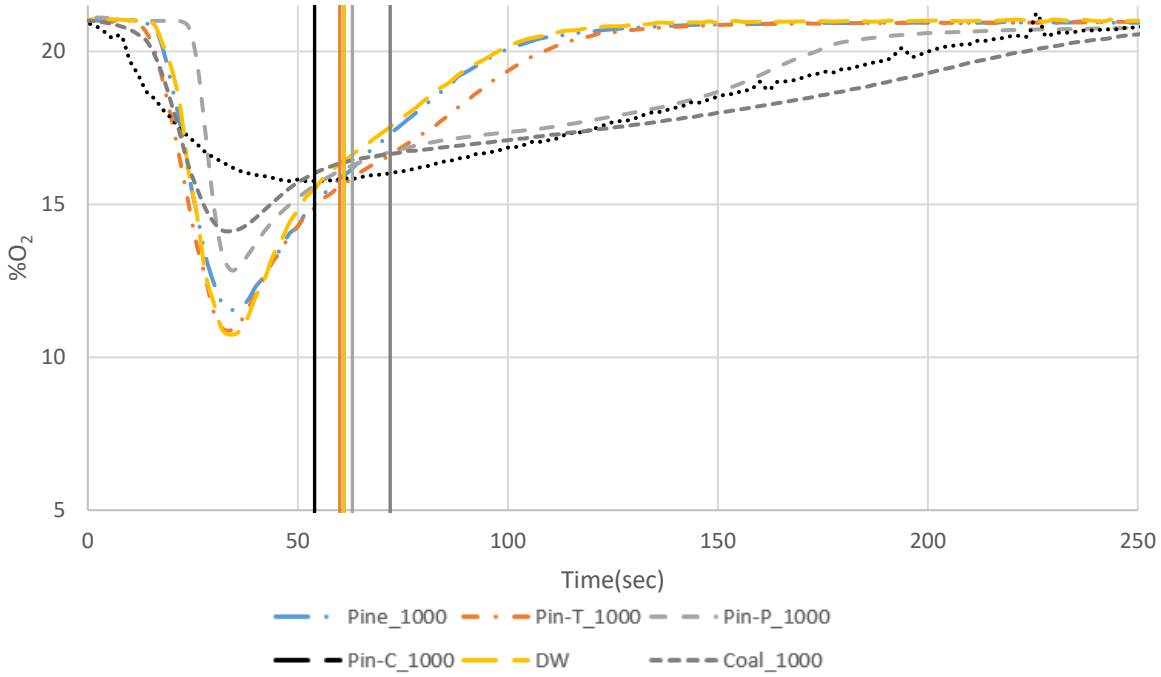

Figure V.8: Comparison of temporal O_2 concentration in HTR at 800°C

Hence, larger amount of volatiles are emitted from Pine during comparable devolatilization times compared to the other fuels. This means that the corresponding flames last similarly but with higher flame intensity and higher oxygen consumption as the volatile content increases. This conclusion has implications also on char oxidation efficiency as well. The intense release of gases may leave behind a more exposed active surface area in the char, increasing its reactivity. P. McNamee et al. [27] reported that the chars produced at high heating rates (like Pine and DW chars) suffer from notable changes in their structure, due to the formation of new passages for volatile matter release. On the other hand, treated biomasses including Pin-T, Pin-P and Pin-C are produced at low heating rates, so they already have increased porosity during preparation. This allows volatiles to flow easily out of the particle during combustion and their chars present high similarity to their original particles.

V.4.3 Carbon conversion

Figure V.9 shows the conversion of carbon in HTR at 800°C. The carbon, initially contained in fuels is converted to CO and CO_2 for the tested fuels in two sizes: 500 µm and 1000 µm. Carbon in biomass (fuel-C) is in two types: volatile carbon (volatile-C), which is oxidized in the gas phase and fixed carbon (FC), which forms the char and oxidizes heterogeneously.

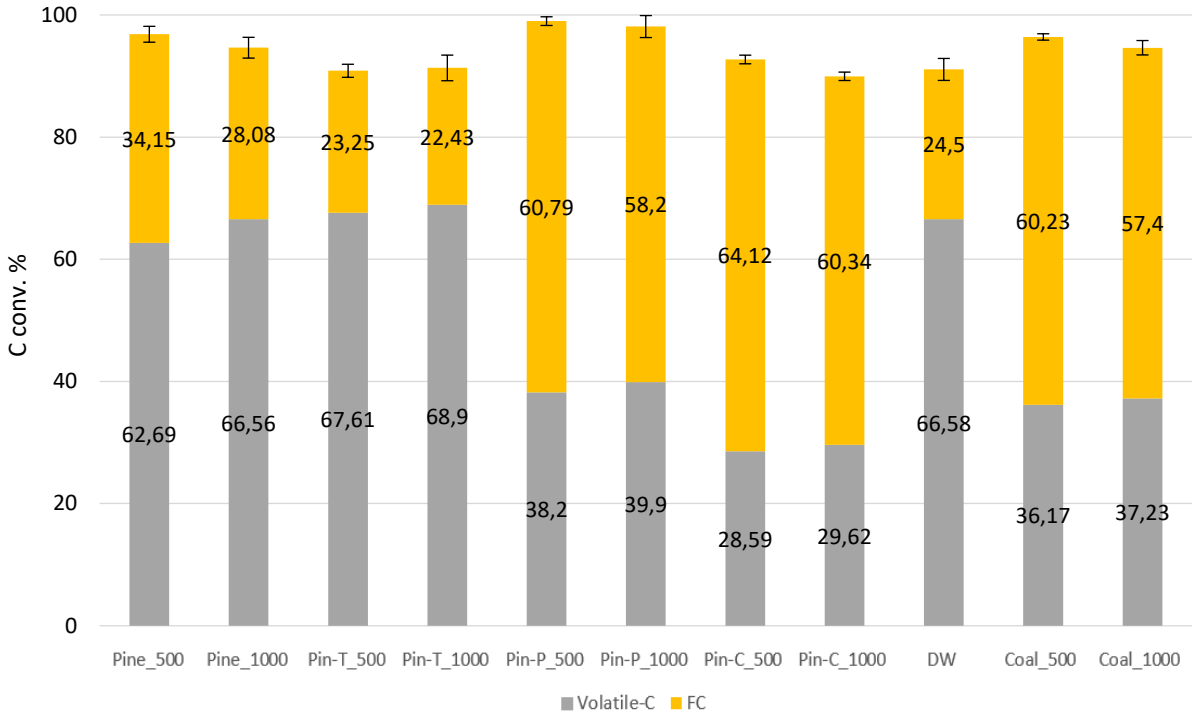

Figure V.9: Char (FC) and volatile (Volatile-C) carbon conversion to CO and CO_2 during two combustion stages for different biomass sizes (500 µm and 1000 µm) in HTR at 800°C

Comparable fuel-C conversion is measured for Pine, Pin-T and DW during the devolatilization stage. Given more carbon in the volatiles with higher VM content, the volatile-C is less converted for Pine, DW and Pin-T respectively. This can be attributed to the similar durations of volatile combustion. However, the total fuel-C conversion for higher VM content fuels is compensated during char combustion, which is promoted by higher active surface area. Pin-P has the highest total fuel-C conversion. This could be attributed not only to its high porosity produced during torrefaction, but also to the role of volatile content promoting the carbon conversion in both combustion stages. Pin-C for instance, is exposed to a more severe torrefaction, yet it has lower fuel-C conversion due to the very low volatile content.

On the other hand, the results verify that the size of the particles influence the combustion process. Larger particles limit the heat and mass transfer with respect to smaller particles. This is confirmed when comparing the fuel-C conversion of the same fuel type with two different sizes. 500 µm fuels show higher fuel-C conversion compared to larger particles.

V.4.4 Nitrogen conversion

Thermal and prompt NOx formation is not likely to contribute to NO production at relatively low temperatures (<1000 °C). Hence, NO released during the combustion of the samples is produced from the oxidation of fuel nitrogen. NO_2 was also measured and it is typically below 10 ppm for the entire experimental duration so it was considered negligible.

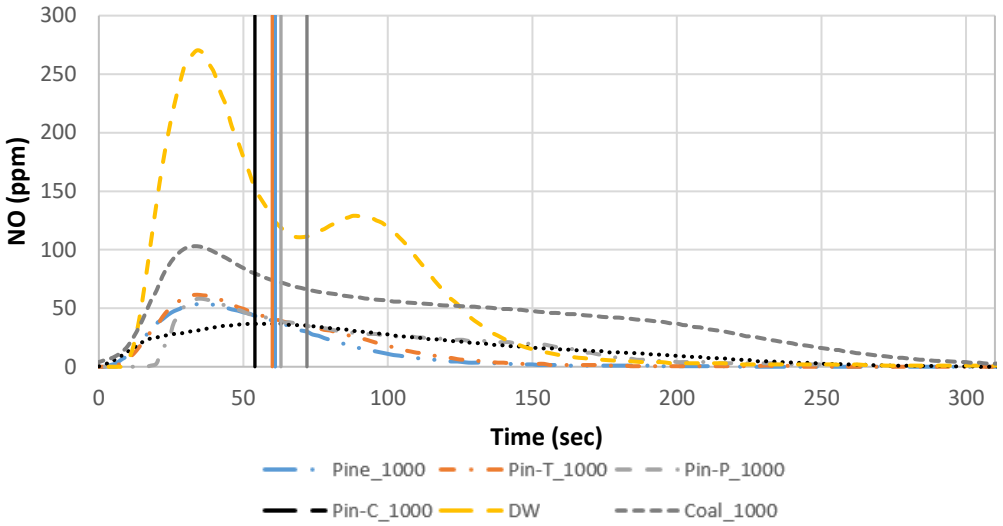

Figure V.10: NO temporal release profiles in HTR at 800°C

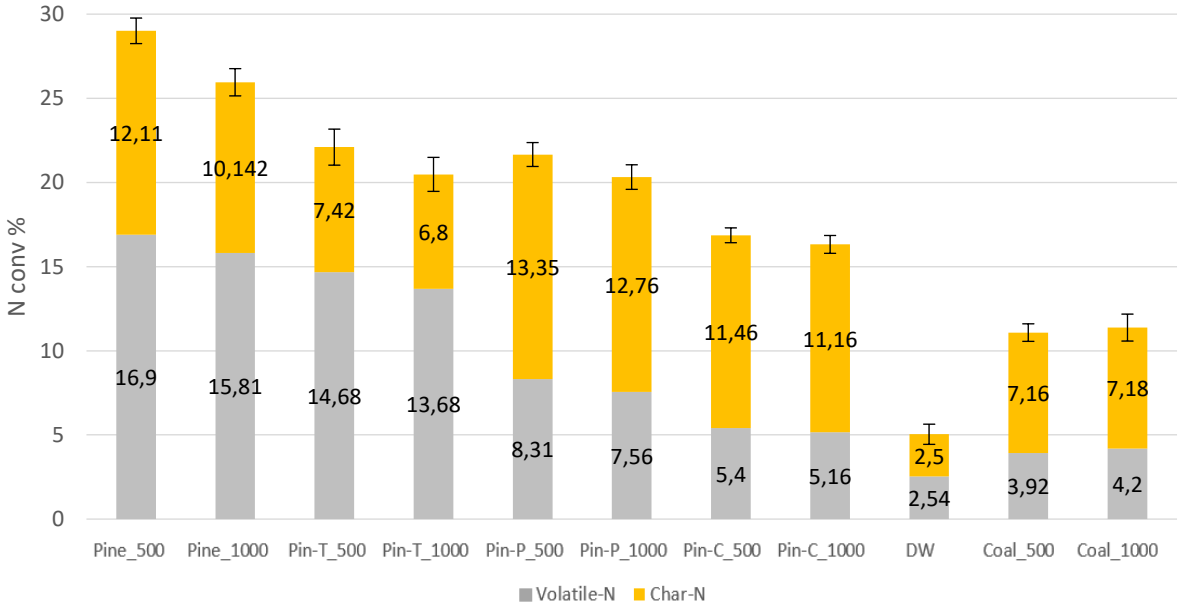

Figure V.11: Char (Char-N) and volatile (Volatile-N) nitrogen conversion to NO during two combustion stages for different biomass sizes (500 µm and 1000 µm) in HTR at 800°C

Figure V.10 presents the NO release profiles during the combustion for the tested fuels. The figure shows the corresponding separation lines of the two combustion stages. The contribution of devolatilization stage (Volatile-N) is considered up to the separation lines. NO released afterwards are the contribution of the char combustion stage (Char-N). Fuel-N conversion to NO is identical to that of fuel-C to CO and CO_2. NO concentration increased rapidly during the flash pyrolysis to a peak point and then decreases to a much slower production rate during the char combustion. Larger amount of NO is released from the combustion of demolition wood with a second peak corresponding to char combustion. Such peaks are reported for other biomasses [54] and it was also observed in the CO emission curves. Demolition wood is followed by coal, Pin-C, Pin-P, Pin-T and Pine respectively matching their N-content arrangement.

Figure V.11 presents the fuel nitrogen conversion to NO during both combustion stages for different fuel sizes (500 µm and 1000 µm). In contrast to C-conversion, higher Volatile-N

conversion during the devolatilization phase is measured for small particles than large ones, as well as during the char-oxidation phase. Pine, Pin-T and DW exhibit higher N-NO conversion during devolatilization than char combustion. On the other hand, coal and biochars (Pin-P and Pin-C) seem to concentrate nitrogen in the char, which has a negative effect on NO formation [64]. Moreover, fuels with higher nitrogen content convert a lower fraction of it to NO. This trend can be explained by the NO reduction mechanisms taking place during the process. In fact, high concentrations of NHi radicals are usually released from the pyrolysis of fuels with high N content, which would enhance the reduction mechanism [61].

V.5 Direct observations of the combustion of a particle

The single particle reactor gave access to the direct observation of the combustion of a particle (see Chapter 2: Particle combustion shadowgraphy (PCS)). Typical particles used for the tests are shown in *Figure V.12*. Their size is in the range 500 and 1500 µm possessing different aspect ratios and their mass is up to maximum 3 mg. Pine particles are mostly flake-like while Pin-T, Pin-P and Coal are between cylindrical and spherical particles. DW particles are mostly thick flakes made of small compressed fragments of wood and other impurities like paint, giving it a brittle nature. Besides, totally carbonized pine (VM~=0) was tested aiming to study the influence of the presence of volatiles.

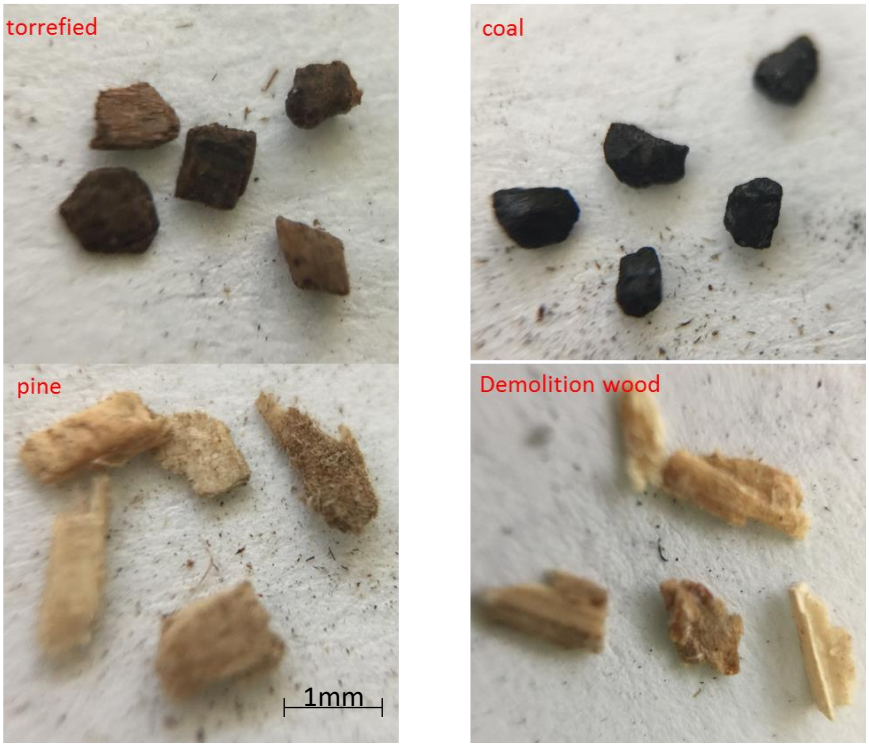

Figure V.12: Typical tested fuel particles

The samples are dried for 24 hours at 105°C before every experiment considering the high variation in moisture content (Pin-C: 13%, Pin-T: 1.9%), which can strongly influence the particles behavior and ignition delay. The particle-to-particle variations are expected to be important, for raw biomass and for the thermally treated samples because of natural heterogeneities in feedstock. This is evident from the color difference among the particles of torrefied and char Pine. For this reason, a high number of particles were tested to take into account the deviations and determine better the trends and average values.

V.5.1 Typical particle behavior

Thanks to this direct visualization technique, a general trend of particle behavior can be observed for biomass. *Figure V.13* presents a typical size evolution of a biomass particle with time (at 800°C). *Figure V.14* captures the timeline of the combustion events of a particle.

After its insertion into the hot zone of the reactor, a series of events is triggered:

- The particle swells at the beginning of devolatilization due to the increasing pressure of volatiles inside it. It can be noticed before the flame ignition in *Figure V.13*. The swelling depends on the biomass type (Pine> Pin-T>>Pin-P).
- The swelling is followed by a flame accompanied by rapid decrease in particle size. This signifies the liberation of volatile matter that rapidly reacts to produce the flame for a certain time depending on the amount of volatiles contained within the particle. Larger particles with a flame that lasts for a long time. The flame intensity and size increases with time and then shrinks back until its extinction.
- Around 40% of the initial projected area is lost during this step, which corresponds to volume loss due to volatile matter release.
- Particle consumption rate slows down after the flame extinguishes.

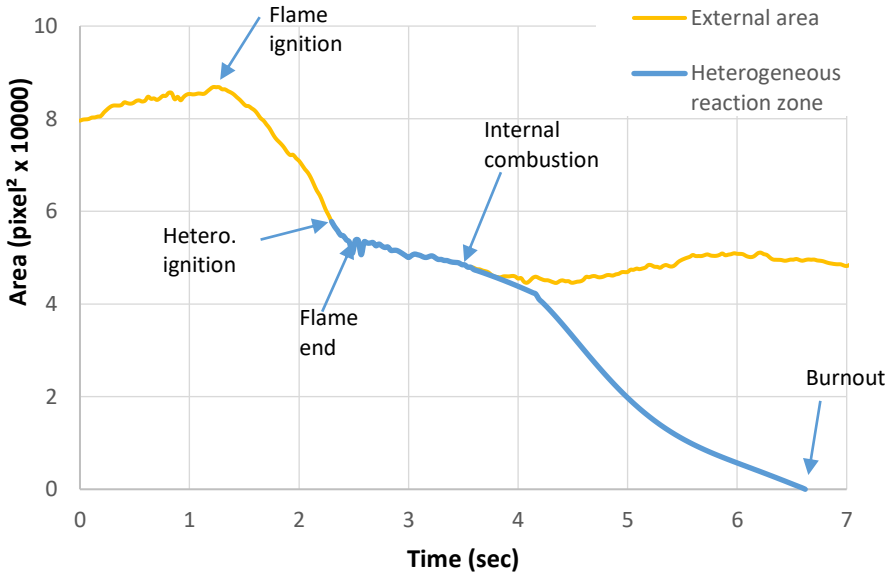

Figure V.13: Typical size evolution of biomass with time in PCS at 800°C

- The char becomes bright glowing red by the effect of carbon oxidation. At first, the particle shrinks with the luminous region signifying the oxidation at the surface of the particle.
- A point of separation between the reaction zone (bright zone) and the external area is detected (denoted as reaction zone shrinks in *Figure V.14*) in all cases except for DW. The bright zone continues to travel inside the particle (internal combustion) leaving a

dark zone behind until the complete burnout. The evolution curve in *Figure V.13* follows the bright zone that separates at a certain moment from the external area curve.

- The result is a hollow particle of ash that swells sometimes at the end. Fragmentation of the particle and even the ash matrix is sometimes observed especially for DW.

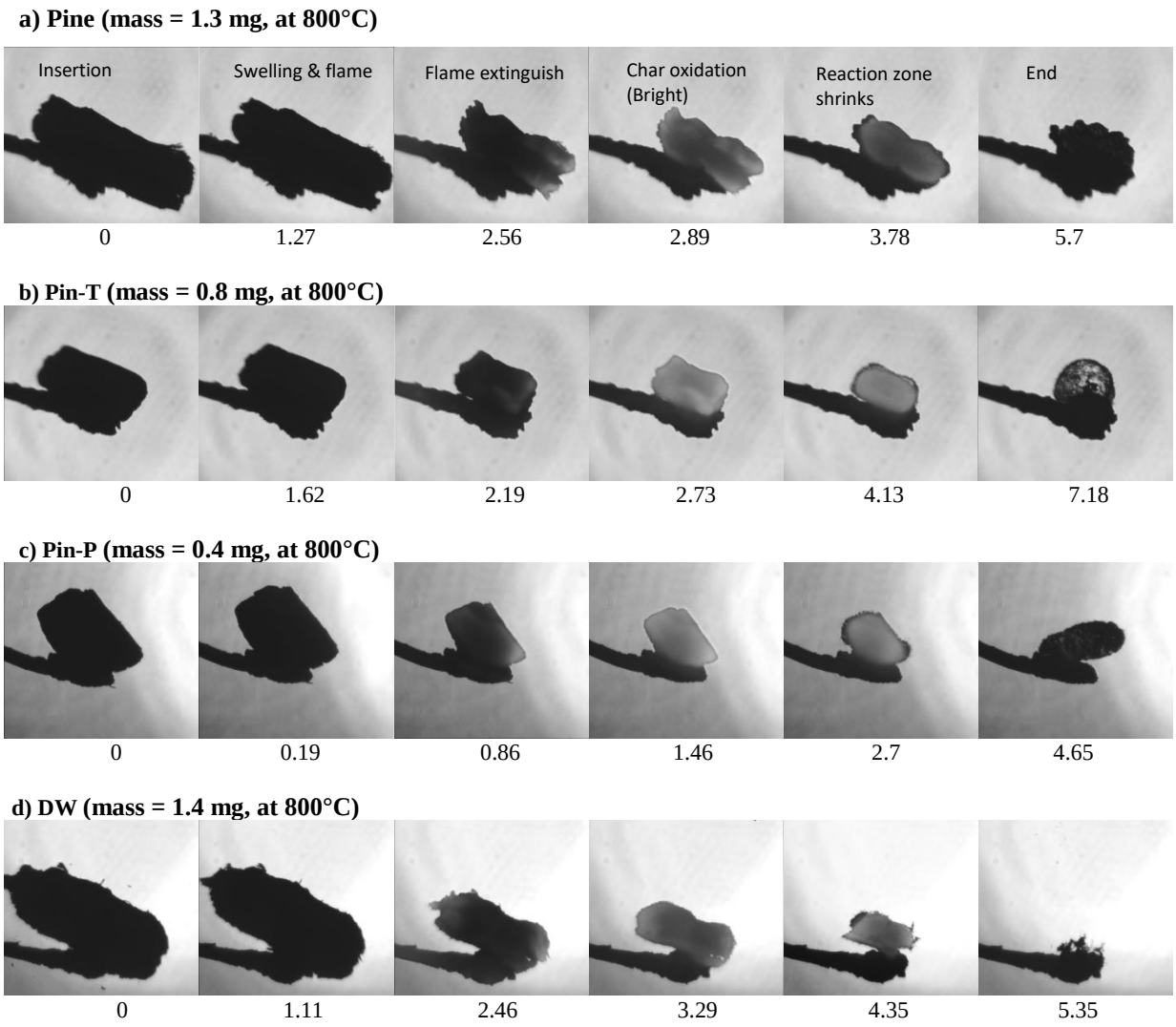

Figure V.14: High magnification images of the combustion of single particles of raw pine, first and second torrefied pine and demolition wood in PCS at 800°C. The displayed number in each frame is the time (sec) passed from the insertion moment

It is important to note that the bright zone travels in an isotropic manner in all directions. This property was discovered by accident when some particles flipped unintentionally during the char combustion.

V.5.2 Temperature-time history of biomass particles

Similar to area evolution, a trend of temperature profile is observed for biomass during their burnout. The temperature variation was measured using a 250 µm thermocouple in continuous contact with the particle. *Figure V.15* demonstrates the measured temperature and its derivative (calculated dT/dt) with time which is proportional to the energy balance of the particle. The insertion is at t=0.

The temperature derivative peaks at three events:

1. Upon insertion and rapid heating
2. Maximum flame size (denoted as Flame max)
3. Flame extinguish

The flame was detected visually in the two videos, when the volatile cloud around the particle is lit, and by the sudden increase in the surface temperature profile giving the ignition temperature. The second peak corresponds to the devolatilization peak where dT decreases afterwards due to lower volatile emission rate. This is also obtained in the DTG curves with the mass degradation peak and in the HTR emission curves with the oxygen consumption peak.

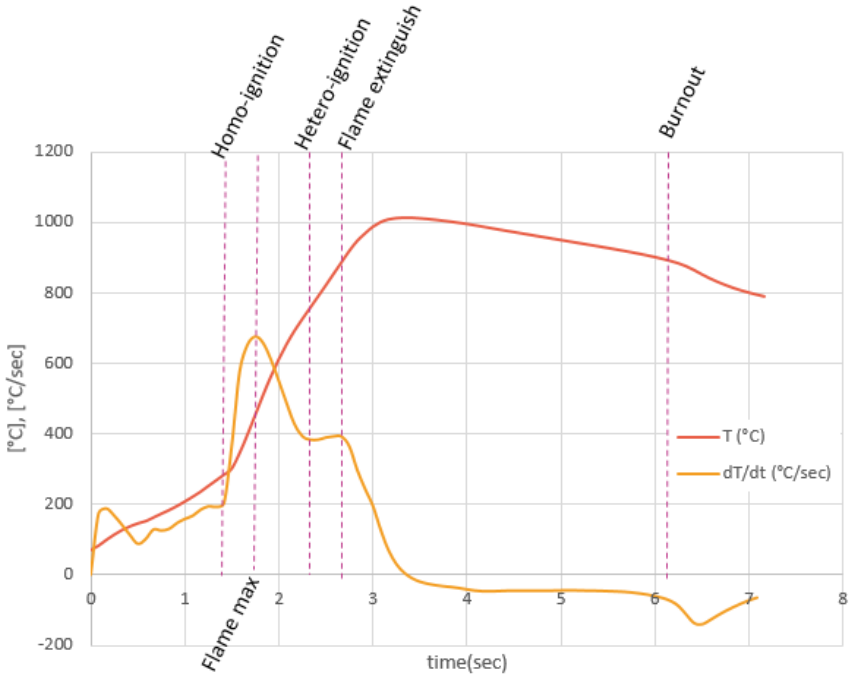

Figure V.15: Temperature variation of biomass particle during combustion in PCS at 800°C

Results in *Figure V.16* show that the peak value declines along with an increasing particle mass, which means that the volatile ejection is less intense. dT reduction reaches a local minimum, which coincides with the heterogeneous ignition detected by the previously mentioned technique. The char combustion heats the particle without losing heat to the high temperature surrounding flame. Once the volatile flame quenches, the particle starts losing heat, whence the second chute. This peak is attributed to the flame extinction. Sometimes a shorter overlap between the volatile and char combustion makes this peak less pronounced (more like a shoulder).

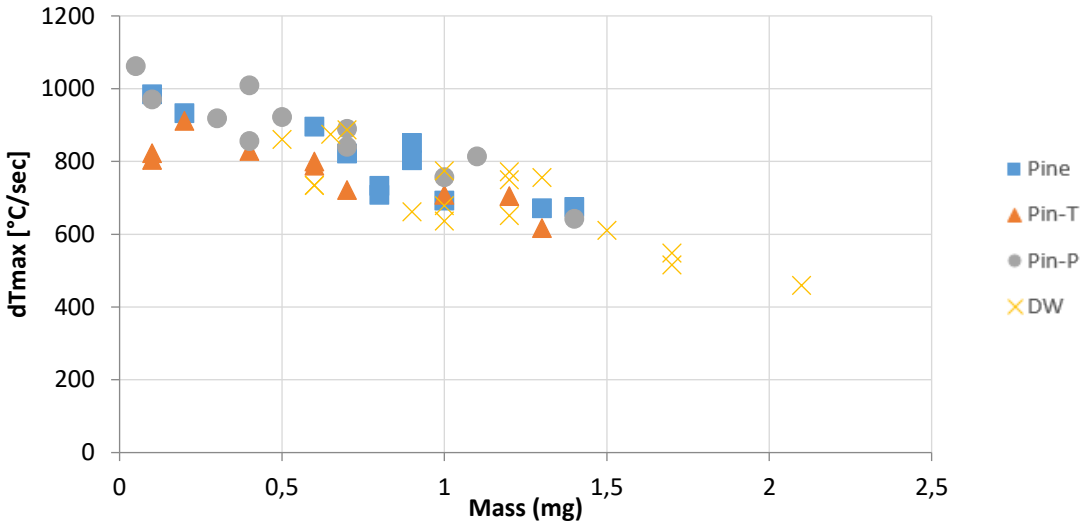

Figure V.16: dT peak upon flame ignition in PCS at 800°C versus the mass of the particle

A significant difference between the wall and particle temperatures reverses the heat flow direction after the particle reaches its maximum temperature. Subsequently, a balance is established between the energy production and loss until the complete burnout, which is characterized by a third chute with no more energy production. The temperature then stabilizes at the chamber temperature (800°C).

V.5.3 Ignition delay

The ignition of biomass particles is in general initiated in the gas phase. The combustion reaction is activated when the volatile cloud around the particle acquires sufficient energy and flammable concentration. The two entities are properties of the volatile gas composition and the heat capacity of the surrounding gas [209]. The devolatilization commences early and it can be detected in the shadowgraph videos by the sudden decrease in the particle volume after building internal pressure. The delay between the release of volatiles and their ignition is so short that they appear simultaneous at 37 frame/sec. The ignition delay is defined by the time needed to have a rapid temperature rise after the insertion of the particle.

Fuel	Pine	Pin-T	Pin-P	Pin-C	DW
Ignition temperature (°C)	240 ± 11	290 ± 22	220 ± 26	346 ± 14	258 ± 41

Table V.4: Ignition temperature of the tested fuels as measured by the PCS

The ignition temperature of the tested fuel as measured by the PCS are listed in *Table V.4*. The ignition temperature of raw pine is 240°C (±11°C), which is close to the temperature reported in [212] for beech wood (235°C). Demolition wood ignites at around 258°C with high disparities (±41°C) due to the presence of impurities and high particle-to-particle variations. Torrefied pine flame appeared at 290°C (±22°C) due to lower volatile concentration. Yet, Pin-P ignites even before raw pine at 220°C (±26°C) where the ignition is dominated by the higher porosity and improved reactivity of Pin-P. The release of pyrolytic water during torrefaction and the significantly lower density may also have a role in the improving ignitability of the Pin-P volatiles. In all cases, the presence of volatiles facilitates the ignition at relatively low

temperatures while the heterogeneous ignition of carbonized pine is delayed until the particle reaches 346°C (±14°C).

Previous investigations pointed out that the ignition delay increased with the increase of the initial particle density and diameter [210]. This is confirmed in our experiments. On the other hand, Pin-T ignites at higher temperature than Pine in contrast to what has been reported in [213], [214] that the improved hydrophobicity of torrefied fuel generally reduces its ignition delay compared to high moisture raw counterpart. However, in the current study, the fuels were dried before the experiments, so the influence of moisture is eliminated and the conclusions are purely based on the particle properties. On the other hand, Li et al. [211] found that torrefied softwood was faster to ignite than raw softwood at high heating rates, whenever the ignition mechanism changes from homogenous to heterogeneous ignition promoted by higher char reactivity of torrefied biomass. In addition, at high heating rates, the volatiles are easily driven out of high porous particles with barely any swelling detected as in the case for Pin-P, while the swelling of raw particles implies that the volatile release is delayed until acquiring sufficient pressure to be liberated from the particle.

V.5.4 Combustion timeline durations

Particle characteristics like mass, size, temperature and composition have an impact on the flame intensity, size and duration, and influence the delivery and consumption of oxygen at the particle surface during the char oxidation.

V.5.4.1 Volatile flame duration

Figure V.17 plots the flame duration as a function of the particle mass. The trend is logical since more volatiles require more time to be released from particles and burn [215]. Beside, bigger particle's temperature rises slower than finer particle's at the same heating conditions. This slows down the devolatilization rate as verified by the dT peaks in *Figure V.16*. However, little to no difference is detected between the flame durations of different fuel types. Only, Pin-P flame duration appears shorter than the other flames due to relatively poor volatile content. The same conclusion is found by the HTR results.

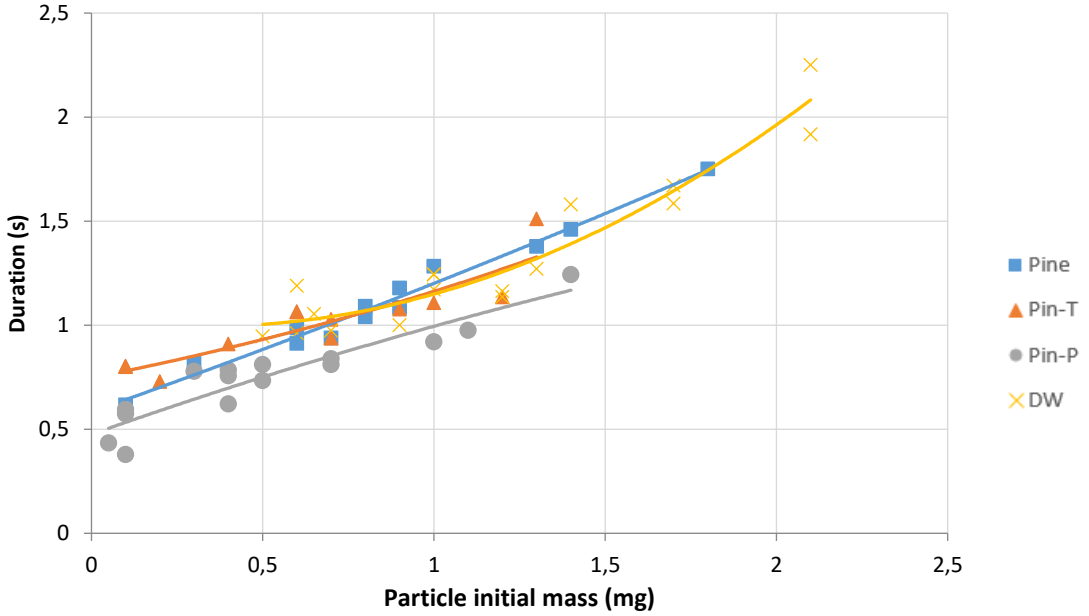

Figure V.17: Volatile combustion duration in PCS at 800°C

Akinrinola et al. [214] reported a similar result of close flame duration for raw and torrefied Nigerian biomass. A possible explanation is the increasing influence of the catalytic metals in the fuels. It is also possible that the new pores created during torrefaction facilitate the emission of volatiles and as mentioned earlier, this assisted the early ignition of Pin-P. In this case, the emission of volatiles is slower for the treated biomass, which elongates the emission time for the same amount of volatiles in their raw counterparts.

V.5.4.2 Homo-hetero combustion overlap

The overlap of flame combustion and char combustion is plotted in *Figure V.18*. Note that the points only correspond to the particles for which the heterogeneous ignition coincides with the local minimum in the temperature derivative curve. The difference between the brightness detection and the local minimum for some particles may be addressed by the fact that the ignition may be triggered from the non-visible side of the particle so that the minimum appears earlier than predicted by the luminosity of the rear view.

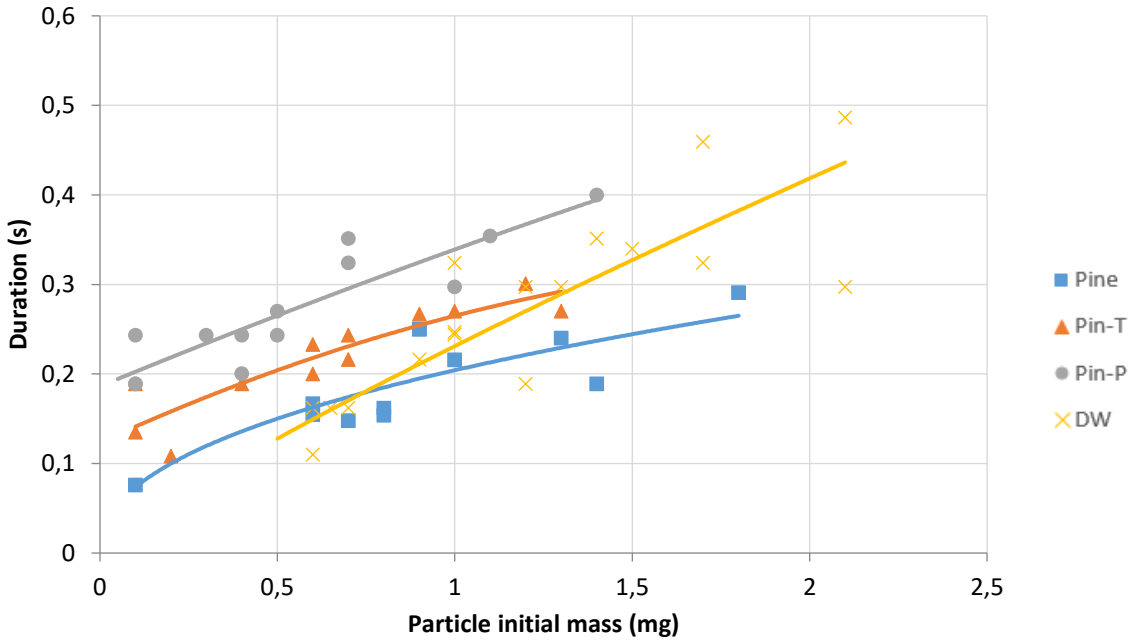

Figure V.18: Homo-hetero overlap in PCS at 800°C

The heterogeneous ignition occurs earlier for larger particles containing lower volatile content, and thus increases the overlap duration. Torrefaction of pine induces an increase of overlap duration. The maximum overlap among the pine-derived fuels was obtained for Pin-P with 0.4 sec for a 1.4 mg particle. On the other hand, a 0.1 mg Pine particle had the minimum overlap of 0.076 s. When the particle is surrounded by flame, the temperature is high enough for the heterogeneous ignition to happen. The heterogeneous ignition of carbonized pine starts at significantly lower temperatures. Nonetheless, the lack of oxygen at the surface induces a delay in the ignition. This may occur early for a particle in a free stream where the motion of the irregularly shaped particle exposes an edge to the hot stream out of the spherical flame envelope. Mock et al. [23] in these conditions observed overlap taking place in the last 40% of the flame duration for coffee waste and sewage sludge particles (150-215 µm). On the other hand, the more spherical obtained from treated wood experienced a relatively short overlap (9% of flame duration). However, for a stationary particle in the current study, the char undergoes

ignition while enveloped by a flame. Therefore, the ignition here is controlled by the diffusion of oxygen to the surface through the volatile cloud without being consumed or diverted away. Larger particles heat slower and their volatile flux is then slower, making it more probable for them to receive locally more oxygen than smaller ones. This explains why larger particles of the same fuel present char ignition earlier.

The same analysis may apply in explaining why the overlap increases with the torrefaction degree. Torrefaction reduces the particle density so that a raw particle of the same mass as a torrefied one has larger size, and thus higher overlap. Moreover, the outward flow of volatile matter seems to obstruct the molecular diffusion of oxygen towards the particle surface. Results show that the volatile flow tends to be more intense with smaller particles and with more VM. Therefore, the probability of oxygen passing the volatile cloud to react with the char is lower for smaller particles and for higher VM content so that the probability of ignition is lower.

V.5.4.3 Burnout time

Figure V.19 shows the total burnout duration of each biomass. An increasing combustion duration versus mass is measured for all fuels. Higher volatile content shortens the combustion duration since more fixed carbon is retained in the char of torrefied biomass. During torrefaction, thermal decomposition of the lignocellulose components increases the C-C bonds, and consequently increases the char content of the product. Yet, the 45% reduction of volatile matter for Pin-P does not lead to a significant difference with Pine and Pin-T as expected. This is attributed to the higher interference between the two combustion phases and to the improved catalytic effect of ash in both torrefied fuels due to higher ash content.

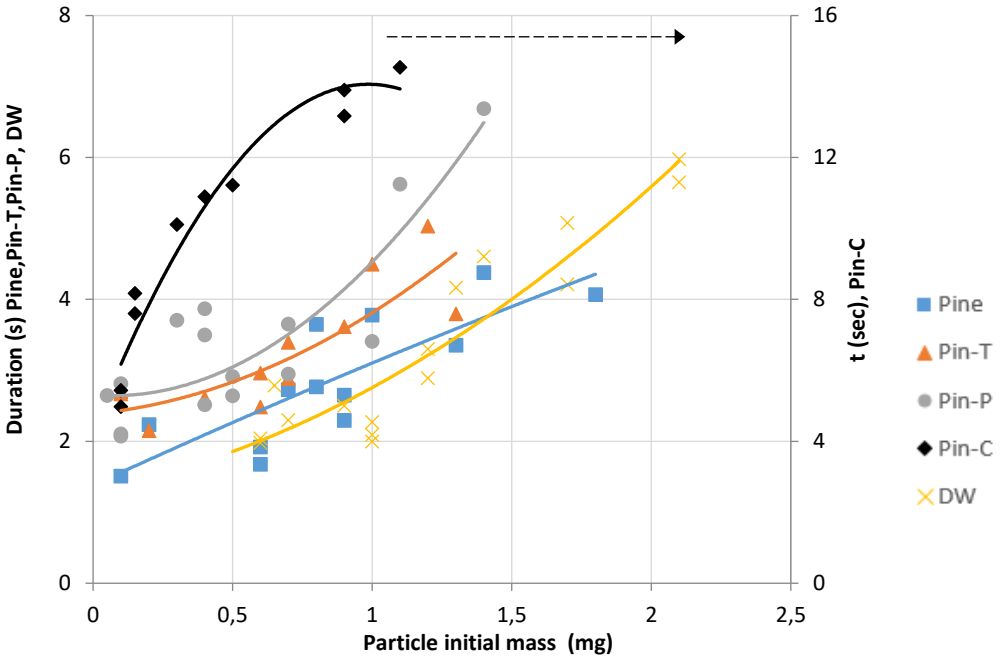

Figure V.19: Total burnout duration in PCS at 800°C

The role of volatile matter on the burnout duration is evident. The carbonized pine indeed takes up to three times more time to complete its oxidation. This is in line with the HTR results where torrefaction shifts the combustion behavior towards that of coal. No volatile matter means that the particle keeps its original surface to volume ratio when oxygen attacks, while volatile

containing particles are found to be hugely deformed after pyrolysis. Moreover, volatile ejection creates new pores in the char structure enhancing its reactivity.

V.5.5 Evolution of the particle projection area

The evolution of the projection area gives an indication of the particle size evolution. In order to compare the area evolution of different particles, the data is normalized to a non-dimensional basis versus a non-dimensional common property of the fuel type. The projection area is normalized by the initial projection area (at t=0) versus the normalized combustion time $t/t_{burnout}$ where $t_{burnout}$ is the total combustion duration. On the other hand, the unburnt fraction U obtained from the HTR results is also normalized versus the normalized combustion time. U is determined from the carbon conversion curves assuming that carbon is released at about the same rate as the total mass release. This assumption is based on experimental data reported by G. Wang et al. [64] showing a linear regression between the release of C, H and N and the total mass release in the drop tube furnace.

$$U = 1 - \frac{consumed\ mass}{initial\ mass}$$

Figure V.20 shows the Normalized area (A/A0) and the unburnt fraction (U) of Pine vs the corresponding normalized time. The end of the flame phase is characterized by the change in both curves slope after all the volatiles were consumed (U=1-VM) and then followed by the same duration of char combustion. Moreover, the curves agree on the instant of the maximum flame area. The latter was detected visually from the colored videos, and was assumed to correspond to the peak of devolatilization in the HTR conversion curves. Hence, correlating both results is reasonable following the agreement in the combustion events and durations between both methods. The procedure is repeated for every particle and the result is the average of all curves. *Figure V.21* displays the experimental data of the Pine particles and their average. The coefficient of determination (R^2) is higher than 0.9 for all fuel types. The variations between the particles are more pronounced during the char combustion. Nevertheless, high similarity is found during the flame phase.

The average curves of each fuel are in *Figure V.22*. 44%, 37%, 40% and 46% of the initial projected area for Pine, Pin-T, Pin-P and DW respectively are lost during the flame phase. The curves follow a power trend ($A = A_0 U^{\alpha}$) for the flame part where α is the power coefficient summarized in *Table V.5* for each fuel. Theoretical corresponding curves are plotted on *Figure V.22* to compare with experimental results.

fuel	Pine	Pin-T	Pin-P	DW	Shrinking core
α	0.32	0.29	0.63	0.40	0.66

Table V.5: Area evolution exponent during flame phase

The table also includes the shrinking core model for char combustion that assumes a constant density and evolution of particle diameter in proportion to the particle conversion to the power of 3. According to the model, char combustion takes place in zone II or III where diffusion processes influence the combustion rate, and diffusion limitations became more crucial towards the end of char combustion. The model assumes that the particle diameter tends to zero at the end of the reaction, which is not a realistic assumption as proved experimentally. DW is the

closest to this behavior for it undergoes fragmentation during the char combustion and leaves little to no ash matrix after the complete burnout. The fragmentation is attributed to the brittle nature of demolition wood as it consists of compressed wood. In this perspective, the model depicts well the evolution of the bright zone rather than the particle volume. In fact, all other fuel chars follow the carbonized pine profile given in *Figure V.23* in comparison with the shrinking particle model as a function of the unburnt char fraction (U here is the ratio of the remaining carbon to the fixed carbon content). The model is fairly correct at the beginning of the char combustion but the data diverge later at the point of separation of the two curves in *Figure V.13*, to an approximately constant volume as the combustion progresses. Carbon is reacting with small variation of the external volume that shadows 33% to 39% of the initial projection area after the complete burnout of all the fuel types (except for DW). Higher ash content accounted for larger ash matrix at the end.

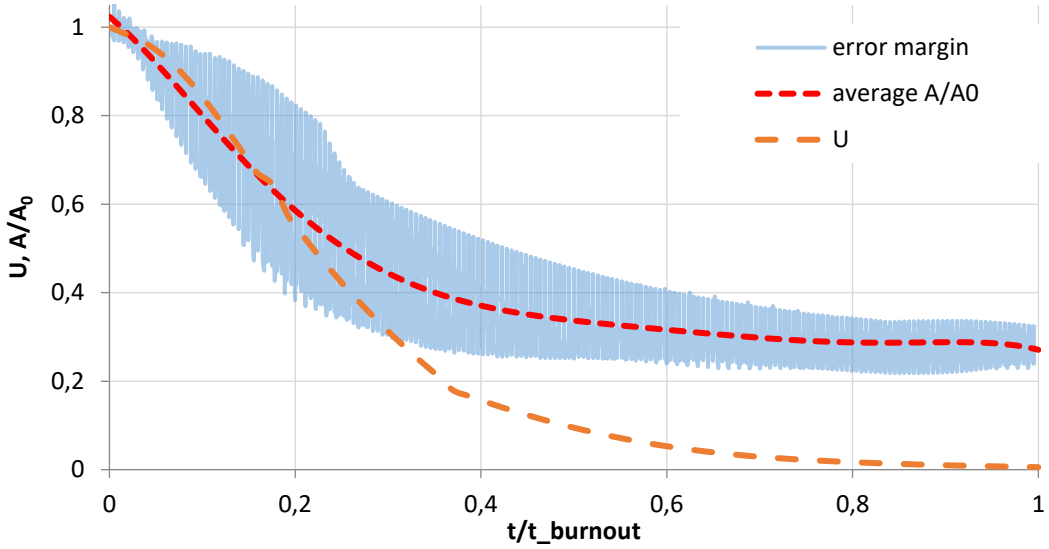

Figure V.20: Normalized area (A/A0) (in PCS) and unburnt fraction (U) (in HTR) vs the normalized combustion time of Pine at 800°C

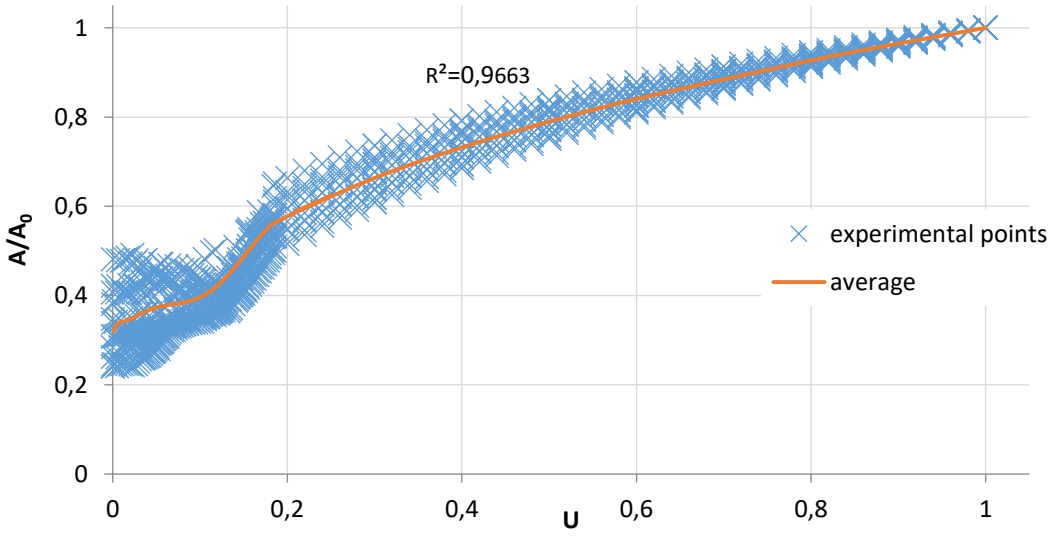

Figure V.21: Average area evolution of Pine versus the unburnt fraction at 800°C

The char was sometimes swelling in the course of its oxidation. This is obvious in the curve of carbonized pine that increases at the end and then shrinks again to 56% of its original shadow. The swelling is probably caused by trapped volatiles in the ash matrix (most likely lignin volatiles) that are liberated at the end because of the build-up pressure or ash melting. Fragments of the particles are ejected at the end when the particle swells. The phenomenon is notable for Pin-T and it can be spotted by the rapid increase in the slope of torrefied pine size as U approaches zero.

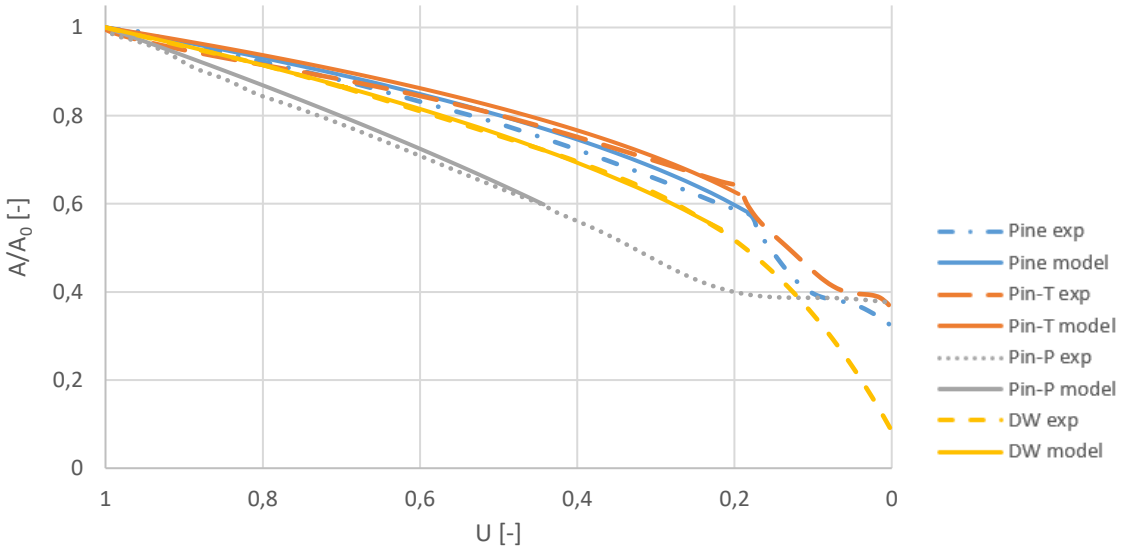

Figure V.22: Evolution of the projection area as a function of the unburnt fraction of all fuels at 800°C and comparison with the power model for the devolatilization stage (U-axis in reverse order)

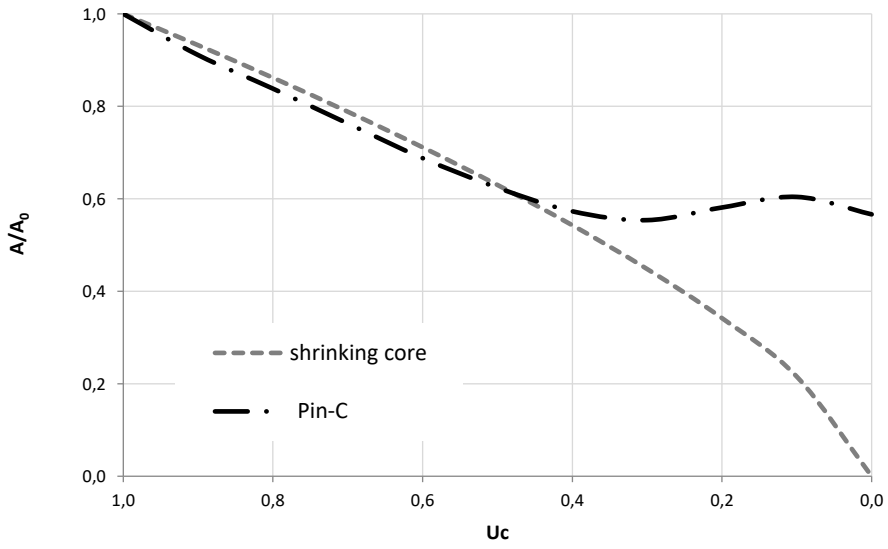

Figure V.23: Comparison between experimental char evolution and shrinking core model (U-axis in reverse order)

Assuming spherical particles and isotropic consumption, the particle volume can be directly evaluated from its projection area:

$$Volume = \frac{4}{3.\pi^{1/2}} Area_{projected}^{\frac{3}{2}}$$

In fact, the initial particle shape was fibrous and irregular for all types. The irregularities tend to disappear in the remaining char, which becomes more rounded than the mother particle [216], [217]. Softening the particle surface is attributed to the surface tension created where the particle partially melts during the combustion [218]. This is caused by the high temperatures encountered during the char combustion, which allow the particle to deform and smooth the edges.

V.5.6 On the difference between biomass particle and coal particle combustion

The difference between the combustion of coal and biomass is obviously demonstrated by the degradation curves in TGA and in the emission curves in the HTR. These differences are the result of the physical and chemical disparities including density, composition (proximate and ultimate analysis), structure and porosity. The huge difference in the volatile content is a prominent difference that defines the flame characteristics and the char properties.

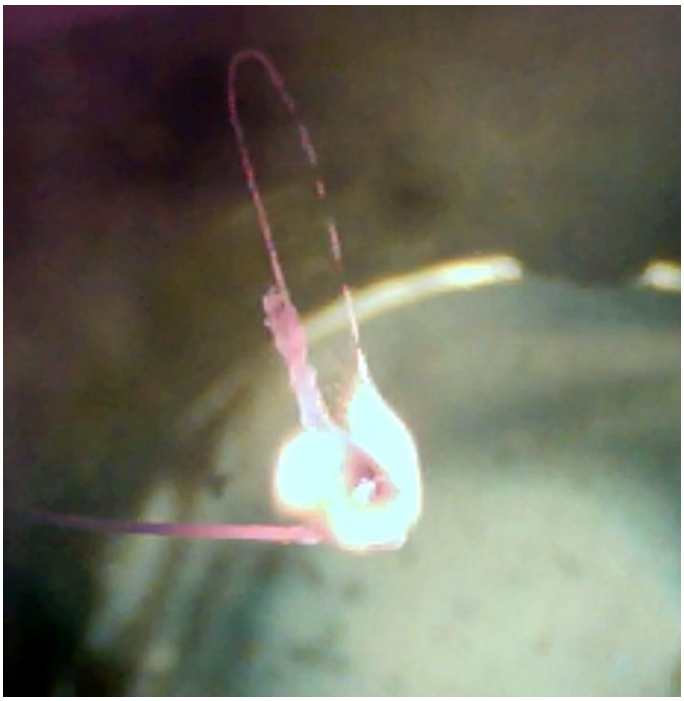

Figure V.24: Soot contrail forming closed loop

Biomass flames are transparent and possess uniform shape (near spherical) regardless of the particle irregular shape, to the contrary of coal flames that are sooty and disturbed. The volatiles released from biomass consist mostly of light hydrocarbons as measured in the drop tube furnace. Tars and heavy hydrocarbons crack expediently into light gases and pyrolytic water before reacting with oxygen. Moreover, biomass volatiles have high oxygen proportion leading to the formation of CO and CO_2. The latter inert gas dilutes the volatile cloud around the particle and reduces the flame luminosity. In contrast, coal volatiles contain mostly heavy hydrocarbons and tars that appeared to condense in a sooty contrail (*Figure V.25*).

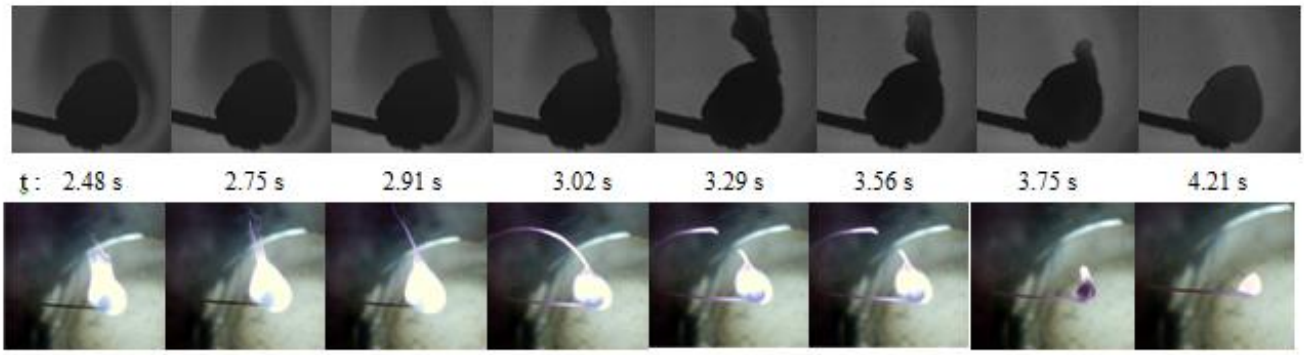

Figure V.25: Selected images from the high magnification monochrome camera (top) and the corresponding direct emission camera (bottom) showing the formation and disappearance of the condensed volatiles (insertion at t=0 s) during combustion of a single Venezuelan coal particle (1.6 mg) in PCS at 800°C

Upon heating, the particle swells considerably indicating high internal pressure due to lower porosity compared to biomass, which does not permit the volatiles to flow out easily [219]. The pressure is relieved by brutal release of jets containing dense volatiles that cast a shadow in the monochrome video. The dense trails are precursors of soot formation so they condense and agglomerate to develop a contrail of intense luminosity inside the flame. It can be distinguished from the flame by its high luminosity while entraining the flame in a chaotic fluctuation. The condensed material extends outwards to a long distance forming a bright tail. The contrail is sometimes long to the point that it cannot be held by the particle causing its far end to bend and break (*Figure V.25*) or it bends back to the particle forming a closed loop (*Figure V.24*). Since more time is needed to oxidize tars especially in an oxygen poor environment like the flame, the attached condensed structure persists after the flame extinction and undergoes oxidation to disappear gradually in less than a second. The same phenomenon is reported for bituminous coal in [220][221][222][223].

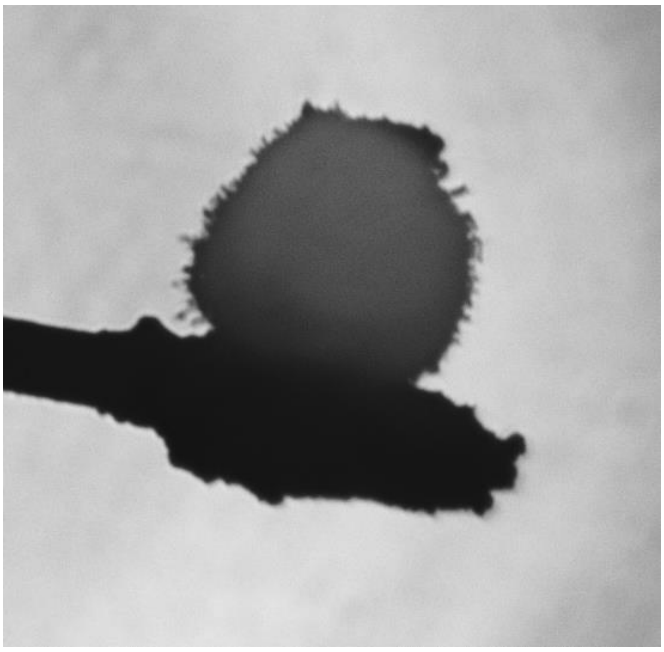

Figure V.26: Heterogeneous combustion of coal particles with the filaments appearing on the surface

The flame is followed by a bright particle that burns gradually. The high magnification of the shadowgraph videos allows observing in details the combustion taking place on the surface of the particle. Note that the heterogeneous combustion of coal is maintained mostly at constant temperature. At the beginning of the char combustion, the particle appears dimmer than the soot contrail. As the burning time goes by, the oxidation reaction intensifies and the char glowing as well. Some chars burn with constant volume where oxygen penetrates the cenosphere interior through the pores and the combustion continues internally similar to the biomass char combustion. In this case, the particle glow fades slowly as the combustion proceeds internally. However, the particle volume shrinks most of the time, with small filaments appearing in the displaced volume (*Figure V.26*). The formation of filaments is also detected by Olsbye et al. on coke formed during methane-to-synthesis gas reactions[224]. These filaments are distributed radially at the surface, and thereafter, separate from the char as fly ash.

Due to lower reactivity and higher FC in coal, the biomass char burns up to five times faster than coal. This also applies for biomass with comparable volatile matter and fixed carbon content. For example, Pin-P with about 52% FC burns four times faster than the 61% FC coal. This is addressed by the faster char gasification reactions [225] the higher oxygen to carbon ratio in biomass char. It is also attributed to enhanced catalytic role of alkali metals in biomass chars due to higher concentration [226].

V.6 Conclusion

The results show the important role of the VM content and particle size in determining the combustion intensity and durations. The fast pyrolysis produced mainly gas with char and pyrolytic water. Higher volatile content fuel ejects more volatiles during the experiments in the DTF with higher CO, H_2 and CH_4 yields. However, higher VM particles undergo intense devolatilization for comparable durations as less volatile containing fuel, and despite being produced in different quantities, the composition of the gases is rather similar. For that reason, the flame duration appears to be more influenced by the particle size than by the particle volatile content. Indeed, larger particles yield considerably less non-condensables during devolatilization. The intense devolatilization of higher VM particles leads to more intense flame combustion that obstructs the oxygen diffusion to the particle and delays the heterogeneous ignition. Nevertheless, the char left is more reactive and burn faster than the char resulting from particles with lower VM content. A char resulting from a particle with no initial VM burns three times slower than its raw counterpart. On the other hand, larger particles mean slower temperature rise before and after ignition and lower devolatilization intensity. This, beside the larger surface area, increases the probability of earlier heterogeneous ignition and longer overlap.

The projection area evolution is traced versus the burnout using gas emission results. VM occupy around 40% of the initial particle shadow, which decreases with devolatilization progress following a power trend. The power coefficient doubles with intense pre-treatment of the fuel. The latter leads to increase the char volume, which shrinks after the flame end following the shrinking core model. But it diverges later to a constant residual ash volume, which increases with more intense pre-treatment. An empirical model can be extracted from the curves assuming spherical particles. A comparison between biomass and coal shows the visual differences of the gas phase composition and the char structure, giving rise to differences in the flame and char combustion of both fuels.

Chapter VI. Numerical study of the combustion of a biomass particle

This chapter presents the numerical results of the combustion of a single particle of biomass in the drop tube furnace. The results in chapter V are used to tune the particle combustion model presented in chapter IV. The model predictions are compared to the experimental data in the drop tube furnace. The identified kinetic parameters are listed here and compared to the ones reported in literature. This chapter also contains a sensitivity study of the determined kinetic parameters to the adopted sub-models of the volume evolution scenario and drag coefficient model of the particle.

The experimental data related to the particle conversion, needed for the particle combustion model, are determined in combustion experiments performed in the drop tube furnace. Oxygen profiles along the furnace axis during the combustion of each fuel type are used as input to the model to optimize it and derive the kinetic parameters of the fuel. The model is then validated versus the CO profiles. The procedure and conditions of the combustion experiments are introduced first before discussing the numerical results.

VI.1 Combustion experiments in the DTF

The pulverized fuels were thoroughly sieved in the size range of 600 - 800 µm. In the view of the limitation set by the length of the sampling probe, the experimental conditions were chosen so that the biomass is not completely pyrolyzed upstream the first sampling point, at 60 cm from the injection point, and reaches at the same time 80% conversion at the final sampling point (150 cm). The temperature set point was varied to achieve these conditions, for it is exponentially related to the conversion rate of the fuel. The required conditions are achieved at a wall temperature of 800°C for biomass particles in the size range of 600 – 800 µm.

The secondary air flow was preheated to the wall temperature before introducing it to the furnace. The solid fuel feed rate was 1 g/min transported by 2 Nl/min of primary air. The preheated gas flow rate was 20 Nl/min for all experiments. As observed from the bottom of the reactor, the biomass particles were falling in a single manner. Besides, the flow was highly diluted so that the particle-to-particle interactions was neglected. At these conditions, the gas residence time inside the furnace was estimated to be 2.8 sec. The particle residence time during the combustion of a Pine particle (600 - 800 µm) was estimated to be 0.674 s using a physical model taking in consideration the size and density evolution of the particle and its slip velocity. During combustion, the conversion of the fuel as a function of the residence time was determined from the partial pressure of oxygen since the oxygen consumption is proportional to the burnout. This method is preferable over the ash tracer method, which bears high uncertainty when dealing with low ash content solid fuels as explained by Ballantyne et al. [227], due to the uncertainty in the ash content measurement and the volatility of ash at high heating rates and temperatures. The concentrations of CO, O_2 and NO were measured using a Testo gas analyzer model 350.

VI.2 Results and discussion

VI.2.1 Kinetic parameters

The biomass fuels were injected at 800°C sufficient airflow so it ends with at least 16% of oxygen fraction at the furnace exit. The model, which is detailed in Chapter IV, iteratively minimizes the difference between the calculated and measured concentration of oxygen to determine the kinetic parameters of devolatilization and char oxidation of the biomass. *Figure VI.1* compares the predicted and the measured evolutions of the oxygen partial pressure on dry basis along the reactor longitudinal axis corresponding to the three tested fuels. The algorithm successfully follows the experimental points leaving a very low margin of error. *Table VI.1* lists the kinetic parameters with the corresponding deviations from the experimental points. The

values are close to those reported elsewhere using a similar model, for the devolatilization and char oxidation of raw and torrefied pine shell in [177] and of Cynara cardunculus in [50].

However, a detailed DTF-model by Wang et al. [64] similar to this study, calculated activation energies for five other biomasses, two to three times higher than the values calculated here. The difference is however compensated by a very high pre-exponential factor (15 - 300 $.10^{+03}$ s^{-1}), but still, the model showed discrepancies between measurements and predictions in the near injector zone where most of the devolatilization takes place. It should be noted that in Wang's study [64], the combustion air was injected at room temperature and consequently the particles were exposed to a different heating rate. Another factor creating this difference between the model predictions is their corresponding particle volume evolution that will be discussed later. Therefore, the low activation energies in *Table VI.1* are in accordance to what can be found in the literature using similar models and experimental conditions.

	Av ***(1/s)***	***Ev*** ***(kJ/mol)***	***Ac*** ***(g/m².s.Pa)***	***Ec*** ***(kJ/mol)***	***δ*** ***(deviation)***
Pine	294	18.3	0.25	43	$1.6 .10^{-04}$
Pin-T	107	19.0	1.65	65	$1.7 .10^{-03}$
DW	380	21.0	3.70	53	$3.1 .10^{-03}$

Table VI.1: Kinetic parameters obtained by our mathematical model for the tested fuels

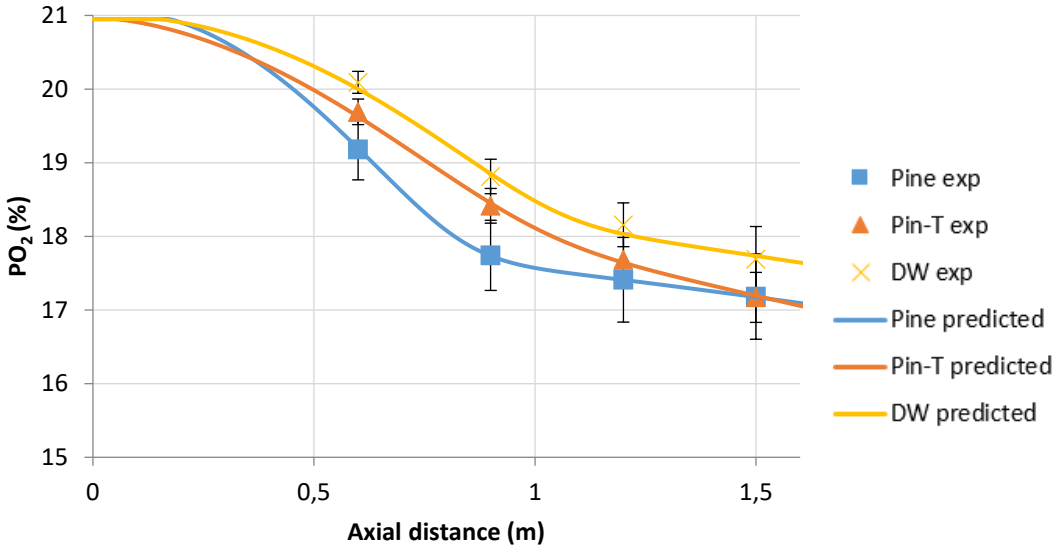

Figure VI.1: Evolution of %O_2 partial pressure along the drop tube furnace axis (600 - 800 µm particles at 800°C)

The results show that higher activation energies are calculated for demolition wood than Pine. Moreover, torrefaction reduces the reactivity of devolatilization and char combustion, which is consistent with previous studies [27].

VI.2.2 Particle conversion

The first sampling point at 60 cm from the injection point marks some oxygen consumption observed for the three fuel types. Upstream this point, the model predicts the combustion parameters based on their measured tendencies later. At this distance, the particles have already started their degradation journey, which is estimated to last for 0.674 sec for Pine, 0.772 sec for Pin-T, and 0.572 sec for DW inside the furnace. The heating rate is around 2000°C/s as calculated by the model.

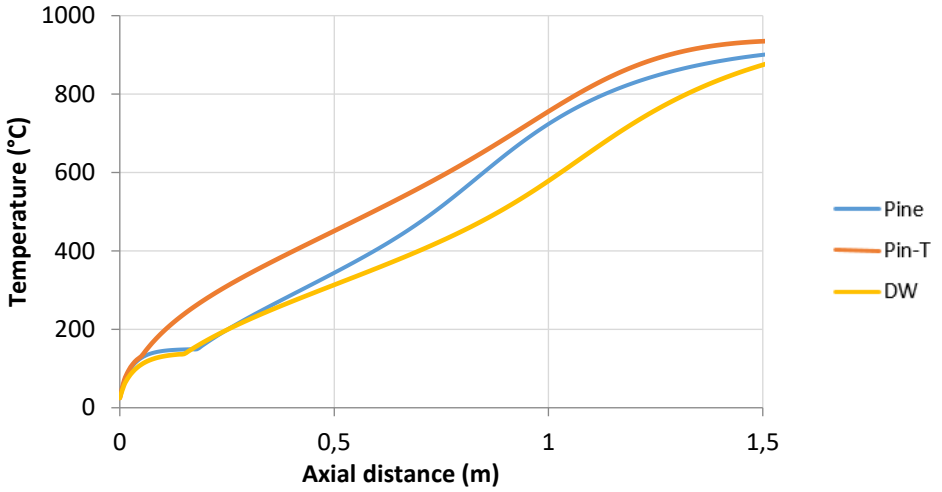

Figure VI.2: The predicted particle temperature along the drop tube furnace axis (600-800 µm particles at 800°C)

After injection, particle temperature increases until around 100°C during the release of moisture from the particle. Most of the received energy at this stage is absorbed as latent heat for drying and thus the particle temperature stabilizes for a certain time as simulated in *Figure VI.2*. Demolition wood and Pine with roughly 6% and 11 % moisture content respectively experience a significant delay in initiation of their devolatilization compared to the relatively dry particles (~2% moisture) of torrefied pine. The latter takes advantage for an early increase in temperature. No oxygen is consumed during the drying stage. Drying is directly followed by a rapid liberation of volatiles associated with high consumption rate of oxygen. Despite the late start, Pine leads the consumption rate given the low activation energy and the more intense devolatilization pointed out in the shadowgraphy results. The heavier demolition wood particles acquire higher speeds than Pine and Pin-T and thus devolatilize over a longer axial distance, which explains their smoother oxygen consumption as well as smoother temperature rise during this phase. Oxygen consumption slows down at the end of devolatilization and the beginning of the char combustion. By now, the particle temperature comes closer to the furnace temperature but does not reach it yet, due to the high thermal inertia of the coarse particles (600-800 µm). Subsequently, the particles are heated by the char oxidation, and then cools down after full consumption until they reach equilibrium with the ambient conditions at 800 °C. Simulations with finer particles (400 µm) reveal faster heating to the extent; they overpass the furnace temperature during the flame phase.

The conversion profiles (*Figure VI.3*) are calculated using the derived optimal kinetic parameters. The model indicates that most of the biomass particle journey is devoted for devolatilization due to high volatile content, and the influence of char conversion is marginal

on the total burnout. Given the obtained data, it was also possible to calculate the overlap between the homogenous and heterogeneous combustion stages. The flame extinction is assumed when 99.9% of the initial volatile content is released, whereas the heterogeneous ignition is the moment when 0.1% of the initial FC is consumed.

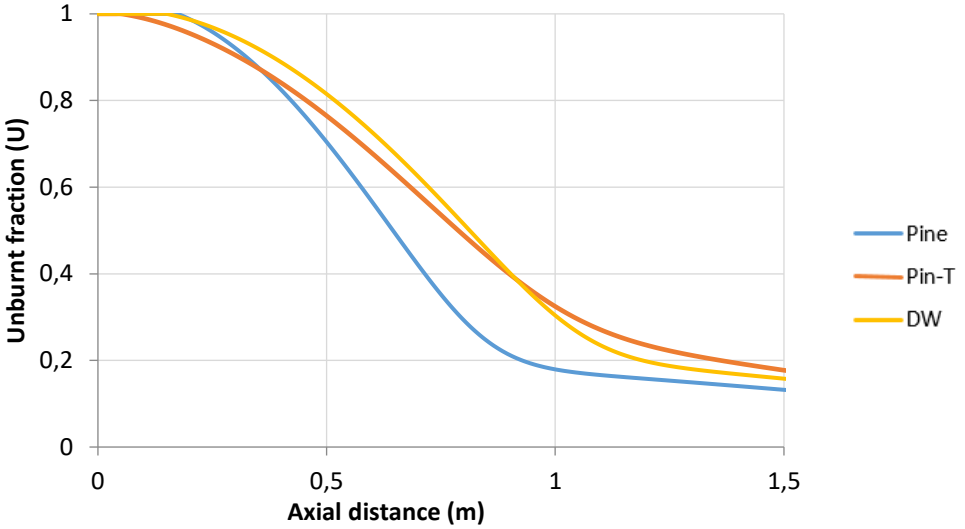

Figure VI.3: The predicted unburnt fraction of the studied fuels in the drop tube furnace (600 - 800 µm particles at 800°C)

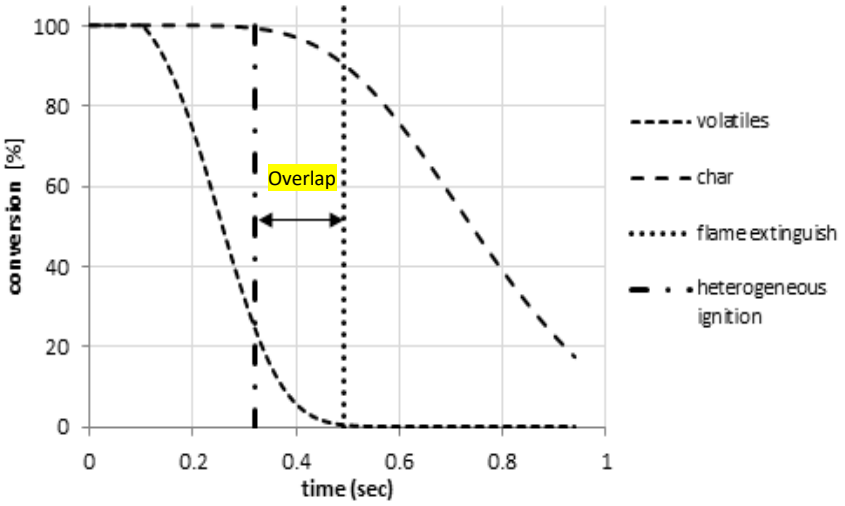

Figure VI.4: overlap of the flame phase and char combustion phase (600 - 800 µm DW particles at 800°C)

Figure VI.4 illustrates this method applied for the combustion of demolition wood. The maximum overlap was obtained for torrefied pine (0.217sec), followed by demolition wood (0.161 sec) and the minimum overlap for pine (0.097 sec). The durations are somehow longer than the measured ones in the PCS for such particle size. This could be attributed to the glue effect used in the latter method, which seems to separate the two combustion phases as observed in TGA experiments. Nevertheless, the arrangement of the overlap durations is consistent. Given similar particle size, the overlap is mainly affected by the volatile matter content and the intensity of devolatilization, leading to Pine-DW-Pin-T series from lower to higher overlap duration.

VI.2.3 Volatiles oxidation

Figure VI.5 shows the prediction and the experimental data of the CO molar fraction along the reactor axis. In comparison to the experimental results, CO is overestimated during devolatilization at 60 cm but then better fits to the experimental data during char combustion. The overestimation may be related to the fact that CO was calculated based on a constant composition of volatiles that was measured during the pyrolysis experiments. Note that the measured CO was not used in the model to determine the kinetic parameters, so this good accordance between the predicted profiles and the measured values of CO validates the model.

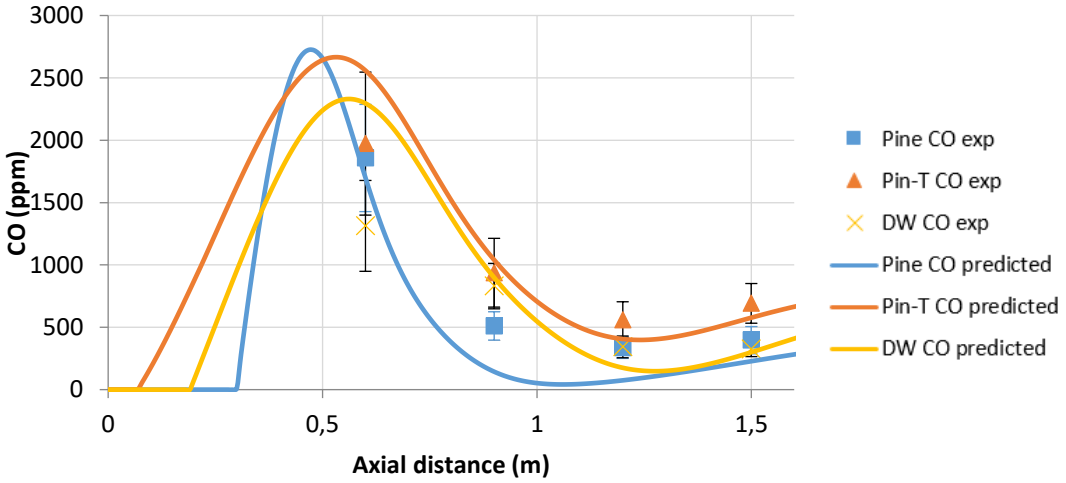

Figure VI.5: Evolution of CO concentration along the drop tube furnace axis (600 - 800 µm particles at 800°C)

The behavior is quite similar for the three fuel types. CO is produced in high concentrations during devolatilization forming a peak before the first sampling point. This peak is directly related to the peak of devolatilization, since CO is the major constituent of the volatiles making more than 50% of the released gases. Despite its delayed start, Pine exhibits earlier peak followed by Pin-T and DW. The concentration then decays upon oxidation and with lower devolatilization rate. The release of moisture promotes the early activation of the CO oxidation reaction and the earlier decay of CO, especially in the case of Pine. CO decay continues to the point where char is ignited and CO emerges again as the major product of the char oxidation reaction at high temperatures. The value of the attained minimum reflects the degree of overlap between the combustion stages. In the case of Pine, CO approaches zero before the second rise, while higher minimum is attained by DW and Pin-T respectively, despite the lower production in the flame phase. This also can be observed from the tendencies of the experimental points.

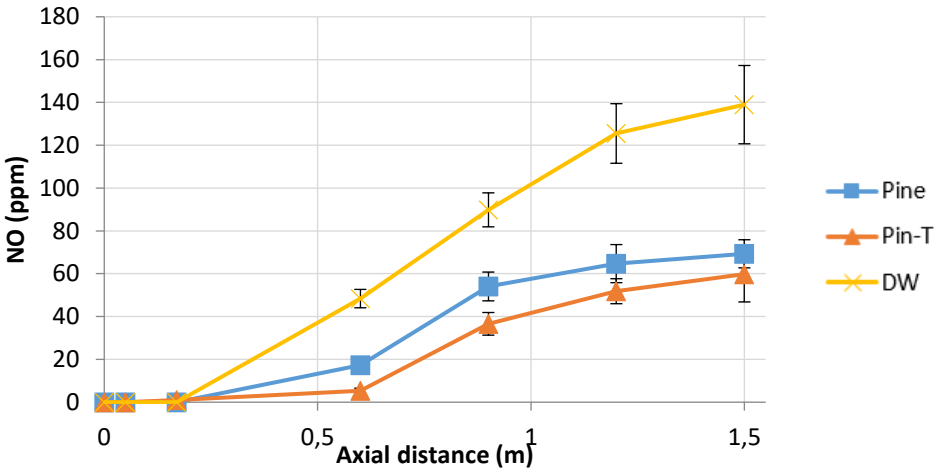

Figure VI.6: Measured NO concentration along the drop tube furnace axis (600 - 800 µm particles at 800°C)

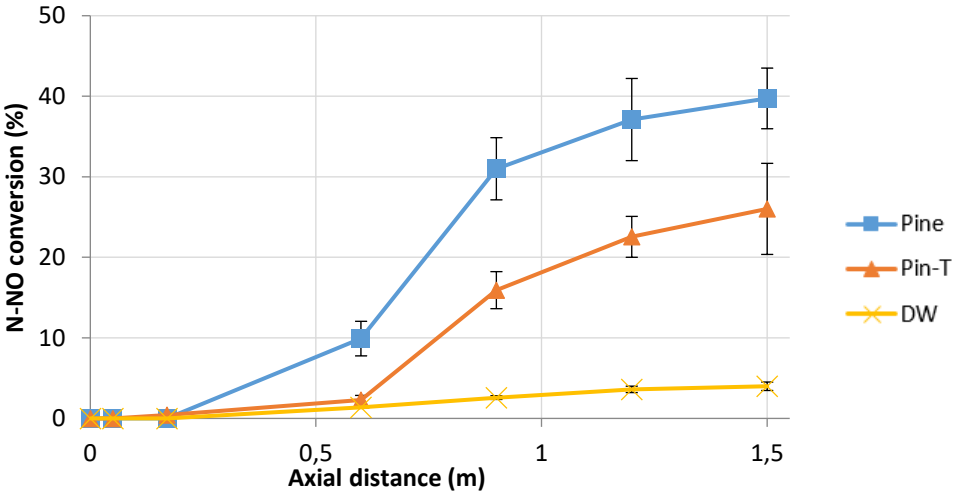

Figure VI.7: Conversion of fuel-N to NO along the drop tube furnace axis (600 - 800 µm particles at 800°C)

Figure VI.6 shows the measured molar concentration of NO along the axis. Fuel-N is converted into NO mainly during the devolatilization as discussed earlier. Previous studies concluded that roughly 75 to 90% of the initial nitrogen is released with the volatiles [50], [228]. An expected increase of NO near the injection is observed and similar to oxygen consumption it slows down after 90 cm during char combustion except for DW. However, an inverse trend is presented in *Figure VI.7* for the percentage of the fuel-N conversion to NO, for it decreases with higher N-content. This result is in agreement with the HTR results.

VI.2.4 Sensitivity study

VI.2.4.1 Influence of the volume evolution model

This section discusses the sensitivity of the model predictions to the particle volume evolution scenario. As discussed earlier, previous studies used similar approaches but employed simplified volume evolution scenarios. They are listed from # 1 to # 4 in *Table VI.2*. The scenario given by the PCS results by direct observation is labelled # 0. Following Wang et al. approach [64], the scenario 1 did not take into account the variation of the particle volume

during devolatilization assuming constant volume but a shrinking core was considered during char oxidation. On the other hand, based on experimental data, Jimenez et al. [50] assumed a constant volume for the particles in the course of their combustion (scenario 2), taking into account a density variation. This assumption is also used for coal in some studies [81]. However, many CFD studies adopt different volume evolution scenarios based on works initially developed for coal: The swelling particle model for devolatilization is often adapted to biomass by setting the swelling coefficient smaller than one. Using intrinsic model for the char oxidation part, a shrinking core model with 0.25 power coefficient has been found to work well for a variety of chars (scenario 3) [229]. However, most CFD studies use a kinetic/diffusion char surface oxidation model with constant particle diameter (scenario 4). *Figure VI.8* shows the five scenarios of diameter evolution during the combustion of Pine.

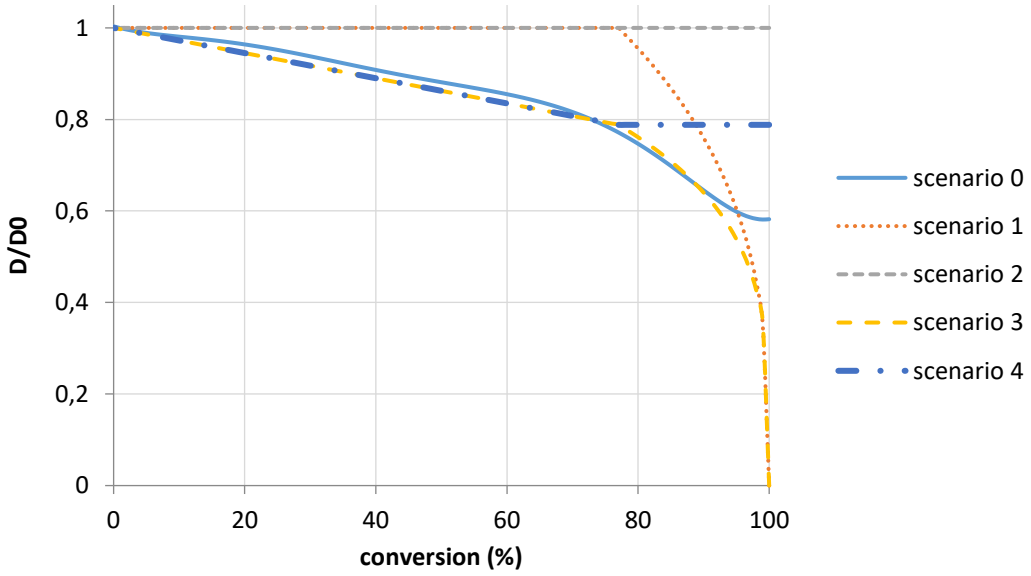

Figure VI.8: Volume evolution scenarios of a pine particle during combustion

Scenario	*Flame phase*	*char combustion*
#0	*Experimental data from PCS*	*Experimental data from PCS*
#1	*Constant volume*	*Shrinking core (α=0.33)*
#2	*Constant volume*	*Constant volume*
#3	*Swelling model*	*Shrinking core (α=0.25)*
#4	*Sweliing model*	*Constant volume*

Table VI.2: Volume evolution scenarios of biomass particle during the flame phase and char oxidation phase

A direct comparison of the parameters obtained in these studies may not be objective, considering that they were applied on different fuel types and experimental conditions. The three volume evolution scenarios from literature were tested here, in addition to our volume model obtained by shadowgraphy (scenario 0). The char conversion is not well established in

our experiments, so the simulation is extended to allow comparison until the complete burnout. *Figure VI.9* shows the model fitting of oxygen partial pressure to the experimental points, using the optimal parameters determined for each case. The curves agree up to the last experimental point, but they diverge afterwards in the absence of experimental data at higher conversion. In order to better judge and compare the results of each case, the model should have the same data input to follow until the complete burnout. Therefore, the oxygen pressure calculated in scenario 0, based on the available experimental points, is taken as a baseline input for the other scenarios. In this case, the model optimizes the oxygen curve of each scenario to reproduce the curve determined in scenario 0.

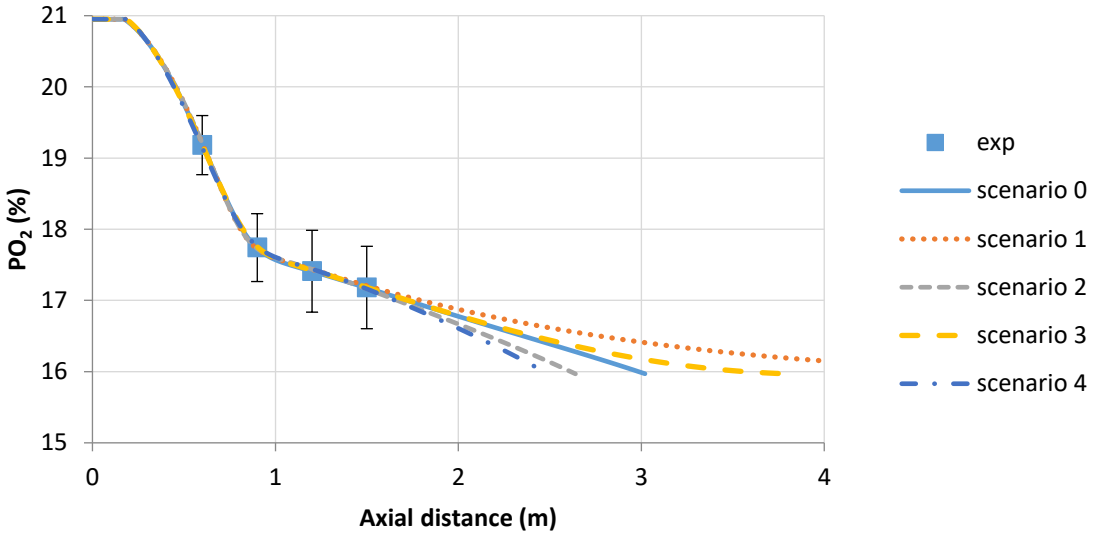

Figure VI.9: Model fitting of oxygen curves to the experimental points (DTF) using different scenarios (600-800 µm Pine particles at 800°C)

Table VI.3 summarizes the kinetic parameters of each fuel in each volume evolution case. The kinetics of scenario 0 and scenario 3 are very similar as expected, since their volume models stick together up to high conversion point. For all scenarios, the values of devolatilization kinetics are comparable considering the same mathematical formulation. Moreover, the impact of shrinkage is negligible on the pyrolysis time and yield in such regime [81]. The one-step reaction is not directly dependent on the particle volume; the volume rather influences the velocity and temperature, which are not fully established after injection. The difference in these entities (velocity in *Figure VI.10* and temperature in *Figure VI.11*) appears after the first 50 cm where devolatilization has already started. Afterwards, a reduced volume pushes the particle faster due to lower drag force. Hence, the volatiles in scenarios 0, 3 and 4 are released over a wider distance so they get more diluted and induce less intense oxidation. Whereas in scenarios 1 and 2, the particles spend more time in intense volatile combustion region, which favors their temperature rise. Ultimately, the particles have longer residence time in the furnace (~+10% longer) in these scenarios (1 and 2) and higher average temperature. The calculations are then performed at lower temperature during the char oxidation for scenarios 0, 3 and 4 (around 100°C lower), and by following the same burnout data, it means that char oxidation is activated at lower temperature, which explains the lower activation energy. It is evident how the algorithm is sensitive to the evolution of the particle size during this stage, because it is directly linked to the consumption rate.

	***Av* (1/s)**	***Ev* (kJ/mol)**	***Ac* (g/m².s.Pa)**	***Ec* (kJ/mol)**
Pine				
Scenario0 (PCS)	294	18.3	0.93	53
Scenario1	220	17	1.50	67
Scenario2	230	17	0.40	60
Scenario3	290	17.8	1.4	53.4
Scenario4	290	17.2	0.51	53
Non-spherical drag (SF = 0.25)	248	27.4	0.92	63.5
Pin-T				
Scenario0	107	19	1.65	65
Scenario1	118	20	3.30	75
Scenario2	122	20	0.78	67
Scenario3	107	19	2.10	65
Scenario4	102	18.5	0.90	61
Non-spherical drag (SF = 0.33)	250	32.4	2.11	72
DW				
Scenario0	380	21	3.70	53
Scenario1	435	22	1.20	59
Scenario2	435	22	0.84	61
Scenario3	430	21.5	2.51	53.7
Scenario4	371	20	0.53	51
Non-spherical drag (SF = 0.25)	331	30	3.40	70

Table VI.3: Comparison of the kinetic parameters due to the model sensitivity to volume evolution and drag coefficient model

Changing the particle volume not only affects chemical kinetics but also affects the diffusion of oxygen pressure to the particle surface. The diffusion kinetics is firstly controlled by the particle and gas temperature, and secondly, by the oxygen pressure in the surrounding gas. Faster particles devolatilize over a wider distance and thus oxygen consumption is slightly smoother. In this case (scenarios 0, 3 and 4), before the end of the flame where it starts to shrink back to the particle surface, the particle is surrounded by slightly higher oxygen pressure than in the other scenarios. This promotes the oxygen diffusion and consequently helps triggering the heterogeneous reaction. This also explains the longer overlap duration of homogeneous and heterogeneous reactions for scenario 0, 3 and 4 in all three fuel types resulting in the series: scenario4 > scenario0 > scenario3 > scenario1 > scenario2.

The predictions of gases concentration (CO in *Figure VI.12*) and burnout using different scenarios do not change dramatically when traced versus the axial distance; because the model in all cases follow the experimental points at a certain position which does not refer to the same residence time in every scenario. Given close apparent kinetics for devolatilization, it is normal for the profiles not to show high variations at this stage. The differences appear more pronounced during char oxidation where the consumption rate varies with the scenario. The kinetics are faster with lower activation energy and attain higher conversion within shorter residence time.

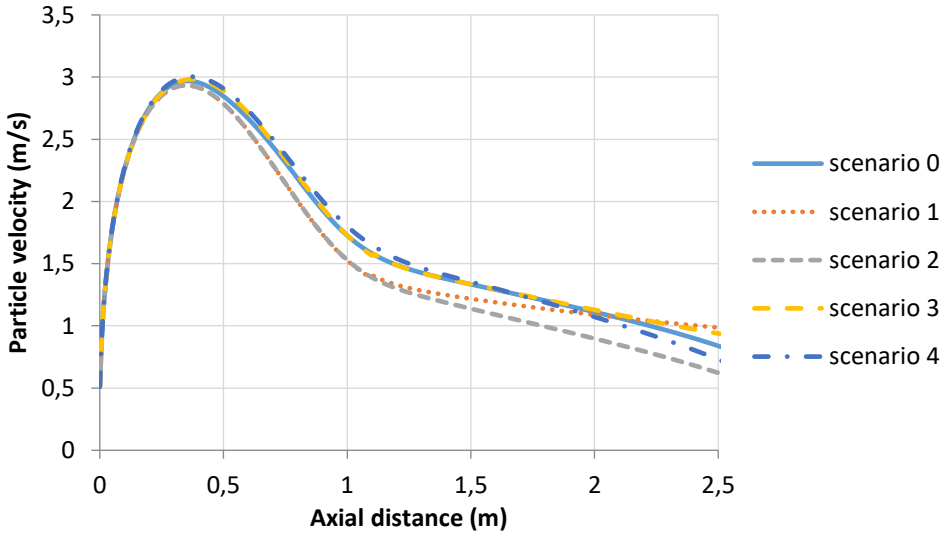

Figure VI.10: Sensitivity of the particle velocity to the volume evolution model (600 - 800 µm Pin-T particles in DTF at 800°C)

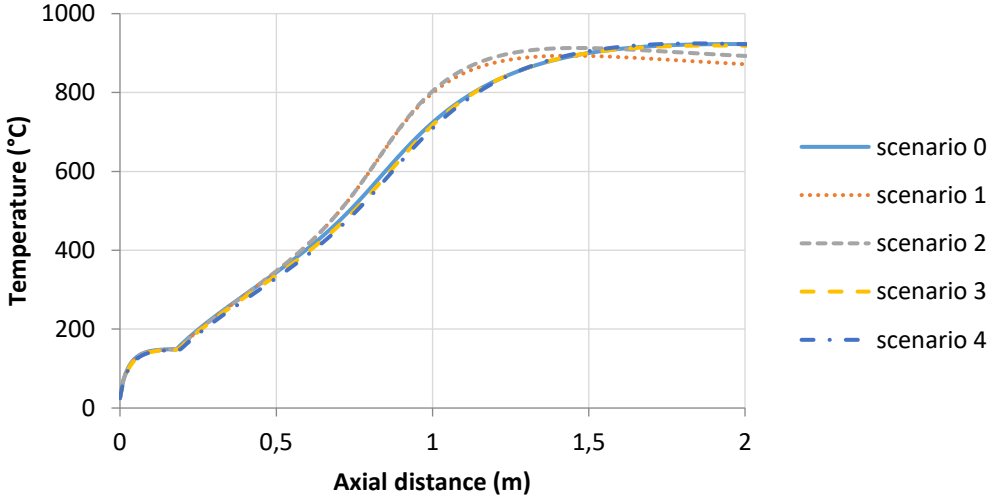

Figure VI.11: Sensitivity of particle temperature to the volume evolution model (600 - 800 µm Pin-T particles in DTF at 800°C)

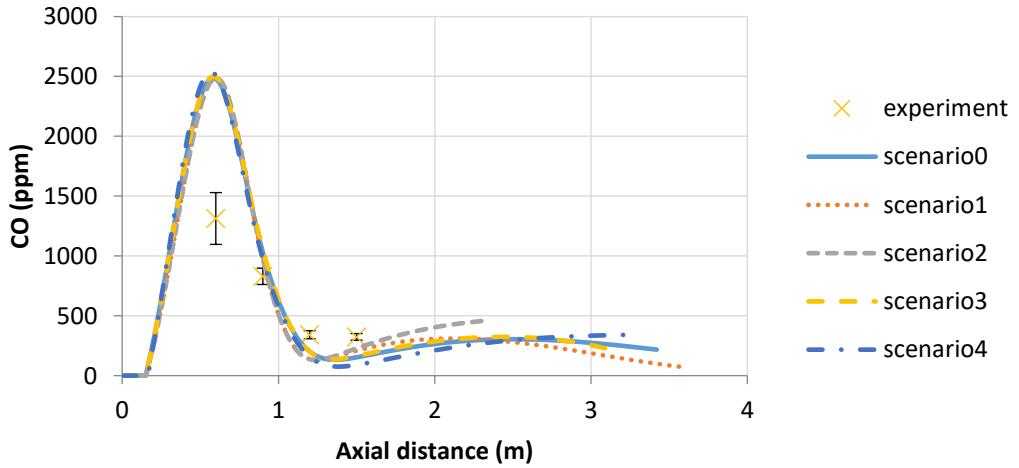

Figure VI.12: CO sensitivity to the volume evolution model (600 - 800 µm DW particles in DTF at 800°C)

VI.2.4.2 Influence of the drag force model

The disparity of the values of the kinetic parameters found in literature results from different used sub-models. Each has some impact on the particle trajectory and/or its thermal history. With the same given burnout data, the models are compelled towards different optimal kinetic values in order to better predict the experimental data. Modeling drag coefficient is very critical to determining the particle trajectory. Considering the uncertainty of the particle initial shape and its change during the degradation process, modeling the drag coefficient is a difficult task requiring simplified approaches. The model adopted in this study is the simplest approach as it treats particles as spherical and ignores the shape evolution in the course of their conversion. In fact, particles with arbitrary shapes are shown to be exposed to a higher drag force compared to the equivalent spherical particles [127], [150]. Several correction methods are proposed in order to include the effect of non-sphericity on the drag force.

The kinetic parameters are recalculated alongside the particle thermal and conversion history, using the non-spherical model proposed by Haider and Levenspiel [195]. Scenario 4 is employed for the volume evolution so that the calculated parameters can be used in the Fluent model later on. *Table VI.3* shows the kinetic parameters of devolatilization and char combustion of the three fuels using the non-spherical drag law. The chosen shape factors are used as surveyed in the literature for raw and torrefied wood [127], [150], [196], [230], [231]. Torrefied biomass is found to have higher SF due to its lower fiber content compared to raw biomass.

Figure VI.13 traces the influence of the drag coefficient modeling on the particle velocity. Particles with non-spherical shape are exposed to high drag effect forcing them to advance slowly in the combustion chamber. This effect is true for all fuel types. The velocity peak of a spherical particle is more than twice faster than the non-spherical one. Consequently, the improved interaction of the random shape particle with the flow gives a faster temperature rise near the injection point (*Figure VI.14*). Water is released in shorter distance allowing the temperature to increase further. However, the initiation of devolatilization is interpolated from the same data points fed to both models. Therefore, the non-spherical particles are supposed to devolatilize at higher temperature. This shift is translated to higher activation energy as seen in *Table VI.3*.

The modified trajectory of the particle also influences the distribution of volatiles in the combustion chamber. A slow-moving particle releases its volatiles more concentrated over shorter distance. This intensifies the reaction rate of oxidation of the volatiles leaving lower concentrations of CO, CH_4 and H_2. *Figure VI.15* presents the comparison of the two drag models with the experimental measurements of CO during the combustion of demolition wood. Accounting for the non-sphericity of the particle reproduces better the experimental data of CO.

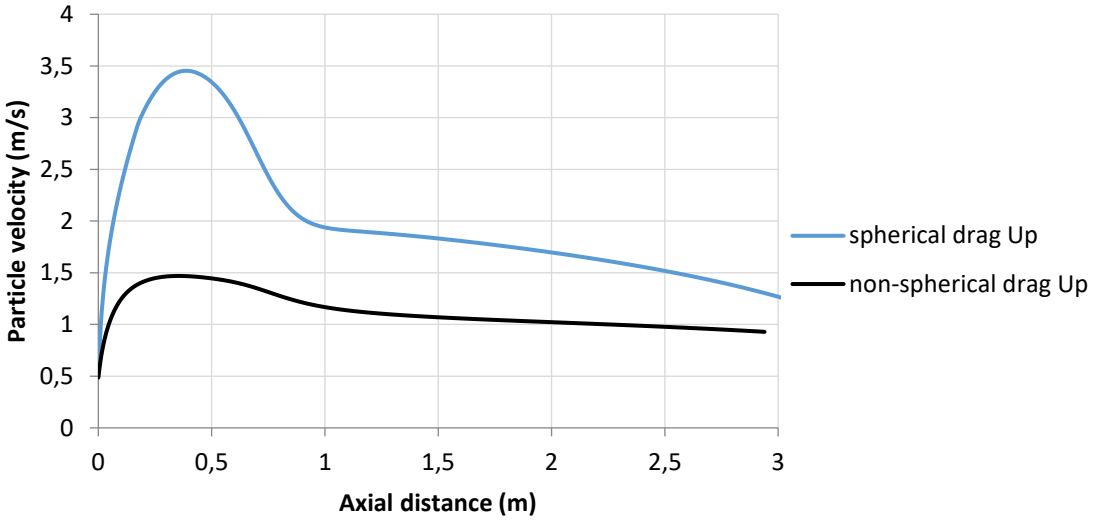

Figure VI.13: Influence of drag modeling on the particle velocity (600 - 800 µm Pine particles in DTF at 800°C)

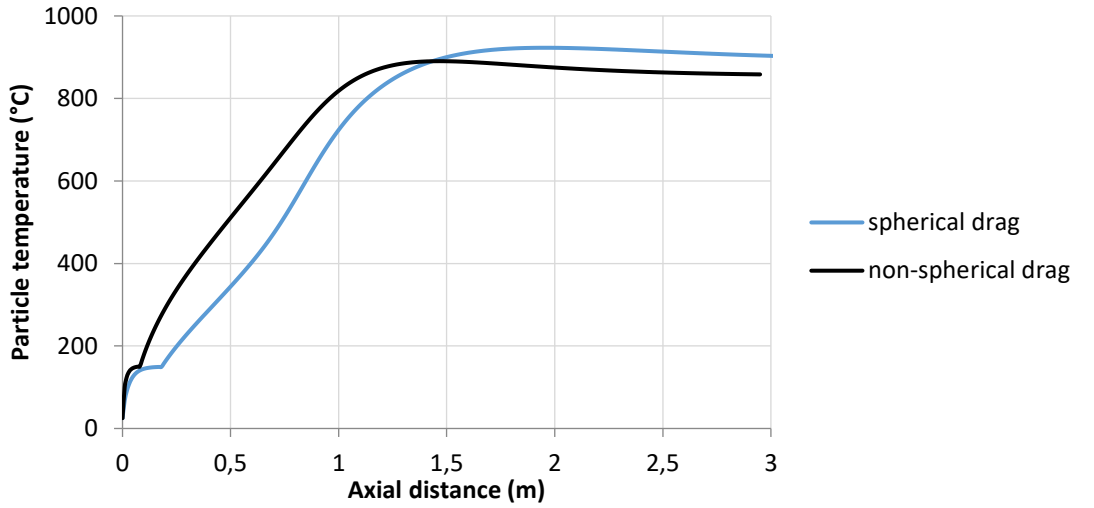

Figure VI.14: Influence of drag modeling on the particle temperature (600 - 800 µm Pine particles in DTF at 800°C)

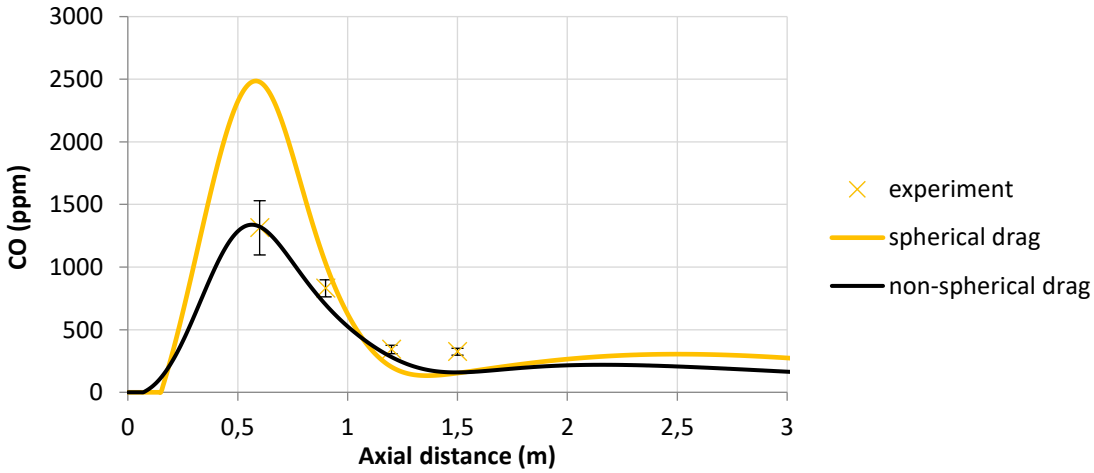

Figure VI.15: Influence of drag modeling on the concentration of CO along the drop tube furnace axis (600 - 800 µm DW particles in DTF at 800°C)

VI.3 Conclusion

In the objective of the development of a predictive model of biomass particle combustion in the pilot experimental rig, the combustion of raw and torrefied pine and demolition wood particles was studied in a drop tube furnace at 800°C. In order to determine the kinetic parameters of devolatilization and char oxidation of each fuel, this study proposes a numerical model using both the pyrolysis gas composition measured during preliminary pyrolysis experiments and an empirical sub-model developed specifically to describe the volume evolution of a single particle observed at 800°C [3].

The model proposed in the present study well predicts the oxygen and carbon monoxide concentrations consistently with the literature. However, the kinetic parameters of char oxidation are lower than those reported in similar studies. This can be related to different experimental conditions and is also partly due to the differences in model approaches, especially considering the volume evolution and the drag coefficient of the particles. Four scenarios of the particle volume evolution found in literature are used, to evaluate how dependent the kinetic parameters are on the volume sub-model. Our previous study using Particle combustion Shadowgraphy generates very close kinetics to those found using a swelling and shrinking scenario during devolatilization and char oxidation respectively. However, when assuming a constant particle volume during devolatilization, the model converges to the experimental points with higher activation energy. The four scenarios generate close profiles of gas concentrations and burnout versus the distance travelled by the particle. Nevertheless, this has to be considered with caution considering the difference in the particle temperature along the furnace axis, in addition to different particle velocities and residence time.

The Influence of drag coefficient model is also addressed in this study. The model compares the kinetic parameters obtained using enhanced non-spherical model of drag versus those obtained using a spherical model. The former model gives higher activation energies for devolatilization (10 kJ/mol to 14 kJ/mol higher) and char oxidation (10 kJ/mol to 19 kJ/mol higher), and better predicts the CO. The particle combustion model and the obtained kinetic parameters (using the non-spherical drag model and scenario 4) in this study will be integrated in a CFD model of biomass flames in a pilot scale reactor.

Chapter VII. Experimental results and model validation of pulverized biomass flames in the pilot scale reactor

This chapter includes the experimental results of the flames in the pilot scale reactor and the predictions of the CFD model. The results in chapter V and chapter VI are used to tune the CFD model presented in chapter IV. A detailed description of the aerodynamics generated by the burner and the particles history is presented in this chapter. Flame development, temperature fields and gas distribution contours are also addressed.

VII.1 Combustion experiments

The combustion experiments in the pilot scale reactor are performed on three fuels: Pine, Pin-T and Pin-P. The three fuels are grinded to the size distribution presented earlier in *Figure IV.2*. After grinding, the moisture content of the three fuels ended as follows: Pine: 3.46%, Pin-T: 2.51%, Pin-P: 7.04%. Prior to an experiment, the pilot gas burner heats the chamber for an entire night. The burner power is controlled so that the temperature of the chamber does not surpass 1000°C. *Figure VII.1* presents the time evolution of the wall temperature before biomass injection and during Pin-T biomass flame operation. Once the upper section of the chamber reaches the defined temperature (950°C), pulverized biomass is injected and the gas burner is shut-off. The flame detector detects the biomass flames presented in *Figure VII.2* through direct imaging. The flame is left for 20 to 30 minutes to reach the steady state temperature. At steady state, the first and second section reach approximately 847°C and the temperature of the lower sections increases slightly with time. The temperature profile is preserved during the experiment that may take up to two-hours.

The boundary conditions of the three numerical cases (presented in *Table IV.6*) are set similar to these experimental conditions of wall temperature and injection conditions.

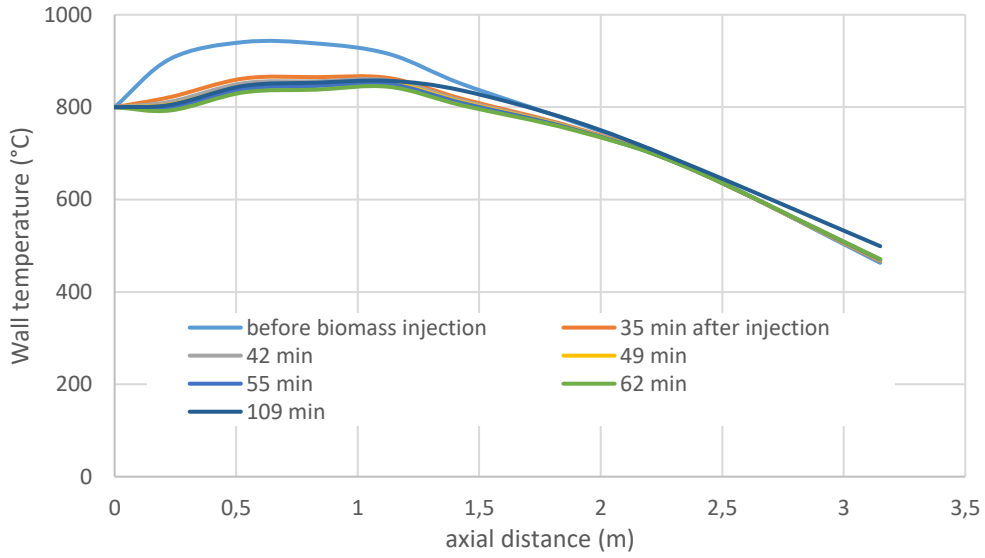

Figure VII.1: Wall temperature before biomass injection and during an hour of Pin-T flame reaching steady state

Figure VII.2: Direct images of the three pulverized biomass flames (from left to right: Pine, Pin-T and Pin-P) at port 7 (94 cm from the burner exit)

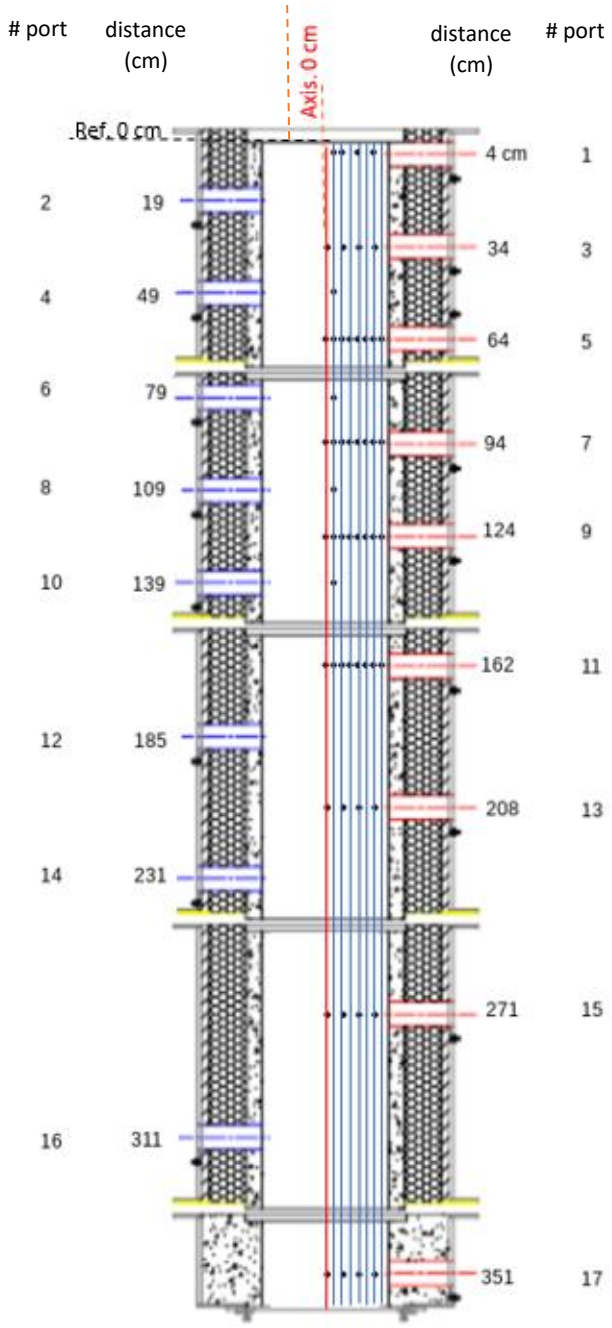

Figure VII.3: Optical accesses for flame imaging and gas sampling points along the reactor length (black dots). They lie on eight vertical axis (blue lines) parallel to the axis of the chamber (red line). The axial distance from the burner (in cm) is indicated next to the port numbers (1 to 17).

The chemiluminescence experiments used the circular ports to construct a full image of the flame. OH* chemiluminescence imaging performed through optical windows with the camera system outside is done via odd ports whereas OH* chemiluminescence endoscopic imaging with the flamoscope is performed through even accesses. Gas concentration measurements are performed using the sampling probe through the odd rectangular access ports. The 52 measurement positions are marked by black points in *Figure VII.3*. The measurements start at each port from the longitudinal axis of the chamber and offsetting 2.5 or 5 cm towards the wall. More points are collected in the region of interest at ports 5, 7, 9 and 11 (respectively 64, 94, 124 and 162 cm from the burner exit) where most of the devolatilization and volatile reactions occur in this region. The probe was inclined by 22° (relative to the axis of the port) inside these ports to sample one point in between the ports. Hence, the sampling points lie on eight vertical axis parallel to the axis of the chamber, with a radial offset of 2.5 cm each. They will be referred to as axis_0, axis_2.5, axis_5, axis_7.5, axis_10, axis_12.5, axis_15 and axis_17.5 respectively.

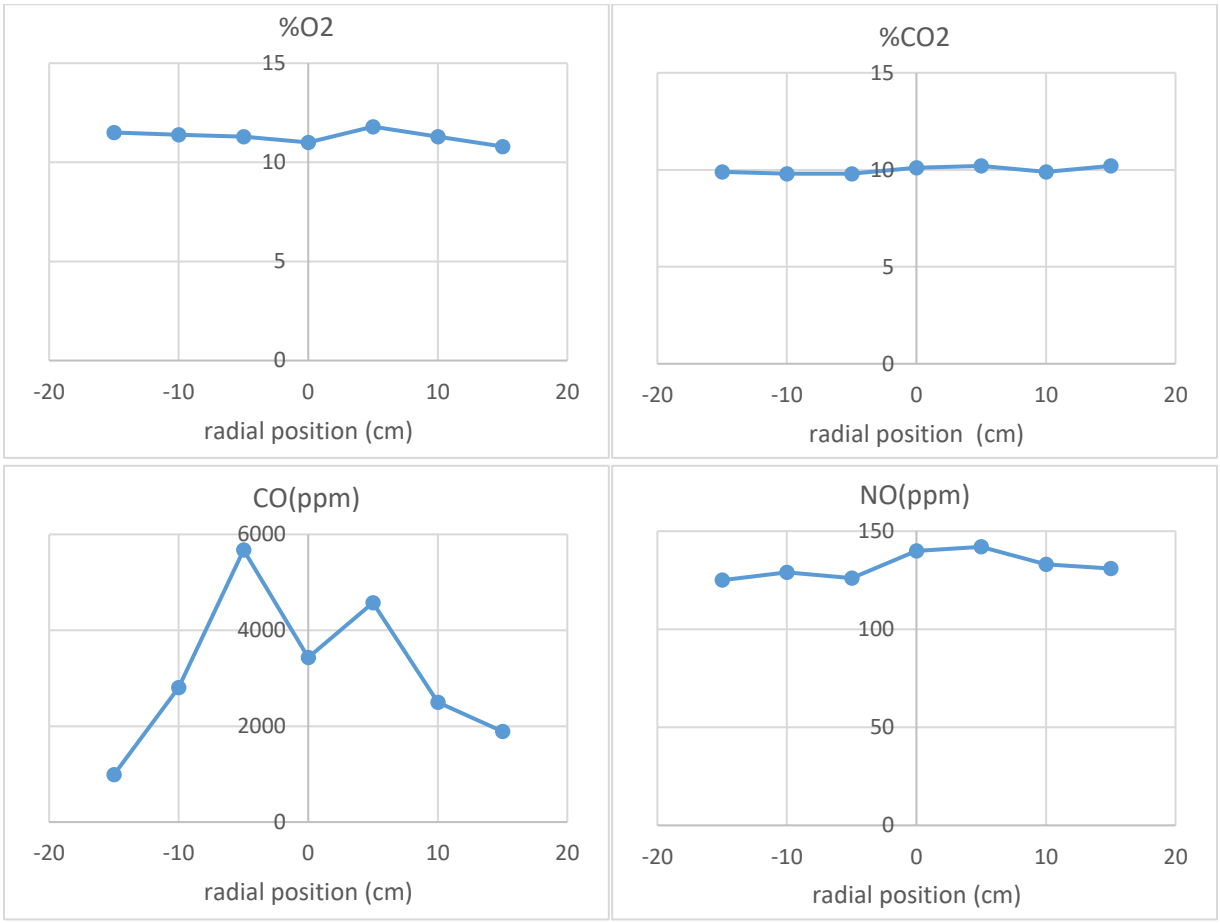

Figure VII.4: Mean gas concentration measurements in the Pin-T flame, from central line (0cm) to both sides of the chamber wall, at port 9 (124 cm from the burner)

The measurements were done from only one side of the flame assuming that the latter is symmetrical. In order to test this assumption, several measurements are collected on both sides of the flame at measurement ports 9 and 11. *Figure VII.4* shows the mean gas concentration of O_2, CO_2, NO and CO at seven sampling points at port 9 on both sides of the torrefied pine flame axis. The probe is inserted from right to left. Considering measurements uncertainty, the

measurements are similar on both sides of the flame, which validates our assumption of a symmetrical flame.

VII.2 Biomass flames simulations in the pilot scale reactor

RANS biomass flames simulations are conducted with the Pressure-Based Steady solver of ANSYS Fluent. It uses the finite volume method to solve the governing equations. The pressure and velocity are coupled with the coupled algorithm [232], and the pressure is discretized with the second order scheme. The energy, species, momentum, and turbulence equations were all discretized with the Second Order Upwind scheme [233]. DO equations were discretized with the First Order Upwind scheme [233]. The pseudo transient algorithm is enabled, which add an unsteady term to the solution equation in order to improve the stability and convergence behavior.

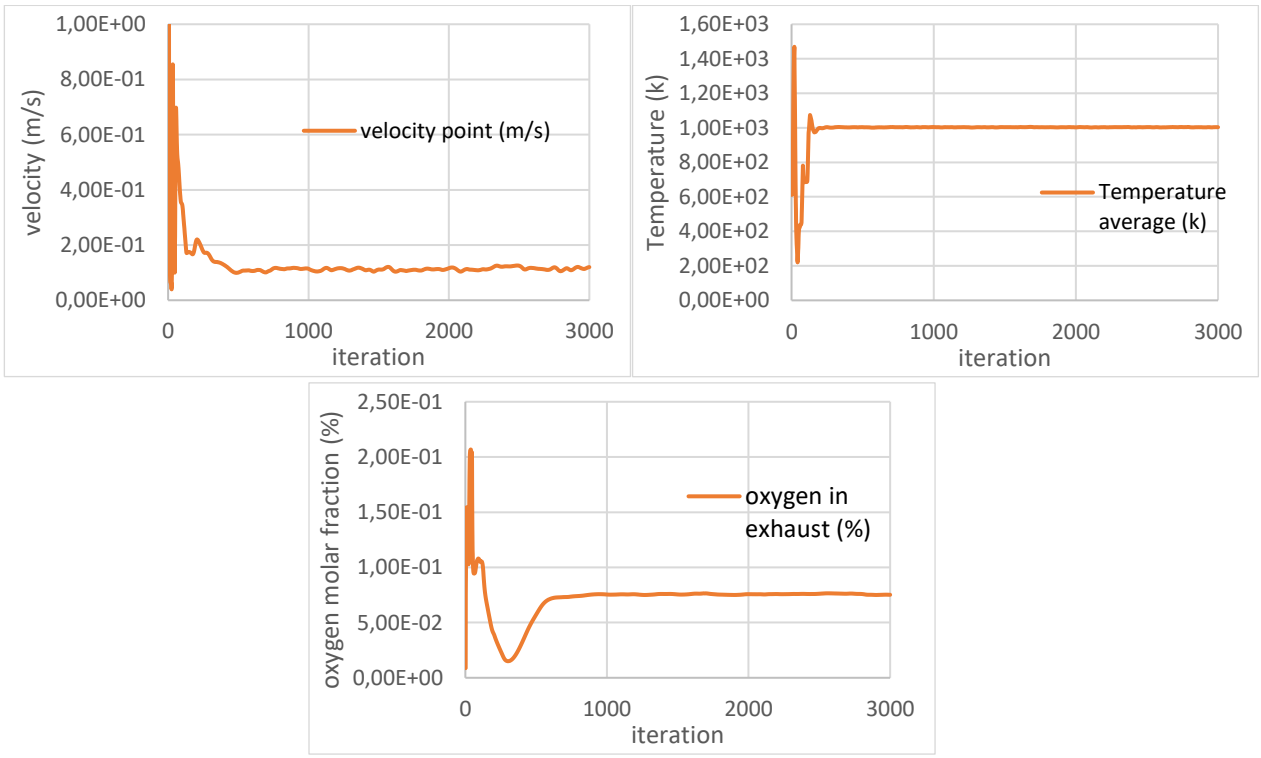

Figure VII.5: The monitored values of velocity, temperature and oxygen fraction during 3000 iterations

During the calculations, a continuous oscillation of the residuals was observed each DPM iteration. This can be resolved either by increasing the number of continuous phase iterations per DPM iteration or/and by reducing the under-relaxation factor of DPM. Both methods increase the stability but require more iterations to converge. The number of continuous phase iterations per DPM iteration was set to 5 and the under-relaxation factors of DPM, volatiles, and CO were adjusted to reduce the magnitude of the oscillations. The convergence of the solutions was judged by monitoring the average temperature of the computational domain, the velocity at a randomly defined point near the axis, and the mole fraction of oxygen at the reactor

outlet. The calculations were stopped after these monitored values did not change between the iterations and the residuals had fallen below sufficient limits (below 10^{-4} for continuity residuals and 10^{-5} for the other residuals). *Figure VII.5* shows the stability of the monitored entities during 3000 iterations of the Pine combustion case, which represents a total calculation time of about 2 hours on Rescale Emerland server (Intel Xeon Platinum P-8124 @ 3.00GHz (Skylake) @ 3.0 GHz) using 18 cores (Memory/core: 4 GB, Interconnect: 25 Gb/s)

VII.3 Results and discussion

VII.3.1 Model Validation

The model predicts the flow dynamics, particle tracks and degradation history, the distribution of gas species concentration and reaction kinetics of the species. On the other hand, the experimental results provide the species concentration from probe sampling, and the flame topology from the chemiluminescence measurements. Analyzing the experimental data necessitates first to understand the aerodynamics generated by the burner and the trajectory of the particles. The degradation history of the particle is also important to explain the distribution of the species in the reactor and the reaction zones and their intensities. The aerodynamic features and particle history are predicted by the model, which needs to be validated first against the experimental data, before using them to characterize the simulated flames. Therefore, in this section, the measured gas species concentrations collected on the centerline of the reactor are compared to the predicted concentrations.

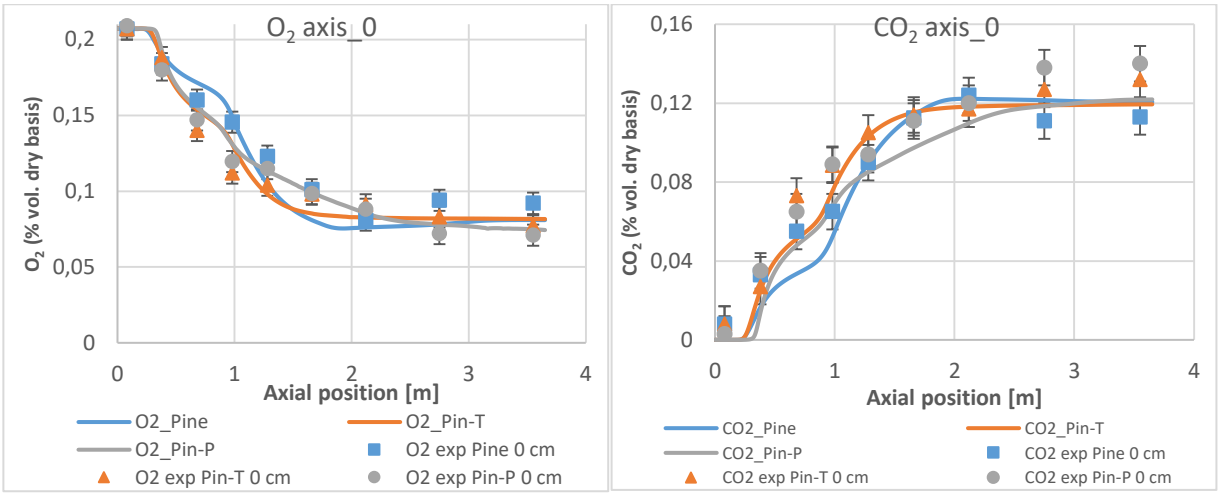

Figure VII.6: Comparison of the concentrations of O_2 and CO_2 measured experimentally (symbols) and the profiles predicted by the CFD model (lines)

Figure VII.6 compares the concentrations of O_2 and CO_2 measured experimentally on the centerline and the profiles predicted by the CFD model. The model reproduces fairly well the experimental data of oxygen consumption on the centerline, which reflects the fine procedure followed to determine the kinetic parameters. CO_2 is slightly underestimated by the model but the deviation is still accepted considering the measurement errors discussed previously. The used probe method overestimated the CO_2 without cooling the probe (§ III.10.2). In addition, a slow surface oxidation model may also be another possibility, which increases the deviation between the experimental and numerical results.

The reaction model adopted in the homogeneous phase of the CFD simulation coming from Fluent database is simplified consisting of a two-reaction mechanism. The model considers CO as a product of oxidation of the volatiles rather than the major constituent of them. This shifts the predicted CO peak location from the real one as seen in *Figure VII.7*. In fact, the real CO peak coincides with the simulated volatiles peak. The devolatilization model reproduces well also the beginning and the end of the volatile region. This means that the devolatilization kinetics are fine-tuned but the chemical kinetics of the homogenous phase reactions need optimization. Therefore, the predicted contours of CO and the experimental data do not represent the same parameter.

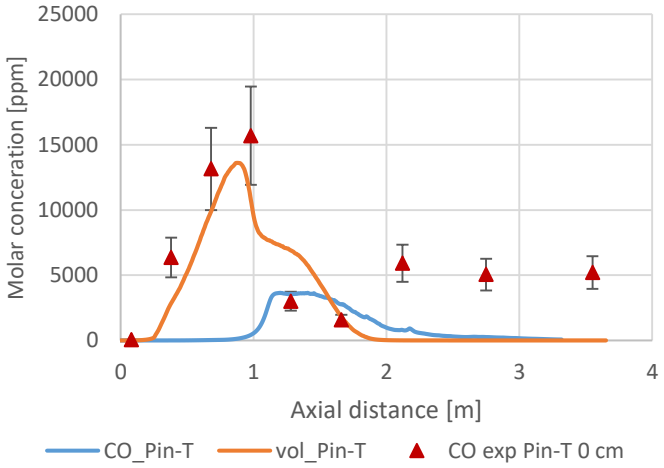

Figure VII.7: Prediction of the volatiles (vol) and CO molar concentration on the axis of Pin-T flame versus the measured CO molar concentration

As reactive species, uncertainty in CO concentrations by probe sampling have been also already mentioned (§ III.10.2). However, comparing the position of volatile release with the measured CO values verifies that the simplified devolatilization model can simulate the devolatilization correctly. Downstream the volatiles flame, the predicted CO contours are not high enough where char combustion is taking place. This is probably due to fast reaction kinetics of CO in the simulation, which causes a rapid oxidation right after being produced by the surface reaction.

VII.3.2 Flow dynamics and particles tracks

The contours of the axial velocity of the continuous phase obtained by flame simulation and presented in *Figure VII.8* show aerodynamic features composed of a long jet, produced by the high injection velocity of the primary and secondary air. The jet decays progressively and a strong reverse flow appears behind, back to the roof where the recirculating flow is entrained again by the jet momentum. This creates as expected a large outer recirculation zone (ORZ) and a stagnant zone near the roof corners. This also helps bringing the hot gas in the reaction zone back to the burner exit and promotes earlier devolatilization of the injected particles. The ORZ extends over 110 cm with its vortex core situated at 38 cm from the burner and at 13 cm off the chamber axis.

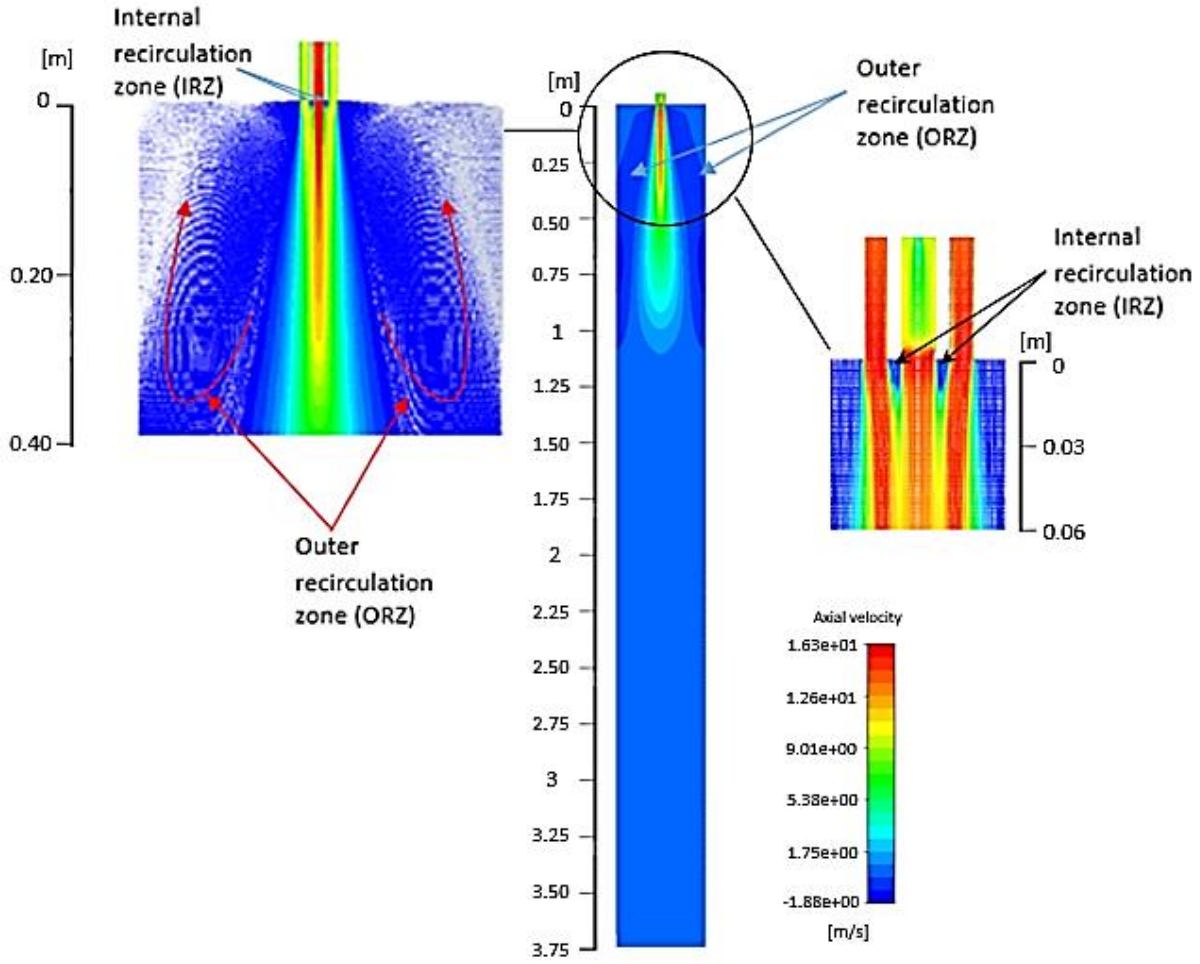

Figure VII.8: Axial velocity contours of the homogeneous phase for Pine flame

Downstream the jet and the recirculation zone, the streamlines uniformly point toward the reactor exit with little turbulence. A close look to the burner region shows a low magnitude internal recirculation zone (IRZ) just behind the bluff body, as intended by design. This allows the central jet to dominate and penetrate the IRZ. The central and annular jets open up right after injection and form boundaries of the IRZ, up to the meeting point about 5 cm ahead from the burner.

Figure VII.9 illustrates the particles trajectories in the reactive flow with different color shadings indicating the particle velocity. The particles are injected at zero velocity at the annular inlet of the burner and they are subsequently entrained by the transport air. Small particles acquire similar injection velocity as the carrier air, while large particles slip faster and enter the furnace at higher velocities. The stream of particles quickly scatters radially with the central jet with no interaction between the particle and the IRZ. They stay confined by the shear layer between the primary and secondary air streams, up to about 14 cm from the injection point. A simulation case was done using the same setup without activating the stochastic tracking of the particles. Without including the effect of turbulence on the particle motion, most of the particles penetrated the outer recirculation zone and the reaction zone was pushed towards the reactor exit. However, when activated, the turbulence shows a significant impact on the particles

trajectories. The aerodynamic flow and the particle trajectories are very similar, which means that the particles stick much more effectively to the fluid flow. Large particles are pushed by inertia down the reactor while smaller particles diverge with the air streamlines towards the outer recirculation zone and the furnace wall. Large eddies are formed by the recirculated particles back to the freshly injected secondary air. Only light ashes and the light chars at this point are entrained back to the top roof, inducing a low DPM concentration in this region.

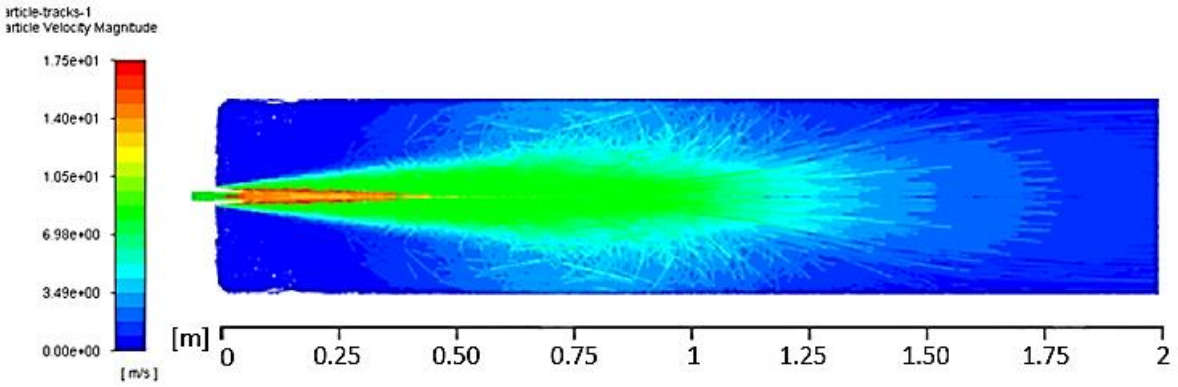

Figure VII.9: Trajectories of 1400 particles of Pine in reactive flow color-scaled by their velocities

VII.3.3 Particle history: drying, devolatilization and surface oxidation

The trajectories of the particles influence the thermal and chemical conditions encountered by the particles after injection. The degradation history and the morphological evolution of the particles play an important role in the competition between the body forces and the flow forces. These forces, as described earlier, determine the particle velocity and trajectory. The figures below trace the trajectories of 1400 particles of Pine, Pin-T and Pin-P. Three consequent time intervals are displayed; each corresponds to a different law in the discrete phase model, activated by each particle individually:

- Law 2: Particle drying tracks colored by the particle's moisture mass fraction (*Figure VII.10*)
- Law 4: Particle devolatilization tracks colored by the particle's volatile mass fraction (*Figure VII.11*)
- Law 5: Char surface oxidation tracks colored by the particle's fixed carbon mass fractions. (*Figure VII.12*)

Particle drying starts about 2 cm ahead the injection point. However, the momentum and the thermal inertia of large particles elongate the drying zone. This zone is shorter for Pin-T considering its rapid heating due to small size and its low moisture content. The fact that small particles heats rapidly with lower inertia than large particles makes the drying length of Pin-P similar to Pine, with twice the initial moisture content of the former but larger particle size of the latter.

Figure VII.10: Particles trajectories during the drying stage colored by liquid mass fraction (single color scale for the three cases, top to bottom: Pine, Pin-T and Pin-P flames)

As shown in *Figure VII.11*, devolatilization already starts for small particles in the drying zone; nevertheless, most of the particles in the jet hold their volatiles in the drying zone. Once the activation energy is attained, the particles start the devolatilization. Particles that interact early with the secondary air stream heat faster and undergo devolatilization outside the jet core. This is the case of some Pin-P particles showing some devolatilization in the shear layer. Also, Pine and Pin-T particles have this effect further. The jet velocity decays later and a part of the gases is recirculated back to the roof. At this stage, light devolatilizing Pin-T particles follow the airstreams to complete the devolatilization in the ORZ or proceed to char oxidation there. Pine particles are also diverted by air but with high momentum, they are less likely to reverse their axial direction, and rather flow towards the wall. A large fraction of large Pine particles is not affected and they continue to form a second volatile-rich zone. Pin-P case is different as no streams are traced for devolatilizing particles in the ORZ. While some particles are diverted early towards the ORZ, they seem to be volatile free before advancing in the zone. Other particles are predicted to flow further in the reactor, which can be explained by the lower calculated drag on the particles due to a higher predefined shape factor compared to the other cases. Large particles, which already dry over a long distance, end up with high velocity deposing their volatiles over a long distance as well. This can be also linked to the observations made at particle scale, where the severe thermal treatment induces more pores in the particle structure causing a smooth ejection of volatiles whenever the treated particle is exposed to heat. PCS results show that Pine, Pin-T and Pin-P has comparable flame durations despite their huge difference in volatile content.

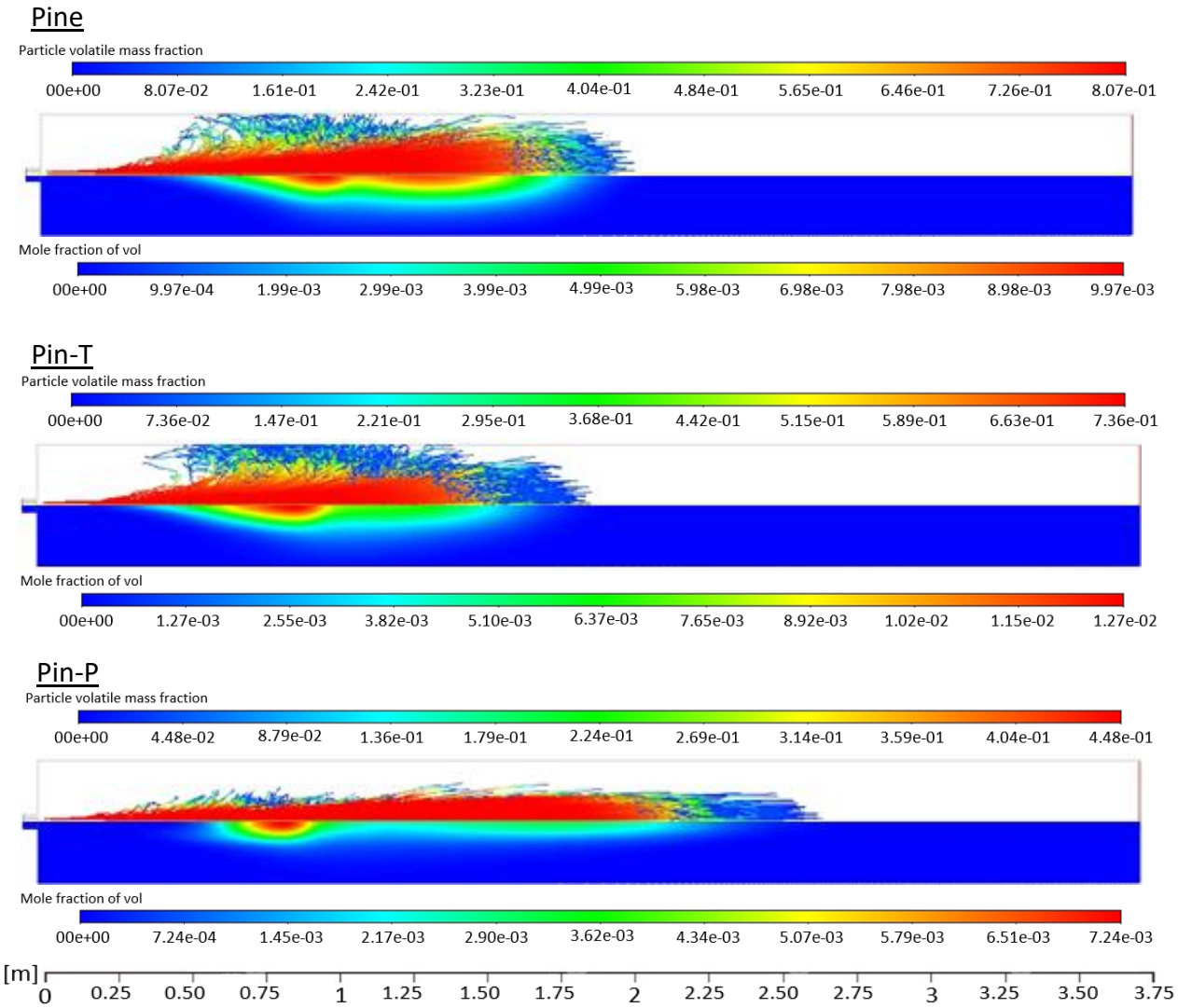

Figure VII.11: Particles trajectories during the devolatilization colored by volatile mass fraction mirrored by the volatile mole fraction contours (top to bottom: Pine, Pin-T and Pin-P flames)

Surface oxidation starts at the end of devolatilization with certain overlap and it continues until the burnout. It is a long process and that is why the surface reaction law is found to be active almost everywhere in the reactor (*Figure VII.12*). Mainly, small char particles oxidize in the jet core or in the ORZ, while particles that dominate the aerodynamic effects burn in the lower part of the reactor. The heterogeneous reaction seems to be active near the walls. However, concentrating the particles near the wall might be caused by poor wall collision treatment in the simulations.

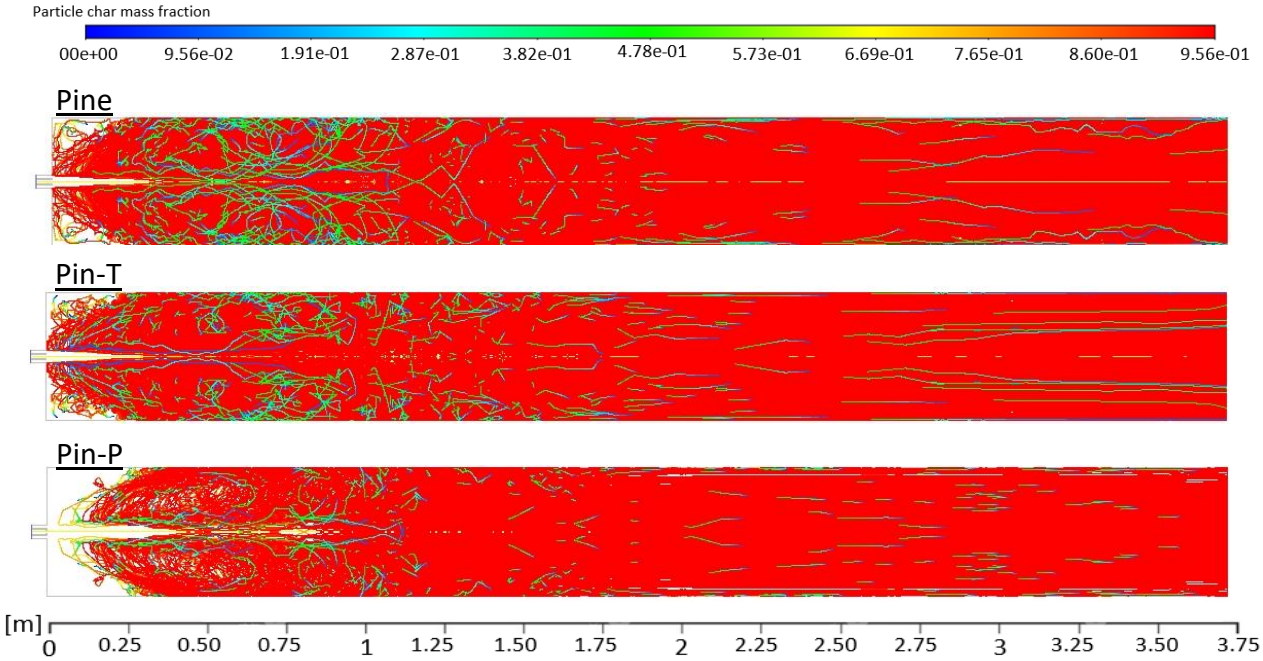

Figure VII.12: Particle trajectories during char oxidation colored by the char mass fraction (single color scale for the three cases, top to bottom: Pine, Pin-T and Pin-P flames)

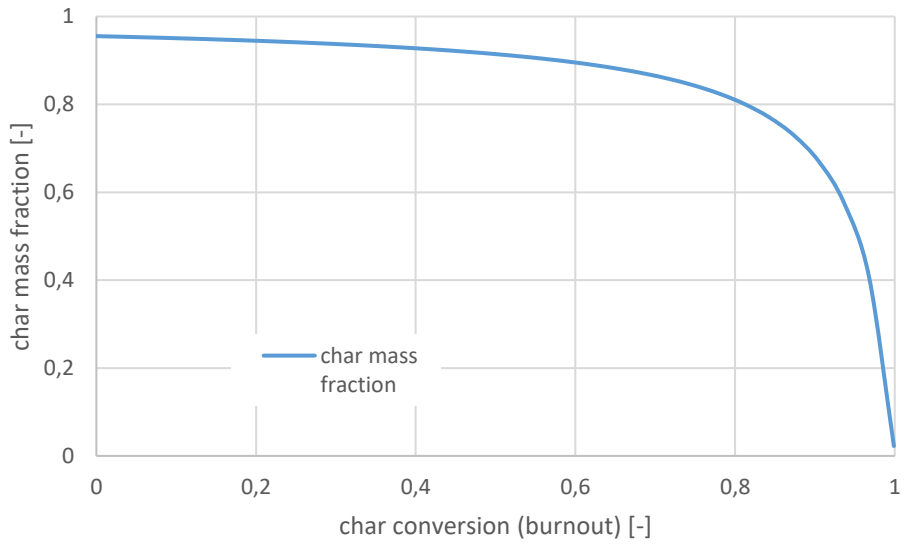

Figure VII.13: Char mass fraction evolution with the progress of the char surface oxidation of Pin-P

It should be noted that the char mass fraction is not a good indicator of the total burnout of the particle. During char oxidation, the particle is mainly composed of char (FC) and few ash content. The char mass fraction is calculated as the ratio of the remaining carbon and the sum of ash and initial FC ($Char\ mass\ fraction = C/(FC + ash)$). Fixed carbon is always dominant in front of the low ash content. As illustrated by *Figure VII.13*, the char mass fraction is still 80% by the time 80% of the initial char is consumed. So it is difficult to observe the advancement of the reaction through the colored tracks. The global burnout of Pine, Pin-T and Pin-P is estimated from the average CO_2 and CO concentrations measured in the flue gases as

90%, 92.5% and 87% respectively. This means that in the three cases, it is normal for many particles to finish their journey red colored in *Figure VII.12* (char burnout is around 80%).

VII.3.4 Flame development

Figure VII.14 shows the contours of the reaction rate of oxidation of volatiles in the three cases. All cases show a lifted long flame. This structure is due to the high injection velocity that shifts the devolatilization zone away from the burner and permits the jet to develop in the combustion chamber. The volatile zone emerges before the end of the drying phase. A volatile rich region is formed that subsequently diffuses and mixes with air in a thin layer triggering the oxidation. This layer of high reaction rate represents the flame front of the volatiles. A cross section of the OH* chemiluminescence images presented in *Figure VII.15* and *Figure VII.16* would give a similar profile to the flame front in *Figure VII.14*. Indeed, OH* chemiluminescence is an indicator of the heat release in gas flames, which means it can be directly related to the zone of volatile oxidation reaction. The predicted reaction zones match well with the emission signal of OH* chemiluminescence.

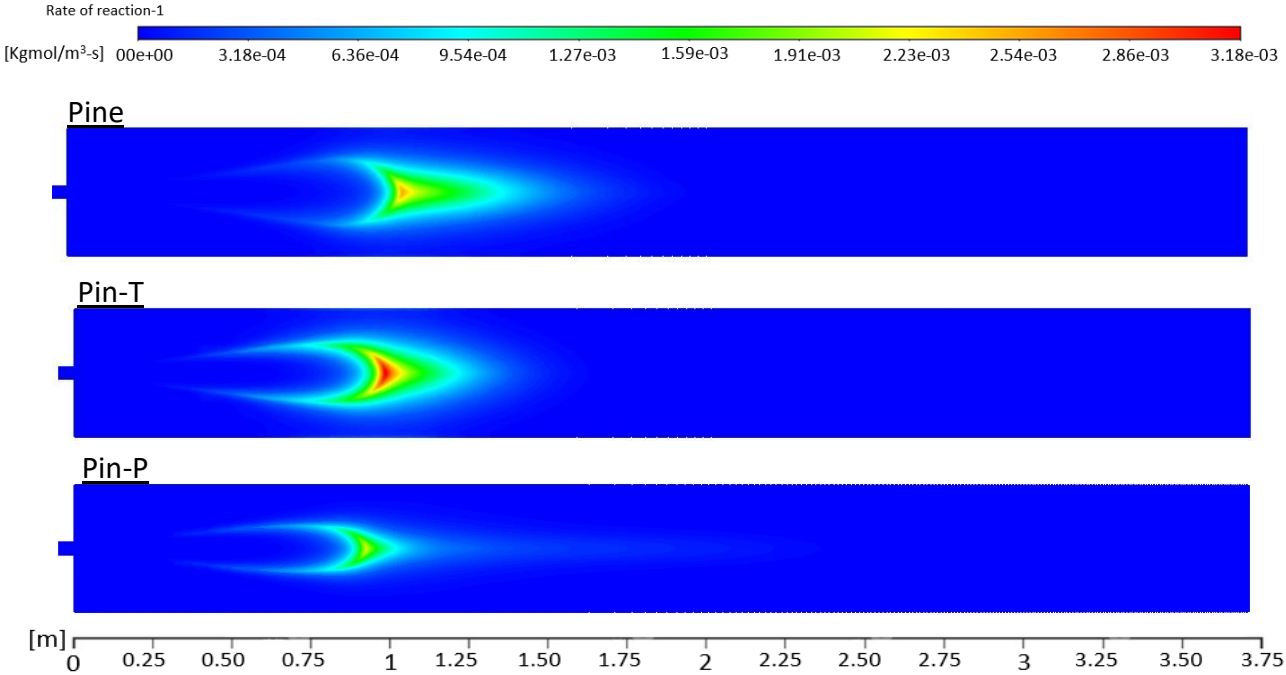

Figure VII.14: Reaction rate of oxidation of volatiles (single color scale for the three cases, top to bottom: Pine, Pin-T and Pin-P flames)

Both experiments and simulations indicate that the reaction starts at port 3 (z = 34 cm) for Pin-T and Pin-P where the particles start devolatilization. Slight chemiluminescence signal is detected by camera 1 at this position while camera 2 shows a clear reaction zone at port 4 (z = 49 cm) in Pin-P flame and a low OH* emission in Pin-T flames. Large PSD increases the lift-off of Pine, where the earliest traces of OH* are detected at port 5 (z = 64 cm). However, the flame front of Pin-P locates higher in the reactor than Pin-T despite having similar PSD and higher moisture content. The earlier reaction can be attributed to the low ignition temperature of Pin-P (220°C) as measured at particle scale compared to Pin-T (290°C). Both OH* chemiluminescence series indicate that the reaction intensity grows progressively from port 7 (z = 94 cm) until reaching its peak at port 8 (z = 109 cm) in the case of Pin-T and Pin-P, while

in Pine flames, OH* signal peaks at port 10 (z = 139 cm). This is attributed to the reaction zone of the volatiles of large particles of Pine. The reaction rate starts to decrease afterwards because the concentration of the remaining volatiles decreases, in addition to the depletion of available oxygen.

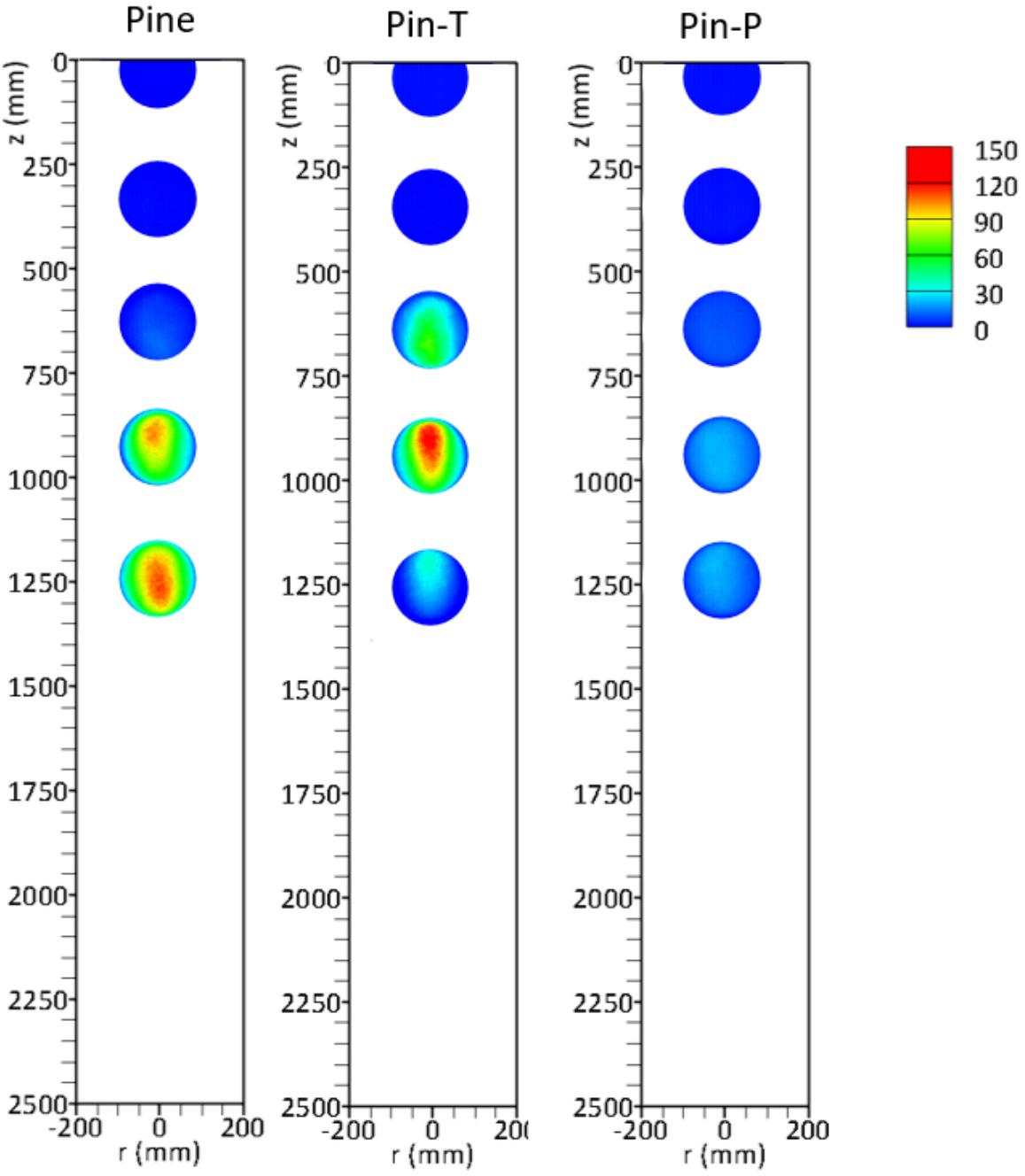

Figure VII.15: Average images of chemiluminescence of Pine, Pin-T and Pin-P flames measured from odd ports by camera 1 set outside the reactor in front of the optical windows

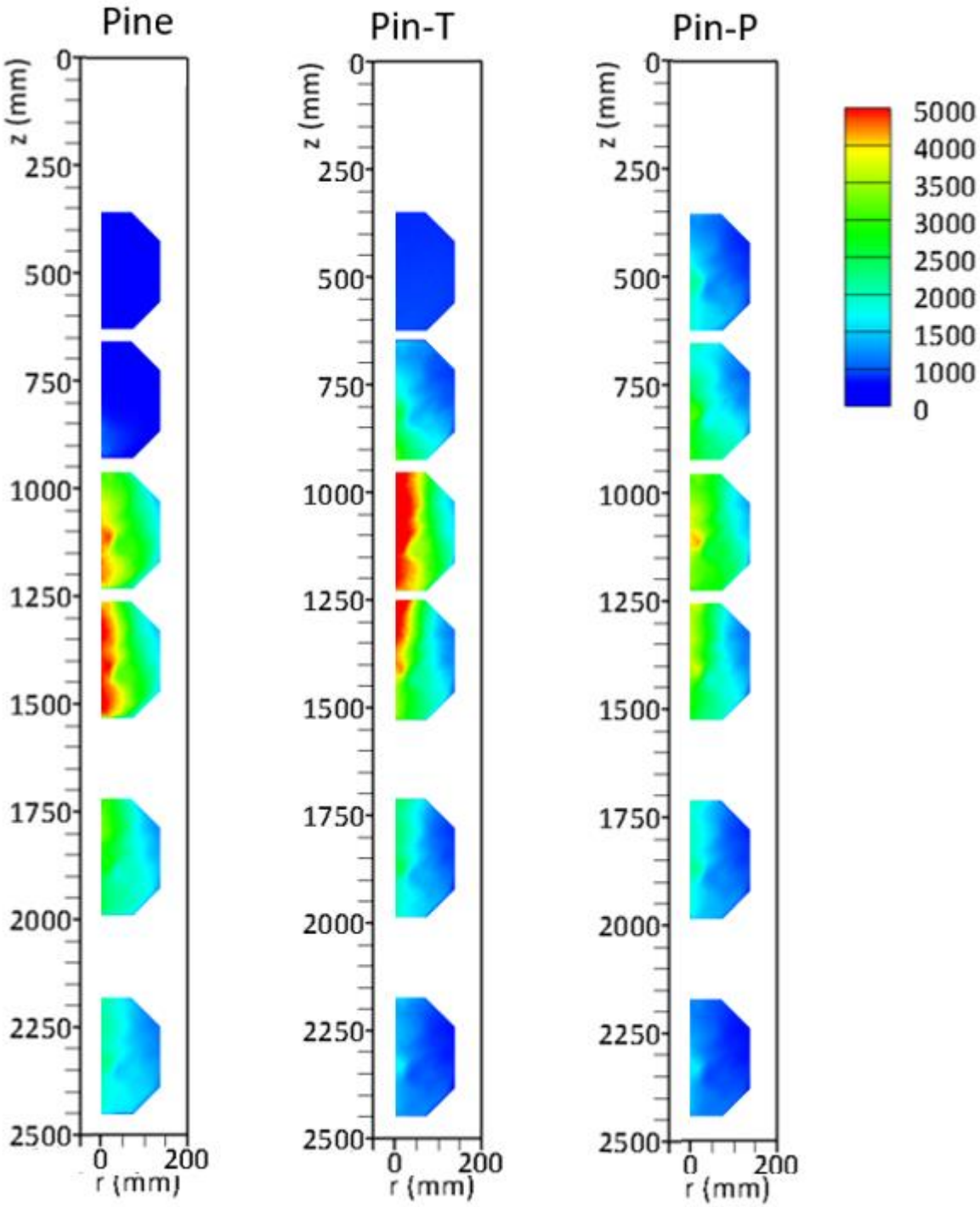

Figure VII.16: Average images of chemiluminescence of Pine, Pin-T and Pin-P flames measured from even ports by camera 2 with the flamoscope system (right-side view)

Pin-P flame contains less volatiles and the reaction is more diluted because of the long devolatilization trajectory. As a result, OH* chemiluminescence of Pin-P is relatively low. To the contrary, Pin-T emits more volatiles in a shorter distance and creates a rich volatile region as demonstrated earlier, which promotes the reaction rate in the flame front. A higher volatile content improves the diffusion of the combustible gases, causing intense oxidation and a larger flame volume. Pine similarly have a large flame volume, however, the two-region

devolatilization reduces the peak of reaction intensity despite having the highest volatile content. Small and large particles react in separate regions, diluting the chemical reaction.

VII.3.5 Temperature field

Figure VII.17 presents the temperature contours in the pilot scale reactor for the three simulated flames. The Temperature profile on the central axis (*Figure VII.18*) resembles the profiles of temperature evolution of the combustion of a single particle of biomass observed in shadowgraphy (*Figure V.15*).

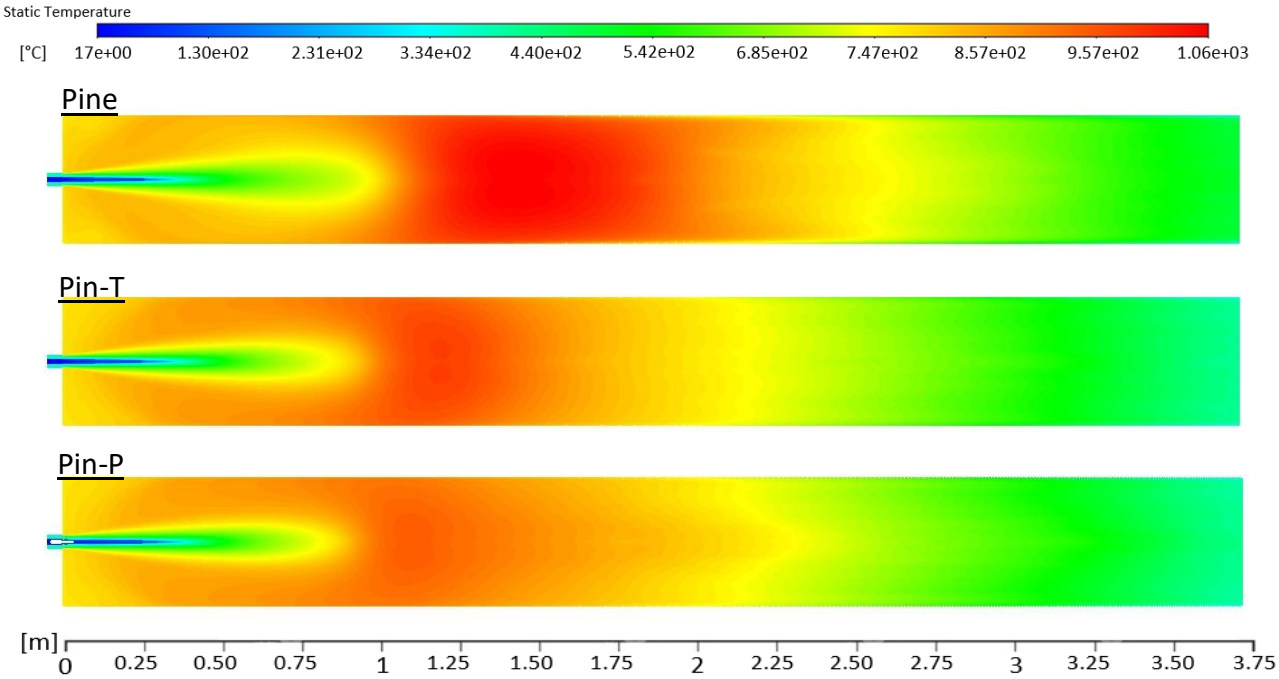

Figure VII.17: Temperature maps of Pine, Pin-T and Pin-P in the pilot scale reactor (single color scale for the three cases, top to bottom: Pine, Pin-T and Pin-P flames)

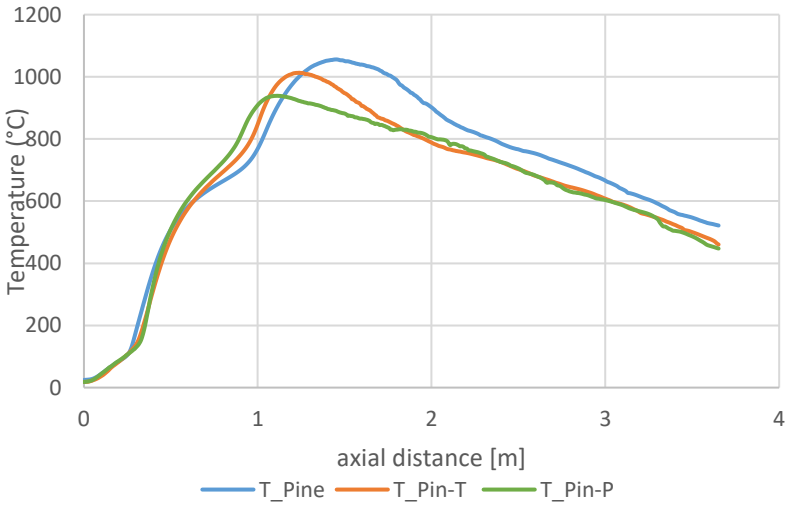

Figure VII.18: Temperature profile of Pine, Pin-T and Pin-P flames on the centerline of the reactor (axis_0)

The injected air temperature heats first by the radiating walls and the hot recirculating gas. A point of deflection is detected after port 3 (z = 34 cm), which coincides with the onset of OH*

chemiluminesence signal and oxygen consumption. This suggests that this temperature rise is caused by the heat liberated by the oxidation of volatiles. Pin-P shows earlier rise than Pin-T and Pine respectively in accordance with the chemiluminescence results. A peak is then attained firstly by Pin-P at 938°C, followed by the peak of Pin-T flame at 1013°C and Pine peak comes last with the highest value at 1056°C. A part of the gases is recirculated back to the burner entraining some particles, while the jet core develops towards the outlet. As a result, the temperature drops on axis_0 because a part of the heat is captured by the recirculation zone. As mentioned earlier, fewer Pine particles are recirculated with the streamlines to the ORZ, whence the higher temperature on the axis of Pine flames after the peak and consequently lower temperature is observed in the ORZ. On the other hand, Pin-T and Pin-P particles are more directed to the ORZ. Therefore, most of their energy is liberated there causing a higher temperature and a more efficient heating of the injected stream. After 2 m from the burner exit (port 13), the jet opens more behind the ORZ and the particles scatter radially. The heat release becomes more radially homogeneous causing less temperature gradients from the axis to the wall and flat radial temperature profiles.

VII.3.6 Oxygen distribution

Figure VII.19 shows the contours of mole fraction of oxygen in the reactor for the three biomass flames. *Figure VII.20* presents the comparison of the predicted oxygen profiles and the measured values along the eight vertical axes. Right after injection, oxygen gets diluted by the liberated moisture and volatiles in the injected jet and by the recirculated gases in the ORZ. The consumption of oxygen takes place mainly in the flame during the oxidation of volatiles. A short flame lift-off for Pin-T is marked by a rapid decrease in the oxygen concentration. Pine reactions are further on the axis where oxygen is largely consumed by the high concentration of volatiles. The oxygen reduction locates higher on the chamber axis for Pin-P but the consumption eases down later on, because of the long diluted devolatilization region.

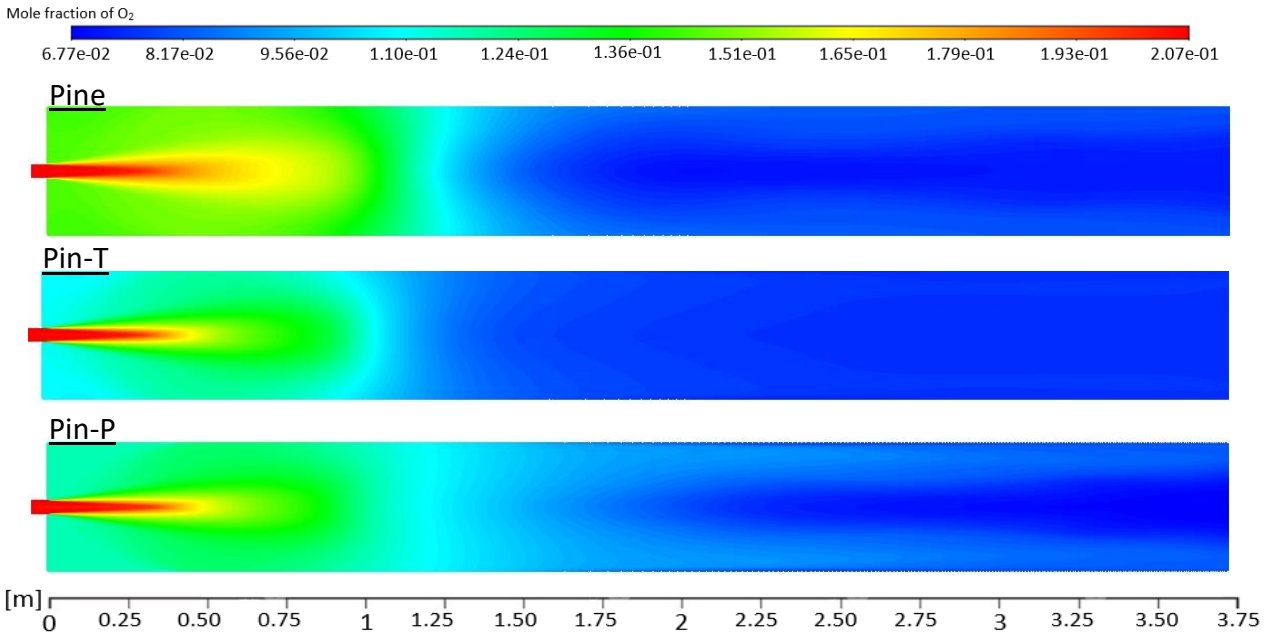

Figure VII.19: Oxygen contours of Pine, Pin-T and Pin-P in the pilot scale reactor (single color scale for the three cases, top to bottom: Pine, Pin-T and Pin-P flames)

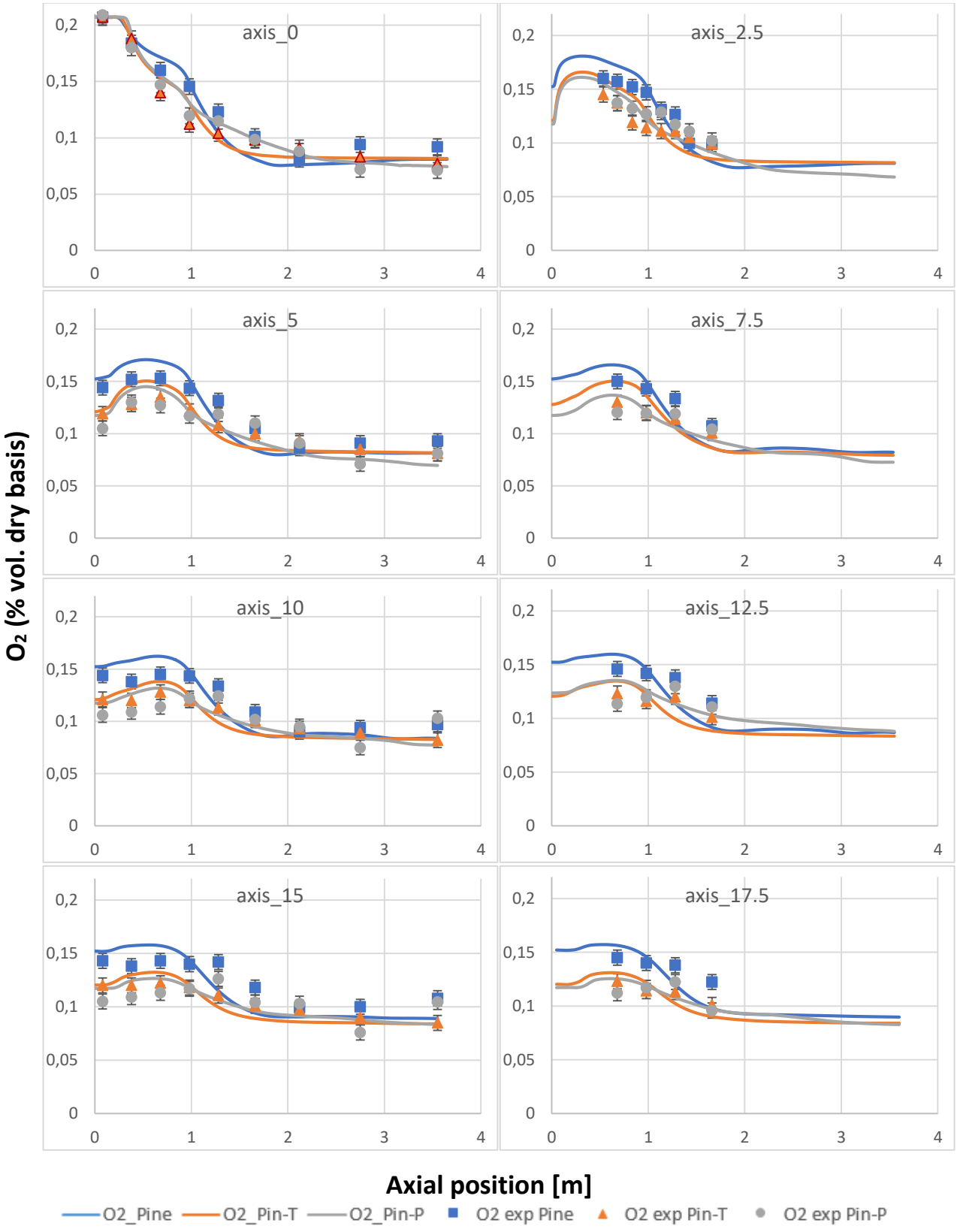

Figure VII.20: Comparison of experimental results and predictions of oxygen profiles on eight vertical axes

Notice that the oxygen concentration on axis_2.5 exhibits a maximum approximately at the same position in the three cases, where it starts later to decrease. A similar profile is noticed experimentally and numerically on the other offset axes but the maximum is found further in the reactor as we approach the wall. The decrease in oxygen concentration happens in the ORZ and the maximum is at the point where the central jet reaches a 2.5cm radius and then further to 5 cm and so on. This means that the maximum is on the shear layer between the jet and the ORZ. This observation shows that the aerodynamics of the three flames is predicted satisfyingly well by the CFD model.

Particles in the ORZ are mainly chars undergoing heterogeneous oxidation. Experiments measure low oxygen concentration for Pin-P in the ORZ, followed by Pin-T and finally Pine with the highest oxygen concentration near the roof. The numerical results predict the same trend. This proves again that particles of Pin-T and Pin-P follow better the aerodynamics of the flame than Pine. Results at particle scale recorded char combustion over a long duration and it gets longer with the severity of the thermal treatment. Particles captured by the ORZ have longer residence time in the reactor, enabling a complete burnout.
However, large particles acquire high velocity and their reaction goes slowly over the last two meters of the reactor. This is the case of the majority of Pine chars and the large particles of Pin-T and Pin-P. Therefore, oxygen consumption is slow in the lower section of the reactor, which explains the flatness of the profile at the end of every axis. However, one can notice from experiments and simulations that the oxygen molar fraction increases slightly as we approach the wall especially in the Pin-P case. The particle tracks of each fuel run by Fluent suggest that particles whose momentum is high enough to escape the aerodynamic effects apt to stay in the center of the reactor afterwards. Consequently, the oxygen consumption is higher on the central axis and decreases towards the wall. The gradient is bigger for Pin-P because Pin-P particles carry their volatiles to a long distance in the reactor as seen earlier, and even after complete devolatilization, they have high fixed carbon content so they tend to be heavier than the chars of Pine and Pin-T.

VII.3.7 Carbon oxides distribution (CO and CO_2)

The experiments in the drop tube furnace showed that CO is the major constituent of the volatiles released by all the tested fuels. Therefore, CO should peak in the devolatilization region then decreases by oxidation, only to increase later as a product of the oxidation of char. This is verified by the measurements as presented in *Figure VII.21* on four vertical axis. The profiles strongly replicate the profiles observed in the drop tube furnace. A minimum is spotted at port 11 (z = 162 cm), where the flame front depletes and many particles either are in the ORZ or escape it to undergo char oxidation later. The value of the minimum is dependent also on the overlap of the homogeneous and heterogeneous oxidation. A longer overlap would increase the CO production in the devolatilization zone preventing the CO level from going near zero as measured for Pine. Particle scale results have showed that the overlap increases with lower volatile content. The order of the CO minimum value at port 11 validates this conclusion. Pine has lower minimum, followed by Pin-T then Pin-P, indicating a minimum overlap for Pine and a maximum overlap for Pin-P. The CO peak position in the devolatilization zone is in

accordance with the volatile contours presented earlier in *Figure VII.11*. Pin-P has the lowest maximum because of its low volatile content. Pine shows lower peak than Pin-T, which may be attributed to the distribution of Pine volatiles in two regions. Indeed, the second increase of CO after port 11 (z = 162 cm) is most probably released by char oxidation and the devolatilization of large particles. Instantaneous images of OH* chemiluminescence captured signals coming from isolated particles of Pine at port 14 (centered at z = 231 cm), which suggests that these particles are enveloped by a flame (*Figure VII.22*).

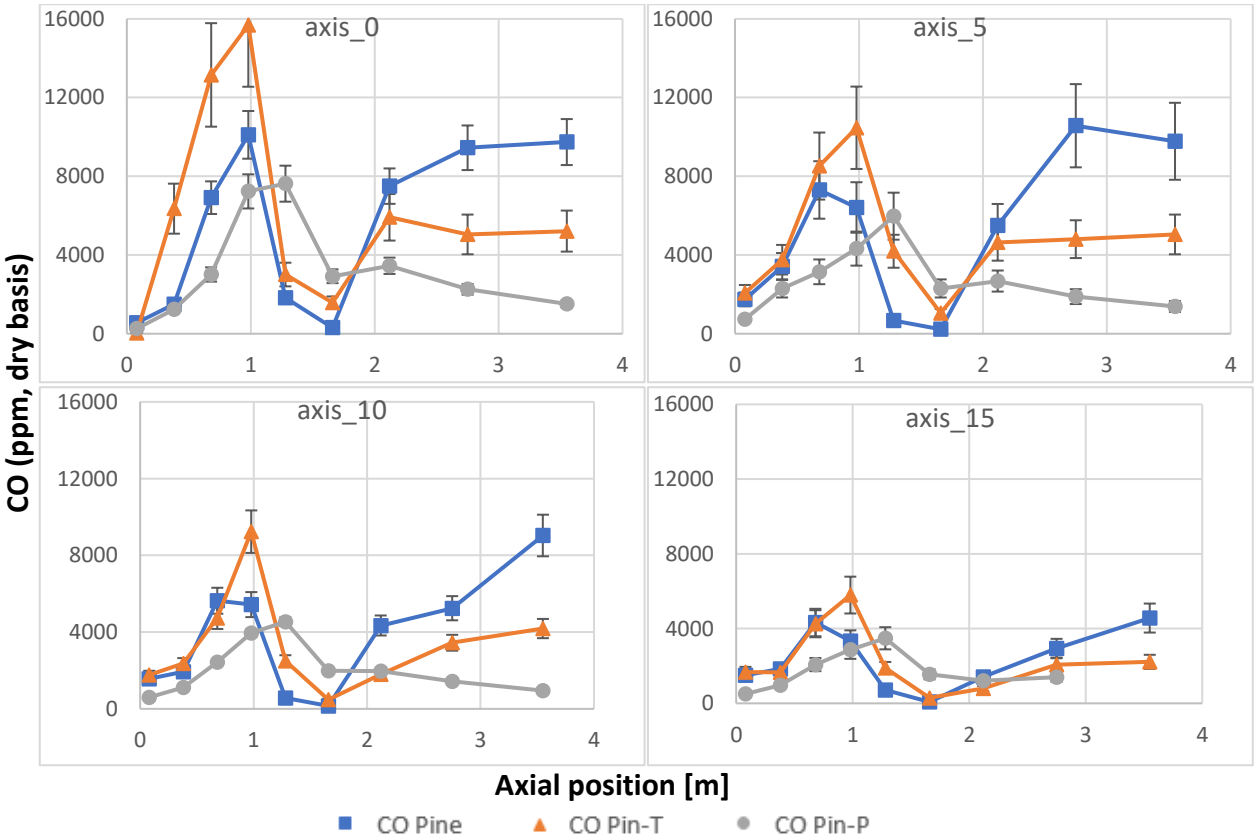

Figure VII.21: Experimental results of CO distribution on four vertical axis for the three pulverized biomass flames

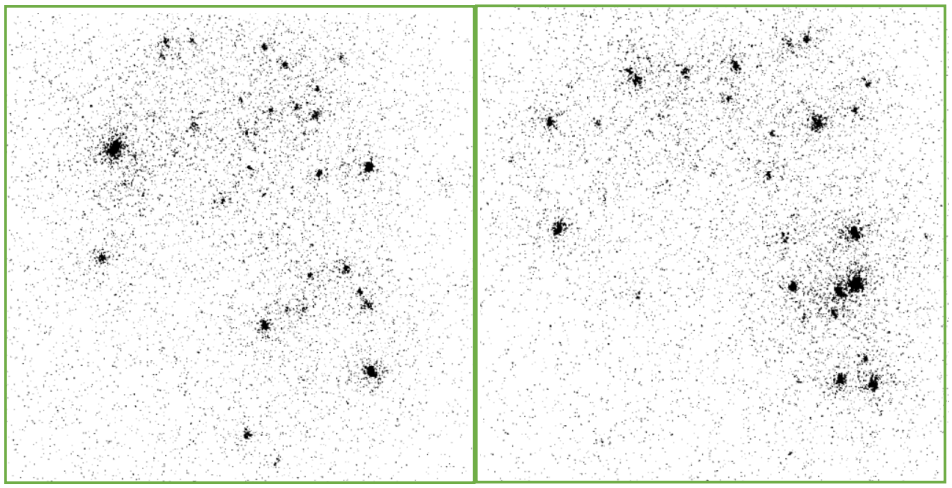

Figure VII.22: Instantaneous images showing Pine particles enveloped by flames and emitting OH signal at port 14 (centered at z= 231 cm) (inverted colors)*

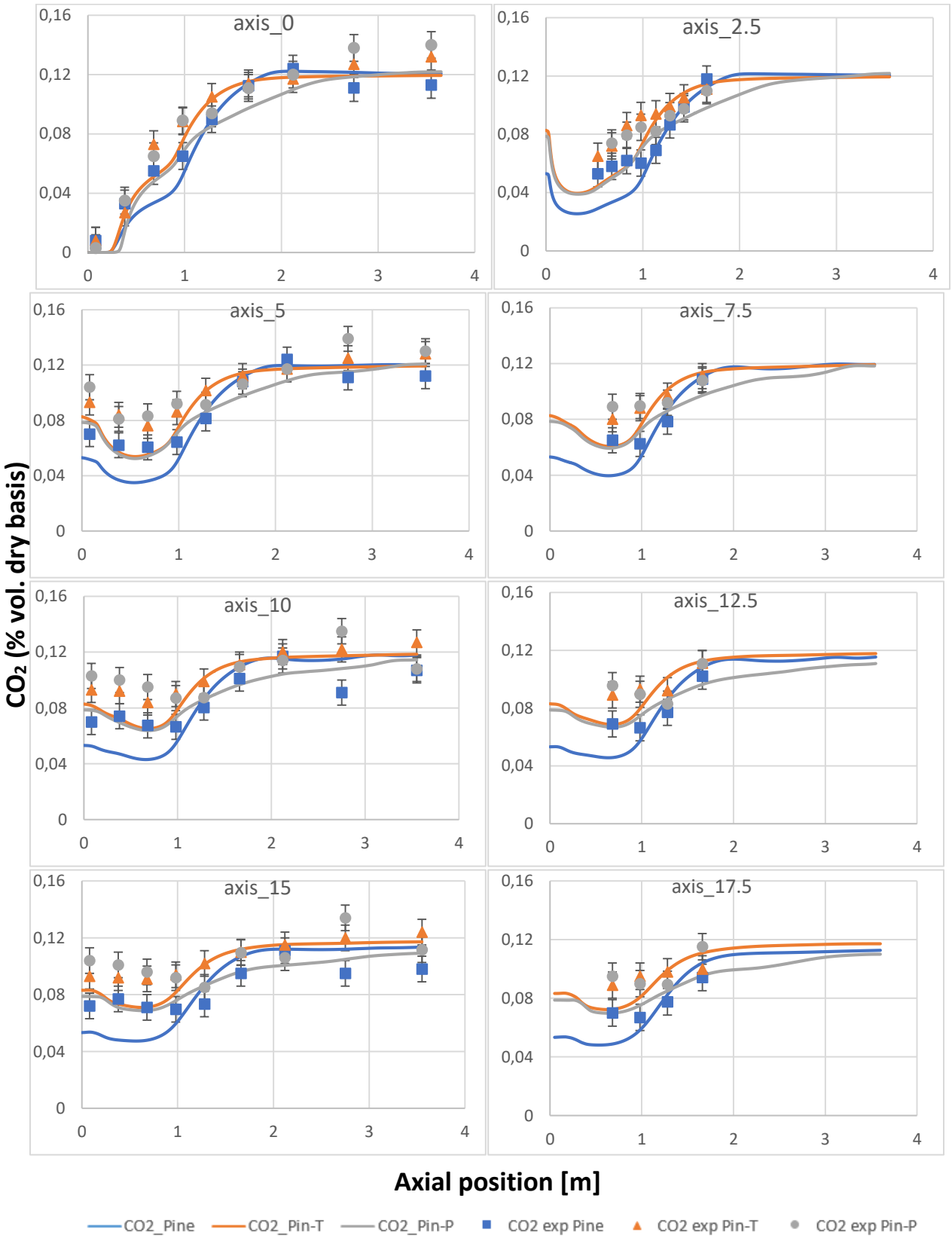

Figure VII.23: Comparison of experimental results and predictions of CO_2 profiles on eight vertical axes

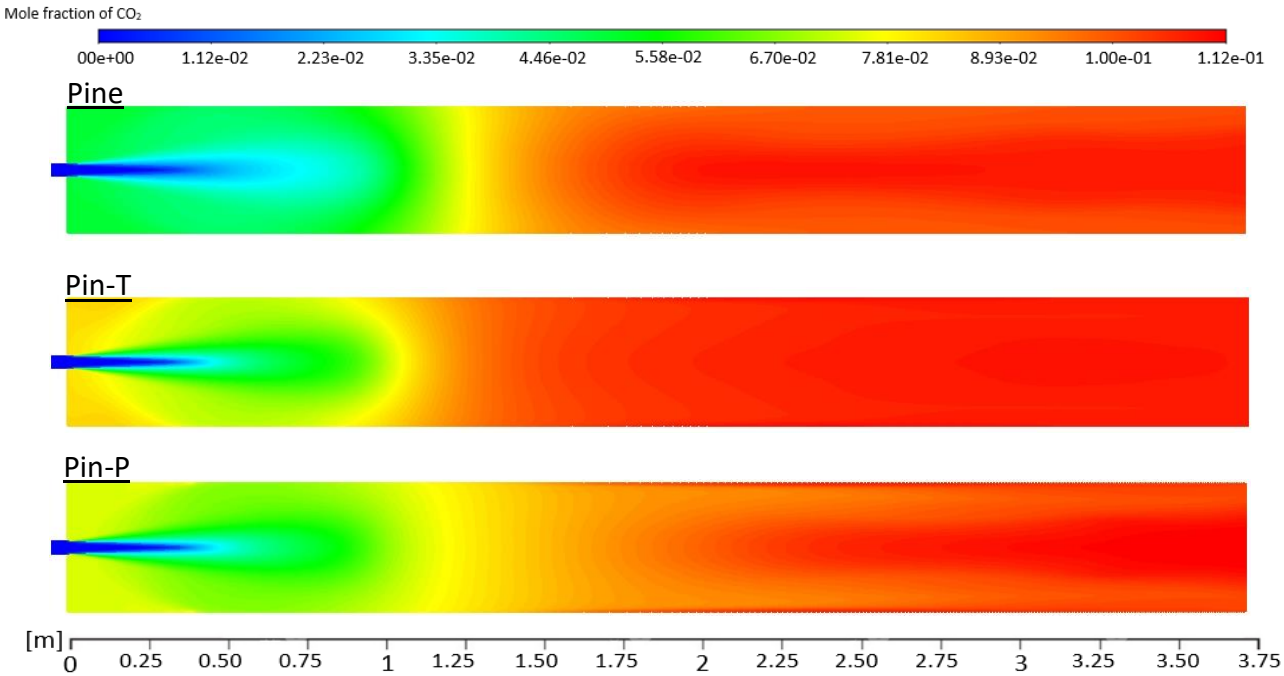

Figure VII.24: Carbon dioxide contours of Pine, Pin-T and Pin-P in the pilot scale reactor (single color scale for the three cases, top to bottom: Pine, Pin-T and Pin-P flames)

Simulations seem to produce similar carbon conversion rate as the experimental data of CO_2 but with some underestimation as presented in *Figure VII.23*. The CO_2 contours of the three flames shown in *Figure VII.24* are directly related to the oxygen consumption considering that carbon forms more than 50% of the biomass. At 30 cm from the injection point, CO_2 level increases due to the oxidation of volatiles. Pine produces CO_2 from the devolatilization of small particles until a point (around 87 cm from the burner exit) where the production accelerates again with the devolatilization of large particles. CO_2 is more smoothly produced in Pin-P flame as the particles devolatilize over a long range. The trends are consistent with the data and the previous analysis of particle history. More CO_2 is observed by Pin-T and Pin-P in the ORZ than Pine. This validates again that Pin-T and Pin-P particles follow better the recirculating flow to undergo char oxidation in the ORZ. Moreover, exhaust gas compositions reveal lower carbon conversion for Pine than Pin-T and Pin-P, which is consistent with the HTR results about the influence of particle size. Similarly, Pin-P showed the maximum carbon conversion at particle scale and pilot-scale.

VII.3.8 Nitrogen oxides distribution

Nitrogen conversion has already been discussed twice in the horizontal tubular reactor and the drop tube furnace (§ V.4.4, § VII.3.7). The conversion mechanism occurs through several routes during devolatilization and char oxidation. The particle scale results showed also routes for NO reduction that are active in some fuel types more than others depending on their nitrogen content.

Figure VII.25 plots the experimental results of the NO distribution on four vertical axes in the pilot reactor. The profiles on the central line increase during devolatilization similar to what was seen in the DTF. The three fuels reach their maximum approximately at the position of the temperature peak. This suggests that the thermal route contributes to the total NOx

concentration with fuel NO formation. Pine NO increases slower than the other fuels and peaks further in the reactor at the second devolatilization peak. Similarly, long devolatilization path explains the delayed peak of Pin-P. Unlike Pin-T and Pin-P, NO decreases significantly in Pine flames after the peak. It seems that the devolatilization of large particles at the end of the reactor as confirmed by OH* chemiluminescence images has a reducing effect on NO concentration.

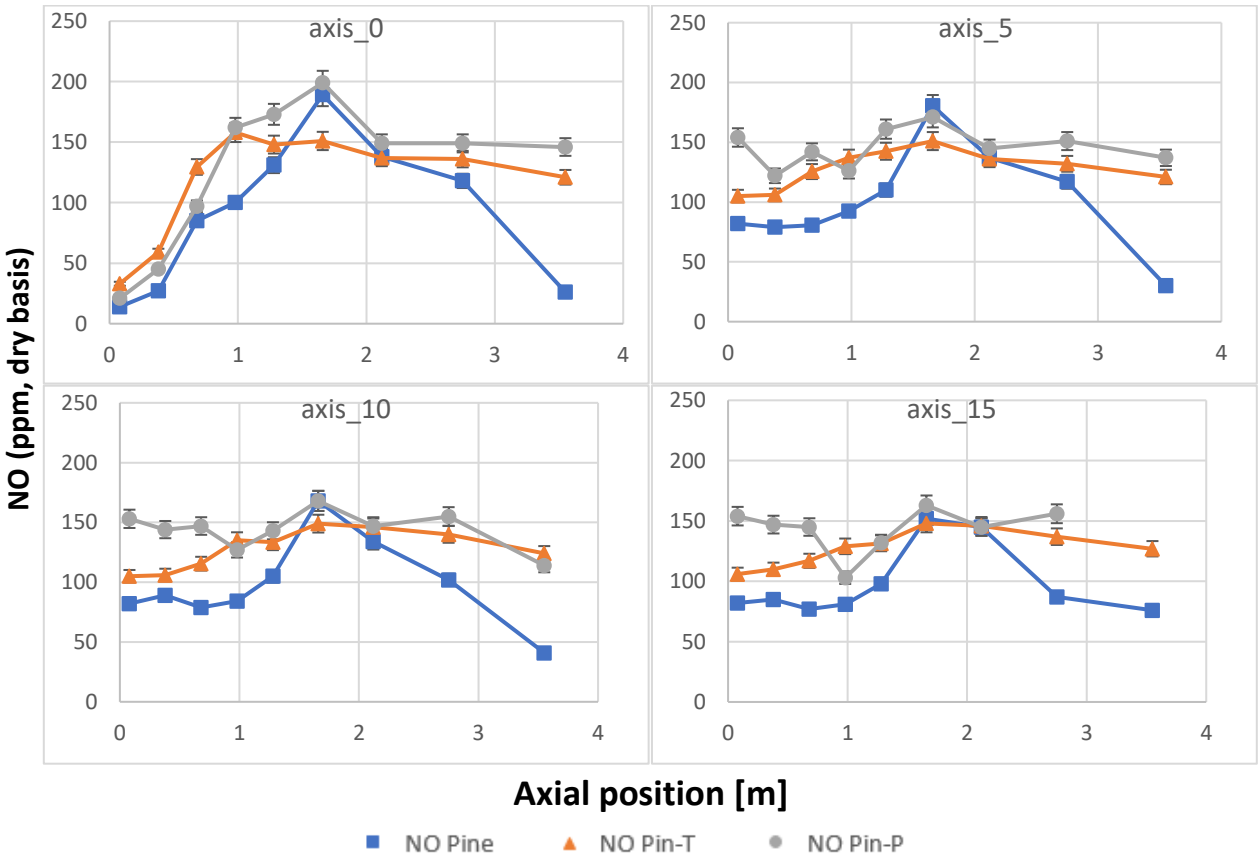

Figure VII.25: Experimental results of NO distribution on four vertical axes

As discussed at particle scale, NO precursors, mainly NHi and HCN, and other gases (CO and CHi) released during the devolatilization of large Pine particles may be responsible of the reduction mechanism of NO in Pine flames. The staging of devolatilization may be a way of reducing NO levels in biomass-fired furnaces [31]. Pin-T and Pin-P also experience a relatively slight decrease in NO at the end, which is probably caused by the fast heterogeneous reaction of NO with the chars.

VII.4 Conclusions

An experimental and numerical study of the combustion of pulverized biomass flames is performed in a pilot scale reactor. Constructing and operating such pilot scale facility during the thesis time was a real challenge. The pilot operated perfectly with some difficulties with the pneumatic transport of the fuel, which were resolved with proper handling of the pressure losses in the pneumatic transport circuit. These difficulties imposed high injection velocity leading to high lift-off length. Secondary air was preheated to facilitate the combustion and reduce the lift-off length. The facility operated more than 30 days to collect experimental data on three tested

flames of Pine, Pin-T and Pin-P. The operating conditions allowed us to study each combustion stage separately as intended by design. The experimental data obtained in the new pilot-scale reactor include a detailed description of the spatial distributions of main species concentrations beside the OH* chemiluminescence images. These results are in accordance with the predictions of the CFD numerical model.

The studied flames are long lifted jet flames, forming a large outer recirculation zone around the central jet, until it reaches the combustion chamber wall. This structure is due to the high injection velocity that shifts the devolatilization zone away from the burner and permits the jet to develop in the reactor. Fuels with finer particle size distribution (Pin-T and Pin-P) are found to be more influenced by the aerodynamic structures, since their particles follow better the flow streamlines. Their devolatilization occurs in the jet and the chars are captured by the ORZ where they get oxidized. This creates a high temperature region in the ORZ, which helps to heat up the injected particles. On the other hand, the wide particle size distribution of Pine manifests in two-devolatilization stages, and the large particles tend to go straightforward and oxidize downstream.

The volatiles start to react with oxygen in the lifted flame, which appears in the mixing layer of the fuel and air jets. The predicted reaction zones of the three flames coincide well with the OH* chemiluminescence images. The topology and intensity of the latter is determined by the volatile content of the fuel and its reactivity. The particle size distribution also plays a key role. Pin-T with fine PSD shows the highest reaction intensity despite a lower volatile content than Pine. The two-devolatilization regions of Pine created by the large PSD, reduces the reaction intensity, while that of Pin-P is more diluted and consequently less intense.

The results show that CO peaks in the devolatilization region, and increases later as a product of char surface oxidation. CO curves arrive to a minimum between the two combustion stages, whose value reflects the degree of overlap of the devolatilization and char oxidation phases of each fuel: Pin-P has higher overlap than Pin-T and Pine respectively. NOx concentration measurements suggest that nitrogen oxides are produced through fuel and thermal routes with high temperature sensitivity. Higher levels are measured in the middle of the reactor where it exhibits higher local temperature that may be associated with thermal NO production on top of fuel NO formation. NOx levels decrease after the flame region. The reduction is slight for Pin-T and Pin-P while it is significant for Pine due to the second devolatilization stage.

Conclusions and Discussion

This work is an experimental and numerical thesis of the combustion of pulverized biomass at both particle and flame scale. A pilot scale reactor was developed during the thesis capable of giving insights to the combustion of pulverized biomass and the behavior of particles in the flame. For this reason, a study is first performed on the combustion of single particles with different properties among which the volatile content and particle size were of main interest. The diversity of biomass was simulated using torrefaction of raw pine, in order to produce other types of biomass with controlled volatile content. Three torrefaction degrees beside demolition wood and coal were studied at particle scale. They were then grinded and milled into different size fractions in order to understand the influence of particle size on the combustion process. The fuels were characterized by proximate, ultimate analysis and TGA. We then proposed a numerical model which was developed on the basis of the approach at particle scale, in order to approach the behavior of a biomass particle at pilot scale. For this reason, we considered in the particle approach parameters such as volume evolution, mass degradation, pyrolysis gas composition, combustion emissions and the combustion timeline. After validation, the particle model is integrated to a CFD model applied to the pulverized biomass flames in the pilot scale reactor. The model is complementary to the experimental work on the reactor, which include gas probing and OH* chemiluminesence imaging.

Particle scale study

Different experimental methods at particle scale were used to provide a detailed characterization of the degradation process of a single particle.

The mass degradation at low heating rates was followed in the macro-TGA and revealed significant influence of the volatile content on the particle reactivity. With higher torrefaction degree, the combustion behavior of biomass is shifted towards the one of coal.

Pyrolysis gas composition was measured at high heating rates in a drop tube furnace. The fast pyrolysis produced mainly gas (with CO as dominant volatile fuel) with char and pyrolytic water. Higher volatile content fuel ejects more volatiles during the experiment with higher CO, H_2 and CH_4 yields.

The combustion emissions were traced with the progress of the degradation process of biomass in a horizontal tubular reactor. The results showed that pine, demolition wood and torrefied pine have a high consumption of oxygen during the flame phase followed by a lower consumption during char oxidation. On the other hand, pyrolyzed and carbonized pine are more coal-like fuels with low oxygen consumption peak during devolatilization and long heterogeneous combustion duration. The flame duration appears to be more influenced by the particle size than the particle volatile content. This leads to more intense combustion for higher volatile matter particles. Moreover, NOx emissions increase with torrefaction due to higher N content, even if the conversion ratio N to NO is lower with higher N content in the solid fuel.

An original optical diagnostic based on Particle Combustion Shadowgraphy (PCS) has been developed in the present study for direct time-resolved observation and characterization of the combustion of a single particle of biomass. It gave insights to the phenomena occurring at the particle surface and around it during the whole process, including the onset of heterogeneous

ignition and the volume and shape evolution. The results verified the important role of the VM content and particle size in determining the combustion intensity and durations. Higher VM particles undergo intense devolatilization for comparable durations as less volatile containing fuel. On the other hand, the left char is more reactive and burn faster than the char resulting from particles with lower VM content. However, the heterogeneous ignition was observed to occur earlier for larger particles containing lower volatile matter, forming larger overlap between the homogeneous and heterogeneous combustion phases. A comparison between biomass and coal showed the visual differences of the gas phase composition and the char structure, giving rise to differences in the flame and char combustion of both fuels.
The projection area evolution of the particle is traced versus the burnout using gas emission results. A specific model is extracted from the curves assuming spherical particles.

The mass loss at high heating rates was followed in a drop tube furnace. A numerical model was developed using the experimental data collected at particle scale to simulate the combustion of a single particle in the drop tube furnace. Using a methodology of model optimization, we could derive the kinetics parameters of devolatilization and char oxidation from the degradation curves. The predictions were in accordance with the oxygen and carbon monoxide concentrations and the conclusions are consistent with those obtained in the above experimental methods.

Pilot scale study

At flame scale, experimental and numerical methods are also employed for the characterization of pulverized biomass flames. The particle combustion model previously developed from particle scale study is implemented in a CFD model to simulate the pulverized flames at pilot-scale. CFD simulation calculates the aerodynamics of the flow, the turbulence and chemical reactions in gas phase, and treats the particles using a discrete phase model. The interaction between the discrete phase and continuous phase is considered.

On the other hand, a pilot scale reactor was designed and constructed during this thesis to replicate the environment of industrial furnaces, while giving access to the whole flame using probing and imaging techniques. The vertical reactor is equipped with bluff-body burner mounted on top of it. It was specially designed with simple aerodynamics in order to uncouple and spread out the combustion stages. The experimental data include a detailed description of the spatial distributions of in-flame species concentrations beside the OH* chemiluminescence images of three biomass flames of pine, torrefied pine and pyrolyzed pine.

The model results are satisfyingly in accordance with the experimental results. The flame structure and the reaction zones are well defined and their dependence on the fuel type is well established. The studied flames are long lifted jet flames, forming a large outer recirculation zone behind the central jet. Fuels with finer particle size distribution (Pin-T and Pin-P) were found to be more influenced by the aerodynamic structures. Their devolatilization occurs in the jet and the chars are captured by the recirculation zone where they get oxidized. On the other hand, the wide particle size distribution of pine created two-devolatilization stages, and the large particles tend to penetrate the recirculation zone and oxidize downstream.

The topology and intensity of the reaction zone is determined by the volatile content of the fuel and its reactivity. The particle size distribution also plays a key role and higher volatile content does not always mean higher reaction intensity.

From particle scale to flame scale

Throughout this thesis, the methodology has been to study the combustion of a single isolated particle to understand its behavior in pulverized biomass flames. The results revealed several links between the two scales.

This work further highlights the fact that significant differences can result from biomass physico-chemical heterogeneities, which correspond to different tuning parameters to the same CFD model under similar boundary conditions. These parameters can be controlled by an exhaustive knowledge of the considered biomass fuel at the inlet. They include:

1. Fuel proximate and ultimate analysis,
2. Size distribution from sieve analysis
3. Volume evolution traced by PCS experiments
4. Volatiles composition measured in the DTF pyrolysis experiments

These entities are properties of each fuel and need to be inspected entirely at particle scale for a proper simulation of the concerned biomass flames. They were first used to develop a model of single particle combustion to derive the kinetic parameters from the degradation curves in the DTF. This particle combustion model was later implemented in a CFD model, which is validated by comparison with the experimental measurements on pilot scale. Both experimental and numerical approaches enable a detailed characterization of pulverized biomass flames.

Coupled experimental and numerical studies of single particle combustion and pulverized flame enable to enlighten common features at both scales:

1. Solid fuel particles size has clearly a significant impact on the flame structure. The investigation at particle level proved that large particles are less reactive and need more time to complete their burnout. This lower reactivity and high thermal inertia explained the delayed ignition and smoother oxygen consumption of pine in the pilot-scale reactor. Besides, the different behavior observed at particle scale between large and small particles, gave rise to two devolatilization regions for pine pulverized flames.
2. Exhaust gas compositions measured in the pilot reactor reveal lower carbon conversion for Pine than Pin-T and Pin-P, which is consistent with the HTR results about the influence of particle size. Similarly, Pin-P showed the maximum carbon conversion at particle scale and pilot-scale.
3. The ignition temperature of single particles was useful to compare the different lift-off length of the reaction zones in the tested flames. The low ignition temperature of Pin-P measured at particle scale explains the upstream location of the reaction zone compared to Pin-T with similar particle size distribution.
4. PCS results show that Pine, Pin-T and Pin-P has comparable flame durations despite the huge differences in volatile content. Severe thermal treatment induces more pores in the particle structure causing a smooth ejection of volatiles whenever the treated particle is exposed to heat. This was also observed at flame scale where the devolatilization and reaction zones were comparable in size for all biomasses despite their different volatile content.
5. PCS also recorded char combustion over a long duration, which gets longer with the severity of the thermal treatment. In all tested flames, oxygen profiles in the lower

section of the reactor were flat with slow oxygen consumption, which can be attributed to the slow oxidation of chars.

6. The experiments in the drop tube furnace showed that CO is the major constituent of the volatiles released by all the tested fuels and the major product of the char oxidation. On the other hand, CO peaked in the devolatilization region of the three pulverized biomass flames, then decreases by oxidation, only to increase later as a product of the surface oxidation of char.
7. A local minimum of the CO profiles was spotted for all three flames and for the tested fuels in the DTF. The value of the minimum is dependent on the overlap of the homogeneous and heterogeneous oxidation. Particle scale results proved that the overlap increases with lower volatile content. The order of the CO minimum value at flame scale validates this conclusion.
8. Nitrogen conversion was discussed in the horizontal tubular reactor and the drop tube furnace. More nitrogen in the particle induces more NOx production. However, fewer fraction of the fuel nitrogen is converted to NO. This is the case in the three pulverized flames also. Moreover, NO reduction by volatiles detected for pulverized pine flames is also observed and discussed at particle scale.

Perspective

The experimental studies carried out during this thesis define a methodology for precise characterization of biomass particles in the objective of a good understanding of their combustion behavior in pulverized flames. This opens up prospects for studying the development of a wide variety of alternative fuels such as woody, non-woody, problematic and waste biomass and their pretreated products. The particle scale investigation is a complete procedure that needs to be followed for future modelling of the potential fuels. The study of different fuels with different volatile matter content may give indications of the behavior of any potential fuel in combustion environment.

However, many aspects of the pulverized biomass flames still need to be investigated. The flames studied here are intended by design to have simple aerodynamics, seeking to focus the study on the particle history within the flame. Industrial flames have more complex features, which induce more particle-to-particle interactions and different residence times. The complex aerodynamics also influence the chemical reactions and may force larger particles to follow the streamlines. The pilot scale reactor is also designed for future investigation of such topics. The combustion chamber is equipped with optical and laser accesses to conduct flow field measurements using particle image velocimetry (PIV), tomographic flame characterization by Planar Laser Induced Fluorescence (PLIF) and other laser diagnostics. The burner is also flexible for modifications of its aerodynamics by adding a swirler stage for example. Development of biomass combustion models and their implementation in CFD simulation performed within this study enable also their use in future projects complementary to experimental investigation in the pilot reactor.

The future perspective is also to move to larger industrial scale. Veolia's future objective is to reduce its dependence on coal in its power plants in East Europe and China. This paves the way for pulverized biomass as a potential candidate for the transition. Beside good performance and environmental benefits, using the same pulverized combustion mode for biomass is

economically beneficial, as no huge modifications are needed. The pilot scale reactor designed in this study is an intermediate step for switching the existing boilers to biomass. Tests on the reactor make it possible to estimate the consequences and possible modifications to be made on existing boilers. Thus by having a better understanding of behavior and impacts through pilot tests, we avoid the complete shutdown of industrial sites and consequently operating losses. This approach is a contribution towards the energetic, environmental and societal transition from fossil fuels usage to alternative renewable sources.

Annex A – Materials and construction

This annex presents the properties of the materials used in the design and fabrication of the pilot scale reactor (Table A.1). The thickness of the wall and that of each layer are estimated for an external wall temperature lower than 60°C. The calculation procedure is presented in Table A.2. The fabrication steps of the reactor are then illustrated.

Properties of the castables used in the construction of the reactor:

	PLASTIL SF 9806	**PLASTIL 3405**
Product definition		
Nature	Dense refractory concrete	Refractory concrete
Class	ISO A 180 / ASTM G	ISO A 150 / ASTM D
Bond nature	Hydraulic	Hydraulic
Maximum operating temperature	1800 °C	1350 °C
Basic constituent	Alumina	Fireclay
Granulometric class	6 mm	5 mm
Chemical composition		
Al2O3 %	97.9	34
SiO2 %	<0.5	50.1
CaO %	1.1	3.1
Fe2O3 %	<0.2	1.6
TiO2 %	<0.1	1.1
Physical characteristics		
Preparation with 5.9% water	**After 5 hours at 1000°C**	
Apparent density (Kg/m3)	3090	1940
Compression resistance (N/mm²)	33	65
Permanent linear variation	-0.06	-0.15
Thermal conductivity (W/m.k) at an average temperature of 1000 °C (ASTM C 417)	2.3	1.2

Table A.1: properties of the castables used in the first and second layer of the reactor

Temperature calculation of the external wall temperature of the reactor

Combustion gases	Gases temperature (°C)	1000
	Internal furnace diameter (mm)	400
	Coefficient of internal heat transfer (W/m²K)	200
External air	External air temperature (°C)	27
	Coefficient of external heat transfer (W/m²K)	23,51
Calculation		
Global heat transfer coefficient (W/m²K)		1.21
Total thermal flow (W)		4462
Internal wall temperature (°C)		994
External steel temperature (°C)		52

Table A.2: Heat transfer calculation through the reactor wall

The calculation is carried out using the heat transfer equations by convection inside and outside the chamber, and by conduction through the wall layers. The gases temperature inside the chamber is assumed as 1000°C. The coefficient of internal heat transfer accounts for radiation and convection and it is typically set between 100 and 200.

The coefficient of external heat transfer is calculated using Churchill and Chu correlation for natural convection and radiation of external flow on vertical cylinders [234], by assuming initial surface and air temperatures and iterate till the surface temperature becomes constant.

The global heat transfer coefficient (R_{global}) is calculated as follows:

$$\frac{1}{R_{global}} = \frac{1}{h_{int}} + \frac{e_1}{\lambda_1} + \frac{e_2}{\lambda_2} + \frac{e_3}{\lambda_3} + \frac{e_4}{\lambda_4} + \frac{1}{h_{ext}}$$

Fabrication

Once the dimensions and materials were chosen, the detailed furnace scheme was constructed using AutoCAD (*Figure A.**1***). The furnace segments are of identical materials except for the last one, which is made only of refractory concrete. An ashtray is placed at the exit of the furnace. It can be disassembled and mounted easily to evacuate the accumulated ash.

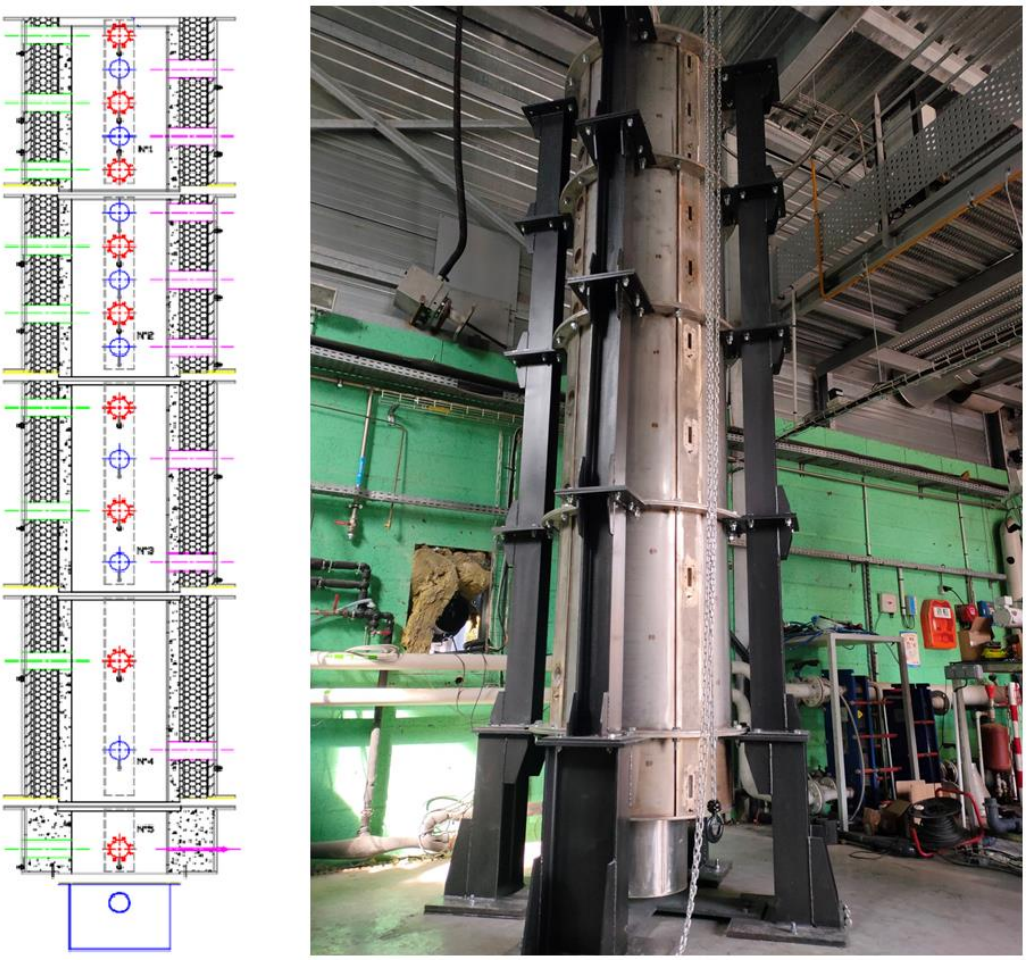

Figure A.1: The final furnace structure with several ports distribution

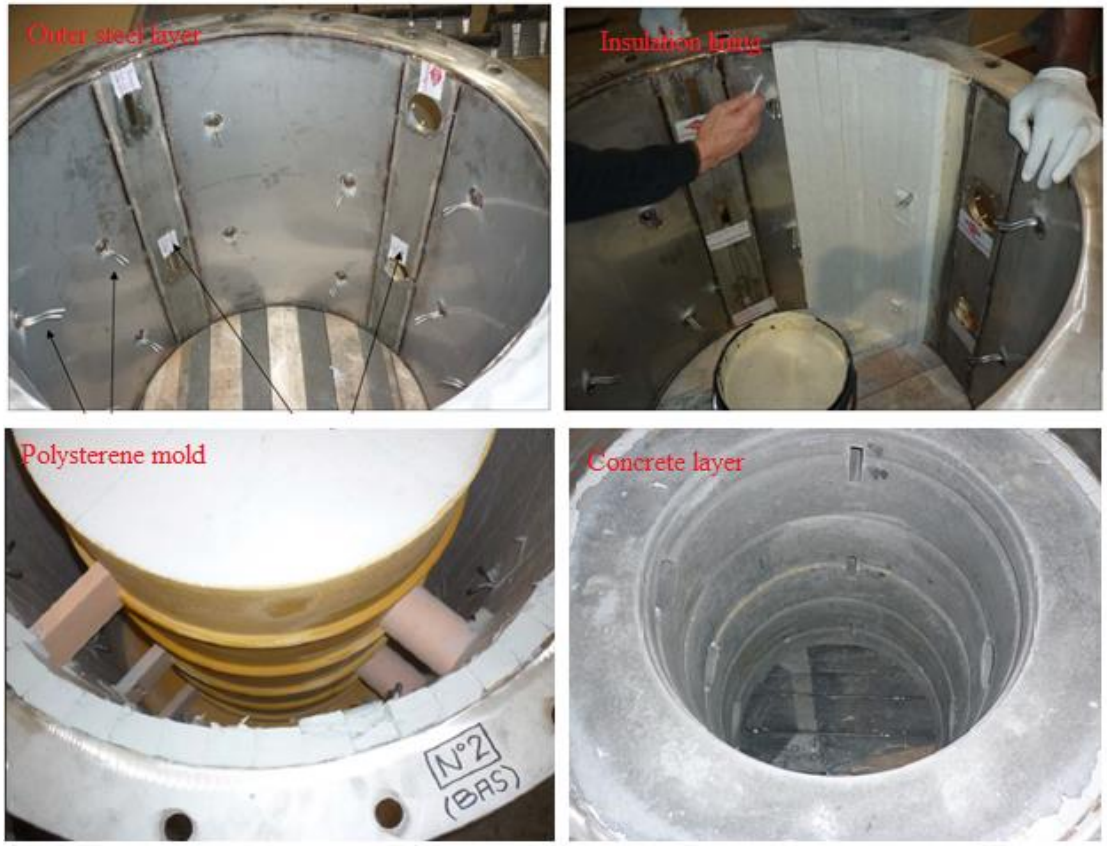

Figure A.2: Fabrication steps of the combustion chamber

The fabrication of the layers started from outside in. The casing or the steel shell was first shaped with the required diameter and with the ports cut by laser at their respective positions. Steel anchors with spaced rods and expansion tips are welded to the inner wall. They help maintain a compact structure of the inner concrete layers and the outer steel shell. The insulation material is then lined as a second layer as shown in *Figure A.**2***. The concrete layers are the most delicate to create. After mixing with water, the concrete is prepared and poured between the outer layer and a polystyrene mold containing plugs at the position of the ports. The concrete solidifies later at room temperature because of hydraulic or chemical setting. While the addition of water activates the bonds used in the castable during preparation, a controlled heat up procedure is necessary to dehydrate the bonds as the castable is put in service. The mold used for the first concrete layer forms some grooves in the concrete to be filled later with the inner refractory concrete.

References

[1] Publications Office of the European Union, “Energy, transport and environment indicators,” 2018.

[2] M. M. E. Moula, J. Maula, M. Hamdy, T. Fang, N. Jung, and R. Lahdelma, “Researching social acceptability of renewable energy technologies in Finland,” *Int. J. Sustain. Built Environ.*, vol. 2, no. 1, pp. 89–98, Jun. 2013.

[3] A. González, H. Sandoval, P. Acosta, and F. Henao, “On the Acceptance and Sustainability of Renewable Energy Projects—A Systems Thinking Perspective,” *Sustainability*, vol. 8, no. 11, p. 1171, Nov. 2016.

[4] European Environment Agency, “How much bioenergy can Europe producewithout harming the environment? EEA Report, No. 7, 2006,” 2006.

[5] “https://www.veolia.com/en/solution/biomass-energy-mix.” .

[6] “Ontario Power Generation, Canada Coal to biomass journey furnace,” IEA Bioenergy, Atitokan & Thunder Bay, Ontario, Canada, 2018. available online: "https://www.ieabioenergy.com/wp-content/uploads/2018/02/9-OPG-Coal-to-biomass_CA_Final.pdf"

[7] U. Nowling, “Successful Torrefied Biomass Test Burn at a Coal Power Plant,” Report, University of Missouri-Kansas City, 2018. available online: "https://www.powermag.com/successful-torrefied-biomass-test-burn-at-a-coal-power-plant/?pagenum=8"

[8] P. Devine-Wright, “Reconsidering public acceptance of renewable energy technologies: A critical review. Delivering a Low Carbon Electricity System: Technologies, Economics and Policy.,” Manchester, 2008.

[9] C. Couhert, “Pyrolyse flash à haute température de la biomasse ligno-cellulosique et de ses composés : production de gaz de synthèse,” Thèse de doctorat, École Nationale Supérieure des Mines de Paris, 2007.

[10] H. V. Lee, S. B. A. Hamid, and S. K. Zain, “Conversion of Lignocellulosic Biomass to Nanocellulose: Structure and Chemical Process,” *Sci. World J.*, vol. 2014, pp. 1–20, 2014.

[11] H. Chen, “Biotechnology of lignocellulosic theory and practice,” in *Biotechnology of lignocellulosic theory and practice*, Illustrate., Springer, 2014, p. 510.

[12] E. Ranzi *et al.*, “Chemical Kinetics of Biomass Pyrolysis,” *Energy & Fuels*, vol. 22, no. 6, pp. 4292–4300, Nov. 2008.

[13] X. Deglise and A. Donnot, *Bois énergie*. Ed. Techniques Ingénieur, 2008.

[14] H. V. Scheller and P. Ulvskov, “Hemicelluloses,” *Annu. Rev. Plant Biol.*, vol. 61, no. 1, pp. 263–289, Jun. 2010.

[15] M. J. Prins, K. J. Ptasinski, and F. J. J. G. Janssen, “Torrefaction of wood,” *J. Anal. Appl. Pyrolysis*, vol. 77, no. 1, pp. 35–40, Aug. 2006.

[16] BerserkerBen, “Hemicellulose,” *Wikipedia*. [Online]. Available: https://en.wikipedia.org/wiki/Hemicellulose.

[17] R. Vanholme, B. Demedts, K. Morreel, J. Ralph, and W. Boerjan, “Lignin Biosynthesis and Structure,” *PLANT Physiol.*, vol. 153, no. 3, pp. 895–905, Jul. 2010.

[18] and A. Sluiter, R. Ruiz, C. Scarlata, J. Sluiter and D. Templeton, “Determination of Extractives in Biomass: Laboratory Analytical Procedure (LAP),” *Natl. Renew. Energy Lab.*, pp. 1–9, 2008.

[19] M. E. Fuentes, D. J. Nowakowski, M. L. Kubacki, J. M. Cove, T. G. Bridgeman, and J. M. Jones, “Survey of influence of biomass mineral matter in thermochemical conversion of short rotation willow coppice,” *J. Energy Inst.*, vol. 81, no. 4, pp. 234–241, Dec. 2008.

[20] C. E. Greenhalf *et al.*, “Thermochemical characterisation of straws and high yielding perennial grasses,” *Ind. Crops Prod.*, vol. 36, no. 1, pp. 449–459, Mar. 2012.

[21] J. F. Saldarriaga, R. Aguado, A. Pablos, M. Amutio, M. Olazar, and J. Bilbao, “Fast characterization of biomass fuels by thermogravimetric analysis (TGA),” *Fuel*, vol. 140, pp. 744–751, Jan. 2015.

[22] V. Cozzani, A. Lucchesi, G. Stoppato, and G. Maschio, “A new method to determine the composition of biomass by thermogravimetric analysis,” *Can. J. Chem. Eng.*, vol. 75, no. 1, pp. 127–133, Feb. 1997.

[23] E. Rodriguez Alonso, C. Dupont, L. Heux, D. Da Silva Perez, J.-M. Commandre, and C. Gourdon, “Study of solid chemical evolution in torrefaction of different biomasses through solid-state 13C cross-polarization/magic angle spinning NMR (nuclear magnetic resonance) and TGA (thermogravimetric analysis),” *Energy*, vol. 97, pp. 381–390, Feb. 2016.

[24] M. A. Saeed, C. H. Medina, G. E. Andrews, H. N. Phylaktou, D. Slatter, and B. M. Gibbs, “Agricultural waste pulverised biomass: MEC and flame speeds,” *J. Loss Prev. Process Ind.*, vol. 36, pp. 308–317, Jul. 2015.

[25] J. M. Jones, M. Pourkashanian, A. Williams, and D. Hainsworth, “A comprehensive biomass combustion model,” *Renew. Energy*, vol. 19, no. 1–2, pp. 229–234, Jan. 2000.

[26] L. Burhenne, J. Messmer, T. Aicher, and M.-P. Laborie, “The effect of the biomass components lignin, cellulose and hemicellulose on TGA and fixed bed pyrolysis,” *J. Anal. Appl. Pyrolysis*, vol. 101, pp. 177–184, May 2013.

[27] P. McNamee, L. I. Darvell, J. M. Jones, and A. Williams, “The combustion characteristics of high-heating-rate chars from untreated and torrefied biomass fuels,” *Biomass and Bioenergy*, vol. 82, pp. 63–72, Nov. 2015.

[28] A. González-Cencerrado, B. Peña, and A. Gil, “Experimental analysis of biomass co-firing flames in a pulverized fuel swirl burner using a CCD based visualization system,” *Fuel Process. Technol.*, vol. 130, pp. 299–310, Feb. 2015.

[29] R. Weber, Y. Poyraz, A. M. Beckmann, and S. Brinker, “Combustion of biomass in jet flames,” *Proc. Combust. Inst.*, vol. 35, no. 3, pp. 2749–2758, 2015.

[30] C. Mock, H. Lee, S. Choi, and V. Manovic, “Flame structures and ignition

characteristics of torrefied and raw sewage sludge particles at rapid heating rates," *Fuel*, vol. 200, pp. 467–480, Jul. 2017.

[31] J. Ballester, J. Barroso, L. Cerecedo, and R. Ichaso, "Comparative study of semi-industrial-scale flames of pulverized coals and biomass," *Combust. Flame*, vol. 141, no. 3, pp. 204–215, May 2005.

[32] C. Huéscar Medina *et al.*, "Comparison of the explosion characteristics and flame speeds of pulverised coals and biomass in the ISO standard 1m3 dust explosion equipment," *Fuel*, vol. 151, pp. 91–101, Jul. 2015.

[33] S. Kim, R. W. Kramer, and P. G. Hatcher, "Graphical Method for Analysis of Ultrahigh-Resolution Broadband Mass Spectra of Natural Organic Matter, the Van Krevelen Diagram," *Anal. Chem.*, vol. 75, no. 20, pp. 5336–5344, Oct. 2003.

[34] Y. Chen, S. Charpenay, A. Jensen, M. A. Wójtowicz, and M. A. Serio, "Modeling of biomass pyrolysis kinetics," *Proc. Combust. Inst.*, vol. 27, no. 1, pp. 1327–1334, Jan. 1998.

[35] M. G. Grønli, G. Várhegyi, and C. Di Blasi, "Thermogravimetric Analysis and Devolatilization Kinetics of Wood," *Ind. Eng. Chem. Res.*, vol. 41, no. 17, pp. 4201–4208, Aug. 2002.

[36] J. Zhang, Y. S. Choi, C. G. Yoo, T. H. Kim, R. C. Brown, and B. H. Shanks, "Cellulose–Hemicellulose and Cellulose–Lignin Interactions during Fast Pyrolysis," *ACS Sustain. Chem. Eng.*, vol. 3, no. 2, pp. 293–301, Feb. 2015.

[37] T. Hosoya, H. Kawamoto, and S. Saka, "Cellulose–hemicellulose and cellulose–lignin interactions in wood pyrolysis at gasification temperature," *J. Anal. Appl. Pyrolysis*, vol. 80, no. 1, pp. 118–125, Aug. 2007.

[38] B. . Jenkins, L. . Baxter, T. . Miles, and T. . Miles, "Combustion properties of biomass," *Fuel Process. Technol.*, vol. 54, no. 1–3, pp. 17–46, Mar. 1998.

[39] James Reeb, "Wood and Moisture Relationships," Rehabilitation, (July), 1–8. Retrieved from http://ir.library.oregonstate.edu/xmlui/handle/1957/12771.

[40] António Biscaia da Silva, "Review of devolatilisation models and their application to pulverised fuel combustion simulation," Working paper, Mechanical Engineering Department, Instituto Superior Técnico, Lisbone, 2008.

[41] W. Fu, Y. Zhang, H. Han, and D. Wang, "A general model of pulverized coal devolatilization," *Fuel*, vol. 68, no. 4, pp. 505–510, Apr. 1989.

[42] C. Di Blasi, G. Signorelli, C. Di Russo, and G. Rea, "Product Distribution from Pyrolysis of Wood and Agricultural Residues," *Ind. Eng. Chem. Res.*, vol. 38, no. 6, pp. 2216–2224, Jun. 1999.

[43] J. Porteiro, J. L. Míguez, E. Granada, and J. C. Moran, "Mathematical modelling of the combustion of a single wood particle," *Fuel Process. Technol.*, vol. 87, no. 2, pp. 169–175, Jan. 2006.

[44] T. R. Nunn, J. B. Howard, J. P. Longwell, and W. A. Peters, "Product compositions and kinetics in the rapid pyrolysis of sweet gum hardwood," *Ind. Eng. Chem. Process Des. Dev.*, vol. 24, no. 3, pp. 836–844, Jul. 1985.

[45] J. Li, E. Biagini, W. Yang, L. Tognotti, and W. Blasiak, “Flame characteristics of pulverized torrefied-biomass combusted with high-temperature air,” *Combust. Flame*, vol. 160, no. 11, pp. 2585–2594, Nov. 2013.

[46] J. Shen, C. Igathinathane, M. Yu, and A. K. Pothula, “Biomass pyrolysis and combustion integral and differential reaction heats with temperatures using thermogravimetric analysis/differential scanning calorimetry,” *Bioresour. Technol.*, vol. 185, pp. 89–98, Jun. 2015.

[47] C. Di Blasi, “Modeling chemical and physical processes of wood and biomass pyrolysis,” *Prog. Energy Combust. Sci.*, vol. 34, no. 1, pp. 47–90, Feb. 2008.

[48] Maryam Momeni, “Fundamental Study of Single Biomass Particle Combustion,” Ph.D. Thesis, Aalborg University, 2012.

[49] D. Neves, H. Thunman, A. Matos, L. Tarelho, and A. Gómez-Barea, “Characterization and prediction of biomass pyrolysis products,” *Prog. Energy Combust. Sci.*, vol. 37, no. 5, pp. 611–630, Sep. 2011.

[50] S. Jiménez, P. Remacha, J. C. Ballesteros, A. Giménez, and J. Ballester, “Kinetics of devolatilization and oxidation of a pulverized biomass in an entrained flow reactor under realistic combustion conditions,” *Combust. Flame*, vol. 152, no. 4, pp. 588–603, Mar. 2008.

[51] J. Hong, “Modeling char oxidation as a function of pressure using an intrinsic langmuir rate equation,” Ph.D. Thesis, Brigham Young University, 2000.

[52] G. Teixeira, “Gazéification de charbon de granules de bois: comportement thermochimique et mécanique d’un lit fixe continu,” Thèse de Doctorat, Institut National Polytechnique de Toulouse (INP Toulouse), 2012.

[53] P. J. Smoot, L.Douglas, Smith, “Coal Combustion and Gasification,” Intergovernmental Panel on Climate Change, Ed. Cambridge: Cambridge University Press.

[54] B. Piednoir, “Comportement en combustion de résidus de biomasse : mise en évidence de synergies par mélange sous forme de granulés,” Thèse de Doctorat, Université de Perpignan Via Domitia, 2017.

[55] W. Heschel, L. Rweyemamu, T. Scheibner, and B. Meyer, “Abatement of emissions in small-scale combustors through utilisation of blended pellet fuels,” *Fuel Process. Technol.*, vol. 61, no. 3, pp. 223–242, Nov. 1999.

[56] Andrius Kavaliauskas, “Straw combustion in a packed bed, Andrius Kavaliauskas, Doctoral Dissertation, Technological Sciences, Power and Thermal Engineering, Kaunas, 2004.”

[57] Enviromental Protection Agency, “Nitrogen Oxides (NOx), Why and How They Are Controlled,”, Technical Bulletin, Epa-456/F-99-006R, (November), 48. https://doi.org/EPA 456/F-99-006R, North Carolina,1999.

[58] Jose Manuel Iglesias Fernández, “Study of Combustion Using a Computational Fluid Dynamics Software (ANSYS),” University of Bacelone, 2015.

[59] Q. Ren, C. Zhao, L. Duan, and X. Chen, “NO formation during agricultural straw

combustion," *Bioresour. Technol.*, vol. 102, no. 14, pp. 7211–7217, Jul. 2011.

[60] M. R. Gerry Hesselmann, "What are the main NOx formation processes in combustion plant?," IFRF Online Combustion Handbook, 1–4.

[61] T. Nussbaumer, "Primary and Secondary Measures for the Reduction of Nitric Oxide Emissions from Biomass Combustion," in *Developments in Thermochemical Biomass Conversion*, Dordrecht: Springer Netherlands, 1997, pp. 1447–1461.

[62] M. Kuang, Z. Wang, Y. Zhu, Z. Ling, and Z. Li, "Regulating Low-NO x and High-Burnout Deep-Air-Staging Combustion under Real-Furnace Conditions in a 600 MW e Down-Fired Supercritical Boiler by Strengthening the Staged-Air Effect," *Environ. Sci. Technol.*, vol. 48, no. 20, pp. 12419–12426, Oct. 2014.

[63] R. Salzmann and T. Nussbaumer, "Fuel Staging for NO x Reduction in Biomass Combustion: Experiments and Modeling," *Energy & Fuels*, vol. 15, no. 3, pp. 575–582, May 2001.

[64] G. Wang, R. B. Silva, J. L. T. Azevedo, S. Martins-Dias, and M. Costa, "Evaluation of the combustion behaviour and ash characteristics of biomass waste derived fuels, Pine and coal in a drop tube furnace," *Fuel*, vol. 117, pp. 809–824, Jan. 2014.

[65] R. Zevenhoven and M. Hupa, "The reactivity of chars from coal, peat and wood towards NO, with and without CO," *Fuel*, vol. 77, no. 11, pp. 1169–1176, Sep. 1998.

[66] J. Commandré, B. R. Stanmore, and S. Salvador, "The high temperature reaction of carbon with nitric oxide," *Combust. Flame*, vol. 138, no. 3, pp. 211–216.

[67] C. Yin, L. A. Rosendahl, and S. K. Kær, "Grate-firing of biomass for heat and power production," *Prog. Energy Combust. Sci.*, vol. 34, no. 6, pp. 725–754, Dec. 2008.

[68] Johnzactruba and L. Stonecypher, "How does a Circulating Fluidized Bed Boiler Work ?," *Bright Hub Inc.*, 2009. [Online]. Available: https://www.brighthubengineering.com/power-plants/26547-how-does-a-circulating-fluidized-bed-boiler-work/#imgn_0.

[69] J. K. Sjaak Van Loo, *The handbook of biomass combustion and co-firing*. 2002.

[70] T. Abbas, P. G. Costen, and F. C. Lockwood, "Solid fuel utilization: From coal to biomass," *Symp. Combust.*, vol. 26, no. 2, pp. 3041–3058, 1996.

[71] D. Toporov, "Combustion and Gasification of Pulverised Fuel in a Mixture of Oxygen and Carbon Dioxide," *Institute of Heat- and Mass Transfer (WSA), RWTH Aachen*, 2017. [Webpage]. Available: http://www.wsa.rwth-aachen.de/cms/WSA/Studium/Sommersemester/Wintersemester/~mdja/Combustion-and-Gasification-of-Pulverise/?lidx=1. [Accessed: 06-Nov-2018].

[72] A. Di Gianfrancesco, *Materials for Ultra-Supercritical and Advanced Ultra-Supercritical Power Plants*, Issue 104. Elsevier Science & Technology, 2016.

[73] P. Basu, C. Kefa, and L. Jestin, "Swirl Burners," Book DOI: 10.1007/978-1-4612-1250-8_8, 2000, pp. 212–241. "http://link.springer.com/10.1007/978-1-4612-1250-8_8"

[74] M. Namazian, J. Kelly, R. W. Schefer, S. C. Johnston, and M. B. Long, "Nonpremixed bluff-body burner flow and flame imaging study," *Exp. Fluids*, vol. 8, no. 3–4, pp.

216–228, Dec. 1989.

[75] R. W. Schefer, M. Namazian, J. Kelly, and M. Perrin, “Effect of Confinement on Bluff-Body Burner Recirculation Zone Characteristics and Flame Stability,” *Combust. Sci. Technol.*, vol. 120, no. 1–6, pp. 185–211, Nov. 1996.

[76] C. Del Taglia, L. Blum, J. Gass, Y. Ventikos, and D. Poulikakos, “Numerical and Experimental Investigation of an Annular Jet Flow With Large Blockage,” *J. Fluids Eng.*, vol. 126, no. 3, p. 375, 2004.

[77] “www.ge.com.” [Online]. Available: https://www.ge.com/power/services/boilers/upgrades/nox-solutions. [Accessed: 11-Sep-2020].

[78] K. Hamilton, “Feasibility Study: Grain-dust Burner,” Ph.D. Thesis, University of Strathclyde, 2016.

[79] “European Biomass Industry Association, http://www.eubia.org.”

[80] E. A. T. Yuntenwi, N. MacCarty, D. Still, and J. Ertel, “Laboratory study of the effects of moisture content on heat transfer and combustion efficiency of three biomass cook stoves,” *Energy Sustain. Dev.*, vol. 12, no. 2, pp. 66–77, Jun. 2008.

[81] K. M. Bryden and M. J. Hagge, “Modeling the combined impact of moisture and char shrinkage on the pyrolysis of a biomass particle☆,” *Fuel*, vol. 82, no. 13, pp. 1633–1644, Sep. 2003.

[82] M. M. Hasan, X. Hu, R. Gunawan, and C. Z. Li, “Pyrolysis of large mallee wood particles: Temperature gradients within a pyrolysing particle and effects of moisture content,” *Fuel Process. Technol.*, 2017.

[83] M. Pollard *et al.*, “Effects of Biomass Moisture Content on Volatile Flame during Cofiring with Coal,” *9th U. S. Natl. Combust. Meet.*, 2015.

[84] Y. . Yang, H. Yamauchi, V. Nasserzadeh, and J. Swithenbank, “Effects of fuel devolatilisation on the combustion of wood chips and incineration of simulated municipal solid wastes in a packed bed☆,” *Fuel*, vol. 82, no. 18, pp. 2205–2221, Dec. 2003.

[85] Y. . Yang, V. . Sharifi, and J. Swithenbank, “Effect of air flow rate and fuel moisture on the burning behaviours of biomass and simulated municipal solid wastes in packed beds,” *Fuel*, vol. 83, no. 11–12, pp. 1553–1562, Aug. 2004.

[86] A. Demirbas, “Effect of initial moisture content on the yields of oily products from pyrolysis of biomass,” *J. Anal. Appl. Pyrolysis*, vol. 71, no. 2, pp. 803–815, Jun. 2004.

[87] G. Lu, Y. Yan, S. Cornwell, M. Whitehouse, and G. Riley, “Impact of co-firing coal and biomass on flame characteristics and stability,” *Fuel*, vol. 87, no. 7, pp. 1133–1140, Jun. 2008.

[88] S. Xiong, J. Zhuo, B. Zhang, and Q. Yao, “Effect of moisture content on the characterization of products from the pyrolysis of sewage sludge,” *J. Anal. Appl. Pyrolysis*, 2013.

[89] M. V. Ramiah, “Thermogravimetric and differential thermal analysis of cellulose, hemicellulose, and lignin,” *J. Appl. Polym. Sci.*, vol. 14, no. 5, pp. 1323–1337, May

1970.

[90] H. Yang, R. Yan, H. Chen, D. H. Lee, and C. Zheng, "Characteristics of hemicellulose, cellulose and lignin pyrolysis," *Fuel*, vol. 86, no. 12–13, pp. 1781–1788, Aug. 2007.

[91] R. Ball, A. C. Mcintosh, and J. Brindley, "Feedback processes in cellulose thermal decomposition: implications for fire-retarding strategies and treatments," *Combust. Theory Model.*, vol. 8, no. 2, pp. 281–291, Jun. 2004.

[92] S. D. Stefanidis, K. G. Kalogiannis, E. F. Iliopoulou, C. M. Michailof, P. A. Pilavachi, and A. A. Lappas, "A study of lignocellulosic biomass pyrolysis via the pyrolysis of cellulose, hemicellulose and lignin," *J. Anal. Appl. Pyrolysis*, vol. 105, pp. 143–150, Jan. 2014.

[93] S. A. El-Sayed and M. E. Mostafa, "Pyrolysis characteristics and kinetic parameters determination of biomass fuel powders by differential thermal gravimetric analysis (TGA/DTG)," *Energy Convers. Manag.*, vol. 85, pp. 165–172, Sep. 2014.

[94] G. Varhegyi, M. J. Antal, T. Szekely, and P. Szabo, "Kinetics of the thermal decomposition of cellulose, hemicellulose, and sugarcane bagasse," *Energy & Fuels*, vol. 3, no. 3, pp. 329–335, May 1989.

[95] E. M. Fisher *et al.*, "Combustion and gasification characteristics of chars from raw and torrefied biomass," *Bioresour. Technol.*, vol. 119, pp. 157–165, Sep. 2012.

[96] L. Therssen, E., Gourichon, L., & Delfosse, "Devolatilization of Coal Particles in a Flat Flame Experimental and Modeling Study," *Combust. Flame*, vol. 2180, no. 95, pp. 115–128, 1995.

[97] J. T. Kuo and C.-L. Hsi, "Pyrolysis and ignition of single wooden spheres heated in high-temperature streams of air," *Combust. Flame*, vol. 142, no. 4, pp. 401–412, Sep. 2005.

[98] A. C. Sarroza, T. D. Bennet, C. Eastwick, and H. Liu, "Characterising pulverised fuel ignition in a visual drop tube furnace by use of a high-speed imaging technique," *Fuel Process. Technol.*, vol. 157, pp. 1–11, Mar. 2017.

[99] T. Grotkjær, K. Dam-Johansen, A. D. Jensen, and P. Glarborg, "An experimental study of biomass ignition," *Fuel*, vol. 82, no. 7, pp. 825–833, May 2003.

[100] B. Damstedt, J. Pederson, D. Hansen, T. Knighton, J. Jones, C. Christensen, L. Baxter, D. Tree, "Biomass cofiring impacts on flame structure and emissions," *Proc. Combust. Inst.*, vol. 31, no. 2, pp. 2813–2820, Jan. 2007.

[101] S. Zellagui, *C. Schönnenbeck, N. Zouaoui-Mahzoul, G. Leyssens, O. Authier, E. Thunin, L. Porcheron, J. Brilhac*, "Pyrolysis of coal and woody biomass under N_2 and CO_2 atmospheres using a drop tube furnace - experimental study and kinetic modeling," *Fuel Process. Technol.*, vol. 148, pp. 99–109, Jul. 2016.

[102] S. K. Ouiminga, T. Rogaume, M. Sougoti, J. M. Commandre, and J. Koulidiati, "Experimental characterization of gaseous species emitted by the fast pyrolysis of biomass and polyethylene," *J. Anal. Appl. Pyrolysis*, vol. 86, no. 2, pp. 260–268, Nov. 2009.

[103] D. Neves, A. Matos, L. Tarelho, H. Thunman, A. Larsson, and M. Seemann, "Volatile

gases from biomass pyrolysis under conditions relevant for fluidized bed gasifiers," *J. Anal. Appl. Pyrolysis*, vol. 127, pp. 57–67, Sep. 2017.

[104] J.-M. Commandré, H. Lahmidi, S. Salvador, and N. Dupassieux, "Pyrolysis of wood at high temperature: The influence of experimental parameters on gaseous products," *Fuel Process. Technol.*, vol. 92, no. 5, pp. 837–844, May 2011.

[105] S. Septien, S. Valin, C. Dupont, M. Peyrot, and S. Salvador, "Effect of particle size and temperature on woody biomass fast pyrolysis at high temperature (1000–1400°C)," *Fuel*, vol. 97, pp. 202–210, Jul. 2012.

[106] A. Dufour *et al.*, "Mechanisms and Kinetics of Methane Thermal Conversion in a Syngas," *Ind. Eng. Chem. Res.*, vol. 48, no. 14, pp. 6564–6572, Jul. 2009.

[107] C. Dupont, J.-M. Commandré, P. Gauthier, G. Boissonnet, S. Salvador, and D. Schweich, "Biomass pyrolysis experiments in an analytical entrained flow reactor between 1073K and 1273K," *Fuel*, vol. 87, no. 7, pp. 1155–1164, Jun. 2008.

[108] H. Lu, E. Ip, J. Scott, P. Foster, M. Vickers, and L. L. Baxter, "Effects of particle shape and size on devolatilization of biomass particle," *Fuel*, vol. 89, no. 5, pp. 1156–1168, May 2010.

[109] L. Chen, C. Dupont, S. Sylvain, G. Boissonnet, and D. Schweich, "Fast Pyrolysis of Biomass Under Gasification Conditions: Influence of Particle Size, Reactor Temperature and Gas Phase Reactions.," 2011.

[110] V. Branco and M. Costa, "Effect of particle size on the burnout and emissions of particulate matter from the combustion of pulverized agricultural residues in a drop tube furnace," *Energy Convers. Manag.*, vol. 149, pp. 774–780, Oct. 2017.

[111] A. Elfasakhany, L. Tao, B. Espenas, J. Larfeldt, and X. S. Bai, "Pulverised wood combustion in a vertical furnace: Experimental and computational analyses," *Appl. Energy*, vol. 112, pp. 454–464, Dec. 2013.

[112] R. Boukara, R. Gadiou, P. Gilot, L. Delfosse, and G. Prado, "Study of the ignition of single coal and char particles in a drop tube furnace by a probability method," *Proc. Combust. Inst.*, vol. 24, no. 1, pp. 1127–1133, Jan. 1992.

[113] C. Avila, C. H. Pang, T. Wu, and E. Lester, "Morphology and reactivity characteristics of char biomass particles," *Bioresour. Technol.*, vol. 102, no. 8, pp. 5237–5243, Apr. 2011.

[114] L. Wei, S. Xu, L. Zhang, H. Zhang, C. Liu, H. Zhu, S. Liu, "Characteristics of fast pyrolysis of biomass in a free fall reactor," *Fuel Process. Technol.*, vol. 87, no. 10, pp. 863–871, Oct. 2006.

[115] R. Zanzi, K. Sjöström, and E. Björnbom, "Rapid pyrolysis of agricultural residues at high temperature," *Biomass and Bioenergy*, vol. 23, no. 5, pp. 357–366, Nov. 2002.

[116] J. H. A. K. P.C.A. Bergman, A.R. Boersma, R.W.R. Zwert, "Torrefaction for biomass co-firing in existing coal-fired power stations."

[117] J. Bourgeois, J. P. ; Doat, "Torrefied wood from temperature and tropical species: Advantages and prospects," in *Bioenergy 84. Proceedings of conference 15-21 June 1984, Goteborg, Sweden. Volume III. Biomass conversion*, 1984, pp. 153–159.

[118] V. Repellin, A. Govin, M. Rolland, and R. Guyonnet, “Energy requirement for fine grinding of torrefied wood,” *Biomass and Bioenergy*, vol. 34, no. 7, pp. 923–930, Jul. 2010.

[119] R. Pentananunt, A. N. M. M. Rahman, and S. C. Bhattacharya, “Upgrading of biomass by means of torrefaction,” *Energy*, vol. 15, no. 12, pp. 1175–1179, Dec. 1990.

[120] C. Di Blasi, “Combustion and gasification rates of lignocellulosic chars,” *Prog. Energy Combust. Sci.*, vol. 35, no. 2, pp. 121–140, Apr. 2009.

[121] H.-S. Shim and R. H. Hurt, “Thermal Annealing of Chars from Diverse Organic Precursors under Combustion-like Conditions,” *Energy & Fuels*, vol. 14, no. 2, pp. 340–348, Mar. 2000.

[122] F. F. Costa and M. Costa, “Particle fragmentation of raw and torrefied biomass during combustion in a drop tube furnace,” *Fuel*, vol. 159, pp. 530–537, Nov. 2015.

[123] X. Gao and H. Wu, “Biochar as a Fuel: 4. Emission Behavior and Characteristics of PM 1 and PM 10 from the Combustion of Pulverized Biochar in a Drop-Tube Furnace,” *Energy & Fuels*, vol. 25, no. 6, pp. 2702–2710, Jun. 2011.

[124] S. Yani, X. Gao, and H. Wu, “Emission of Inorganic PM 10 from the Combustion of Torrefi ed Biomass under Pulverized-Fuel Conditions,” 2015.

[125] D. Ristic, A. Schuster, J. Santamaria, P. Plion, G. Hesselmann, J. Wünning, D. Honoré, D. Giannakopoulos, H. Stadler, M. Förster, B. Swiatkowski, E. Kinal, “Development of a pilot-scale flameless oxidation burner for ultra-low NOx combustion of pulverised coal,” Working paper 2008, DOI: 10.2777/80339.

[126] M. Weidmann, D. Honoré, V. Verbaere, G. Boutin, S. Grathwohl, G. Godard, C. Gobin, R. Kneer, G. Scheffknecht, “Experimental characterization of pulverized coal MILD flameless combustion from detailed measurements in a pilot-scale facility,” *Combust. Flame*, vol. 168, pp. 365–377, Jun. 2016.

[127] M. Mandø, L. Rosendahl, C. Yin, and H. Sørensen, “Pulverized straw combustion in a low-NOx multifuel burner: Modeling the transition from coal to straw,” *Fuel*, vol. 89, no. 10, pp. 3051–3062, Oct. 2010.

[128] C. Yin, L. Rosendahl, and S. K. Kær, “Towards a better understanding of biomass suspension co-firing impacts via investigating a coal flame and a biomass flame in a swirl-stabilized burner flow reactor under same conditions,” *Fuel Process. Technol.*, vol. 98, pp. 65–73, Jun. 2012.

[129] R. Weber, T. Kupka, and K. Zając, “Jet flames of a refuse derived fuel,” *Combust. Flame*, vol. 156, no. 4, pp. 922–927, Apr. 2009.

[130] E. C. Efika, J. A. Onwudili, and P. T. Williams, “Products from the high temperature pyrolysis of RDF at slow and rapid heating rates,” *J. Anal. Appl. Pyrolysis*, vol. 112, pp. 14–22, Mar. 2015.

[131] H. W. Daniel Nordgren, N. Berglin, L. Rangmark, T. Ekman, C. Grönberg, “Studies of heat transfer and furnace temperature uniformity during combustion of oil and wood using oxygen enrichment technology,” in *Swedish-Finnish Flame Days*, 2011.

[132] “Office National des Forets.” [Online]. Available:

http://www1.onf.fr/activites_nature/sommaire/decouvrir/arbres/resineux/20071025-083844-82532/@@index.html.

[133] D. A. da Silva, E. Eloy, B. O. Caron, and P. F. Trugilho, "Elemental Chemical Composition of Forest Biomass at Different Ages for Energy Purposes," *Floresta e Ambient.*, vol. 26, no. 4, 2019.

[134] K. Slopiecka, P. Bartocci, and F. Fantozzi, "Thermogravimetric analysis and kinetic study of poplar wood pyrolysis," *Appl. Energy*, vol. 97, pp. 491–497, Sep. 2012.

[135] J. Andrzejewski, A. Charlet, P. Higelin, A. Sapinski, and G. Vaitilingom, "Procédé et dispositif de mesure de la vitesse d'évaporation et du délai d'inflammation d'un carburant liquide .," Brevet FR2694092 A1.

[136] Sternberg, "Biomedical Image Processing," *Computer (Long. Beach. Calif).*, vol. 16, no. 1, pp. 22–34, Jan. 1983.

[137] T. Ridler and Calvard, "Picture Thresholding Using an Iterative Selection Method," *IEEE Trans. Syst. Man. Cybern.*, vol. 8, no. 8, pp. 630–632, 1978.

[138] "https://imagej.net/Auto_Threshold#Try_all." .

[139] S. A. Scott, J. F. Davidson, J. S. Dennis, and A. N. Hayhurst, "The devolatilisation of particles of a complex fuel (dried sewage sludge) in a fluidised bed," *Chem. Eng. Sci.*, vol. 62, no. 1–2, pp. 584–598, Jan. 2007.

[140] L. Van de Steene, "Thermochimie de la combustion à basses températures de solides pulvérisés : application à un charbon," Thèse de Doctorat, INPT Toulouse, 1999.

[141] J.-M. Commandré, "Formation des oxydes d'azote lors de la combustion de cokes de pétrole dans des conditions de précalcinateur de cimenterie," Thèse de Doctorat, L'Institut National Polytechnique de Toulouse, 2002.

[142] J. Cances, "NOx formation and reduction by a coal, a lignite, an anthracite and a petroleum coke in conditions of cement plant calciner," Thèse de Doctorat, INP Toulouse, 2006.

[143] C. Dupont, "Vapogazéification de la biomasse : contribution à l'étude de la phénoménologie entre 800 et 1000 °C," Thèse de Doctorat, Lyon 1, 2006.

[144] L. Chen, "Fast pyrolysis of millimetric wood particles between 800°C and 1000°C," Thèse de Doctorat, Lyon 1, 2009.

[145] J. Billaud, "Gazéification de la biomasse en réacteur à flux entrainé : études expérimentales et modélisation," l'Ecole nationale des Mines d'Albi-Carmaux, 2015.

[146] L. A. Juniper and J. H. Pohl, "Design of Pilot scale rigs to simulate combustion processes," in *Australian symposium on combustion*, 1995, pp. 1–6.

[147] Z. Xi, Z. Fu, X. Hu, S. Sabir, and Y. Jiang, "An Investigation on Flame Shape and Size for a High-Pressure Turbulent Non-Premixed Swirl Combustion," *Energies*, vol. 11, no. 4, p. 930, Apr. 2018.

[148] J. Saastamoinen, M. Aho, A. Moilanen, L. H. Sørensen, S. Clausen, and M. Berg, "Burnout of pulverized biomass particles in large scale boiler: Single particle model approach," *Biomass and Bioenergy*, vol. 34, pp. 728–736, 2010.

[149] C. A. G. Veras, J. Saastamoinen, and João Andrade De Carvalho Jr., "Effect of particle size and pressure on the conversion of fuel N to no in the boundary layer during devolatilization stage of combustion," *Proc. Combust. Inst.*, vol. 27, no. 2, pp. 3019–3025, 1998.

[150] L. Ma, J. M. Jones, M. Pourkashanian, and A. Williams, "Modelling the combustion of pulverized biomass in an industrial combustion test furnace," *Fuel*, vol. 86, no. 12–13, pp. 1959–1965, Aug. 2007.

[151] G. E. Ogden, "Pulverized coal combustion: Flame attachement and NOx emissions," Ph.D. Thesis, The University of Arizona, 2002.

[152] N. Muanza, "Investigation into fly ash production during co-firing of biomass with pulverised coal," Ph.D. Thesis, University of the Witwatersrand, 2009.

[153] R. Gupta, T. Wall, and L. Baxter, *Impact of Mineral Impurities in Solid Fuel Combustion*, Illustrate. Springer Science & Business Media, 2007.

[154] Gregory Edwin Ogden, "Pulverized coal combustion: Flame attachement and NOx emissions," Ph.D. Thesis, The University of Arizona, 2002.

[155] J. Zhang, "Oxy-coal combustion: Stability of coaxial pulverized coal flames in O2/CO2 environments," Ph.D. Thesis, The University of Utah.

[156] P. Ayazi Shamlou, *Processing solid-liquid suspension*. Book ISBN: 1483129721, Butterworth-Heinemann, 2013.

[157] "Bluff-body and flames," *The University of Sydney*, 2002. [Online]. Available: http://web.aeromech.usyd.edu.au/thermofluids/bluff.php. [Accessed: 15-Jan-2019].

[158] A. M. K. P. Taylor and J. H. Whitelaw, "Velocity characteristics in the turbulent near wakes of confined axisymmetric bluff bodies," *J. Fluid Mech.*, vol. 139, pp. 391–416, 1984.

[159] Jerrod D. Isaak and N. Wibisono, "Biomass Combustion Evaluation Final Report," Report, Western Research Institute, Energy Production and Generation, 2016.

[160] A. Burge, B. King, and B. Nitsch, "Reducing NOx via Replacement Burners, Overfire Air & Optimized Combustion," Technical paper, Nebraska Public Power District NPPD, 2006.

[161] P. Molcan, G. Lu, T. Le Bris, Y. Yan, B. Taupin, and S. Caillat, "Characterisation of biomass and coal co-firing on a 3MWth Combustion Test Facility using flame imaging and gas/ash sampling techniques," *Fuel*, vol. 88, no. 12, pp. 2328–2334, Dec. 2009.

[162] G. Richards, D. Towle, R. Lewis, K. Connolly, R. Donais, and T. Hellewell, "Development of an enhanced combustion low NOx pulverized coal burner," Technical report, ALSTOM Power Inc., Windsor, CT 06095, 2006.

[163] S. Su, J. . Pohl, D. Holcombe, and J. . Hart, "Techniques to determine ignition, flame stability and burnout of blended coals in p.f. power station boilers," *Prog. Energy Combust. Sci.*, vol. 27, no. 1, pp. 75–98, Jan. 2001.

[164] K. L. Cashdollar, "Overview of dust explosibility characteristics," *J. Loss Prev. Process Ind.*, vol. 13, no. 3–5, pp. 183–199, May 2000.

[165] L. Mihăescu, T. Prisecaru, G. Manuela Elena, G. Lăzăroiu, I. Oprea, I. Pâşă, G Negreanu, E. Pop, V. Berbece, "Construction and testing of a 600 KW burner for sawdust in suspension," 2011.

[166] White Frank M., *Fluid Mechanics (Mcgraw-hill Series in Mechanical Engineering)*, 7th ed. 2010.

[167] T. Morel, "Comprehensive design of axisymmetric wind tunnel contractions," *J. Fluids Eng.*, vol. Contribute, 1975.

[168] N. Lallemant, J. Dugué, and R. Weber, "Measurement techniques for studying oxy-natural gas flames," *J. Energy Inst.*, vol. 76, no. 507, pp. 38–53, 2003.

[169] T. Kathrotia, U. Riedel, and J. Warnatz, "A Numerical Study on the Relation of OH*, CH*, and C_2* Chemiluminescence and Heat Release in Premixed Methane Flames," in *Proceedings of the European Combustion Meeting*, 2009.

[170] T. Kathrotia, "Reaction Kinetics Modeling of OH*, CH*, and C2* Chemiluminescence," Ph.D. Thesis, Universität Heidelberg, 2011.

[171] D. Honoré, "Une approche expérimentale par diagnostics optiques de nouveaux concepts de combustion dans les foyers industriels," Habilitation à Diriger des Recherches de l'Université de Rouen, 2014.

[172] C. Moon, Y. Sung, S. Ahn, T. Kim, G. Choi, and D. Kim, "Effect of blending ratio on combustion performance in blends of biomass and coals of different ranks," *Exp. Therm. Fluid Sci.*, vol. 47, pp. 232–240, May 2013.

[173] C. Moon, Y. Sung, S. Ahn, T. Kim, G. Choi, and D. Kim, "Effect of blending ratio on combustion performance in blends of biomass and coals of different ranks," *Exp. Therm. Fluid Sci.*, vol. 47, pp. 232–240, May 2013.

[174] Y. Sung and G. Choi, "Non-intrusive optical diagnostics of co- and counter-swirling flames in a dual swirl pulverized coal combustion burner," *Fuel*, vol. 174, pp. 76–88, Jun. 2016.

[175] Y. Sung *et al.*, "Optical non-intrusive measurements of internal recirculation zone of pulverized coal swirling flames with secondary swirl intensity," *Energy*, vol. 103, pp. 61–74, May 2016.

[176] J.-M. Commandré, S. Salvadore, L. Van de Steen, and R. Gadiou, "The Formation and Reduction of NO During The Combustion of Petroluem Coke- The case of Cement Plant Precalciner Condtions," *Combust. Sci. Technol.*, vol. 177, no. 3, pp. 579–611, Feb. 2005.

[177] F. F. Costa, G. Wang, and M. Costa, "Combustion Kinetics and Particle Fragmentation of Raw and Torrified Pine shells and olive stones in a Drop Tube Furnace," *Proc. Combust. Inst.*, vol. 35, no. 3, pp. 3591–3599, 2015.

[178] T. S. Farrow, C. Sun, and C. E. Snape, "Impact of CO_2 on biomass pyrolysis, nitrogen partitioning, and char combustion in a drop tube furnace," *J. Anal. Appl. Pyrolysis*, vol. 113, pp. 323–331, May 2015.

[179] J. Ballester and S. Jiménez, "Kinetic parameters for the oxidation of pulverised coal as measured from drop tube tests," *Combust. Flame*, vol. 142, pp. 210–222, 2005.

[180] S. Pereira, P. C. R. Martins, and M. Costa, “Kinetics of Poplar Short Rotation Coppice Obtained from Thermogravimetric and Drop Tube Furnace Experiments,” *Energy & Fuels*, vol. 30, no. 8, pp. 6525–6536, Aug. 2016.

[181] “Air - Diffusion Coefficients of Gases in Excess of Air.,” *Engineering ToolBox*, 2018. [Online]. Available: https://www.engineeringtoolbox.com/air-diffusion-coefficient-gas-mixture-temperature-d_2010.html. [Accessed: 27-Sep-2018].

[182] M. De Souza-Santos, *Solid Fuels Combustion and Gasification Modeling, Simulation, and Equipment Operations*, Second edi. New York: Taylor & Francis Group, 2010.

[183] K. M. Bryden, K. W. Ragland, and C. J. Rutland, “Modeling thermally thick pyrolysis of wood,” *Biomass and Bioenergy*, vol. 22, no. 1, pp. 41–53, Jan. 2002.

[184] A. Aissa, M. Abdelouahab, A. Noureddine, M. El Ganaoui, B. Pateyron, “Ranz and Marshall Correlations Limits on Heat Flow Between a Sphere and its Surrounding Gas at High Temperature To cite this version : HAL Id : hal-01599788,” 2017.

[185] C. Dupont, R. Chiriac, G. Gauthier, and F. Toche, “Heat capacity measurements of various biomass types and pyrolysis residues,” *Fuel*, vol. 115, pp. 644–651, Jan. 2014.

[186] R. S. Subramanian, “Heat transfer in Flow Through Conduits,” Working paper, Department of Chemical and Biomolecular Engineering, Clarkson University 2014.

[187] N. Darabiha, E. Esposito, F. Lacas, and D. Veynante, *Combustion*, Combustion, Book Edition 2.2, 2006.

[188] T. Poinsot and D. Veynante, *Theoretical and Numerical Combustion*, 2nd edition. Philadelphia, USA: R.T. Edwards Inc., 2005.

[189] T. F. Dixon, A. P. Mann, F. Plaza, and W. N. Gilfillan, “Development of advanced technology for biomass combustion—CFD as an essential tool,” *Fuel*, vol. 84, no. 10, pp. 1303–1311, Jul. 2005.

[190] K. S. Shanmukharadhya, “Simulation and Thermal Analysis of the Effect of Fuel Size on Combustion in an Industrial Biomass Furnace,” *Energy & Fuels*, vol. 21, no. 4, pp. 1895–1900, Jul. 2007.

[191] F. Marias, “A model of a rotary kiln incinerator including processes occurring within the solid and the gaseous phases,” *Comput. Chem. Eng.*, vol. 27, no. 6, pp. 813–825, Jun. 2003.

[192] D. Gera, M. P. Mathur, M. C. Freeman, and A. Robinson, “Effect of Large Aspect Ratio of Biomass Particles on Carbon Burnout in a Utility Boiler,” *Energy & Fuels*, vol. 16, no. 6, pp. 1523–1532, Nov. 2002.

[193] J. W. Rogerson, J. H. Kent, and R. W. Bilger, “Conditional moment closure in a bagasse-fired boiler,” *Proc. Combust. Inst.*, vol. 31, no. 2, pp. 2805–2811, Jan. 2007.

[194] A. Elorf and B. Sarh, “Case Studies in Thermal Engineering Excess air ratio effects on flow and combustion caracteristics of pulverized biomass (olive cake),” *Case Stud. Therm. Eng.*, vol. 13, no. November 2018, p. 100367, 2019.

[195] A. Haider and O. Levenspiel, “Drag coefficient and terminal velocity of spherical and nonspherical particles,” *Powder Technol.*, vol. 58, no. 1, pp. 63–70, May 1989.

[196] N. Niemelä, "Computational fluid dynamics modeling of pulverized biomass combustion using optimized reactivity paramaters," Master Thesis, Tampere University of Technology, 2015.

[197] J.-M. Commandré, H. Lahmidi, S. Salvador, and N. Dupassieux, "Pyrolysis of wood at high temperature: The influence of experimental parameters on gaseous products," *Fuel Process. Technol.*, vol. 92, no. 5, pp. 837–844, May 2011.

[198] J. Zhao, S. Niu, Y. Li, K. Han, and C. Lu, "Thermogravimetric Analysis and Kinetics of Combustion of Raw and Torrefied pine Sawdust," *J. Chem. Eng. Japan*, vol. 48, no. 4, pp. 320–325, 2015.

[199] S. Y. Yorulmaz and A. T. Atimtay, "Investigation of combustion kinetics of treated and untreated waste wood samples with thermogravimetric analysis," *Fuel Process. Technol.*, vol. 90, no. 7–8, pp. 939–946, Jul. 2009.

[200] M. Stalin and G. Teixeira, "Comportement thermochimique de la biomasse pour une application en combustion pulvérisée,", Raport de Master de L'Université de Rouen, 2015.

[201] N. Gao, A. Li, C. Quan, L. Du, and Y. Duan, "TG–FTIR and Py–GC/MS analysis on pyrolysis and combustion of Pine sawdust," *J. Anal. Appl. Pyrolysis*, vol. 100, pp. 26–32, Mar. 2013.

[202] D. K. Shen, S. Gu, K. H. Luo, A. V. Bridgwater, and M. X. Fang, "Kinetic study on thermal decomposition of woods in oxidative environment," *Fuel*, vol. 88, no. 6, pp. 1024–1030, Jun. 2009.

[203] A. Dhaundiyal and J. Gangwar, "Kinetics of the thermal decomposition of Pine needles," *Acta Univ. Sapientiae, Agric. Environ.*, vol. 7, no. 1, pp. 5–22, Dec. 2015.

[204] O. P. Korobeinichev, A. A. Paletsky, M. B. Gonchikzhapov, I. K. Shundrina, H. Chen, and N. Liu, "Combustion Chemistry and Decomposition Kinetics of Forest Fuels," *Procedia Eng.*, vol. 62, pp. 182–193, 2013.

[205] N. Yub Harun and M. T. Afzal, "Thermal Decomposition Kinetics of Forest Residue," *J. Appl. Sci.*, vol. 10, no. 12, pp. 1122–1127, Dec. 2010.

[206] J. Bai, C. Yu, L. Li, P. Wu, Z. Luo, and M. Ni, "Experimental Study on the NO and N_2O Formation Characteristics during Biomass Combustion," *Energy & Fuels*, vol. 27, no. 1, pp. 515–522, Jan. 2013.

[207] J. Giuntoli, W. de Jong, A. H. M. Verkooijen, P. Piotrowska, M. Zevenhoven, and M. Hupa, "Combustion Characteristics of Biomass Residues and Biowastes: Fate of Fuel Nitrogen," *Energy & Fuels*, vol. 24, no. 10, pp. 5309–5319, Oct. 2010.

[208] E. Houshfar, L. Wang, N. Vähä-Savo, A. Brink, and T. Løvås, "Characterisation of CO/NO/SO2 emission and ash-forming elements from the combustion and pyrolysis process," *Clean Technol. Environ. Policy*, vol. 16, no. 7, pp. 1339–1351, Oct. 2014.

[209] J. Riaza, R. Khatami, Y.A. Levendis, L. Álvarez, M.V. Gil, C. Pevida, F. Rubiera, J.J. Pis, "Combustion of single biomass particles in air and in oxy-fuel conditions," *Biomass and Bioenergy*, vol. 64, pp. 162–174, May 2014.

[210] P. J. Austin, C. W. Kauffman, and M. Sichel, "Ignition and Volatile Combustion of

Cellulosic Dust Particles," *Combust. Sci. Technol.*, vol. 112, no. 1, pp. 187–198, Jan. 1996.

[211] J. Li, M. C. Paul, and K. M. Czajka, "Studies of Ignition Behavior of Biomass Particles in a Down-Fire Reactor for Improving Co-firing Performance," *Energy & Fuels*, vol. 30, no. 7, pp. 5870–5877, Jul. 2016.

[212] E. Gucho, K. Shahzad, E. Bramer, N. Akhtar, and G. Brem, "Experimental Study on Dry Torrefaction of Beech Wood and Miscanthus," *Energies*, vol. 8, no. 5, pp. 3903–3923, May 2015.

[213] P. E. Mason, L. I. Darvell, J. M. Jones, M. Pourkashanian, and A. Williams, "Single particle flame-combustion studies on solid biomass fuels," *Fuel*, vol. 151, pp. 21–30, Jul. 2015.

[214] F. S. Akinrinola, "Torrefaction and Combustion Properties of some Nigerian Biomass," The University of Leeds, 2014.

[215] T. G. Bridgeman, J. M. Jones, I. Shield, and P. T. Williams, "Torrefaction of reed canary grass, wheat straw and willow to enhance solid fuel qualities and combustion properties," *Fuel*, vol. 87, no. 6, pp. 844–856, May 2008.

[216] A. Panahi, Y. A. Levendis, N. Vorobiev, and M. Schiemann, "Direct observations on the combustion characteristics of Miscanthus and Beechwood biomass including fusion and spherodization," *Fuel Process. Technol.*, vol. 166, pp. 41–49, Nov. 2017.

[217] C. Meesri and B. Moghtaderi, "Experimental and numerical analysis of sawdust-char combustion reactivity in a drop tube reactor," *Combust. Sci. Technol.*, vol. 175, no. 4, pp. 793–823, Apr. 2003.

[218] J. Riaza, J. Gibbins, and H. Chalmers, "Ignition and combustion of single particles of coal and biomass," *Fuel*, vol. 202, pp. 650–655, Aug. 2017.

[219] M. V. Gil, J. Riaza, L. Álvarez, C. Pevida, J. J. Pis, and F. Rubiera, "Oxy-fuel combustion kinetics and morphology of coal chars obtained in N2 and CO2 atmospheres in an entrained flow reactor," *Appl. Energy*, vol. 91, no. 1, pp. 67–74, Mar. 2012.

[220] W. J. McLean, D. R. Hardesty, and J. H. Pohl, "Direct observations of devolatilizing pulverized coal particles in a combustion environment," *Proc. Combust. Inst.*, vol. 18, no. 1, pp. 1239–1248, 1981.

[221] R. Khatami, C. Stivers, and Y. A. Levendis, "Ignition characteristics of single coal particles from three different ranks in O_2/N_2 and O_2/CO_2 atmospheres," *Combust. Flame*, vol. 159, no. 12, pp. 3554–3568, Dec. 2012.

[222] J. Riaza, R. Khatami, Y.A. Levendis, L. Álvarez, M.V. Gil, C. Pevida, F. Rubiera, J.J. Pis, "Single particle ignition and combustion of anthracite, semi-anthracite and bituminous coals in air and simulated oxy-fuel conditions," *Combust. Flame*, vol. 161, no. 4, pp. 1096–1108, Apr. 2014.

[223] E. Marek and B. Świątkowski, "Experimental studies of single particle combustion in air and different oxy-fuel atmospheres," *Appl. Therm. Eng.*, vol. 66, no. 1–2, pp. 35–42, May 2014.

[224] U. Olsbye, O. Moen, Å. Slagtern, and I. M. Dahl, “An investigation of the coking properties of fixed and fluid bed reactors during methane-to-synthesis gas reactions,” *Appl. Catal. A Gen.*, vol. 228, no. 1–2, pp. 289–303, Mar. 2002.

[225] K. Matsumoto, K. Takeno, T. Ichinose, T. Ogi, and M. Nakanishi, “Gasification reaction kinetics on biomass char obtained as a by-product of gasification in an entrained-flow gasifier with steam and oxygen at 900–1000°C,” *Fuel*, vol. 88, no. 3, pp. 519–527, Mar. 2009.

[226] P. Ollero, A. Serrera, R. Arjona, and S. Alcantarilla, “The CO_2 gasification kinetics of olive residue,” *Biomass and Bioenergy*, vol. 24, no. 2, pp. 151–161, Feb. 2003.

[227] T. R. Ballantyne, P. J. Ashman, and P. J. Mullinger, “A new method for determining the conversion of low-ash coals using synthetic ash as a tracer,” *Fuel*, vol. 84, no. 14–15, pp. 1980–1985, Oct. 2005.

[228] C. Storm, H. Rüdiger, H. Spliethoff, and K. R. G. Hein, “Co-Pyrolysis of Coal/Biomass and Coal/Sewage Sludge Mixtures,” *J. Eng. Gas Turbines Power*, vol. 121, no. 1, pp. 55–63, 1999.

[229] I. W. Smith, “The kinetics of combustion of pulverized semi-anthracite in the temperature range 1400–2200 K,” *Combust. Flame*, vol. 17, no. 3, pp. 421–428, Dec. 1971.

[230] Palo Sidwell Pokothoane, “Analysis of co-firinf of biomass with South African coal in pulverised coal boilers.,” Ph.D. Thesis, University of the Witwatersrand, 2010.

[231] R. C. R. Lima, R. F. B. Gonçalves, Manoel F. M. Nogueira, and Danielle R. S. Guerra, “Simulation study of biomass powder combustion in cyclonic furnace,” in *23rd ABCM International Congress of Mechanical Engineering*, 2015.

[232] “Fluent theory guide: Pressure-Velocity Coupling, ‘https://www.afs.enea.it/project/neptunius/docs/fluent/html/th/node373.htm,’” *Ansys Inc.* .

[233] “Fluent theory guide: Spatial Discretization, ‘https://www.afs.enea.it/project/neptunius/docs/fluent/html/th/node366.htm,’” *Ansys Inc.* .

[234] “https://en.wikipedia.org/wiki/Heat_transfer_coefficient.” [Online]. Available: https://en.wikipedia.org/wiki/Heat_transfer_coefficient. [Accessed: 10-Feb-2018].

Abstract

The world efforts to reduce the dangerous levels of pollution present biomass as an attractive fuel for the industrial power plants. Its abundance, sustainability and its resemblance to coal, makes it a potential candidate of incorporating it with coal in the existing infrastructure. This work is an experimental and numerical study of the combustion of pulverized biomass at both particle and flame scale. The diversity of biomass was simulated using torrefaction of raw Pine, in order to produce other types of biomass with controlled volatile content (VM). Three torrefaction degrees beside demolition wood and coal were studied at particle scale. Different experimental methods including horizontal tubular reactor, drop tube furnace and single particle reactor were used to provide a detailed characterization of the degradation process of a single particle. The results provided the proximate and ultimate analysis, pyrolysis gas composition, particle degradation, combustion gas emissions, combustion timeline, and the morphological evolution of the particle. The results show that higher VM particles undergo intense devolatilization for comparable durations as less volatile containing fuel. On the other hand, the char left is more reactive and burn faster than the char resulting from particles with lower VM content. However, the heterogeneous ignition is observed to occur earlier for larger particles containing lower volatile matter, forming larger overlap between the combustion phases. A numerical model was developed using the experimental data collected at particle scale to simulate the combustion of a single particle in the drop tube furnace. The model could derive the kinetics parameters of devolatilization and char oxidation from the degradation curves. The predictions are in accordance with the experimental measurements of oxygen and carbon monoxide concentrations and the conclusions are consistent with those obtained in the above experimental methods. The particle model was integrated in a CFD model applied to a pilot scale combustion facility specially designed for pulverized biomass combustion. The model is validated and completed by the experimental data collected on the pilot scale reactor including a detailed description of the spatial distributions species concentrations beside the OH* chemiluminescence images of three flames of Pine, torrefied pine and pyrolyzed pine. The model results match satisfyingly well the experimental results. The studied flames are long lifted jet flames, forming a large outer recirculation zone around the central jet. The topology and intensity of the reaction zone is determined by the volatile content of the fuel and its reactivity. The particle size distribution also plays a key role on the onset and the position of the reaction zone. Fuels with finer particle size distribution are found to be more influenced by the aerodynamic structures. Their devolatilization occurs in the jet and the chars are captured by the recirculation zone where they get oxidized. On the other hand, the wide particle size distribution of Pine creates two-devolatilization stages leading to lower NOx, and the large particles tend to penetrate the recirculation zone and oxidize downstream.

Keywords: Combustion, Flame, Biomass, Wood, Torrefaction, Pulverized fuel, Pilot scale reactor, OH* chemiluminescence

Résumé

Les efforts pour réduire les niveaux dangereux des émissions polluantes à l'échelle de la planète, présentent la biomasse comme un combustible attractif pour les centrales thermiques industrielles. Son abondance, sa durabilité et ses caractéristiques physico-chimiques comparables à celles du charbon, en font un candidat potentiel pour l'intégrer au charbon dans les infrastructures existantes.

Ce travail est une étude expérimentale et numérique sur la combustion de la biomasse pulvérisée à l'échelle des particules et de la flamme. La diversité de la biomasse a été simulée en torréfiant du pin natif, afin de produire des biomasses à teneur contrôlée en matière volatile (MV). Trois degrés de torréfaction, en plus d'un bois de démolition et d'un charbon, ont ainsi été étudiés à l'échelle des particules. Différentes méthodes expérimentales comprenant un four tubulaire horizontal, un four à chute et un réacteur à particule isolée ont été utilisées pour fournir une caractérisation détaillée du processus de dégradation d'une seule particule. Les résultats donnent l'analyse immédiate et élémentaire de la particule, la composition chimique du gaz de pyrolyse, le degré de dégradation des particules, les émissions gazeuses de combustion, les temps caractéristiques de combustion et l'évolution morphologique de la particule. Ils montrent que les particules de teneur en matière volatile plus élevée subissent une dévolatilisation plus intense, à durées de flamme comparables. D'autre part, le char résiduel est plus réactif et brûle plus vite que le char résultant des particules de teneur en matière volatile inférieure. Cependant, on observe que l'allumage hétérogène se produit plus tôt pour les particules plus grosses contenant moins de matières volatiles. Un modèle numérique a été développé en utilisant les données expérimentales recueillies à l'échelle des particules, pour simuler la combustion d'une seule particule dans le four à chute. Le modèle permet de déterminer les paramètres cinétiques de la dévolatilisation et de l'oxydation du char à partir des courbes de dégradation de la biomasse. Les résultats sont en accord avec les mesures expérimentales de concentration d'oxygène et de monoxyde de carbone, et amènent des conclusions cohérentes avec celles obtenues à l'échelle de la particule. Le modèle de particules a été intégré dans un modèle CFD, appliqué à un pilote de combustion spécialement conçu pour la combustion de biomasse pulvérisée. Ce modèle a été validé et complété par les données expérimentales obtenues sur le réacteur à l'échelle pilote, comprenant une description détaillée des distributions spatiales des concentrations d'espèces chimiques ainsi que le suivi par chimiluminescence des radicaux OH* de trois flammes de pin, pin torréfié et pin pyrolysé. Les résultats du modèle sont en accord satisfaisant avec les résultats expérimentaux. Les flammes étudiées sont de longues flammes de jet non attaché, formant une grande zone de recirculation extérieure autour du jet central. La topologie et l'intensité de la zone réactionnelle sont déterminées par la teneur en matières volatiles du combustible et par sa réactivité. La distribution granulométrique joue également un rôle clé sur l'initiation et la position de la zone réactionnelle. Les biomasses de distribution granulométrique plus fine sont plus influencées par la structure aérodynamique. Leur dévolatilisation se produit dans le jet et les chars sont entraînés par la zone de recirculation où ils s'oxydent. D'autre part, la distribution granulométrique plus étalée du pin crée deux zones de dévolatilisation conduisant à une réduction des NOx, et les grosses particules ont tendance à pénétrer la zone de recirculation et à s'oxyder plus loin du brûleur.

Mots-clés: Combustion, Biomasse, Bois, Torréfaction, Combustible pulvérisé, Réacteur pilote, Chimiluminescence OH*